université PARIS-SACLAY

Search for optical nonlinearity in vacuum with intense laser fields, with the DeLLight experiment

Recherche de non linéarité optique du vide avec des lasers intenses auprès de l'expérience DeLLight

Thèse de doctorat de l'université Paris-Saclay

École doctorale n° 576, particules, hadrons, énergie et noyau : instrumentation, imagerie, cosmos et simulation (PHENIICS)
Spécialité de doctorat : physique des particules
Graduate School : Physique. Référent : Faculté des sciences d'Orsay

Thèse préparée dans l'unité de recherche **IJCLab (Université Paris-Saclay, CNRS)**, sous la direction de **Xavier SARAZIN**, Directeur de recherche, le co-encadrement de **François COUCHOT**, Directeur de recherche

Thèse soutenue à Paris-Saclay, le 9 février 2023, par

Aurélie Max Mailliet

Composition du jury

Membres du jury avec voix délibérative

Fabian Zomer Professeur, IJCLab, CNRS, Université Paris-Saclay	Président
Eric Constant Directeur de Recherche CNRS, Institut Lumière Matière, CNRS, Université Claude Bernard Lyon	Rapporteur & Examinateur
Guido Zavattini Professeur, Université de Ferrare	Rapporteur & Examinateur
Sophie Kazamias Professeure, IJCLab, CNRS, Université Paris-Saclay	Examinatrice
Catherine Le Blanc Ingénieure de recherche CNRS, Laboratoire Charles Fabry, Institut d'Optique Graduate School, Ecole Polytechnique	Examinatrice

THESE DE DOCTORAT

NNT : 2023UPASP017

université PARIS-SACLAY

ÉCOLE DOCTORALE
Particules, hadrons, énergie et noyau : instrumentation, imagerie, cosmos et simulation (PHENIICS)

Titre : Recherche de non linéarité optique du vide avec des lasers intenses auprès de l'expérience DeLLight

Mots clés : Vide QED non-linéaire en champ intense, Interférométrie, Analyse d'images CCD, Métrologie, Laser intense femtoseconde

Résumé : L'électrodynamique quantique (QED) prédit que le vide doit être un milieu optique non linéaire : la vitesse de la lumière dans le vide devrait diminuer lorsque le vide est soumis à des champs électromagnétiques intenses. Cet effet optique, similaire à l'effet Kerr optique dans les milieux matériels, n'a encore jamais été observé.

L'expérience DeLLight (Deflection of Light by Light) cherche à mesurer cet effet en utilisant des impulsions laser femtosecondes intenses délivrées par la plateforme LASERIX ($\mathcal{E} = 2.5$ J, 30 fs, 10 Hz) à l'IJCLab (Université Paris-Saclay). La méthode expérimentale consiste à mesurer par interférométrie la réfraction d'une impulsion laser (sonde) de basse énergie, induite par le gradient d'indice du vide produit par une impulsion externe (pompe) de haute intensité. On utilise alors un interféromètre de Sagnac, avec des impulsions pompe et sonde focalisées, qui permet de mesurer en sortie sombre le décalage transverse associé Δy du profil d'intensité grâce à une caméra CCD. L'avantage de la méthode interférométrique est que ce décalage transverse Δy est amplifié, comparé au décalage δy produit par la méthode standard de pointée. Le facteur d'amplification $\mathcal{A}$ (égal à $\Delta y/\delta y$) est inversement proportionnel à la racine carrée du facteur d'extinction $\mathcal{F}$, défini comme le rapport de l'intensité en sortie sombre par l'intensité du faisceau incident. La sensibilité de l'expérience dépend essentiellement de trois paramètres : le facteur d'extinction, la résolution spatiale et la qualité de la focalisation des impulsions pompe et sonde. L'objectif est d'atteindre une extinction $\mathcal{F} = 4 \times 10^{-6}$ (correspondant à une amplification $\mathcal{A} = 250$), une résolution spatiale $\sigma_y = 10$ nm et une largeur des faisceaux focalisés au foyer dans la zone d'interaction $w = 5$ μm. Cela correspond à un signal attendu $\Delta y = 0.015$ nm, pouvant être observé à 5 sigma avec un mois de données collectées.

Deux prototypes successifs d'interféromètre en régime femtoseconde ont été développés pendant la thèse (avec/sans focalisation). Ils ont permis de démontrer la faisabilité du projet et de caractériser les paramètres critiques limitant actuellement la sensibilité de l'expérience. Premièrement, le prototype avec focalisation a permis d'atteindre un facteur d'extinction de $\mathcal{F} = 3 \times 10^{-6}$, comme en était l'objectif. Ensuite, un banc de test dédié a permis de mesurer la résolution ultime de la caméra CCD sélectionnée qui correspond au bruit quantique : nous avons mesuré $\sigma_y = 13$ nm. Par ailleurs, la mesure de la résolution spatiale du signal d'interférence en sortie sombre a permis de montrer que les fluctuations de pointé du faisceau, mesurées simultanément, sont supprimées de façon effective permettant ainsi d'atteindre le bruit quantique avec un facteur d'amplification faible. En revanche avec une forte amplification, la résolution reste pour l'instant limitée par le bruit de phase, induit par le bruit mécanique de l'interféromètre. Une méthode pour mesurer le bruit de phase et le supprimer est en cours de test.

Finalement, nous avons pu valider la méthode de mesure interférométrique de l'expérience DeLLight en mesurant l'effet Kerr dans un milieu matériel en utilisant une impulsion pompe de faible énergie (μJ). Nous avons tout d'abord mesuré l'effet Kerr dans une lame de silice, sans focalisation des impulsions pompe et sonde dans l'interféromètre. Puis, nous avons mesuré l'effet Kerr dans l'air, avec focalisation de la sonde et de la pompe, et avec une amplification de 25. Nous avons vérifié que le signal Δy variait comme attendu en fonction de quatre paramètres expérimentaux : l'énergie de la pompe, le paramètre d'impact entre la pompe et la sonde en zone d'interaction, la polarisation relative pompe-sonde, et le délai de synchronisation temporelle de la pompe avec la sonde. La mesure dans l'air a été réalisée avec l'interféromètre pilote qui sera utilisé prochainement pour les premières mesures dans le vide.

Title : Search for optical nonlinearity in vacuum with intense laser fields, with the DeLLight experiment

Keywords : Nonlinear quantuum QED in intense field, Interferometry, CCD images analysis, Metrology, High intense femtosecond laser

Abstract : Quantum electrodynamics predicts that vacuum should be a non-linear optical medium : the speed of light in vacuum should decrease when the vacuum is stressed by intense electromagnetic fields. This optical phenomenon is similar to the optical Kerr effect in a material medium and has never been observed before.

The DeLLight (Deflection of Light by Light) experiment aims at measuring this effect using high intense femtosecond laser pulses delivered by the LASERIX platform ($\mathcal{E}$ = 2.5 J, 30 fs, 10 Hz) located at IJCLab laboratory (Paris-Saclay University). The experimental principle uses interferometry to measure the refraction of a low energy laser pulse (probe) on the vacuum index gradient induced by an external, high energy pulse (pump). To this end, we use a Sagnac interferometer with focalised probe and pump pulses, in order to measure the transverse shift Δy of the intensity profile in the dark output using a CCD camera. The benefit of this interferometric technique is to amplify the transverse shift Δy, unlike the shift δy obtained by the standard pointing measurement method. The amplification factor $\mathcal{A}$ (equal to the ratio $\Delta y/\delta y$) is inversely proportional to the square root of the extinction factor $\mathcal{F}$, which is defined by the ratio between the signal intensity in the dark output of the interferometer and the incident intensity. The experiment sensitivity mainly depends on three parameters : the extinction factor, the spatial resolution and the focalisation quality of the probe and pump pulses. The goal is to reach an extinction of $\mathcal{F} = 4\times10^{-6}$ (corresponding to an amplification of $\mathcal{A} = 250$), a spatial resolution of $\sigma_y = 10$ nm and a waist at focus of the beams in the interaction area of $w = 5$ μm. Thus, the expected signal is $\Delta y = 0.015$ nm, which can be measured at 5 sigma with one month of data collection.

During this PhD thesis, two interferometer prototypes in femtosecond regime were consecutively developed (with and without focalisation). They proved the feasibility of the project and the characterisation of critical parameters limiting the sensitivity of the experiment. First of all, we reached an extinction factor of $\mathcal{F} = 3 \times 10^{-6}$ using the prototype with focalisation, as was the goal. Then, a test bench was developed to measure the ultimate CCD camera resolution, which corresponds to the shot noise. We measured $\sigma_y = 13$ nm. Additionally, the spatial resolution measurement in the dark output led to prove that beam pointing fluctuations (simultaneous measurement) are completely suppressed, which allowed to reach the shot noise with a low amplification factor. However, the resolution is still limited by the phase noise induced by mechanical noise of the interferometer, with a high amplification factor. A technique to measure and suppress the phase noise is currently being tested.

At last, the interferometric measurement technique of the DeLLight experiment was validated by measuring the Kerr effect in a material medium using a low energy probe pulse (μJ). We first measured the Kerr effect in a silica slide, without focalisation of the probe and pump pulses in the interferometer. We then measured the Kerr effect in air, with focalisation of the probe and pump pulses, with an amplification of 25. We checked that the shift Δy fluctuated with four experimental parameters as expected, namely the pump energy, the impact parameter between the probe and the pump in the interaction area, the relative polarisation probe-pump, and the temporal synchronisation delay of the pump with the probe. The measurement in air was conducted with the pilot interferometer that will be used for the first measurements in vacuum in the near future.

Remerciements

Ces quatre années passées au sein de l'équipe DeLLight ont été pour moi une expérience magique ! Je me souviens encore de ce premier entretien avec Xavier et François pour mon stage de M2. Je ne savais absolument pas à quoi m'attendre mais je me suis tout de suite senti à l'aise. Ils me racontaient l'histoire et les origines du projet DeLLight avec des étoiles dans les yeux. Je ne m'en rendais pas compte à l'époque mais ils m'ont instantanément contaminé avec leur joie de vivre et leur passion pour la physique. Puis, dès le début du stage, ils m'ont inclus sans retenue au projet DeLLight et m'ont chaleureusement accueilli au sein de l'équipe. Pendant toute la thèse, je ne me suis jamais senti de côté et ça a été un réel plaisir de partager des discussions allant de la physique à des anecdotes personnelles pendant les repas. Ils m'ont beaucoup appris et je me rend compte maintenant de l'énorme chemin que j'ai parcouru depuis ce fameux entretien il y a quatre ans. Il m'ont montré qu'il fallait croire en ses idées, aussi peu orthodoxes soit-elles.

Merci Xavier pour ta patience et ta dévotion. Tu m'as transmis ton savoir sans restriction, toujours avec le sourire, et je saurai en faire bon usage pour la suite de mon parcours. Je n'aurais pas pu rêver mieux comme directeur de thèse !

Merci François pour ta bonne humeur, ton savoir et ta sagesse. Que ce soit autour d'un chocolat, à distance ou dans les bureaux, je n'ai jamais trouvé porte fermée lorsque j'avais besoin et je t'en remercie du fond du coeur. Apprendre auprès de vous deux a été une expérience extrêmement enrichissante et je vous en serai à jamais infiniment reconnaissant. Vous allez me manquer ~

Très cher Scott. Partager ces années avec toi au sein de l'équipe a été un réel plaisir. Échanger avec toi était très enrichissant de part ton profil de théoricien si différent du mien. Ta rigueur et ta passion pour la physique m'ont toujours impressionné. J'ai trouvé en toi un ami avec qui on peut parler de tout et de rien, et je t'en suis infiniment reconnaissante.

Merci Adrien pour ta bonne humeur et ton expertise. Nous n'avons travaillé ensemble que pendant un an et demi mais tu as toujours été là lorsque j'avais besoin, que ce soit pour des questions de physique ou des conseils personnels. Merci à toi et bon courage pour la suite (et ne manges pas tous les Spéculos !).

Je tiens à remercier très chaleureusement l'équipe LASERIX avec qui j'ai travaillé presque au quotidien en salle de manip pendant toute la thèse. Merci Moana pour ton savoir et ta rigueur. Tes conseils en salle laser ont toujours été les bienvenues et m'ont permis d'avancer. Merci Elsa pour ton expertise et ta bienveillance. Tu as toujours été là lorsque j'avais besoin d'aide et je t'en remercie du fond du coeur. Merci Julien pour ton expérience et ton soutien au quotidien.

Je n'ai jamais trouvé porte fermée lorsque j'en avais besoin et je t'en suis reconnaissant. Merci à Olivier et Sophie pour leur savoir et leur soutien depuis la licence. Vous m'avez donné goût aux lasers et l'optique alors que je débarquais à peine à Orsay. En passant par maîtres de stage, professeur.e.s, et ensuite collègues, vous avez toujours su m'aiguiller et me soutenir lorsque j'en avais besoin. Merci infiniment pour votre sagesse. Encore merci LASERIX pour votre joie de vivre et votre passion ~

Adeline, Randy et Robin. Cette année de master à vos côtés a été un reél plaisir et tellement plus fun que si nous n'avions pas eu notre petit groupe. J'imagine que passer ensemble par les mêmes galères forge des liens ! Et les restos pendant la thèse bien sur ~ Ça y est, nous sommes des adultes maintenant et c'était incroyable de passer ces années à vos côtés !

Merci à ma famille pour leur soutien au quotidien depuis le début. Ils ont toujours su être là pour moi et m'aiguiller lorsque je perdais mon chemin. Dans la vie comme dans les études, votre soutien compte beaucoup pour moi. Je suis docteur maintenant, j'espère que vous êtes fiers ! Je tiens tout particulièrement à remercier ma mère qui a toujours été là pour moi, dans les galères comme dans les moments joyeux. Sans toi, je ne ne serais pas là où j'en suis aujourd'hui. Je n'aurais jamais fait de bac S, j'aurais probablement abandonné la prépa, et je ne serais jamais venu à Orsay pour poursuivre mes études en physique jusqu'à la thèse. Merci maman, je t'aime ~ Merci également à ma tante pour sa joie de vivre et sa passion pour mon travail de thèse (oui oui !). J'espère que tu seras enfin contente de pouvoir lire ce manuscrit ~

Et pour finir, et ce n'est pas des moindres, un ÉNORME merci à mes meilleur.e.s ami.e.s ! Très chère Laura. Ta bonne humeur a toujours su me réconforter. Tu as toujours été là pour moi depuis le lycée et au cour de nos études, et je t'en serai toujours reconnaissant. Je t'aime, ma chère ~

Ensuite, Stefano l'immigré™. Depuis notre rencontre en licence, tu as toujours été un rocher sur lequel s'appuyer, et ce sans restrictions. Ta gentillesse m'a toujours touché et ton soutien au quotidien a été inestimable. Que ce soit pour s'amuser, me nourrir ou encore m'écouter quand j'en avais besoin, tu n'as jamais failli. Sans toi, ces années de licence, master et thèse auraient été bien ternes. Je t'aime fort, poto ~

Finalement, my lady Clara. Tu as toujours été là pour moi depuis le lycée et je ne pourrai jamais te remercier assez pour ta bienveillance. Malgré la distance pendant ces dernières années, ton soutien et l'amour que tu me portes sont restés sans faille. Ta présence et tes conseils ont toujours su me pousser à me dépasser et à ne pas lâcher malgré les contraintes. Ta bonne humeur (oui, ton humour aussi) a toujours su me remonter le moral, même dans les jours sombres. Tu sais que je t'aime, beauté ~

Regardez moi ça ! On s'est connu encore boutonneux et maintenant on compte parmi nous une prof de math, une ingénieure et deux docteurs. Je pense qu'on a fait du beau boulot, je suis trop fier de nous ! Je vous aime les potos !! *Peace out* ~

Contents

Introduction

The speed of light in vacuum is one of the most fundamental constants in physics. It defines the unit of length and plays a major role in the definition of the unit of time. However, in Quantum Electrodynamics (QED), vacuum is considered as a non-linear optical medium, and the speed of light in vacuum should decrease when the vacuum is stressed by intense electromagnetic fields. This optical phenomenon is similar to the optical Kerr effect in a material medium, which is a non linear variation of the refraction index n of a medium with the intensity I of the field it may encounter, such as: $n \propto I^2$. Such an effect has never been observed in vacuum.

The goal of the DeLLight (Deflection of Light by Light) experiment is thus to measure this effect using high intensity femtosecond laser pulses delivered by the LASERIX platform ($\mathcal{E}$ = 2.5 J per pulse, 30 fs, 10 Hz repetition rate), located at IJCLab laboratory (Paris-Saclay University, France). It is a probe-pump type experiment which uses interferometry to measure the refraction of a low energy laser pulse (probe) on the vacuum index gradient induced by an external, high energy pulse (pump) with peak intensities up to a few 10^{20} W/cm^2 for a pump waist at focus of 5 μm. At this intensity, the expected deflection angle is about a tenth of picoradian. In order to measure such a small deflection, we use a Sagnac interferometer ("closed" configuration) with focalised probe and pump pulses, and we measure with a CCD camera the destructive interference of the refracted probe pulse with the unperturbed reference pulse in the dark output of the interferometer. The signal of refraction corresponds to a transverse vertical shift Δy of the barycenter of the interference intensity profile in the dark output. The benefit of the interferometric technique is to amplify the transverse shift, unlike the shift obtained by the standard pointing measurement method. The higher the extinction in the dark output of the interferometer, the more the deflection signal is amplified.

The sensitivity of the DeLLight experiment depends on three critical parameters: the extinction factor $\mathcal{F}$ (defined as the ratio between the interference intensity in the dark output of the interferometer and the incident intensity), the spatial resolution σ_y of the position measurement of the interference intensity profile and the focusing quality of the probe and pump pulses. The goal is to reach an extinction of $\mathcal{F} = 4 \times 10^{-6}$ (corresponding to an amplification factor of the deflection signal of $\mathcal{A} = 250$), a spatial resolution $\sigma_y = 10$ nm, limited by the shot noise of the available CCD cameras, and a waist at focus of the pump and probe beams in the interaction area of $w_0 = 5$ μm. Thus, the expected QED deflection signal is $\Delta y = 0.015$ nm, which could be measured at 5 sigma with one month of data collection.

During this thesis, I actively participated to the experimental development of the DeLLight experiment which was quite extensive, considering that these were only just starting when I

started working on this project. With the help of my thesis supervisor, we developed several prototypes of Sagnac interferometer, all of which are not all presented in this manuscript, going from "basic" experimental setups to the current imposing one (located in the LASERIX laser clean room). The goal of these prototypes was to demonstrate the feasibility of the project and to study and characterise the critical parameters which currently limit the sensitivity. The main efforts were devoted to the improvement of the extinction quality of the Sagnac interferometer and to the study and measurement of the spatial resolution of the interference intensity profile in the dark output of the interferometer. The spatial resolution being limited by the inherent shot noise of the CCD camera, by the beam pointing fluctuations, and by the mechanical vibrations of the interferometer, we have studied in details these three critical parameters. Finally, with the most advanced current prototype, we validated the DeLLight experimental method by measuring the deflection signal in air with a low energy pump pulse. A relatively high amplification of the signal has been reached thanks to the interferometric technique, which constitutes an important achievement of the DeLLight project.

The overall experimental setup underwent a lot of changes over the years to optimise it, in terms of optics quality or experimental efficiency and practicality. Moreover, I also worked on different transverse projects for the DeLLight experiment, like for instance the beam pointing MRC stabilisation system, which is not presented in this manuscript.

Another large part of my work consisted of the analysis of all data collected over the years, which were essential to continue enhancing the experimental setup in order to reach the expected DeLLight signal and spatial resolution. With the help of my colleagues, we improved the analysis programs and methods to the well-oiled machine that it is today.

In this manuscript, we will first expose the optical non linearity in vacuum, with the theoretical context and state of the art experiments in Quantum Electrodynamics (QED). Secondly, we will thoroughly detail the DeLLight experiment, with its experimental principle and expected sensitivity. Following, we will explain the data analysis method used to extract the DeLLight signal. We will then present both Sagnac interferometer prototypes used in this experiment. Afterwards, we will detail the measurement of the extinction factor in the dark output of the interferometer, which is one of the crucial parameters of the DeLLight experiment. The measurement of the shot noise resolution of the CCD cameras used on the experimental setup will be next, followed by the spatial resolution measurements in the dark output, which is another crucial parameter. Finally, we will thoroughly detail the Kerr measurement results in silica with low energy pump pulses (Prototype 1), as well as the results in air (Prototype 2).

Chapter 1

Optical non linearity in vacuum

1.1 Nonlinear Quantum Electrodynamics (QED)

The classical electromagnetic vacuum is described as a linear optical medium. The speed of light c in vacuum, as well as the related vacuum permeability μ_0 and permittivity ϵ_0 are universal constants. The Maxwell equations for the electromagnetic field $(\mathbf{E}, \mathbf{B})$ are linear and the vacuum constants c, μ_0 and ϵ_0 do not depend on externally applied fields, such as:

$$\begin{cases} \mathbf{D} &= \epsilon_0 \mathbf{E} \\ \mathbf{B} &= \mu_0 \mathbf{H} \end{cases} \text{ and } c = \frac{1}{\sqrt{\epsilon_0 \mu_0}} \tag{1.1}$$

where $\mathbf{D}$ is the electric displacement field and $\mathbf{H}$ is the magnetising field.

1.1.1 Nonlinear optics

In media, however, the dependence of the optical index on the electromagnetic field has been known since the 19th century, first with Faraday's discovery of circular birefringence induced by an external magnetic field in the direction of propagation (Faraday effect) [1], and then with Kerr's discovery of birefringence induced by a transverse electric field (Kerr effect) [2]. Both effects can be interpreted as polarisation-dependent changes of the refractive index, and while the Faraday effect is linear in the magnetic field $\mathbf{B}$, the Kerr effect is nonlinear and proportional to the intensity $I \propto |\mathbf{E}|^2$.

Thus, the general form of the nonlinear Maxwell equations is:

$$\begin{cases} \mathbf{D} &= \epsilon_0 \mathbf{E} + \mathbf{P}(\mathbf{E}, \mathbf{B}) = \epsilon(\mathbf{E}, \mathbf{B})\, \mathbf{E} \\ \mathbf{B} &= \mu_0 \mathbf{H} + \mu_0 \mathbf{M} = \mu(\mathbf{E}, \mathbf{B})\, \mathbf{H} \end{cases} \text{ and } v = \frac{1}{\sqrt{\epsilon(\mathbf{E}, \mathbf{B})\, \mu(\mathbf{E}, \mathbf{B})}} \tag{1.2}$$

where $\mathbf{P}$ is the polarisation field, $\mathbf{M}$ is the magnetisation field, v is the phase velocity, and ϵ and μ are the permittivity and the permeability of the medium.

The nonlinear Kerr effect occurring in an optical medium is the optical Kerr effect, in which the electric field responsible for the index change is due to light itself, has been extensively studied and measured thanks to the availability of high-intensity lasers in the last twenty years [3]. Thus, the index n_0 of a given medium is modified by the intensity (in W/cm^2) of the

laser pulse it encounters, and the change of index $\delta n = n - n_0$ is then proportional to the laser intensity I_{laser}, such as:

$$\delta n = n_2 \times I_{\text{laser}} \tag{1.3}$$

where n_2 is the Kerr coefficient of the nonlinear refractive index of the medium (in cm^2/W).

1.1.2 Vacuum as a nonlinear optical medium

By analogy with the case of media, we may wonder whether the vacuum also behaves like a nonlinear optical medium, i.e. whether the vacuum index increases when stressed by intense external fields. Born and Infeld [4] were the first to introduce nonlinear electrodynamics terms in vacuum by assuming an absolute maximum of the electric field E_{abs} in order to regularise the electromagnetic field of a point charge, and thus to obtain a finite electromagnetic mass of the electron equal to its observed mass. The polarisation and magnetisation fields can then be written as:

$$\mathbf{P} = \frac{\epsilon_0}{2E_{abs}^2}\left[(E^2 - c^2B^2)\mathbf{E} + 2c^2(\mathbf{E}.\mathbf{B})\mathbf{B}\right] \tag{1.4}$$

$$\mathbf{M} = -\frac{\epsilon_0}{2E_{abs}^2}\left[(E^2 - c^2B^2)\mathbf{B} - 2c^2(\mathbf{E}.\mathbf{B})\mathbf{E}\right] \tag{1.5}$$

where E and B are the amplitudes of the electromagnetic field.

Soon after, Euler, Kockel and Heisenberg [5] derived an effective nonlinear electromagnetic field theory with nonlinear terms induced by the coupling of the fields with the electron-positron virtual pairs in vacuum. This is described by the so-called Euler-Heisenberg nonlinear Lagrangian, with the corresponding nonlinear Maxwell equations:

$$\begin{aligned} \mathbf{P} &= \xi\epsilon_0^2\left[2(E^2 - c^2B^2)\mathbf{E} + 7c^2(\mathbf{E}.\mathbf{B})\mathbf{B}\right] \\ \mathbf{M} &= -\xi\epsilon_0^2c^2\left[2(E^2 - c^2B^2)\mathbf{B} - 7(\mathbf{E}.\mathbf{B})\mathbf{E}\right] \\ \xi^{-1} &= \frac{45m_e^4c^5}{4\alpha^2\hbar^3} \simeq 3\times10^{29}\,\text{J/m}^3 \end{aligned} \tag{1.6}$$

where ξ^{-1} is a constant corresponding to an energy in volume unit (J/m^3), α is the fine structure constant, m_e is the electron mass, and $\hbar$ is the reduced Planck constant.

The Euler-Heisenberg result was later reformulated by Schwinger as the photon-photon scattering phenomenon (four-waves interactions) in nonlinear Quantum Electrodynamics (QED) with strong fields. The equivalent Feynman diagram is illustrated in figure 1.1. Non-elastic photon–photon scattering becomes possible when the combined energy is large enough to create virtual electron–positron pairs spontaneously.

1.1.3 The Schwinger limit

In nonlinear QED, a critical field E_{cr}, named the Schwinger limit, is introduced, which corresponds to the limit electrical field value over which virtual electron-positron pairs in

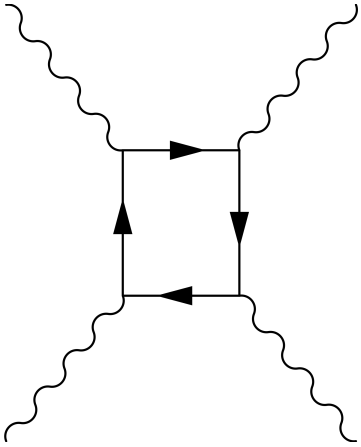

Figure 1.1: Four waves Feynman diagram illustrating the photon–photon scattering phenomenon.

vacuum become real and escape the vacuum. The critical electromagnetic fields are given by:

$$\begin{aligned} E_{cr} &= \frac{m_e^2 c^3}{e\hbar} \approx 1.3 \times 10^{18}\,\mathrm{V/m} \\ B_{cr} &= \frac{E_{cr}}{c} \approx 4.4 \times 10^{9}\,\mathrm{T} \end{aligned} \tag{1.7}$$

The Schwinger field, E_{cr}, is the field required to extract a virtual electron-positron pair from vacuum and make it real. It can be calculated classically as the electric field needed to accelerate an electron charge e on a distance equal to its reduced Compton wavelength $\lambda\!\!\!^{-}_e = \hbar/(m_e c)$ and to reach the rest mass energy of the electron $m_e c^2$. The equivalent electric force is $F = eE_{cr}$. The work, i.e. the energy transferred to the electron via the application of the force F along the displacement $\lambda\!\!\!^{-}_e$, is then equal to the rest energy of the electron. It gives:

$$F \times \lambda\!\!\!^{-}_e = e \times E_{cr} \times \frac{\hbar}{m_e c} = m_e c^2 \tag{1.8}$$

corresponding to the Schwinger electric field given in equation 1.7.

1.2 Measurements of photon-photon scattering

The first observation of photon-photon scattering was obtained in 1997 at the Stanford Linear Accelerator Center (SLAC) by measuring the collision and fusion between a high energy (46.6 GeV) gamma and several laser photons at a wavelength of 527 nm (intensities of TW/cm^2) to produce an electron-positron pair (multi-photon Breit-Wheeler reaction) [6]. However, in order to realise this reaction, the photon energy required would be an order of magnitude (at 527 nm) over the maximal photon energy the SLAC can produce. Therefore, the Breit-Wheeler reaction became possible by using high intense laser photons, which were first back-scattered to GeV energies by the electron beam. Then, the collision between the high-energy gamma and

the laser photons produced the electron-positron pair. Thus, they managed to measure a signal of about 100 positrons above background.

A new project (submitted in 2019), called the LUXE experiment (Laser Und XFEL Experiment) [7], proposes to do same experiment with higher statistics, by using the high-quality and high-energy electron beam delivered by the European X-Ray Free-Electron Laser Facility (XFEL), as well as high-energy photons produced by Bremsstrahlung radiation, in order to obtain stronger fields up to three times larger than the Schwinger critical field (see equation 1.7). Their main focus is to study nonlinear Compton scattering and nonlinear Breit-Wheeler pair production.

More recently, high energy gamma-gamma pair emission from virtual gamma-gamma scattering in ultra peripheral Pb-Pb collisions has been observed by the ATLAS and CMS detectors at the Large Hadron Collider (LHC) [8, 9]. Both cases involve inelastic high-energy photon-photon scattering, described by a four-photons Feynman diagram shown in figure 1.1.

1.3 Search for optical nonlinearity in vacuum

In all the observations of the photon-photon scattering discussed in the previous section, the vacuum appears in the exchange of an electron-positron virtual pair, which can even become real in the case of the Breit-Wheeler process. However, in these scattering processes, there is no modification of the optical properties of vacuum, i.e. no modification of the vacuum electromagnetic constants c, ϵ_0 and μ_0.

Another approach is to search for a direct manifestation of a nonlinear optical effect in vacuum, a coherent phenomenon corresponding to a pure undulatory process at large scale and treated classically in the long-wavelength limit. This effect differs drastically from the inelastic photon-photon scattering since it corresponds to a nonlinear modification of the fundamental level of the electromagnetic vacuum, with a change of the speed of light in vacuum at macroscopic scale.

1.3.1 Vacuum birefringence

Experimental efforts have mainly involved testing vacuum magnetic birefringence in the presence of an external magnetic field of 2-30 Tesla [10, 11, 12, 13]. This process is predicted by Euler-Heisenberg and often referred to as the Cotton-Mouton effect (in vacuum). Howerver, it is worth noting that the vacuum birefringence is expected to be absent within the Born-Infeld model.

As of yet, no signal has been observed. The best experimental sensitivity has been achieved by the PVLAS experiment, for which the experimental uncertainty is about one order of magnitude above the predicted QED value [10] [14]. The PVLAS experiment aims at measuring the vacuum birefringence using an external magnetic field of $B = 2.5$ T. The expected birefringence predicted by QED is $\delta n_{\mathrm{QED}} = 2.5 \times 10^{-23}$. As shown on figure 1.2, the experimental principle of the PVLAS polarimeter consists of sending a linearly polarised light beam through a Fabry–Perot cavity, in which a magnetic field is generated using two rotating permanent magnets at a frequency of 8 Hz and 8.5 Hz. The Fabry-Perot cavity is necessary to reach a long

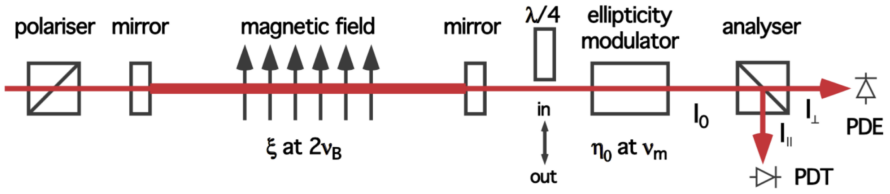

Figure 1.2: Experimental principle of the PVLAS polarimeter, as shown in [10].

optical path which allows to detect such small birefringence values, as is the case for vacuum. Then, a time dependence of the beam polarisation rotation is generated and is measured in the output using an analyser and photo-diodes. After about 100 days of collected data, no signal has been observed. The corresponding current best limit on vacuum magnetic birefringence, at 1 σ confidence level, is $\delta n_{\text{PVLAS}} = (12 \pm 17) \times 10^{-23}$, which is about a factor 7 above the predicted QED value of $\delta n_{\text{QED}} = 2.5 \times 10^{-23}$ at 2.5 T. It corresponds to an experimental sensitivity of $10^{-2}\sigma \times \sqrt{T_{obs}(\text{days})}$, where $T_{obs}(\text{days})$ is the number of days of collected data.

More recently, in 2018, they proposed a new experiment at CERN [15], called the VMB@CERN experiment, which aims at measuring vacuum birefringence using a LHC superconducting magnet to reach higher fields and higher rotating frequencies, as well as a new polarisation modulation scheme for the polarimeter. An advanced technical study of the proposed experiment was recently published in [16].

Several theoretical works considered the possibility of using high-intensity laser pulses to increase the strength of the fields [17, 18, 19, 20].

A first theoretical study was proposed by Aleksandrov et al. in 1985 [17]. They studied the scattering of light by light (i.e. photon-photon scattering), by calculating the polarisation of interacting high intense laser beams based on the Euler-Heisenberg formalism. They showed that, after such an interaction, a linearly polarised wave becomes elliptically polarised, and that the ellipse axis is rotated by a certain angle relative to the direction of the initial polarisation.

Additionally, Heinzl et al. proposed in 2016 [18, 19] to observe vacuum birefringence induced by intense laser fields. A high-intensity laser pulse is focused to a ultra-high intensity and polarises the vacuum which then acts like a birefringent medium. The latter is probed by a linearly polarised X-ray pulse, the rotation of the polarisation can thus be measured. In 2016, Schlenvoigt, Heinzl et al. [20] proposed a similar experiment but using intense laser fields and X-rays delivered by the European XFEL facility.

1.3.2 Change of the vacuum optical index

Alternatively, a complementary approach can be introduced, one that is independent of the occurrence of birefringence, by directly exploiting the change of the refractive index induced by the non linearity of vacuum. The refraction of a light beam in response to this index change is thus expected.

A test of refraction due to nonlinear electrodynamical effects was last performed in 1960 by Jones [21, 22], who looked for the deviation of a light beam passing through a transverse

static magnetic field of about 1 T, generated by a triangular coil, in order to illustrate the index variation of vacuum (without considering the polarisation). Results indicated that the deflection of the light beam was less than $\sigma_{noise} = 0.5\,\text{prad}$ (r.m.s.), which was a remarkable angular resolution. However, the deflection angle predicted by the Euler-Heisenberg model was about 12 orders of magnitude below this limit. Indeed, the expected signal can be derived from equations 1.2 and 1.7, by considering $E = 0$ and $B = 1\,\text{T}$:

$$\mathbf{B} = \mu_0\mathbf{H} + 2\mu_0\,\xi\,\epsilon_0^2\,c^4\,B^2\,\mathbf{B} = \mu_0\mathbf{H} + 2\,\xi \times \frac{B^2}{\mu_0}\mathbf{B} \tag{1.9}$$

At first order, we have:

$$\mathbf{B} \simeq \mu_0\,(1 + 2\,\xi \times \frac{B^2}{\mu_0})\,\mathbf{H} \tag{1.10}$$

which can be written as:

$$\mathbf{B} \simeq \mu_0(1+\delta)\,\mathbf{H} \;\text{ where: }\; \delta = 2\,\xi \times \frac{B^2}{\mu_0} \tag{1.11}$$

The modified speed of light $\tilde{c}$, modified by the transverse magnetic field, is then equal to:

$$\tilde{c} = \frac{1}{\sqrt{\epsilon_0\mu_0(1+\delta)}} \simeq c\,(1 - \frac{\delta}{2}) \tag{1.12}$$

Thus, the index variation δn in vacuum caused by the magnetic field B is:

$$\delta n = \delta/2 = \xi\,B^2/\mu_0 \tag{1.13}$$

and the expected signal for Jones' experiment was $\delta n_{QED} \simeq 3 \times 10^{-24}$. It corresponds to a deflection angle of the order of $\delta\theta_{QED} \approx \delta n_{QED} \approx 3 \times 10^{-24}$ rad.

As for birefringence-based experiments, there are several theoretical works considering the use of high-intensity laser pulses to achieve larger index changes and to measure it by studying the scattering of a probe beam by an intense pump beam. The principle is as follows. At the interaction area of the two laser pulses (pump and probe), the nonlinear quantum coupling of the intense electromagnetic fields produces an increase of the vacuum refractive index. Then, the optical index imprinted on the vacuum induces the scattering of the probe beam.

Several configurations have been studied. We can mention some examples: the diffraction of a high-intensity laser pulse which crosses another counter propagating high-intensity laser pulse with smaller diameter [23] [24], the diffraction of a probe beam by a standing electromagnetic wave formed by two counter propagating intense laser pulses [25], and more recently the reflection of a probe beam on the interaction area of pump laser pulses [26].

In all these proposals, the scattering of the laser pulse is similar to the classical diffraction or reflection of a light beam by an optical aperture. Here, the optical aperture corresponds to the vacuum area where the optical index is enhanced by the interaction of an intense laser pump pulse with a lower energy probe pulse.

The DeLLight (Deflection of Light by Light) project also proposes to use intense laser pulses to measure a change of refractive index, independent of the occurrence of birefringence. However, instead of measuring a diffraction or a reflection of the probe pulse, it proposes to measure the refraction - the deflection - of the probe pulse, crossing a transverse index gradient engendered by an energetic (Joule) and ultra-short (femtosecond) pump pulse. This is formally similar to the induction of an index change by the optical Kerr effect in a medium. Thus, the DeLLight project proposes a similar test to that of Jones, by using a much stronger electromagnetic field ($B \approx 10^5$ T) delivered by intense lasers. The DeLLight idea was first proposed in 2016 [27], using a simplified theoretical model to calculate the expected signal and a simplified experimental model to roughly estimate the sensitivity.

Chapter 2

The DeLLight experiment

The DeLLight (Deflection of Light by Light) project proposes to test the optical Kerr effect in vacuum by measuring the refraction of a probe pulse crossing an index gradient engendered by an energetic (Joule) and ultra-short (femtosecond) laser pulse. The DeLLight idea was first proposed in [27] using a simplified theoretical model to calculate the expected signal and a simplified experimental model to roughly estimate the sensitivity.

2.1 Principle of the DeLLight experiment using high intense laser pulses

The DeLLight experiment is installed in the LASERIX facility (IJCLab, Orsay), which delivers ultra-high intense laser pulses with a repetition rate of 10 Hz. The energy is 1.5 J per pulse with a duration of $\tau_0 = 40$ fs, which is measured at the Full Width at Half Maximum (FWHM) in intensity (W/cm^2). The laser will be upgraded in the coming years to reach 2.5 J per pulse with a duration of $\tau_0 = 30$ fs, corresponding to an intensity of 3×10^{20} W/cm^2 with a minimum waist at focus of 5 μm, which is equivalent to a magnetic field at peak intensity of $B \sim 10^5$ T or an electric field of $E \sim 3 \times 10^{13}$ V/m. The principle of the DeLLight experiment, illustrated in figures 2.1 and 2.2, is to cross two counter-propagating ultra-short laser pulses at their focus point. One pulse is very intense and is called the *pump* ; the other is of much lower intensity and is called the *probe*. The pump engenders a propagating refractive index profile $\delta n = n_2 I_{\text{pump}}$, where I_{pump} is its intensity in W/cm^2 (averaged over the rapid oscillations of the carrier wave), and where the non-linear index n_2 is given in the Euler-Heisenberg model derived from QED [28]:

$$n_2 = n_{2,\max}\, r_{\text{pol}} \cos^4\left(\frac{\theta_{\text{tilt}}}{2}\right) \tag{2.1}$$

with

$$n_{2,\max} = n_{2,\text{QED}} = 1.56.10^{-33}\,\text{cm}^2/\text{W}. \tag{2.2}$$

The factor $r_{\text{pol}} \in \left[\frac{4}{7}, 1\right]$ accounts for the birefringence of the model and its dependence on the polarisation state of the pump. We shall here assume the optimised case $r_{\text{pol}} = 1$, which

occurs when the pump and probe are each linearly polarised, with their electric (or magnetic) fields orthogonal to each other. Finally, θ_{tilt} is the tilt angle between the propagation directions of the pump and the probe, defined to be zero when they are exactly counter-propagating (i.e., when the collision is "head-on"). The expected Euler-Heisenberg value of the vacuum Kerr index $n_{2,\text{QED}}$ is orders of magnitude smaller than the Kerr index values measured in silica [29] and in air [30]:

$$\begin{aligned} n_{2,\text{Si}} &\simeq 2 \times 10^{-16}\,\text{cm}^2/\text{W} \\ n_{2,\text{air}} &\simeq 3 \times 10^{-19}\,\text{cm}^2/\text{W} \end{aligned} \tag{2.3}$$

Once the weak probe pulse crosses the pump pulse, it will "see" and react to the refractive index profile δn induced by the pump. In particular, in the interaction area where the pump intensity is rather highly concentrated, which can be achieved by strong focusing, the index profile δn will have a significant gradient in the transverse directions, which will tend to bend the rays of the probe towards regions of higher index or intensity. Thus, the wave-fronts of the probe pulse are rotated (refracted), as illustrated in figures 2.1 and 2.2, and the probe is deflected by an angle $\langle \delta\theta_y \rangle$.

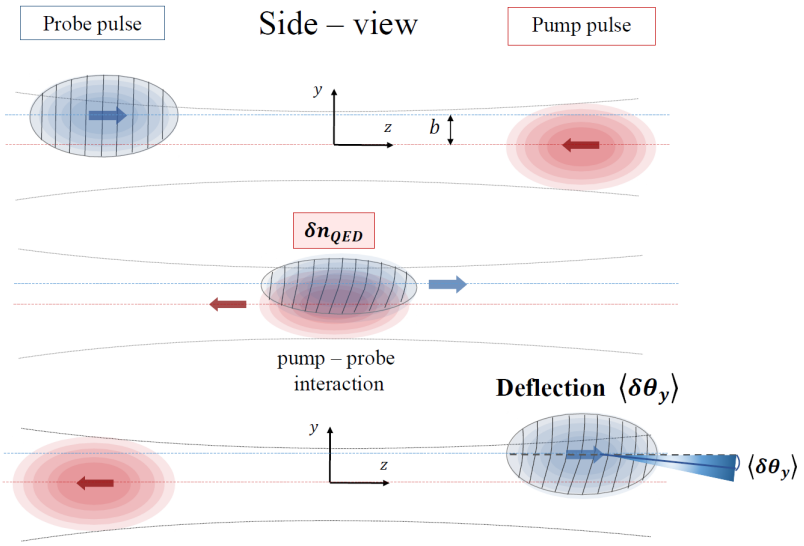

Figure 2.1: Schematic view of the interaction between the probe pulse (in blue) and the counter-propagating pump pulse (in red), seen from the side. The lines inside the probe pulse correspond to the wave fronts, which are gradually rotated by the vacuum index gradient induced by the pump. The axis of the pump beam is vertically (y-axis) shifted with respect to the axis of the probe beam, thus engendering an impact parameter b so that the perturbation of the probe is asymmetric and the refraction corresponds to a non-zero mean deflection along the vertical y-axis.

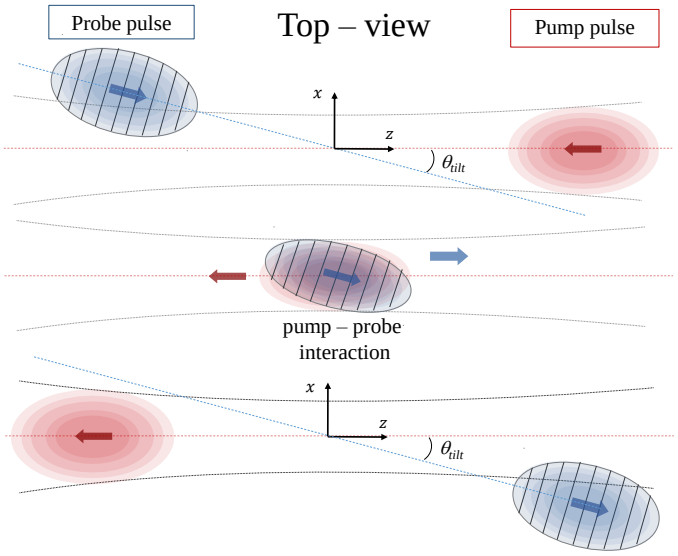

Figure 2.2: Same as figure 2.1 but from the top-view. In the horizontal plane (corresponding to the Sagnac interferometer $x-z$ plane), the axis of the pump beam is tilted by an angle θ_{tilt} with respect to the axis of the probe beam. The perturbation of the probe is symmetric and the mean deflection is zero along the horizontal x-axis.

The probe and pump pulses must be counter-propagating in order to maximise this deflection. Indeed, the interaction is only possible when at least one of the Lorentz invariant field terms "$\mathbf{E}.\mathbf{B}$" or "$E^2 - c^2B^2$" in equation 1.7 is not null.

2.2 Expected deflection with Gaussian pulses

The deflection of the probe pulse on the index gradient δn caused by the pump pulse is characterised by the mean deflection angle $\langle\delta\theta_y\rangle$, which has been calculated by S. Robertson [31]. We consider a head-on collision which correspond to a tilt angle $\theta_{\text{tilt}} = 0°$ between the orientations of the probe and the pump. For Gaussian pulses, we have:

$$\langle\delta\theta_y\rangle = \langle\delta\theta_y\rangle_{\max} \frac{b}{b_{\text{opt}}} e^{\frac{1}{2}\left(1-\left(\frac{b}{b_{\text{opt}}}\right)^2\right)} \tag{2.4}$$

where b is the impact parameter between the probe and the pump in the focalisation area. Its optimal value b_{opt} corresponds to a pump/probe overlap giving the maximal deflection angle $\langle\delta\theta_y\rangle_{\max}$, given the pump energy $\mathcal{E}$ and the pulse widths w_0 and W_0 of the probe and the pump respectively. These two parameters are defined by:

$$b_{\text{opt}} = \frac{1}{2}\sqrt{w_0^2 + W_0^2} \tag{2.5}$$

and

$$\langle\delta\theta_y\rangle_{\max} = A\,\frac{\mathcal{E}}{b_{\text{opt}}^3}, \quad A = \frac{c\,n_{2,\max}}{4\pi\sqrt{e}} = 2.25\,\text{prad}\,\mu\text{m}^3/\text{J} \tag{2.6}$$

For achievable pump energy $\mathcal{E} = 2.5\,\mathrm{J}$ with the LASERIX facility, and with minimum waists at focus $w_0 = W_0 = 5\,\mu\mathrm{m}$, the average deflection angle is $\langle\delta\theta_y\rangle = \langle\delta\theta_y\rangle_{\max} = 0.13\,\mathrm{prad}$ for a head-on collision.

This deflection is challengingly small, so the experimental setup of the DeLLight experiment is designed such as to amplify the signal, bringing the deflection into an observable range, by using a Sagnac interferometer which has a "closed" configuration, as will be explained in section 2.4.

Measurements of the deflection of a laser beam through amplification with a Sagnac interferometer have already been developed with continuous laser beams in the search for gravitational anomalies at short distance, as well as angular deflections of a mirror down to the sub-picoradian scale [32][33]. However, no refraction measurement has yet been performed in femtosecond pulsed mode with a Sagnac interferometer, as is the case in the DeLLight experiment.

On the other end, experimental constraints dictate that the tilt angle θ_{tilt} cannot be exactly zero. Analytical calculations [31] show that the effect of the tilt angle is to introduce an overall correction factor r_{tilt} and the deflection angle $\langle\delta\theta_y\rangle$ becomes:

$$\langle\delta\theta_y\rangle = \langle\delta\theta_y\rangle_{\max}\,\frac{b}{b_{\mathrm{opt}}}\,e^{\frac{1}{2}\left(1-\left(\frac{b}{b_{\mathrm{opt}}}\right)^2\right)} \times r_{\mathrm{tilt}} \tag{2.7}$$

where

$$r_{\mathrm{tilt}} = \frac{\cos^3(\theta_{\mathrm{tilt}}/2)}{\sqrt{1+(R^2-1)\sin^2(\theta_{\mathrm{tilt}}/2)}}\,, \qquad R^2 = \frac{w_z^2 + W_z^2}{w_0^2 + W_0^2}\,. \tag{2.8}$$

Here w_z and W_z are the longitudinal sizes of the probe and pump pulses respectively, defined analogously to their transversal waists at focus w_0 and W_0. The parameter R measures the ratio of the longitudinal to transverse sizes of the pulses. It is the only parameter that depends on their longitudinal size. Turning to values achievable with the LASERIX facility with a pulse duration of $\tau = 30\,\mathrm{fs}$, which corresponds to a longitudinal size of $w_z = W_z = 7.6\,\mu\mathrm{m}$, and a minimum waist at focus of $w_0 = W_0 = 5\,\mu\mathrm{m}$, we find $R = 1.5$. For a experimentally realistic example at $\theta_{\mathrm{tilt}} = 30°$, we find $r_{\mathrm{tilt}} = 0.9$. Thus, it represents only a slight reduction (10% only) with respect to the case of a head-on collision.

2.3 Additional phase delay $\langle\delta\psi\rangle$ caused by the DeLLight effect in the Sagnac interferometer

In addition to a deflection, the perturbed probe is also characterised by a phase delay $\langle\delta\psi\rangle$, on account of the slower wave speed due to the index gradient δn induced by the pump in the Sagnac interferometer. The mean delay $\langle\delta t\rangle$ accumulated at any point within the probe is defined by:

$$\langle\delta t\rangle = \frac{n_{2,\max}\,\mathcal{E}}{4\pi\,b_{\mathrm{opt}}^2}\,e^{-\frac{1}{2}\left(\frac{b}{b_{\mathrm{opt}}}\right)^2} \times r_{\mathrm{tilt}} \tag{2.9}$$

This leads to an average phase delay $\langle \delta\psi \rangle = \omega_0 \langle \delta t \rangle$, where ω_0 is the carrier frequency of the probe, and at $b = 0$ and $\theta_{\text{tilt}} = 0°$, we have:

$$\langle \delta\psi \rangle = \frac{2c\, n_{2,\max}\, \mathcal{E}}{\lambda_0 \,(w_0^2 + W_0^2)} \times r_{\text{tilt}} \tag{2.10}$$

where λ is the wavelength of the laser ($\lambda = 815\,\text{nm}$ at the LASERIX facility). For achievable pump energy $\mathcal{E} = 2.5\,\text{J}$ and minimum waists at focus $w_0 = W_0 = 5\,\mu\text{m}$, and $r_{\text{tilt}} = 0.9$, the average phase delay caused by the DeLLight effect is $\langle \delta\psi \rangle = 5 \times 10^{-12}$.

NB: with the impact parameter $b = b_{\text{opt}}$, the deflection $\langle \delta\theta_y \rangle$ is maximised and the phase delay is reduced by a factor $\sqrt{e}$.

2.4 Experimental setup of the DeLLight experiment using a Sagnac interferometer

The deflection $\langle \delta\theta_y \rangle$ caused by the DeLLight effect is measured using a Sagnac interferometer to amplify said deflection, which translates as a transverse vertical displacement Δy of the residual intensity profile in the dark output and is collected on a CCD camera. The experimental setup of the DeLLight project is shown on figure 2.3. First of all, the pump pulse, with a polarisation s, is focused by an off-axis parabolic mirror (OAP) in the interaction area. Additionally, a much weaker pulse (few tens of μJ), with a perpendicular polarisation p, is sent into a Sagnac interferometer via a 50/50 beamsplitter (BS-2), generating two daughter pulses (Probe and Ref) that circulate in opposite directions in the interferometer. The interferometer is in a right-angled isosceles triangle configuration, formed by the beamsplitter and two dielectric mirrors (M1 and M2). Both counter-propagating pulses are then focused in the interaction area via two optical lenses (L1 and L2) of focal length f inserted between the two mirrors. One pulse (Probe) refers to the probe pulse that is counter-propagating with respect to the pump, and a delay stage (Delay Stage Timing) ensures the time coincidence of the arrival of said probe pulse with that of the pump pulse in the interaction area. The second pulse (Ref) is not in time coincidence with either the probe or pump pulses and does not overlap with the latter. This pulse is therefore unaffected by the pump and will be used as a reference pulse to monitor the beam pointing fluctuations of the laser. The focus axis of the pump is transversally and vertically shifted with respect to the focus axis of the probe, thus engendering an impact parameter b so that the perturbation of the probe is asymmetric and the mean deflection is non-zero, as illustrated on figure 2.1.

Furthermore, in the absence of the pump, the two counter-propagating probe and reference pulses are phase-shifted by π in the dark output of the interferometer, where a CCD camera measures the transverse position of the residual intensity profile, as will be explained in section 2.5. However, when the pump pulse is present and interacts with the probe pulse at focus, the wave fronts of the probe are refracted by the induced vacuum index gradient δn, while those of the reference pulse are unaffected. The refracted probe pulse is then recollimated using a lens (L1) of focal length f and is transversally and vertically shifted with respect to

the unrefracted reference pulse by an average distance $\langle \delta y \rangle = \langle \delta \theta_y \rangle \times f$, where $\langle \delta \theta_y \rangle$ is the average deflection angle of the refracted probe pulse. Finally, the interference of the probe and reference pulses in the output of the interferometer produces a transverse vertical displacement Δy of the barycenter in the y-axis of the residual intensity profile, which is measured by the CCD camera. This displacement Δy corresponds to the final DeLLight *spatial signal*.

The DeLLight deflection signal is a differential measurement between interference intensity profile measurements in the dark output of the interferometer with and without interaction between the pump and probe pulses, which are respectively labelled "ON" ($I_{ON}(2i)$) and "OFF" ($I_{OFF}(2i+1)$) measurements for successive laser shots i.

The advantage of the proposed interferometric method is an amplification of the measured signal Δy, as compared to the would-be signal $\langle \delta y \rangle$ when using a standard direct pointing method (no interferometry). We will see, in the next section, that the amplification factor, defined as $\mathcal{A} = \Delta y / \langle \delta y \rangle$, scales as $\mathcal{F}^{-1/2}$ where $\mathcal{F}$ is the extinction factor of the Sagnac interferometer, defined as $\mathcal{F} = I_{out}/I_{in}$, where I_{in} is the incident intensity and I_{out} is the intensity of the interference signal in the dark output of the interferometer.

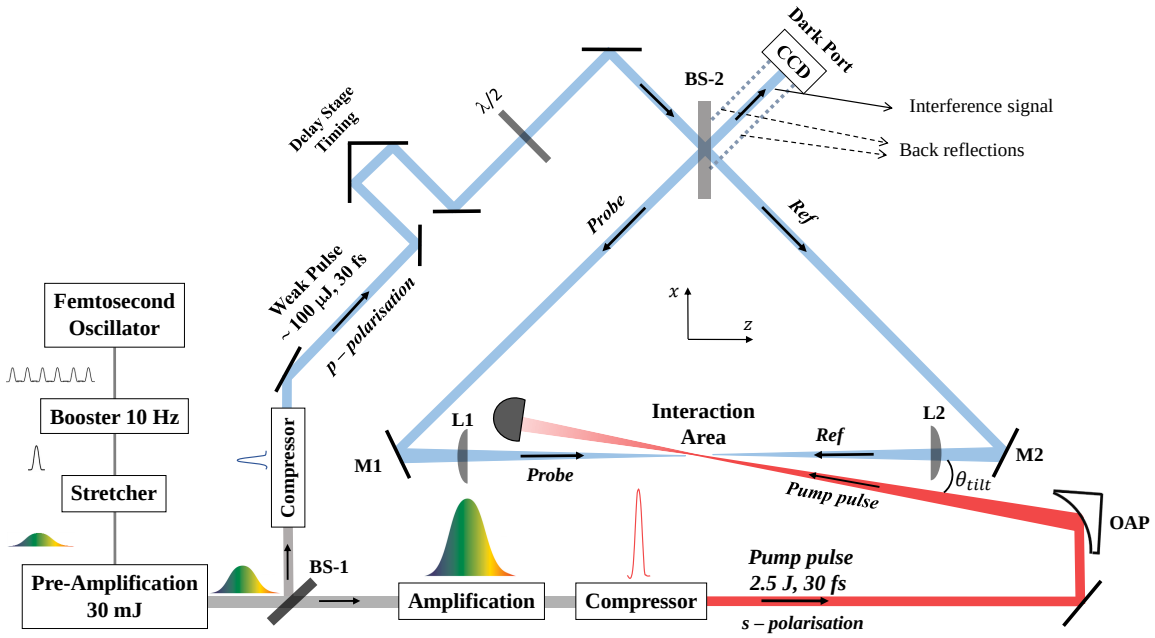

Figure 2.3: Schematic view of the DeLLight experimental setup

2.5 Calculation of the interference intensity profile: amplification of the DeLLight signal

2.5.1 Notations

In the Sagnac interferometer used in the DeLLight experiment, two counter-propagating laser pulses - the probe and the reference - travel the same optical path and interfere in the dark

output thanks to their π phase-shift. The interference intensity profile in the dark output of the Sagnac interferometer is written $I_{out}(x, y)$. In order to compute the latter, we first need to define the following parameters:

- r and t are the reflexion and transmission factors of the beam splitter in amplitude.
- δa represents the asymmetry between the reflexion and the transmission of the beam splitter in intensity, such as:
$$\begin{cases} r^2 = \frac{1}{2}(1 - \delta a) \\ t^2 = \frac{1}{2}(1 + \delta a) \end{cases} \tag{2.11}$$
- $\delta\phi(x, y)$ is the phase noise between the probe and the reference in the dark output of the Sagnac interferometer, with (x, y) the frame of reference of the CCD camera. This phase delay is mostly due to the fact that both beams travel through slightly different optical paths and thus don't encounter the same imperfections on the optics (bump on a mirror for example).
- δy is the un-amplified deflection signal of the probe caused by the interaction with the pump and is written $\delta y = f \times \delta\theta$ in the small angles approximation where f is the focal length of the focalising lenses in the Sagnac interferometer and $\delta\theta$ is the deflection angle.
- $\delta\psi$ is the Kerr signal phase-shift of the probe due to the interaction with the pump which corresponds to a phase delay of the probe with respect to the reference.
- $I_{in}(x, y)$ is the transverse intensity profile of the input pulse entering the Sagnac interferometer.

2.5.2 Analytical calculation of the intensity profile of the interference signal in the dark output of the interferometer

The electric fields of the probe and the reference in the dark output of the Sagnac interferometer are defined by:

$$\begin{cases} E_{probe} = E_0(y - \delta y)e^{-i\delta\psi}(1 - \delta a)/2 \times e^{-i\pi} \\ E_{ref} = E_0(y)e^{2i\delta\phi}(1 + \delta a)/2 \end{cases} \tag{2.12}$$

The electric field of the probe includes the effects of the Kerr signal deflection δy and phase-shift $\delta\psi$ due to the interaction with the pump in the Sagnac interferometer. The reference is unperturbed by the pump. The probe is reflected two times on the beam splitter on each side of the beam splitting coating, hence the term in $r^2 = \frac{1}{2}(1 - \delta a)$ whereas the reference is transmitted two times (term in $t^2 = \frac{1}{2}(1 + \delta a)$). We arbitrarily chose to put the phase noise term $\delta\phi(x, y)$ in the electric field of the reference. The term "$e^{-i\pi}$" in E_{probe} comes from the π phase-sift between the probe and the reference, as is explained in details in appendix A.

The intensity profile $I_{out}(x, y)$ of the interference between the probe and the reference in the dark output of the Sagnac interferometer is:

$$I_{out} = |E_{probe} + E_{ref}|^2 = (E_{probe} + E_{ref}) \times (E_{probe} + E_{ref})^* \tag{2.13}$$

In order to simplify the calculations, we will note the derivative of the initial electric field $E_0(y)$ in amplitude such as: $E'_0(y) = \frac{\partial E_0(y)}{\partial y}$. We develop equation 2.12:

$$\begin{cases} 2E_{probe} = (E_0(y) - \delta y E'_0(y))(1 - \delta a)e^{-i\delta\psi} \times e^{-i\pi} \\ 2E_{ref} = E_0(y)(1 + \delta a)e^{2i\delta\phi} \end{cases} \tag{2.14}$$

Each term in equation 2.13 can be written as:

$$\begin{cases} 2(E_{probe} + E_{ref}) = e^{i\pi} \times (E_0(y) - \delta y E'_0(y))(1 - \delta a)e^{-i\delta\psi} + E_0(y)(1 + \delta a)e^{2i\delta\phi} \\ 2(E_{probe} + E_{ref})^* = e^{-i\pi} \times (E_0(y) - \delta y E'_0(y))(1 - \delta a)e^{i\delta\psi} + E_0(y)(1 + \delta a)e^{-2i\delta\phi} \end{cases} \tag{2.15}$$

Thus, the residual intensity profile $I_{out}(x, y)$ is:

$$\begin{aligned} 4 \times I_{out} =& [(E_0(y) - \delta y E'_0(y))(1 - \delta a)]^2 \\ &+ [E_0(y)(1 + \delta a)]^2 \\ &- 2\cos(\delta\psi + 2\delta\phi)E_0(y)(E_0(y) - \delta y E'_0(y))(1 - (\delta a)^2) \end{aligned} \tag{2.16}$$

Considering the small angles approximation, the cosine term can be simplified:

$$\cos(\delta\psi + 2\delta\phi) \approx 1 - (\delta\psi + 2\delta\phi)^2/2 \tag{2.17}$$

Finally, the general expression of the residual intensity profile I_{out} in the dark output of the Sagnac interferometer is:

$$\begin{aligned} 4 \times I_{out} =& [(E_0(y) - \delta y E'_0(y))(1 - \delta a)]^2 \\ &+ [E_0(y)(1 + \delta a)]^2 \\ &- 2E_0(y)(E_0(y) - \delta y E'_0(y))[1 - (\delta\psi + 2\delta\phi)^2/2](1 - (\delta a)^2) \end{aligned} \tag{2.18}$$

The parameter δa corresponds to an asymmetry in amplitude between the probe and the reference, while the parameters $\delta\psi$ and $\delta\phi$ correspond to a phase difference. Hence, we separate these two effects and define the amplified intensity profile I_{out}^{ampl} in the dark output and the phase term I_{out}^{phase}, such as:

$$I_{out} = I_{out}^{ampl} + I_{out}^{phase} \tag{2.19}$$

with

$$\begin{aligned} 4 \times I_{out}^{ampl} =& [(E_0(y) - \delta y E'_0(y))(1 - \delta a)]^2 + [E_0(y)(1 + \delta a)]^2 \\ &- 2E_0(y)(E_0(y) - \delta y E'_0(y))(1 - (\delta a)^2) \end{aligned} \tag{2.20}$$

$$4 \times I_{out}^{phase} = (\delta\psi + 2\delta\phi)^2 E_0(y)(E_0(y) - \delta y E'_0(y))(1 - (\delta a)^2) \tag{2.21}$$

2.5.3 Interference dominated by the amplitude asymmetry δa

In this section, we assume that the phase terms $\delta\psi$ and $\delta\phi$ are null ($\delta\psi = \delta\phi = 0$) and calculate the amplified intensity profile I_{out}^{ampl} in the dark output due to the amplitude asymmetry δa only. Equation 2.20 becomes:

$$\begin{aligned} 4 \times I_{out}^{ampl} =& (1-\delta a)^2 (E_0(y)^2 + \delta y^2 E_0'(y)^2 - 2\delta y E_0(y) E_0'(y)) \\ &+ (1+\delta a)^2 E_0(y)^2 - 2(E_0(y)^2 - \delta y E_0(y) E_0'(y))(1-(\delta a)^2) \end{aligned} \tag{2.22}$$

$$\begin{aligned} 4 \times I_{out}^{ampl} =& 4E_0(y)^2(\delta a)^2 - 2\delta y E_0(y) E_0'(y)[(1-\delta a)^2 - (1-(\delta a)^2)] \\ &+ (1-\delta a)^2 \delta y^2 E_0'(y)^2 \end{aligned} \tag{2.23}$$

To simplify the computations, let's note: $I_{in}(y) = E_0(y)^2$; $I_{in}'(y) = \frac{\partial I_{in}(y)}{\partial y} = 2E_0(y)E_0'(y)$. Thus, the amplified intensity profile I_{out}^{ampl} in the dark output is:

$$\begin{aligned} I_{out}^{ampl} &= (\delta a)^2 \times I_{in}(y) - \frac{\delta y I_{in}'(y)}{2}((\delta a)^2 - \delta a) \\ &= (\delta a)^2 \times (I_{in}(y) - \frac{\delta y I_{in}'(y)}{2}(1 - \frac{1}{\delta a})) \end{aligned} \tag{2.24}$$

$$I_{out}^{ampl} = (\delta a)^2 \times I_{in}(y + \frac{1-\delta a}{2\delta a} \times \delta y) \tag{2.25}$$

2.5.4 Interference dominated by the phase shift $\delta\Phi$

We now consider a non-null phase-shift to calculate the phase term I_{out}^{phase} and equation 2.21 becomes:

$$\begin{aligned} 4 \times I_{out}^{phase} &= (\delta\psi + 2\delta\phi)^2 E_0(y)(E_0(y) - \delta y E_0'(y))(1-(\delta a)^2) \\ &= 4(\delta\phi + \delta\psi/2)^2 (1-(\delta a)^2)(I_{in}(y) - \delta y I_{in}'(y)/2) \\ &= 4(\delta\phi + \delta\psi/2)^2 (1-(\delta a)^2) I_{in}(y - \delta y/2) \end{aligned} \tag{2.26}$$

By neglecting the term in $(\delta\psi)^2$, we can approximate the intensity phase term to:

$$I_{out}^{phase} \approx (1-(\delta a)^2)\,(\delta\phi)^2\,(1 + \delta\psi/\delta\phi) I_{in}(y - \delta y/2) \tag{2.27}$$

The phase noise term is thus shifted, but its barycenter isn't amplified like it was for the amplified profile in equation 2.25. However, it undergoes an attenuation factor of $(1-(\delta a)^2)$.

Without any approximations, the phase intensity profile I_{out}^{phase} is:

$$I_{out}^{phase} = (\delta\phi + \delta\psi/2)^2 (1-(\delta a)^2) I_{in}(y - \delta y/2) \tag{2.28}$$

2.5.5 Final expression of the interference intensity profile with and without pump

The final expression of the residual intensity profile in the dark output of the Sagnac interferometer is obtained by combining equation 2.25 and 2.28. It corresponds to the intensity profile obtained when the probe interacts with the pump ("ON" measurement), so it will be named $I_{ON}(x, y)$:

$$\boxed{\begin{aligned} I_{ON}(x,y) =& (\delta a)^2 \times I_{in}\left(x, y + \frac{1-\delta a}{2\delta a} \times \delta y\right) \\ &+ \left(\delta\phi(x,y) + \frac{\delta\psi}{2}\right)^2 \times (1 - (\delta a)^2) \times I_{in}\left(x, y - \frac{\delta y}{2}\right) \end{aligned}} \tag{2.29}$$

When the pump is OFF ("OFF" measurement), the phase shift $\delta\psi$ and the deflection signal δy are null ($\delta\psi = \delta y = 0$) and the "OFF" intensity profile, named $I_{OFF}(x, y)$, is:

$$\boxed{I_{OFF}(x,y) = \left((\delta a)^2 + (\delta\phi(x,y))^2\right) \times I_{in}(x,y)} \tag{2.30}$$

The extinction factor $\mathcal{F}$ of the Sagnac interferometer is defined by the intensity ratio between the OFF profile $I_{OFF}(x, y)$ and the input intensity $I_{in}(x, y)$ entering the interferometer, such as:

$$\boxed{\mathcal{F} = \frac{I_{OFF}(x,y)}{I_{in}(x,y)} = (\delta a)^2 + (\delta\phi(x,y))^2} \tag{2.31}$$

2.5.6 Signal in barycenter position Δy : *Deflection of Light by Light*

The DeLLight barycenter signal Δy corresponds to the interference signal dominated by the amplitude asymmetry δa of the Sagnac beamsplitter ($\delta\phi(x, y) << \delta a$). In this case, the intensity profile $I_{ON}(x, y)$ in the dark output of the interferometer for the ON measurement (equation 2.29) becomes:

$$I_{ON}(x,y) = (\delta a)^2 \times I_{in}(x, y + \Delta y) \tag{2.32}$$

where the deflection signal amplified by interferometry is:

$$\boxed{\begin{aligned} \Delta y &= \mathcal{A} \times \delta y \\ \mathcal{A} &= \frac{1-\delta a}{2\delta a} \end{aligned}} \tag{2.33}$$

$\mathcal{A}$ is the amplification factor of the interferometer.

The intensity profile $I_{OFF}(x, y)$ in the dark output for the OFF measurement (equation 2.30 with $\delta y = 0$) becomes:

$$I_{OFF}(x,y) = (\delta a)^2 \times I_{in}(x,y) \tag{2.34}$$

with an extinction factor (equation 2.31) of $\mathcal{F} = (\delta a)^2$, which corresponds to an amplification factor of $\mathcal{A} = (1 - \sqrt{\mathcal{F}})/(2\sqrt{\mathcal{F}})$. The amplification of the deflection signal δy is considered

large when the term δa is small, which corresponds to a good extinction and a good reflection/transmission symmetry of the beamsplitter of the Sagnac interferometer. Thus, for a large amplification, we would need an extinction factor of $F << 1$ ($\delta a << 1$) which corresponds to an amplification factor of:

$$\boxed{\mathcal{A} = \frac{1}{2\delta a} = \pm\frac{1}{2\sqrt{\mathcal{F}}} \text{ (when } \delta\phi(x,y) \ll \delta a \ll 1)} \tag{2.35}$$

On the contrary, the amplification is degraded when δa becomes too large.

The goal of the DeLLight experiment is to reach an extinction factor of $\mathcal{F} = 4 \times 10^{-6}$ which corresponds to an amplification factor of $A = 250$. It is important to note that the sign of the amplification depends on the sign of δa.

2.5.7 Signal in intensity $\Delta I/I$: *Deceleration of Light by Light*

The DeLLight intensity signal $\Delta I/I$ corresponds to the interference signal dominated by the phase shift $\delta\phi(x,y)$ ($\delta a << \delta\phi(x,y)$). In this case, the intensity profile $I_{ON}(x,y)$ in the dark output of the interferometer for the ON measurement (equation 2.29) becomes:

$$I_{ON}(x,y) = (\delta\phi(x,y) + \delta\psi/2)^2 \times I_{in}(y - \delta y/2) \tag{2.36}$$

and the intensity profile $I_{OFF}(x,y)$ in the dark output for the OFF measurement (equation 2.30) becomes:

$$I_{OFF}(x,y) = (\delta\phi(x,y))^2 \times I_{in}(x,y) \tag{2.37}$$

with an extinction factor (equation 2.31) of $F = (\delta\phi(x,y))^2$.

The intensity signal $\Delta I/I$ is defined as the relative difference in intensity for successive ON and OFF measurement:

$$\frac{\Delta I}{I} = \frac{I_{\text{ON}} - I_{\text{OFF}}}{I_{\text{OFF}}} \tag{2.38}$$

Using equations 2.36 and 2.37, the intensity signal $\Delta I/I$ becomes:

$$\frac{\Delta I}{I} = \frac{(\delta\phi(x,y) + \delta\psi/2)^2 \times I_{in}(y - \delta y/2) - (\delta\phi(x,y))^2 \times I_{in}(x,y)}{(\delta\phi(x,y))^2 \times I_{in}(x,y)} \tag{2.39}$$

The Gaussian intensity profile $I_{in}(y)$ does not change if it is shifted by a given value "$\delta y/2$", namely between ON and OFF measurements. Thus, we can consider that both profiles $I_{in}(y - \delta y/2)$ and $I_{in}(y)$ are equivalent and the previous equation becomes:

$$\frac{\Delta I}{I} = \frac{(\delta\phi(x,y) + \delta\psi/2)^2 - (\delta\phi(x,y))^2}{(\delta\phi(x,y))^2} \tag{2.40}$$

The final expression of the DeLLight intensity signal $\Delta I/I$ is:

$$\frac{\Delta I}{I} = \frac{(\delta\psi)^2}{4(\delta\phi(x,y))^2} + \frac{\delta\psi}{\delta\phi(x,y)} \tag{2.41}$$

Since $\delta\psi \ll \delta\phi(x, y)$, the linear term dominates in equation 2.41 and we finally obtain:

$$\boxed{\frac{\Delta I}{I} = \frac{\delta\psi}{\delta\phi(x, y)}} \tag{2.42}$$

The intensity signal (the relative variation in intensity) is proportional to the QED phase signal $\delta\psi$ and is amplified by an amplification factor $\mathcal{A} = 1/(\delta\phi(x, y))$. Smaller the phase $\delta\phi(x, y)$ is, higher the intensity signal is ($\delta\phi(x, y)$ for the intensity signal is equivalent to δa for the barycenter signal).

2.6 Expected sensitivity of the DeLLight experiment

2.6.1 Deflection Signal

The DeLLight deflection signal is a differential measurement between interference intensity profiles measurement in the dark output of the interferometer with and without interaction between the pump and probe pulses, which are respectively labelled "ON" and "OFF" measurements.

The deflection signal corresponds to a shift of the barycenter of these intensity profiles in the dark output caused by the probe/pump interaction. We compute these barycenters for successive ON and OFF measurements, which are respectively named $\bar{y}^{\mathrm{ON}}(i)$ and $\bar{y}^{\mathrm{OFF}}(i)$. Thus, the corresponding signal $\Delta y(i)$ of the i^{th} "ON-OFF" measurement is given by:

$$\Delta y(i) = \bar{y}^{\mathrm{ON}}(i) - \bar{y}^{\mathrm{OFF}}(i) \tag{2.43}$$

The measured $\Delta y(i)$ have a certain distribution characterised by its mean value $\Delta y = \langle \Delta y(i) \rangle_i$ over all laser shots and its standard deviation σ_y. The mean value Δy corresponds to the final DeLLight deflection signal and the standard deviation σ_y corresponds to the *spatial resolution*.

The extraction and computation of the signal are explained in chapter 3. Study and measurement of the spatial resolution are thoroughly detailed in chapter 6.

As mentioned in the section 2.5.6, since the amplification factor of the Sagnac interferometer for the spatial signal is $A = \frac{1}{2\sqrt{\mathcal{F}}}$, the expected theoretical QED spatial signal Δy_{QED} becomes:

$$\Delta y_{\mathrm{QED}} = A \times \delta y_{\mathrm{QED}} = \frac{f \times \delta\theta_{\mathrm{QED}}}{2\sqrt{\mathcal{F}}} \tag{2.44}$$

where f is the focal length of the lenses inside the interferometer, $\mathcal{F}$ is the extinction factor of the interferometer and $\delta\theta_{\mathrm{QED}}$ is the deflection signal in radian.

To estimate the sensitivity of the DeLLight experiment, we assume that the measured mean signal Δy is equal to the expected theoretical QED signal Δy_{QED}. The statistical error at one standard deviation of the observed mean Δy is equal to $\sigma_y/\sqrt{N}$, where N is the number of "ON-OFF" measurements. Thus, the DeLLight signal is measured with a significance of N_{std} standard deviations, such as:

$$\Delta y_{\mathrm{QED}} = N_{\mathrm{std}} \times \sigma_y/\sqrt{N} \tag{2.45}$$

where $N = r_{\text{laser}}/2 \times T_{\text{obs}}(\text{s}) = 43200 \times r_{\text{laser}} \times T_{\text{obs}}(\text{days})$, with r_{laser} the repetition rate of the laser (corresponding to a repetition rate of "ON-OFF" measurements of $r_{\text{laser}}/2$) and T_{obs} the total duration of the experiment in days.

Using equations 2.44 and 2.45, the number of standard deviations N_{std} becomes:

$$N_{\text{std}} = \frac{f \times \delta\theta_{\text{QED}}}{2\sqrt{F}} \times \frac{\sqrt{43200 \times r_{\text{laser}}(\text{Hz}) \times T_{\text{obs}}(\text{days})}}{\sigma_y} \tag{2.46}$$

Assuming that the impact parameter b between the probe and the pump at focus is optimised ($b = b_{\text{opt}}$), and using equations 2.6 and 2.7, the sensitivity of the experiment, in terms of number of standard deviations becomes:

$$\begin{aligned} N_{\text{std}} \quad = \quad & 0.65 \times r_{\text{tilt}}\,(R, \theta_{\text{tilt}}) \times \\ & \frac{\mathcal{E}(\text{J}) \times f(\text{mm}) \times \sqrt{r_{\text{laser}}(\text{Hz}) \times T_{\text{obs}}(\text{days})}}{(w_0^2(\mu\text{m}) + W_0^2(\mu\text{m}))^{3/2} \times \sqrt{\mathcal{F}/10^{-5}} \times \sigma_y(\text{nm})} \end{aligned} \tag{2.47}$$

where $\mathcal{E}$ is the pump energy ; $r_{\text{tilt}}\,(R, \theta_{\text{tilt}})$ is the correction factor due to the angle θ_{tilt} between the probe and the reference at the interaction point in the interferometer (defined in equation 2.8) ; R is the ratio of the longitudinal to transverse sizes of the pulses. For a waist at focus of the probe and the pump of $w_0 = W_0 = 5\,\mu$m and their longitudinal size of $w_z = W_z = 7.6\,\mu$m (pulse duration of $\tau_0 = 30$ fs), the R parameter is $R = 1.5$ and the correction factor is $r_{\text{tilt}}\,(R, \theta_{\text{tilt}}) = 0.9$ at $\theta_{\text{tilt}} = 30°$ which is more realistic in practice than $\theta_{\text{tilt}} = 0°$. The sensitivity N_{std} becomes:

$$\boxed{N_{\text{std}} = 0.6 \times \frac{\mathcal{E}(\text{J}) \times f(\text{mm}) \times \sqrt{r_{\text{laser}}(\text{Hz}) \times T_{\text{obs}}(\text{days})}}{(w_0^2(\mu\text{m}) + W_0^2(\mu\text{m}))^{3/2} \times \sqrt{\mathcal{F}/10^{-5}} \times \sigma_y(\text{nm})}} \tag{2.48}$$

The energy $\mathcal{E}$ of the pump pulse and the repetition rate r_{laser} are today determined by the LASERIX facility (2.5 J per pulse, 10 Hz). Therefore, from equation 2.48, three parameters are crucial to reach a high measurement sensitivity:

- A high extinction of the interferometer, corresponding to a low extinction factor $\mathcal{F}$;
- A waist of the probe and pump beams at focus (in the interaction area), w_0 and W_0, as small as possible, while using a relatively large focal length f for the probe;
- A good spatial resolution σ_y for the position measurement of the interference intensity profile.

The goal is to reach the following parameters:

- An extinction $\mathcal{F} = 4 \times 10^{-6}$, corresponding to an amplification factor $\mathcal{A} = 250$. It requires a residual phase noise lower to 10^{-6};

- A minimum waist at focus $w_0 = W_0 = 5\mu$m for both the pump and the probe, with a focal length as large as possible ($f = 500$ mm corresponds to a waist $w = 25$ mm for the collimated probe beam before focus);

- A spatial resolution $\sigma_y = 10$ nm, limited by the ultimate shot noise of the CCD cameras.

We will show in chapter 5 that $\mathcal{F} = 4 \times 10^{-6}$ corresponds to the extinction measured in our current DeLLight pilot experiment. We will show in chapter 6 that $\sigma_y = 10$ nm is the current shot noise measured with our best sensitivity commercial CCD camera. However, as discussed in chapter 7, the spatial resolution in the dark output of the interferometer is today limited by the presence of a mechanical noise due to not suitable mechanical mounts and environment. This noise must be reduced by almost two orders of magnitude. We will explain in chapter 7 the proposed experimental method to measure and suppress this noise, allowing to reach the goal spatial resolution. Finally, focusing a pump pulse to a minimum waist of 5 μm is a realistic value. However, reaching a small waist at focus for the probe, while keeping a large focal length is an issue, as will be discussed in section 2.8.

With these goal values for the critical parameter, and with an energy of 2.5 J for the pump pulses and a laser repetition rate of 10 Hz as delivered by the LASERIX facility, the expected spatial DeLLight signal is $\Delta y_{\mathrm{QED}} = 14$ pm at $\theta_{\mathrm{tilt}} = 30°$ ($\Delta y_{\mathrm{QED}} = 16$ pm at $\theta_{\mathrm{tilt}} = 0°$) and the number of standard deviations is $N_{\mathrm{std}} = \sqrt{T_{\mathrm{obs}}(\mathrm{days})}$. Thus, the QED signal could be observed at a 5-sigma statistical confidence level with 25 days of collected data.

It is important to add that in the future, the DeLLight experiment could benefit from the new generation of ultra-intense lasers with high repetition rate, as the HALPS laser ($\mathcal{E} > 30$ J, 30 fs, 10 Hz) currently in commissioning at ELI Beamlines Centre (Czech Republic). With this laser, the DeLLight signal would be increased by an order of magnitude with an expected signal $\Delta y_{\mathrm{QED}} = 0.18$ nm at 30 J.

2.6.2 Intensity Signal

The intensity signal $\frac{\Delta I}{I}(i)$ of the i^{th} "ON-OFF" measurement is given by:

$$\frac{\Delta I}{I}(i) = \frac{I_{\mathrm{ON}}(i) - I_{\mathrm{OFF}}(i+1)}{I_{\mathrm{OFF}}(i+1)} \tag{2.49}$$

$$\tag{2.50}$$

The DeLLight intensity signal $\frac{\Delta I}{I}$ corresponds to the mean of the successive ON-OFF measurements:

$$\frac{\Delta I}{I} = \left\langle \frac{\Delta I}{I}(i) \right\rangle \tag{2.51}$$

This distribution is characterised by its standard deviation $\sigma_{\Delta I/I}$, which corresponds to the *intensity resolution*. The extraction and computation of the signal are explained in chapter 3. Study and measurement of the spatial resolution are thoroughly detailed in chapter 6.

The expected QED intensity signal $\frac{\Delta I}{I}\Big|_{\rm QED}$ at an impact parameter $b = 0$ (for which the intensity signal is maximal) is:

$$\left.\frac{\Delta I}{I}\right|_{\rm QED} = \frac{\langle\delta\psi\rangle}{\sqrt{F}} = \frac{2c\, n_{2,\max}\, \mathcal{E}}{\lambda_0\,(w_0^2 + W_0^2)\,\sqrt{F}} \times r_{\rm tilt} \tag{2.52}$$
$$= 3.7\times10^{-8} \times \frac{\mathcal{E}(\mathrm{J}) \times r_{\rm tilt}}{(w_0^2(\mu\mathrm{m}) + W_0^2(\mu\mathrm{m})) \times \sqrt{\mathcal{F}/10^{-5}}}$$

where λ is the wavelength of the laser and $\sigma_{\Delta I/I}$ is the intensity resolution in the dark output of the interferometer.

Analogously to the spatial signal (previous section), the DeLLight intensity signal is measured with a significance of $N_{\rm std}$ standard deviations, such as:

$$\left.\frac{\Delta I}{I}\right|_{\rm QED} = N_{\rm std} \times \frac{\sigma_{\Delta I/I}}{\sqrt{N}} \tag{2.53}$$

Assuming that the impact parameter b between the probe and the pump at focus is optimised ($b = 0$) and using equations 2.53 and 2.53, the sensitivity of the experiment, in terms of the number of standard deviations $N_{\rm std}$, is:

$$N_{\rm std} = 7.9\times10^{-6} \times \frac{\mathcal{E}(\mathrm{J}) \times r_{\rm tilt} \times \sqrt{r_{\rm laser}(\mathrm{Hz}) \times T_{\rm obs}(\mathrm{days})}}{(w_0^2(\mu\mathrm{m}) + W_0^2(\mu\mathrm{m})) \times \sqrt{\mathcal{F}/10^{-5}} \times \sigma_{\Delta I/I}} \tag{2.54}$$

We want to reach the same sensitivity as the one obtained with the spatial deflection signal, i.e. $N_{\rm std} = \sqrt{T_{\rm obs}(\mathrm{days})}$. Then, the needed intensity resolution is:

$$\sigma_{\Delta I/I} = 7.9\times10^{-6} \times \frac{\mathcal{E}(\mathrm{J}) \times r_{\rm tilt} \times \sqrt{r_{\rm laser}(\mathrm{Hz})}}{(w_0^2(\mu\mathrm{m}) + W_0^2(\mu\mathrm{m})) \times \sqrt{\mathcal{F}/10^{-5}}} \tag{2.55}$$

Assuming the same experimental parameters as those assumed for the deflection signal in the previous section 2.6.1 ($\mathcal{F} = 4\times10^{-6}$, $w_0 = W_0 = 5$ μm, $\mathcal{E} = 2.5$ J, and $r_{\rm laser} = 10$ Hz), we need to reach an intensity resolution of $\sigma_{\Delta I/I} = 1.8\times10^{-6}$. This value includes the ON-OFF subtraction (factor $\sqrt{2}$) and the beam pointing corrections (another factor $\sqrt{2}$). Therefore, the requested intrinsic intensity resolution of the optical readout for a single spot intensity measurement is $\sigma_I = \sigma_{\Delta I/I}/2 = 0.9\times10^{-6}$. This resolution is limited by the inherent shot noise, which is equal to $\sigma_I = 1/\sqrt{N_{\rm p.e.}}$, where $N_{\rm p.e.}$ is the number of detected photo-electrons. Noting QE the quantum efficiency, the requested number of photons reaching the optical readout in the dark output of the interferometer is then:

$$N_\gamma^{\rm out} = \frac{N_{\rm p.e.}}{\rm QE} = \frac{1}{\rm QE \times \sigma_I^2} = 1.4\times10^{12}\ \text{photons} \tag{2.56}$$

Taking into account the extinction factor $\mathcal{F} = 4\times10^{-6}$, it corresponds to a number of photons per incident laser pulse entering the Sagnac interferometer equal to $N_\gamma^{\rm in} = N_\gamma^{\rm out}/\mathcal{F} = 3.5\times10^{17}$ photons. It corresponds to an incident energy of about 100 mJ per pulse which is relatively

high. A way to reduce the needed incident energy is to reduce the waist of the pump and probe beam at focus, using a shorter focal length, in order to increase the signal. However, reducing the waist at focus of the probe is very challenging, as will be discussed in section 2.8. It also becomes very challenging to maintain a good spatial overlap of the pump and the probe in the interaction area with very small waists at focus. Last but not least, it will be measured on the prototypes that the intensity resolution is much more sensitive to the phase noise of the interferometer than for the spatial resolution (barycenter). Therefore, it is more difficult to reach the shot noise resolution when measuring the interference signal intensity rather than the barycenter.

In conclusion, the measurement of the deflection signal, i.e. the spatial signal in barycenter, seems to be more sensitive than the measurement of the intensity signal.

2.7 Beam pointing fluctuations

It is essential to note that the presence of beam pointing fluctuations between successive laser shots induces fluctuations of the position of the residual intensity profile in the dark output of the interferometer of typical magnitude much larger than the expected displacement signal $\langle \delta y \rangle$. However, as illustrated in figure 2.4, an essential advantage of the Sagnac interferometer is that the interference pattern and the extinction factor in the dark output do not change in the presence of beam pointing fluctuations, assuming that the phase noise defined in section 2.5 is negligible. Fluctuations of the beam pointing produce a simple translation of the intensity profile on the CCD camera, which can be measured and suppressed by monitoring the position of the intensity profile with respect to the back-reflections from the rear side of the beamsplitter. The analysis method to measure and suppress the beam pointing fluctuations is explained in section 3.3.2.

Figure 2.5 shows a scheme of the back-reflections ray tracing. One back reflection, named $I_{AR,1}$, is the direct incident probe beam first reflected on the beamsplitter and then reflected on its backside. It will be used as a reference in order to correct the beam pointing fluctuations of the probe, as explained in section 3.3.2. The second back reflection, named $I_{AR,2}$, is the interference of four transmitted and reflected beams on the beamsplitter. Their intensities are:

$$I_{AR,1} = (r_{AR} \times r)^2 \times I_0 \tag{2.57}$$

$$I_{AR,2} = \left(-r_{AR} \times rt^2 + r_{AR} \times rt^2 + r_{AR} \times r(t^2 - r^2)\right)^2 \times I_0 \tag{2.58}$$

where r and t are the reflection and transmission coefficient in amplitude of the beamsplitter as defined in equation 2.11, r_{AR} is the back-reflection coefficient in amplitude on the back side of the beamsplitter, and I_0 is the incident intensity.

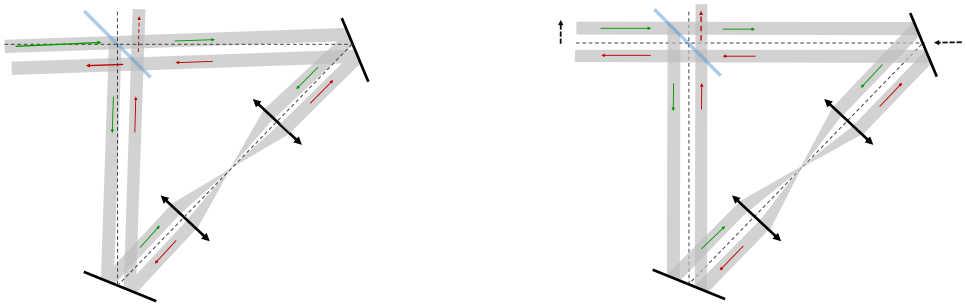

Figure 2.4: Schematic view of the Sagnac interferometer showing how the extinction in the dark output of the Sagnac interferometer is insensitive to the beam pointing fluctuations. (Left) The incident beam is tilted by a small angle. (Right) The beam, or equivalently a mirror, is transversally shifted in the horizontal plane. In both cases, the extinction in the dark output of the interferometer is maintained. Only the position of the intensity profile is transversally shifted. This shift is measured and suppressed by monitoring online the same shift of the back-reflections from the rear side of the beamsplitter.

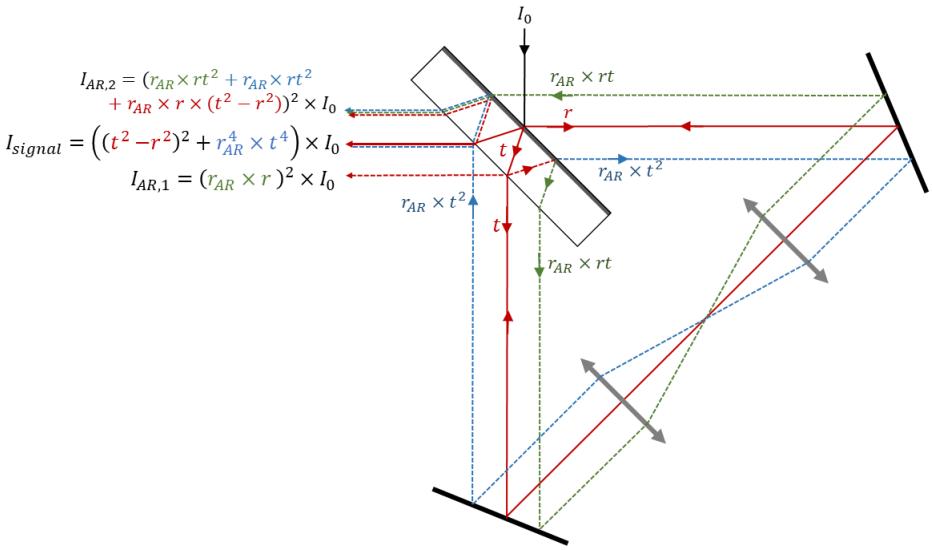

Figure 2.5: Schematic view of the Sagnac interferometer and the ray tracing of the main back-reflections on the rear side of the Sagnac beamsplitter.

Note that a third back reflection is superposed to the interference signal but is not in time (delayed). Its intensity, equal to

$$I_{AR,3} = (r_{AR}^4 \times t^4) \times I_0 = 1/4 \times R_{AR}^2 \times I_0 \tag{2.59}$$

is added to the interference signal. It limits the extinction factor to $\mathcal{F}_{min} = R_{AR}^2/4$. As discussed in appendix B, for the beamsplitter used in the pilot DeLLight setup, the back reflection coefficient (in intensity) is $R_{AR} = 10^{-3}$ and $\mathcal{F}_{min} = 2.5 \times 10^{-7}$.

2.8 Minimum waist at focus w_0

The minimum waist at focus of the pump and probe pulses in the interaction area is one of the most critical parameter since the DeLLight expected signal is inversely proportional to the cube w_0^3 of the beam minimal waist at focus (from equations 2.45 and 2.48). The best course of action would be to choose the smallest waist possible in order to maximise the signal. Focusing the pump pulse to a minimum waist of 5 μm is realistic. Even smaller waists have been achieved using large beam size before focalisation and expensive parabolic mirrors. It is however more difficult for the probe beam. Indeed, for a Gaussian beam, the waist at focus w_0 is proportional to the focal length f and inversely proportional to the waist w of the incident collimated beam before focus, such as:

$$w_0 = \frac{\lambda \times f}{\pi \times w} \tag{2.60}$$

where λ is the wavelength of the laser. Thus, a small focal length is required to reach a small waist at focus. However, we need to use a large focal length since the DeLLight signal is directly proportional to said parameter (see equation 2.44). Therefore, reaching a small waist at focus while keeping a large focal length requires to work with a large waist w for the collimated beam before focus in the Sagnac interferometer.

The goal of the DeLLight experiment is to reach a waist at focus $w_0 = 5$ μm with a focal length $f = 500$ mm, which requires an incident collimated waist $w = 25$ mm and a beamsplitter of thickness of about 75 mm in order to properly distinguish the interference signal from the back-reflections in the dark output (see figure 2.5). In comparison, we are working at the moment with a focal length $f = 100$ mm, a waist before focus $w = 1$ mm and a beamsplitter thickness of 3 mm on the current DeLLight pilot experiment.

There are unfortunately two difficulties when using larger beam sizes in the interferometer. Firstly, it requires more stringent constraints regarding the surface qualities of the optics over larger transverse dimensions (low spatial frequency). Indeed, the phase noise increases when the interference signal is integrated over a larger transverse dimension. This comes from the fact that a perfect surface (a plan surface, for instance) is easier to ensure on a small transverse dimension rather than on a large one. Secondly, a larger beam size requires a thicker beamsplitter in order to separate the back-reflections from the interference signal in the dark output.

A way to maintain a relatively small waist of the collimated probe beam in the interferometer is to optimise the focal length. To this end, we calculate the expected DeLLight deflection signal Δy in the dark output as a function of the focal length f, for three different incident collimated probe waist w (25, 12.5 and 7 mm), and with the pump waist at focus equal to its nominal goal value $W_0 = 5$ μm. These results are displayed on figure 2.6, for a wavelength $\lambda = 800$ nm. The signal is maximal at $\Delta y = 14 \pm 1$ pm for a focal length corresponding to a minimum probe waist at focus $w_0 \simeq 3.5$ μm, and a collimated probe waist $w = 12.5$ mm with a focal length $f \approx 150 - 200$ mm. This signal is equivalent to the one obtained with the DeLLight goal parameters $w = 25$ mm and $f = 500$ mm (except that the probe waist at focus is slightly bigger than half the pump waist at focus in the first case). Therefore, it is preferable to

work with a smaller focal length and a probe waist more or less equal to half the pump waist at focus in the interaction area, in order to ensure a relatively small diameter of the collimated beam inside the Sagnac interferometer, and thus reduce the integrated phase noise.

Moreover, another approach to maintain a small size of the collimated beam in the interferometer is to lower the probe wavelength from 800 nm to a 400 nm for instance, using the frequency doubling technique by placing a thin, non-linear BBO crystal before the Sagnac interferometer (with appropriate beamsplitter and optics for 400 nm). Figure 2.7 shows the expected signal Δy as a function of the focal length f with a wavelength of the probe beam equal to 400 nm. By comparing figures 2.6 and 2.7, we see that we can reach the same DeLLight sensitivity if we use a 800 nm probe beam with a beam size in the interferometer $w = 25$ mm, a focal length $f = 500$ mm and a waist at focus $w_0 = 5\mu$m (DeLLight goal parameters), as if we use a 400 nm probe beam with $w = 7$ mm, $f = 200$ mm and $w_0 = 3.5\mu$ m, which is experimentally easier to set up and provides a lower phase noise value.

In summary, using a 400 nm probe beam and a focal length $f = 200$ mm in the interferometer allows to reach the DeLLight goal sensitivity with a collimated beam size of the probe of only $w = 7$ mm, which is 4 times smaller than the initial goal value. However, along the non-linearity effects within the beamsplitter at high energy (see section 2.9), a smaller beam size will further limit the allowed incident energy of the probe in the interferometer because the saturation per pixel on the CCD camera will be reached sooner.

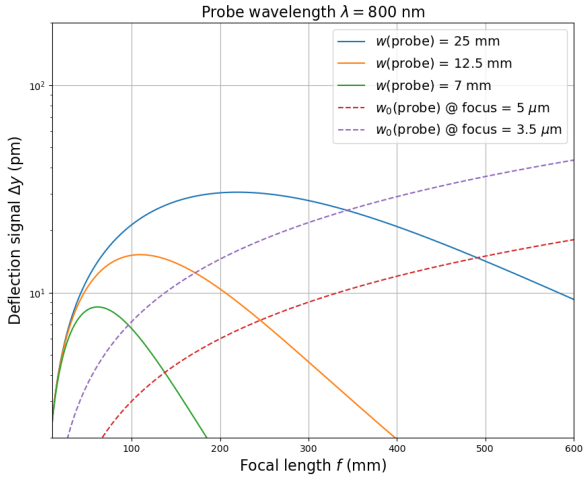

Figure 2.6: Plot of the DeLLight signal Δy (in nm) in the dark output of the interferometer as a function of the focal length f for three different waists w (25 mm in blue, 12.5 mm in orange and 7 mm in green) of the collimated probe beam in the interferometer, and for a pump waist at focus $W_0 = 5\mu$m. In dashed lines is plotted the signal Δy depending on the focal length, with the minimum waist w_0 of the probe beam at focus fixed at 5 μm (red) and 3.5 μm (purple), while w is a free parameter. The wavelength of the probe beam is 800 nm. The DeLLight signal is $\Delta y = 14 \pm 1$ pm for either $f \approx 500$ mm, $w_0 = 5$ μm, $w = 25$ mm or $f \approx 150$ mm, $w_0 = 3.5$ μm, $w = 12.5$ mm.

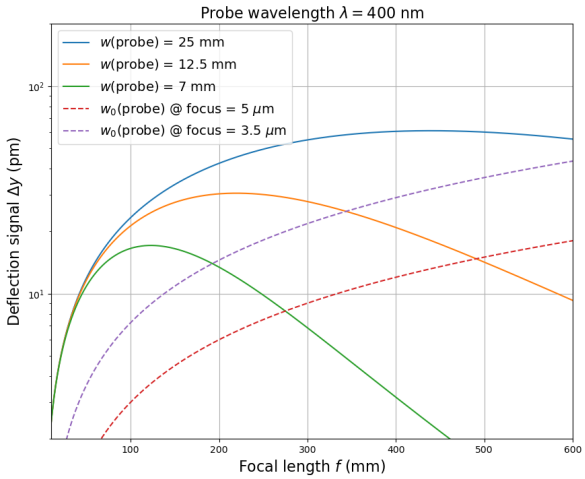

Figure 2.7: Same as figure 2.6 but with a wavelength of the probe beam equal to 400 nm. The DeLLight signal is $\Delta y = 14.5 \pm 0.5$ pm for either $f \approx 500$ mm, $w_0 = 5$ μm, $w = 12.5$ mm or $f \approx 200$ mm, $w_0 = 3.5$ μm, $w = 7$ mm.

2.9 Input intensity limitation: non linearity in the beam splitter

The DeLLight experiment requires a very low extinction factor $\mathcal{F}$ in the dark output of the Sagnac interferometer in order to get a high amplification. Moreover, in order to reach a good spatial resolution, the incident energy $\mathcal{E}_{in}$ in the interferometer must be high to be able to collect a high number of photons on the CCD camera in the dark output. However, the intensity between transmitted and reflected pulses on their respective first crossing through the beamsplitter (BS) is different. Indeed, the reflected pulse travels through the whole interferometer before crossing the BS for the first time, while the transmitted pulse crosses the BS before travelling through the interferometer. Hence, both pulses have different intensity values because of the losses caused by the reflections on the mirrors. Therefore, the intensity difference between transmitted and reflected pulses can lead to nonlinear effects in the beamsplitter at high intensities, which induces a phase-shift in intensity and in turns limits the extinction in the dark output. The schematic of the interferometer is presented figure 2.8.

Moreover, the transverse sizes of both pulses are different due to their respective divergence, which depends on the optical path travelled by each pulse. Indeed, the reflected pulse diverged before crossing the BS for the first time, while the transmitted pulse did not. Hence, the contrast of the interference signal in the dark output is degraded since both pulses have different transverse sizes, which also degrades the extinction.

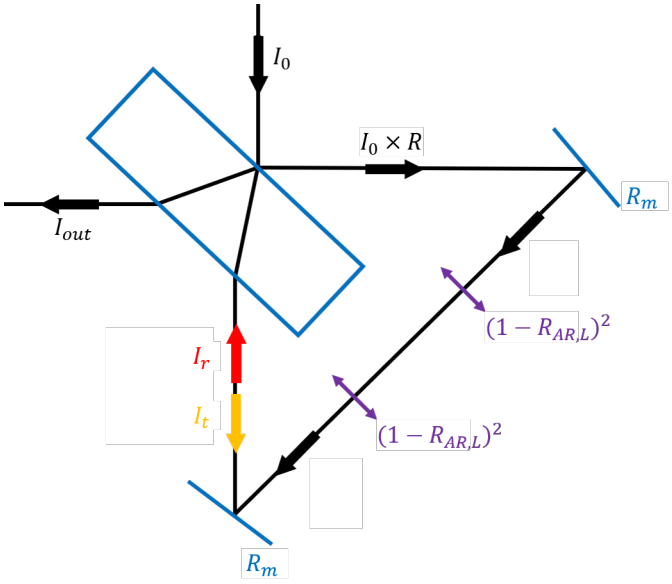

Figure 2.8: Schematic of the Sagnac interferometer in triangle configuration with two focusing lenses. I_0 is the incident beam intensity ; I_r and I_t are the intensities of the reflected and transmitted pulses respectively ; R, R_m and $R_{AR,L}$ are the reflection coefficients of the beamsplitter, the mirrors and lenses respectively.

2.9.1 Phase-shift due to the intensity variation between reflected and transmitted beams

The intensity difference between the transmitted I_t and reflected pulses I_r mostly comes from energy losses on the two dielectric mirrors of the Sagnac interferometer (see figure 2.3), as well as on the coating of the BS itself, for which the reflection R and transmission T coefficients are defined equation 2.11. Therefore, on the first transmission through the BS (see figure 2.8), the transmitted pulse sustains less intensity losses than the reflected pulse, such as:

$$I_t = \frac{I_0}{2} \times (1 + \delta a) \tag{2.61}$$

$$I_r = \frac{I_0}{2} \times R_m^2 \times (1 - R_{AR,L})^4 \times (1 - \delta a) \tag{2.62}$$

$$\simeq \frac{I_0}{2} \times R_m^2 \times (1 - 4R_{AR,L}) \times (1 - \delta a) \tag{2.63}$$

where I_0 is the input intensity entering the Sagnac interferometer, R_m is the reflection factor of the mirrors and $R_{AR,L}$ is the reflection factor of the anti-reflective coating of the lenses. The variation of intensity δI between the transmitted and reflected pulses is then:

$$\delta I = I_t - I_r = \frac{I_0}{2}\Big[(1 + \delta a) - R_m^2 \times (1 - 4R_{AR,L}) \times (1 - \delta a)\Big] \tag{2.64}$$

Moreover, this variation δI induces a relative change of the optical index in the BS due to the optical Kerr effect in the silica substrate, such as $\delta n = \delta I \times n_2$ where n_2 is the Kerr index in

silica ($n_2 \approx 2 \times 10^{-16}$ cm^2/W) and δn is the index variation between the transmitted and the reflected pulses. This relative difference of index crossed by the two pulses during the first transmission through the BS produces a phase shift $\delta\Phi$ equal to:

$$\delta\Phi = \frac{2\pi z}{\lambda} \times \delta n \tag{2.65}$$

where $\lambda = 815$ nm is the wavelength of the laser, $z = f(e) \simeq 1.25 \times e$ is the travelled distance by the beam in the BS and e is the width of the BS. If the phase shift becomes too high, the extinction factor of the interferometer becomes dominated by this non linear phase. Then, we have $\mathcal{F} = (\delta\Phi)^2$ and:

$$\delta n = \frac{\lambda}{2\pi z} \times \sqrt{\mathcal{F}} \tag{2.66}$$

Moreover, the maximal input energy $\mathcal{E}_{in}$ allowed to enter the Sagnac interferometer is defined by:

$$\mathcal{E}_{in} \simeq I_0 \times \tau \times w^2 \tag{2.67}$$

where τ is the pulse duration of the laser, w is the size of the collimated beam in the interferometer (FWHM). Finally, using equations 2.64 to 2.66, the allowed energy becomes:

$$\mathcal{E}_{in} = \frac{\lambda\, \tau\, w^2}{n_2\, \pi\, z} \times \frac{\sqrt{\mathcal{F}}}{(1+\delta a) - R_m^2 \times (1 - 4R_{AR,L}) \times (1 - \delta a)} \tag{2.68}$$

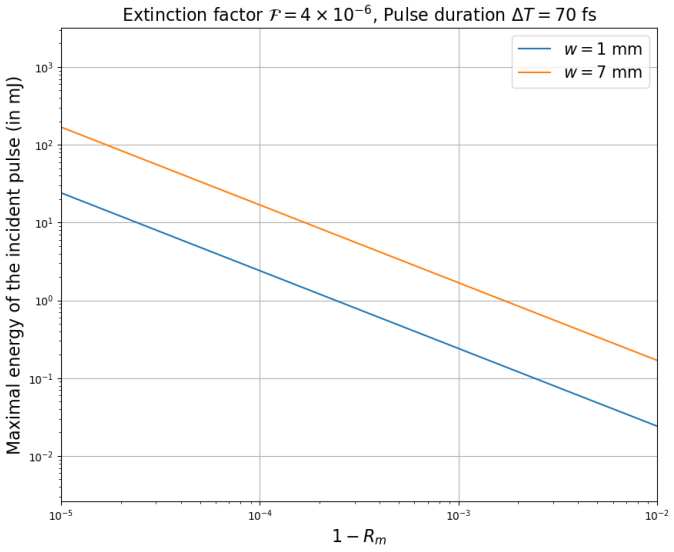

Figure 2.9: Evolution of the maximal input energy $\mathcal{E}_{in}$ entering the Sagnac interferometer depending on the factor $1 - R_m$, where R_m is the reflection factor of the mirrors. This plot corresponds to an extinction factor of $\mathcal{F} = 4 \times 10^{-6}$, a waist of the collimated beam in the interferometer of $w = 1$ mm (blue) and $w = 7$ mm (orange), and a laser pulse duration is chosen at $\tau \approx 70$ fs.

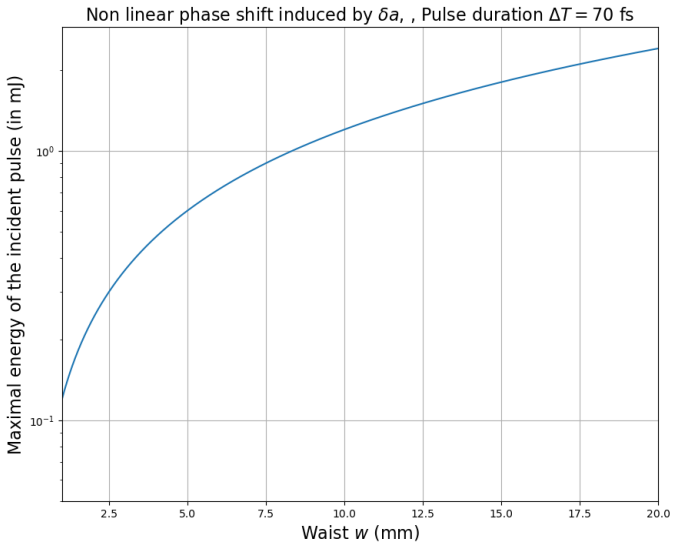

Figure 2.10: Evolution of the maximal input energy $\mathcal{E}_{in}$ entering the Sagnac interferometer as a function of the beam size w, when $R_m = 1$ and $R_{AR} = 0$, and taking into account only δa. The laser pulse duration is chosen at $\tau \approx 70\,\text{fs}$.

In figure 2.9, we calculated the maximal incident energy as a function of $(1 - R_m)$ (assuming $\delta a = R_{AR,L} = 0$), with an extinction factor $\mathcal{F} = 4 \times 10^{-6}$ and for two different values of the beam waist: $w = 1$ mm corresponds to the current beam size in the pilot experiment, and $w = 7$ mm is the optimised goal waist for the DeLLight experiment in vacuum. We have also assume that $e = 3 \times w$ as in the BS used in the pilot experiment (minimum thickness in order to separate efficiently the signal from the back reflections). We will see in chapter 6 that the requested incident energy to reach the shot noise spatial resolution is about 8 mJ with a beam size $w = 7$ mm. Therefore, from figure 2.9, a mirror reflectivity of $R = 99.99\%$ $(1 - R_m = 10^{-4})$, as is the case for the current mirrors used in the pilot experiment, is appropriate. Same calculation can be done with R_{AR} and we also verify that $R_{AR} = 10^{-4}$ is needed in order to avoid any non linear limitation.

We can also calculate the requirements on the parameter δa. We assume $R_{AR} = 1 - R_m = 0$. The extinction is now limited only by δa and we have $\mathcal{F} = (\delta a)^2$. Equation 2.68 becomes:

$$\mathcal{E}_{in} = \frac{\lambda\,\tau\,w^2}{2\,n_2\,\pi\,z} \tag{2.69}$$

The maximal incident energy is thus independent of δa and $\mathcal{F}$. Its value depends only on the beam size w and is plotted on figure 2.10. For a beam size of $w = 7$ mm, corresponding to the target value (as discussed in the previous section), the maximal energy of the incident probe pulse is of the order of 1 mJ. However, the incident energy that will be needed to reach the shot noise spatial resolution of 10 nm (with $\mathcal{F} = 4 \times 10^{-6}$) is 8 mJ for a beam-size $w = 7$ mm. We conclude that the non linearity asymmetry in the beamsplitter induced by the δa asymmetry (R/T asymmetry) is possibly a limiting effect to reach the ultimate shot noise spatial resolution.

A way to get rid of it is either to work with a lower extinction, reducing the signal amplitude, or to reduce the spot size in the dark output. This subject must be carefully studied in the future.

2.9.2 Phase-shift due to the natural divergence of the beams in the interferometer

The natural divergence of the transmitted and reflected pulses in the interferometer also induces a phase-shift between them on the first transmission through the BS, and thus limits the authorised input energy. Indeed, the reflected pulse travels on a longer optical path than the transmitted pulse before going through the BS for the first time. Thus, the waist (FWHM) of the collimated reflected pulse w_r is larger than the waist of the collimated transmitted pulse w_t on the first transmission, such as:

$$w_t \approx w_{in} \tag{2.70}$$

$$w_r(L) = w_{in}\sqrt{1+\left(\frac{L\lambda}{\pi w_{in}^2}\right)} \tag{2.71}$$

where w_{in} is the waist (FWHM) of the input pulse in the Sagnac interferometer and L is the length travelled by the reflected pulse in the interferometer. It is approximately $L \approx 1$ m.

With a similar reasoning as for the intensity phase-shift explained in the previous section, we can calculate the index variation δn in the BS between the transmitted and reflected pulses:

$$n_{t,r} = n_2 \times I_0 = n_2 \times \frac{\mathcal{E}_{in}}{\tau\, w_{t,r}^2} \tag{2.72}$$

$$\delta n = n_t - n_r = \frac{n_2\,\mathcal{E}_{in}}{\tau}\left(\frac{1}{w_t^2} - \frac{1}{w_r^2}\right) \tag{2.73}$$

Finally, using equations 2.66 and 2.73, we can calculate the evolution of the maximal input energy E_{in} allowed in the interferometer, depending on the input waist w_{in}:

$$\mathcal{E}_0(w_{in}) = \frac{\tau\,\delta n}{n_2} \times \frac{1}{\left(\frac{1}{w_{in}^2} - \frac{1}{w_r^2}\right)} = \frac{\tau\,\lambda\sqrt{F}}{2\,n_2\pi z} \times \frac{1}{\left(\frac{1}{w_{in}^2} - \frac{1}{w_r^2}\right)} \tag{2.74}$$

The result is presented on figure 2.11. For a beam size $w = 7$ mm, corresponding to the target value, the maximal energy of the incident probe pulse is of the order of 100 mJ which is much higher than the requested energy. We conclude that the beam divergence is not an issue for large beam size. However, this can be a limitation for small beam size as the one used in the current pilot experiment ($w = 1$ mm) if the optical path length is too large.

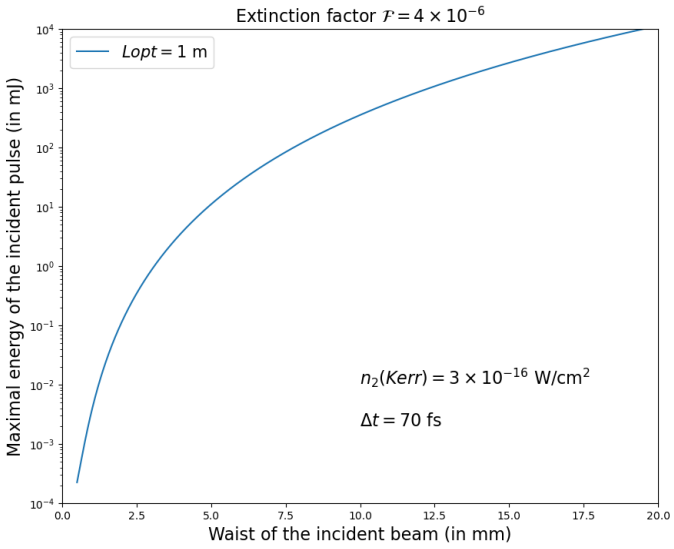

Figure 2.11: Evolution of the maximal input energy $\mathcal{E}_{in}$ entering the Sagnac interferometer as a function of the beam size w, for an extinction factor $\mathcal{F} = 4 \times 10^{-6}$ and taking into account the divergence of the beam.

2.10 Residual gas

2.10.1 Contribution of residual gas

When trying to observe the DeLLight effect in vacuum, there ought to be some residual gas inside the vacuum chamber with which the intense pump pulse might interact and produce an artefact signal.

The optical Kerr effect in the residual gas is, at first sight, a nonlinear effect much stronger than the corresponding effect in vacuum. For instance, the Kerr index in air at atmospheric pressure ($n_{2,\text{air}} \approx 10^{-19}\,\text{cm}^2/\text{W}$) is about 10^{14} times larger than the expected nonlinear index of vacuum ($n_{2,\text{QED}} \approx 1,56.10^{-33}\,\text{cm}^2/\text{W}$). Since this value is proportional to the pressure, setting a Kerr index n_2 to lie an order of magnitude below the index of vacuum $n_{2,\text{QED}}$ requires a residual pressure of about 10^{-12} mbar. However, this result is only true if the pump-probe interaction volume V is large enough to contain a few atoms. For the DeLLight experiment, the interaction volume is very small, of the order of $V \approx w_0^2\,\Delta t\,c \approx 225\,\mu\text{m}^3$. The vacuum chamber of the DeLLight experiment is designed to ensure a nominal pressure for the full chamber below 10^{-6} mbar and a local pressure in the interaction area below 10^{-8} mbar. At this local pressure, there is, on average, only 0.1 residual atom inside the pump-probe interaction volume V. Therefore, at achievable pressures, we are already in a regime far below that of the coherence required for a possible refraction effect, and where the notion of refractive index for air can no longer be defined.

However, the Kerr effect in residual gas should not be an issue. Indeed, in the DeLLight

setup at the LASERIX facility, the intensity of the pump in the interaction area is of the order of 10^{20} W/cm^2. At this intensity, the residual gas is completely ionised by the pump and all the electrons are removed from the atoms. We thus have an electromagnetic wave crossing a pure uniform relativistic plasma. Investigating the dynamics of this system will require numerical simulations, but its effect on the DeLLight signal is expected to be negligible. Indeed, the plasma density and the plasma index is transversely uniform in the pump-probe interaction area, so that the perturbation of the probe phase is symmetric and the mean deflection $\langle \delta\theta_y \rangle$ (DeLLight signal) is null. This is here an important feature of the Sagnac interferometry measurement. While the residual plasma signal is expected to be null, let us estimate here the plasma index for a residual gas at pressure p. The plasma index is $n_p = \sqrt{1 - n_e/n_c}$, where n_c is the critical density equal to:

$$n_c = \frac{\omega_0^2 \times m_e}{\mu_0 \times c^2 \times e^2} = 1.75 \times 10^{27} \text{ m}^{-3} \ (\lambda_0 = 800 \text{ nm}) \tag{2.75}$$

and $n_e = 2.7 \times 10^{22} \times p(\text{mbar})$ is the electron density. The change of the vacuum index $1 - n_p$ due to the residual plasma is then equal to the QED change of vacuum index δn_{QED} ($I = 10^{20}$ W/cm^2) when $p = 10^{-8}$ mbar.

2.10.2 Experimental tests to distinguish between possible artefacts induced by residual gas and the vacuum signal

Experimental tests which could distinguish between a possible artefact induced by the residual gas and the vacuum signal are available.

The first test would be to delay the probe pulse with a delay of the order of 100 ps to ns, in order for it to cross the interaction area after the pump pulse, but still crossing the residual plasma (for which the lifetime is larger that the added delay). Then, the vacuum QED signal would disappear since the probe is not in coincidence with the pump anymore, while an artefact plasma signal would still be present. This is an important crosscheck.

The second possible test would be to invert the propagation directions of the probe and reference pulses (i.e., moving from a counter-propagating pump-probe interaction to a co-propagating one). Thus, any plasma signal should remain (and should even be increased since the signal is integrated along the longitudinal interaction), while the vacuum signal would be suppressed according to the correctional factor r_{tilt} (equation 2.1).

Another possible test would be to decrease the intensity of the pump pulse by a factor of 10 in order to reduce the vacuum signal by the same factor, while any artefact due to the plasma should be constant, since the intensity would still be high enough to completely ionise the atoms.

Let us add that the Kerr effect in air will be used to calibrate and validate the DeLLight experimental method. The measurement will be carried out with a relatively low pump intensity ($\approx 10^{11}$ W/cm^2) in order to avoid generating a plasma via ionisation of air molecules, and the optical Kerr effect will be measured as a function of the pressure in the interaction area. More generally, the use of the Kerr or plasma signals can be used to monitor and control the spatial and temporal overlap of the pump and probe pulses in the interaction area.

2.11 Summary

In conclusion, with a waist at focus $w_0 = 5$ for the pump and probe pulses and with an energy of 2.5 J for the pump pulses as delivered by the LASERIX facility, the expected deflection angle due to a QED change of the optical index of vacuum is about 0.1 prad. With an extinction factor of the Sagnac interferometer of $\mathcal{F} = 4 \times 10^{-6}$ (corresponding to an amplification factor $\mathcal{A} = 1/(2\sqrt{\mathcal{F}}) = 250$), it corresponds to a transverse shift of the interference intensity profile in the dark output of $\Delta y = 0.015$ nm. With a spatial resolution of $\sigma_y = 10$ nm, it can be observed at a 5-sigma statistical confidence level with 25 days of collected data (1 sigma per square root of number of days of collected data). With the HALPS laser ($\mathcal{E} > 30$ J, 30 fs, 10 Hz) currently in commissioning at ELI Beamlines Centre (Czech Republic), the expected signal would be an order of magnitude higher, $\Delta y = 0.02$ nm, and could be measured at 5-sigma with only 6 hours of collected data.

Therefore, the sensitivity of the DeLLight experiment relies on three crucial parameters: the quality of the focalisation, the extinction factor of the interferometer, and the spatial resolution. The difficulties and limitations to reach a small waist of the probe at focus have been discussed here. In chapters 5 and 7 respectively, we will show that the goal extinction factor and spatial resolution are reachable.

Chapter 3

Analysis method to extract the DeLLight signal

The DeLLight signal consists of two distinct signals: the barycenter and the intensity signals, as discussed in section 2.5.2. On one end, the barycenter signal corresponds to the transversal shift of the intensity profile in the dark output of the interferometer due to the DeLLight effect. We note Δx and Δy the barycenter signals along the horizontal x-axis and the vertical y-axis respectively. On the other end, the intensity signal corresponds to the intensity variation in the dark output caused by the DeLLight effect. We note $\frac{\Delta I}{I}$ the intensity signal normalised by the reference intensity.

In this chapter, we describe the method to reconstruct both spatial and intensity signals.

3.1 Definition of the interference signal and the back reflections in the dark output of the interferometer

The intensity profile of the Dellight signal is recorded by a CCD camera in the dark output of the interferometer and stored as Tagged Image File Format images (TIFF) at a repetition rate of 10 Hz. Then, they are analysed using Python computation programs developed within the DeLLight team. These TIFF images provides three distinct beam spots. A typical TIFF image, here collected on December, the 20th (2021) with the DeLLight pilot experiment, is provided on figure 3.1. The spot in the centre corresponds to the interference signal and both spots on the outskirts correspond to the back-reflections of the incident beam on the back side of the beamsplitter, as described in section 2.7.

3.2 Choice of the Region of Interest and efficiency

3.2.1 Definition of the Region of Interest

The first step of the analysis is to define the Region of Interest (RoI) of both the interference signal and the reference (back reflection spot) from which the barycenter and intensity signals

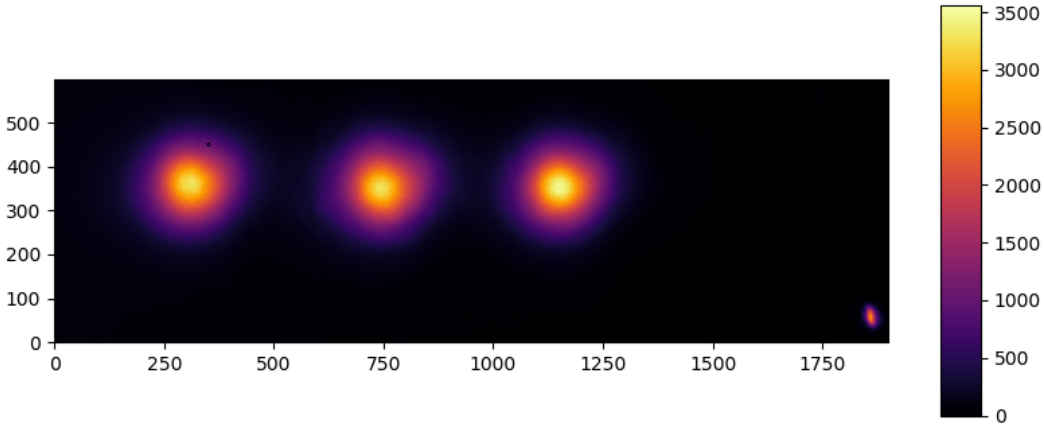

Figure 3.1: Raw CCD image of the signal (middle spot) and the reference (right spot) in the dark output of the interferometer using a Basler CCD camera (acA1920-40gm) of pixel side size 5.86 μm and a Pixel Bit Depth (ADU resolution) of 12 bits. The left spot is the other back-reflection from the beamsplitter (unused in the analysis). The colour scale corresponds to the ADU content of each pixel (dataset 6, collected on December, the 22th, 2021).

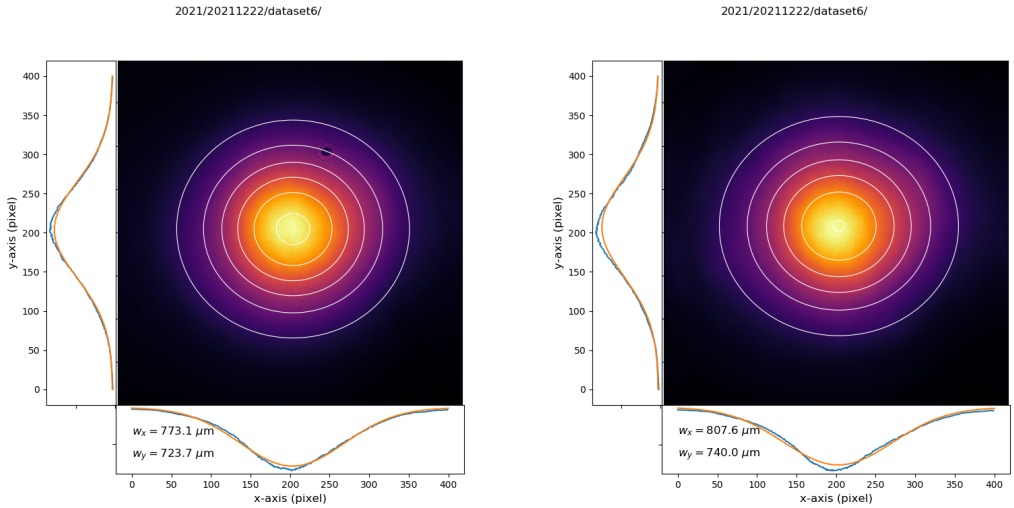

Figure 3.2: CCD images of the beam profiles of the reference (left) and the interference signal (right) from the same image as figure 3.1. A 2-dimensional Gaussian fit delivers the beam waists: $w_{ref} \approx 745\,\mu$m and $w_{sig} \approx 775\,\mu$m, which correspond to $FWHM_{ref} \approx 875\,\mu$m and $FWHM_{sig} \approx 910\,\mu$m (dataset 6, collected on December, the 22th, 2021).

will be extracted. The coordinates of the centre of the RoI, $(x_{0,sig}, y_{0,sig})$ for the interference signal and $(x_{0,ref}, y_{0,ref})$ for the reference, are obtained by fitting a 2D Gaussian function of the transverse intensity profile $I_{sig}(x, y)$ of the first image of the given data-set, with two main axes

(horizontal x-axis and vertical y-axis). An example of these profiles is shown on figure 3.2. Then we define a square RoI, of side length w_{RoI}, centred around each of these positions.

The size w_{RoI} of the RoI on which the analysis is performed is crucial in order to obtain the best sensitivity possible. Indeed, choosing too large a RoI would degrade the spatial and intensity resolutions (as will be explained thoroughly in chapter 6) because more noise is integrated. Moreover, for even greater RoI, the tail distributions of the other two spots would also be integrated which would skew the barycenter and the intensity values. On the opposite, too small a RoI would truncate the signal and thus skew the barycenter and intensity values.

3.2.2 Influence of the RoI-size on the barycenter shift efficiency

The measured DeLLight signals along the horizontal x-axis, Δx_{mes}, and vertical y-axis, Δy_{mes}, depend on the size of the RoI w_x and w_y respectively, such as:

$$\Delta x_{mes} = \frac{\int_{-w_x/2}^{w_x/2} x \times I_{sig,y}(x + \Delta x)\,\mathrm{d}x}{\int_{-w_x/2}^{w_x/2} I_{sig,y}(x + \Delta x)\,\mathrm{d}x} \tag{3.1}$$

$$\Delta y_{mes} = \frac{\int_{-w_y/2}^{w_y/2} y \times I_{sig,x}(y + \Delta y)\,\mathrm{d}y}{\int_{-w_y/2}^{w_y/2} I_{sig,x}(y + \Delta y)\,\mathrm{d}y} \tag{3.2}$$

The efficiencies ϵ_x and ϵ_y to measure the DeLLight signals Δx and Δy respectively are defined by:

$$\epsilon_x = \Delta x_{mes}/\Delta x \tag{3.3}$$

$$\epsilon_y = \Delta y_{mes}/\Delta y \tag{3.4}$$

We have $\epsilon_x = \epsilon_y = 1$ when $w_{RoI} = \infty$.

We now calculate the efficiency ϵ_s as a function of the RoI-size w_x and w_y, in the case of a Gaussian intensity profile for the interference signal defined as:

$$\begin{aligned} I_{sig,x}(x) &= \exp\left(-\frac{(x - \Delta x)^2}{2\sigma_{b,x}^2}\right) \\ I_{sig,y}(y) &= \exp\left(-\frac{(y - \Delta y)^2}{2\sigma_{b,y}^2}\right) \end{aligned} \tag{3.5}$$

Additionally, equation 3.5 can be linearized using the following mathematical approximation:

$$a \exp -\frac{(x - \frac{b\sigma^2}{a})^2}{2\sigma^2} \approx (a + bx) \exp -\frac{x^2}{2\sigma^2} \tag{3.6}$$

when $\frac{b\sigma^2}{a} << 1$. Considering equations 3.5, these constants are: $a = 1$, $\Delta x = \frac{b_x \sigma_{b,x}^2}{a} << 1$, $\Delta y = \frac{b_y \sigma_{b,y}^2}{a} << 1$, hence $b_x = \frac{\Delta x}{\sigma_{b,x}^2}$ and $b_y = \frac{\Delta y}{\sigma_{b,y}^2}$.

Thus, the Gaussian intensity profiles can be written as:

$$I_{sig,x}(x) = (1 + x\frac{\Delta x}{\sigma_{b,x}^2}) \exp(-\frac{x^2}{2\sigma_{x,y}^2}) \tag{3.7}$$

$$I_{sig,y}(y) = (1 + y\frac{\Delta y}{\sigma_{b,y}^2}) \exp(-\frac{y^2}{2\sigma_{b,y}^2}) \tag{3.8}$$

By noting $A_x = \frac{w_x}{2\sqrt{2}\times\sigma_{b,x}}$ and $A_y = \frac{w_y}{2\sqrt{2}\times\sigma_{b,y}}$, and by using *Wolfram Alpha* (computing program), we obtain:

$$\Delta x_{mes} = \Delta x \times \frac{\sqrt{2\pi} \times \sigma_{b,x} \times \mathrm{erf}(A_x) - w_x \exp(-A_x^2)}{\sqrt{2\pi} \times \sigma_{b,x} \times \mathrm{erf}(A_x)} \tag{3.9}$$

$$\Delta y_{mes} = \Delta y \times \frac{\sqrt{2\pi} \times \sigma_{b,y} \times \mathrm{erf}(A_y) - w_y \exp(-A_y^2)}{\sqrt{2\pi} \times \sigma_{b,y} \times \mathrm{erf}(A_y)} \tag{3.10}$$

where erf is the error function defined by $\mathrm{erf}(x) = \frac{2}{\sqrt{\pi}} \int_0^x \exp -t^2 \, \mathrm{d}t$.

Finally, if we suppose the beam to be perfectly Gaussian in all directions, the efficiencies ϵ_x and ϵ_y in both directions are equal, such as: $\epsilon_s = \epsilon_x = \epsilon_y$. After further computations, the efficiency ϵ_s for a squared RoI $w_{RoI} = w_x \times w_y$ is:

$$\epsilon_s = \frac{\Delta y_{mes}}{\Delta y} = 1 - \frac{w_{RoI} \times \exp(-A_y^2)}{\sqrt{2\pi} \times \sigma_{b,x} \times erf(A_y)} \tag{3.11}$$

The theoretical efficiency ϵ_s is plotted in figure 3.3 (orange) as a function of the RoI-size w_{RoI}, normalised to the FWHM of the Gaussian beam profile. We have $\epsilon_s = 0.12$ when $w_{RoI} = 0.5 \times FWHM$ and $\epsilon_s = 0.4$ when $w_{RoI} = 1 \times FWHM$.

Additionally, we have measured the real efficiency (purple plot on figure 3.3) in order to crosscheck it with the theoretical one. This measurement has been done by sending a direct Gaussian beam on the CCD camera via a reflection on a mirror mounted on a micrometric translation stage. The beam was translated horizontally by step of 50 μm and for each beam position, we measured the horizontal shift Δx while keeping a fixed RoI. When doing the analysis process of DeLLight data images collected by the CCD camera in the dark output of the interferometer, we can optimise the RoI-size accordingly in order to optimise the figure of merit which is proportional to the efficiency over spatial resolution ratio ϵ_y/σ_y.

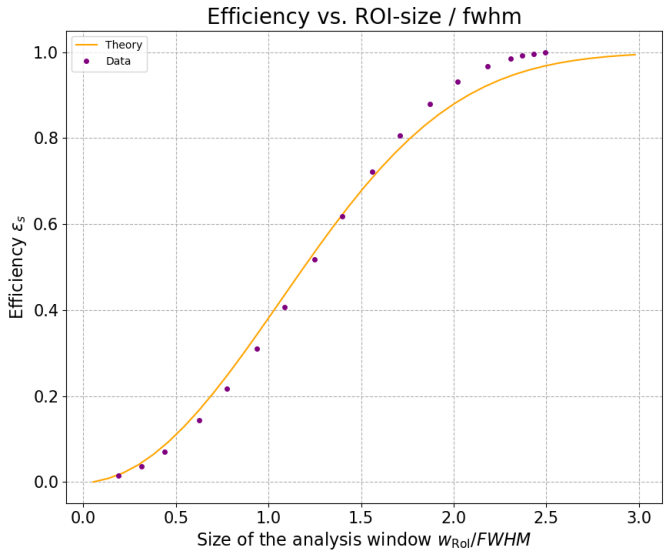

Figure 3.3: Evolution of the theoretical efficiency ϵ_s (orange) as a function of the RoI-size w_{RoI}, normalised to the FWHM of the Gaussian beam profile. The measured efficiency is plotted in purple.

3.3 Extraction of the DeLLight signal in the dark output using the barycenter

3.3.1 Computation of the barycenter of the intensity profiles

The second step of the analysis consists of calculating the barycenter of the reference and signal beams for successive laser shots $2i-1$ and $2i$ of a given dataset. The barycenter of the signal along the horizontal x-axis $\bar{x}_{\text{sig}}(i)$ is defined by:

$$\bar{x}_{\text{sig}}(i) = \frac{\sum_{i,j=1}^{w_{RoI}} x_k \times I_x^i(x_k, y_k)}{\sum_{i,j=1}^{w_{RoI}} I_x^i(x_k, y_k)} \tag{3.12}$$

where $I_x^i(x_k, y_k)$ is the intensity profile along the horizontal x-axis of the pixel k in the given RoI of an odd $(2i-1)$ or even $(2i)$ image.

Similarly, we define the barycenter of the signal along the vertical y-axis:

$$\bar{y}_{\text{sig}}(i) = \frac{\sum_{i,j=1}^{w_{RoI}} y_k \times I_y^i(x_k, y_k)}{\sum_{i,j=1}^{w_{RoI}} I_y^i(x_k, y_k)} \tag{3.13}$$

and the barycenter of the reference (back-reflection) along the horizontal x-axis and vertical y-axis respectively:

$$\bar{x}_{\text{ref}}(i) = \frac{\sum_{i,j=1}^{w_{RoI}} x_k \times I_x^i(x_k, y_k)}{\sum_{i,j=1}^{w_{RoI}} I_x^i(x_k, y_k)} \tag{3.14}$$

$$\bar{y}_{\mathrm{ref}}(i) = \frac{\sum_{i,j=1}^{w_{RoI}} y_k \times I_y^i(x_k, y_k)}{\sum_{i,j=1}^{w_{RoI}} I_y^i(x_k, y_k)} \tag{3.15}$$

Once these barycenters are calculated, they are separated into ON and OFF barycenters (corresponding to odd and even images) since we successively alternate laser shots with (ON) and without (OFF) pump/probe interaction in the interferometer. The ON and OFF barycenters are written $\bar{x}_{\mathrm{sig}}^{\mathrm{ON}}(i)$, $\bar{y}_{\mathrm{sig}}^{\mathrm{ON}}(i)$, $\bar{x}_{\mathrm{sig}}^{\mathrm{OFF}}(i)$ and $\bar{y}_{\mathrm{sig}}^{\mathrm{OFF}}(i)$ for the interference signal, and $\bar{x}_{\mathrm{ref}}^{\mathrm{ON}}(i)$, $\bar{y}_{\mathrm{ref}}^{\mathrm{ON}}(i)$, $\bar{x}_{\mathrm{ref}}^{\mathrm{OFF}}(i)$ and $\bar{y}_{\mathrm{ref}}^{\mathrm{OFF}}(i)$ for the reference spot.

3.3.2 Suppression of the beam pointing fluctuations

The next step of the analysis is to suppress the beam pointing fluctuations of the laser, using the back-reflection of the Sagnac interferometer beamsplitter, namely the reference. Indeed, it directly corresponds to the incident beam entering the interferometer, and thus has the same beam pointing fluctuations as the signal. So, for each ON and OFF measurements, we suppress the beam pointing fluctuations using the correlation of the barycenters of the signal ($\bar{x}_{\mathrm{sig}}(i)$,$\bar{y}_{\mathrm{sig}}(i)$) and the reference ($\bar{x}_{\mathrm{ref}}(i)$,$\bar{y}_{\mathrm{ref}}(i)$). The corrected barycenters are then:

$$\begin{aligned}
\bar{x}_{\mathrm{corr}}^{\mathrm{OFF}}(i) &= \bar{x}_{\mathrm{sig}}^{\mathrm{OFF}}(i) - \left(a_x^{\mathrm{OFF}} \times \bar{y}_{\mathrm{ref}}^{\mathrm{OFF}}(i) + b_x^{\mathrm{OFF}}\right) \\
\bar{x}_{\mathrm{corr}}^{\mathrm{ON}}(i) &= \bar{x}_{\mathrm{sig}}^{\mathrm{ON}}(i) - \left(a_x^{\mathrm{OFF}} \times \bar{y}_{\mathrm{ref}}^{\mathrm{ON}}(i) + b_x^{\mathrm{OFF}}\right) \qquad (3.16) \\
\bar{y}_{\mathrm{corr}}^{\mathrm{OFF}}(i) &= \bar{y}_{\mathrm{sig}}^{\mathrm{OFF}}(i) - \left(a_y^{\mathrm{OFF}} \times \bar{y}_{\mathrm{ref}}^{\mathrm{OFF}}(i) + b_y^{\mathrm{OFF}}\right) \\
\bar{y}_{\mathrm{corr}}^{\mathrm{ON}}(i) &= \bar{y}_{\mathrm{sig}}^{\mathrm{ON}}(i) - \left(a_y^{\mathrm{OFF}} \times \bar{y}_{\mathrm{ref}}^{\mathrm{ON}}(i) + b_y^{\mathrm{OFF}}\right) \qquad (3.17)
\end{aligned}$$

where a_x^{OFF}, a_y^{OFF}, b_x^{OFF} and b_y^{OFF} are constants obtained by fitting the linear correlation between the signal and the reference, using only the OFF measurements.

3.3.3 Computation of the DeLLight barycenter signal

The DeLLight signals $\Delta x(i)$ and $\Delta y(i)$, along the x and y-axis respectively, are obtained by applying the zero suppression (”ON-OFF”), and thus for the i^{th} ”ON-OFF” measurement, we have:

$$\begin{aligned}
\Delta x(i) &= \bar{x}_{\mathrm{corr}}^{\mathrm{ON}}(i) - \bar{x}_{\mathrm{corr}}^{\mathrm{OFF}}(i) \qquad (3.18) \\
\Delta y(i) &= \bar{y}_{\mathrm{corr}}^{\mathrm{ON}}(i) - \bar{y}_{\mathrm{corr}}^{\mathrm{OFF}}(i) \qquad (3.19)
\end{aligned}$$

Their average values $\Delta x = \langle \Delta x(i) \rangle$ and $\Delta y = \langle \Delta y(i) \rangle$, calculated over a set of ON-OFF measurements, correspond to the final measured DeLLight signal in the horizontal and vertical axis respectively.

In the absence of pump/probe interaction, there are only successive OFF measurements, corresponding to a so-called ”OFF-OFF” measurement. In this case, the associated standard deviations of $\Delta x(i)$ and $\Delta y(i)$ corresponds to the spatial resolutions σ_x and σ_y respectively.

An example of dataset analysis of ”ON-OFF” measurements of the Kerr effect in air is presented on figure 3.4, showing the suppression of the beam pointing fluctuation thanks to the correlation between interference signal and reference, and the extraction of the ”ON-OFF” DeLLight signal Δy.

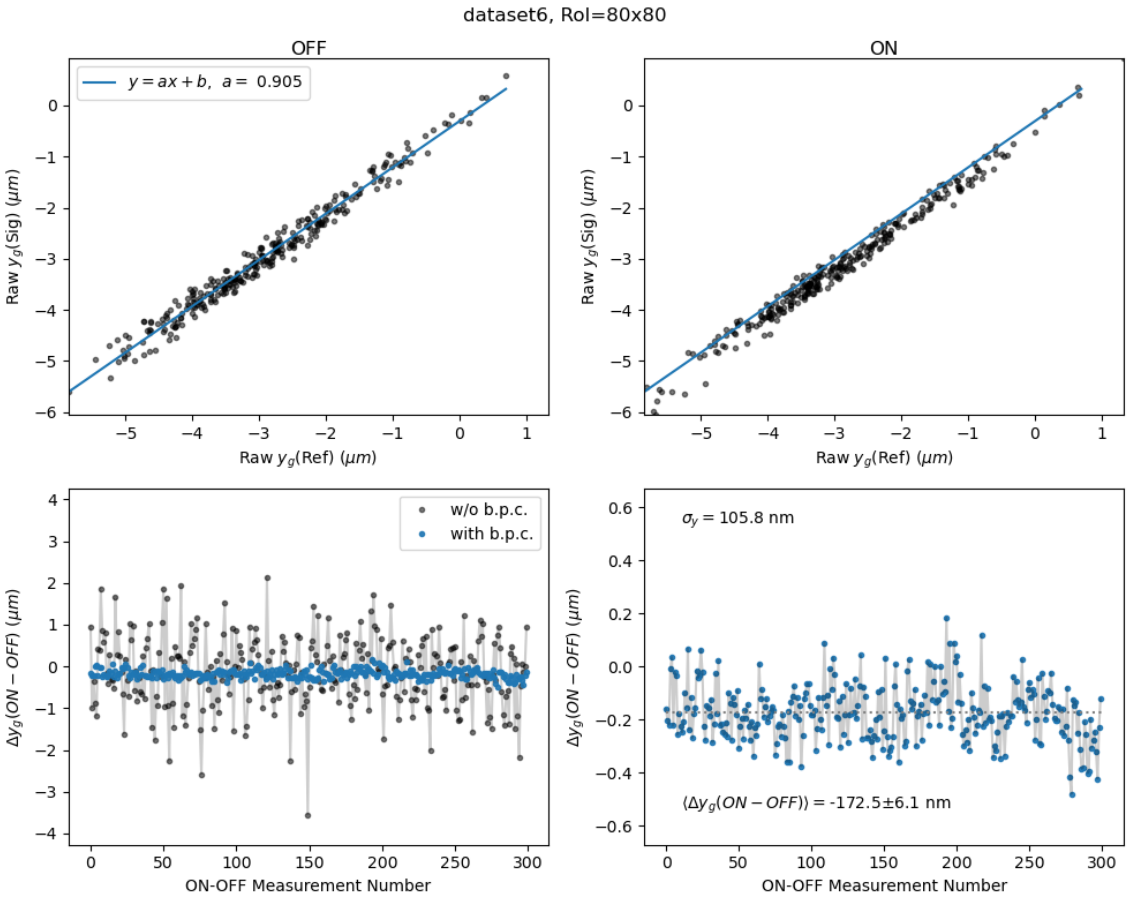

Figure 3.4: (Upper plots) Linear correlation of the barycenters in intensity of the interference signal $\bar{y}_{sig}(i)$ and the back-reflection $\bar{y}_{ref}(i)$, calculated along the vertical axis y. The data are shown as black points, for both OFF (left panel) and ON (right panel) measurements, while the result of the linear fit obtained using the OFF data only is shown in both panels as a blue line. (Lower plots) black points: ON-OFF raw signal $\bar{y}^{ON}_{sig}(i) - \bar{y}^{OFF}_{sig}(i)$ without beam pointing correction; blue points: ON-OFF reconstructed signal $\Delta y(i) = \bar{y}^{ON}_{corr}(i) - \bar{y}^{OFF}_{corr}(i)$ after beam pointing correction. The signal $\Delta y(i)$ is clearly identifiable in the lower right plot with an average value $\Delta y = \langle \Delta y(i) \rangle = -172.5 \pm 6.1$ nm. In this example, data have been collected on December, the 22th, 2022, dataset6.

3.4 Calculation of the DeLLight intensity signal

The transverse shift of the intensity profile in the dark output of the Sagnac interferometer caused by the DeLLight effect can also translate as an intensity differential between ON and OFF measurements. The intensity in a chosen RoI corresponds to the sum of the quantity of photo-electron received by each pixel of the RoI in ADU.

Similarly to the barycenter calculation method described in the previous section, the first step of the intensity signal calculation method is to define a square RoI around the signal and reference spots on the TIFF images collected by the CCD camera in the dark output of the interferometer. For a given laser shot, the intensity of the signal is written $I_{sig}(i)$ and the intensity of the reference is written $I_{ref}(i)$.

The second step of the analysis is to separate ON and OFF intensity values which are written $I_{\text{sig}}^{\text{ON}}(i)$ and $I_{\text{sig}}^{\text{OFF}}(i)$ for the signal ; $I_{\text{ref}}^{\text{ON}}(i)$ and $I_{\text{ref}}^{\text{OFF}}(i)$ for the reference. Moreover, the reference intensities are used to normalise the signal intensities which is mandatory since the beam intensity fluctuates over time and from laser shot to laser shot. The normalised ON and OFF intensities are then:

$$I_{\text{norm}}^{\text{ON}}(i) = \frac{I_{\text{sig}}^{\text{ON}}(i)}{I_{\text{ref}}^{\text{ON}}(i)} \tag{3.20}$$

$$I_{\text{norm}}^{\text{OFF}}(i) = \frac{I_{\text{sig}}^{\text{OFF}}(i)}{I_{\text{ref}}^{\text{OFF}}(i)} \tag{3.21}$$

Similarly to the barycenter analysis method, we can remove the slow drifts linked to low frequencies to obtain the DeLLight signal $\delta I(i)$ in intensity for the i^{th} "ON-OFF" measurement:

$$\delta I(i) = I_{\text{norm}}^{\text{ON}}(i) - I_{\text{norm}}^{\text{OFF}}(i) \tag{3.22}$$

The final normalised DeLLight signal $\frac{\Delta I}{I}$ for all laser shot is:

$$\frac{\Delta I}{I} = \left\langle \frac{\Delta I}{I}(i) \right\rangle = \left\langle \frac{I_{\text{norm}}^{\text{ON}}(i) - I_{\text{norm}}^{\text{OFF}}(i)}{I_{\text{norm}}^{\text{OFF}}(i)} \right\rangle \tag{3.23}$$

The intensity resolution $\sigma_{\Delta I/I}$ corresponds to the standard deviation of $\frac{\Delta I}{I}$.

Chapter 4

Prototypes of Sagnac interferometers

The DeLLight experiment went through several stages of development with different prototypes of Sagnac interforemeters. The first one consists of a rectangular configuration composed of three mirrors, without focalisation of the probe beam. It was used to validate the experimental and analysis methods by doing sensitivity and Kerr measurements in silica (results presented in chapter 8). The second prototype is a triangular configuration composed of two mirrors, with focalisation in the interaction area using two optical lenses. It was used to refine the sensitivity of the experiment, in order to reach the final DeLLight goal parameters described in chapter 2. Kerr measurements also have been conducted in air with this prototype (results in chapter 9).

In this chapter, we thoroughly describe the experimental setups of these two prototypes.

4.1 Prototype 1: square configuration of the Sagnac interferometer (no focalisation)

4.1.1 Experimental setup

The goal of the first DeLLight prototype was to measure the extinction factor and the spatial resolution of a Sagnac interferometer in femtosecond regime, using a simple square interferometer with 3 mirrors and without focalisation of the probe beam inside the interferometer. This prototype has then been used to validate measurement and analysis techniques by measuring the non-linear Kerr effect in fused silica. This setup was developed in the LASERIX facility on an optical table where air disturbances and mechanical vibrations were greater than it would have been in a vacuum chamber.

The experimental setup of this square configuration is shown on figure 4.1 (photograph on figure 4.2). This first prototype was initially developed at low energies, without the full potential of the laser delivered by the LASERIX facility. The delivered energy per pulse is $\mathcal{E}_{\text{pulse}} \approx 20\,\mu\text{J}$, the pulse duration is $\tau = 70\,\text{fs}$, and the repetition rate is 10 Hz. The central wavelength is $\lambda_0 = 815\,\text{nm}$, with a spectral width of $\Delta\lambda = 30\,\text{nm}$ (measured at FWHM).

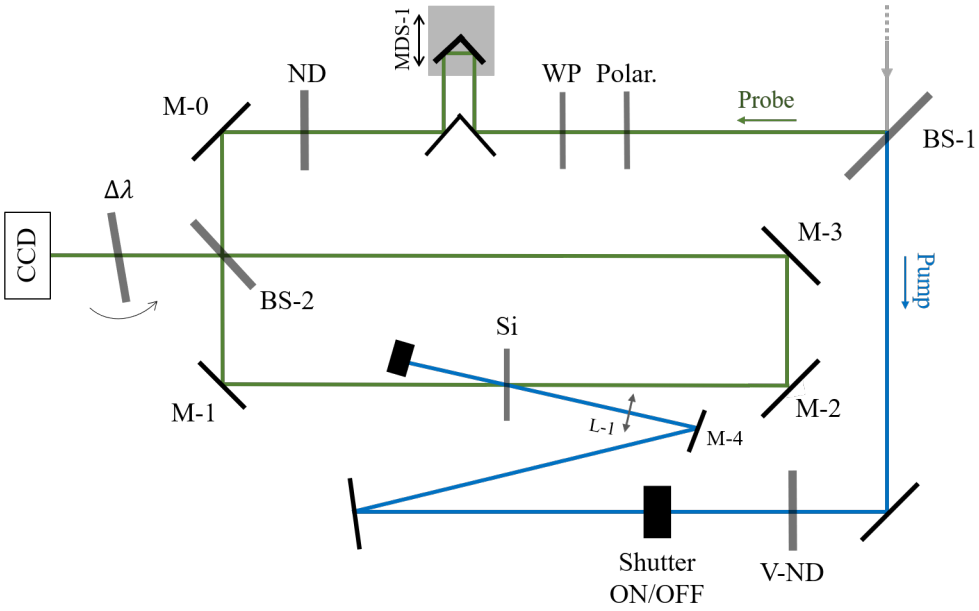

Figure 4.1: Schematic of the DeLLight Prototype 1: square Sagnac interferometer, composed of three mirrors and without any focalisation of the pump (blue) and probe (green).

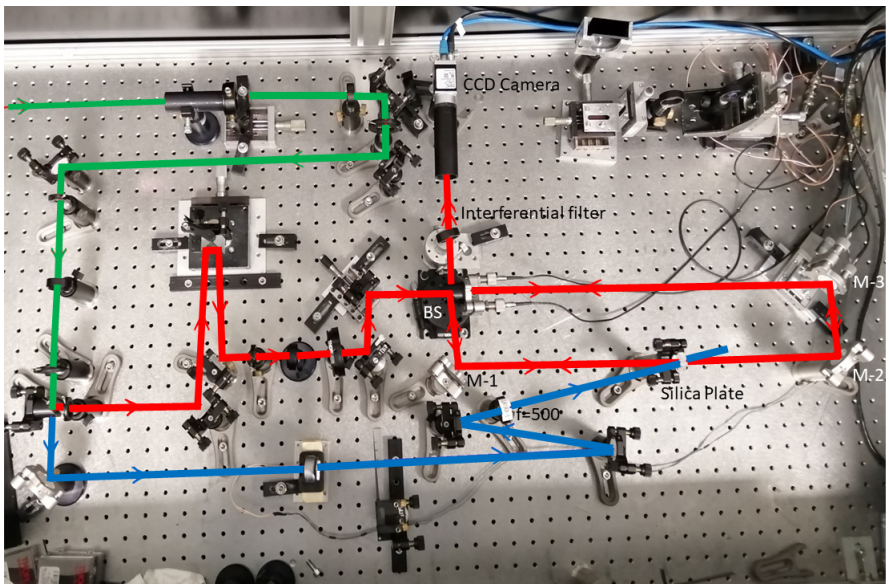

Figure 4.2: Photograph of the experimental setup of the square Sagnac interferometer, composed of three mirrors and without any focalisation of the pump (blue) and probe (red) beams. The green beam is the incident beam before pump/probe division.

Before sending the laser beam inside the Sagnac interferometer, we use a confocal telescope composed of two spherical lenses and a pinhole placed at the focal point to deliver a smooth transverse intensity profile that is close to a Gaussian, with a transverse beam size of about 1 mm at FWHM.

On this prototype, there is no need for distinct optical paths between the probe and the pump because of the low energies involved, so the initial beam is split in half using a 50/50 beamsplitter (BS-1) to provide two distinct beams of energies $\mathcal{E} \approx 10\,\mu$J each. The reflected beam is the probe, which will be used on its own to study the resolution (see chapter 6) and the extinction factor (see chapter 5). The transmitted beam is the pump, which will be used in a second step to validate the DeLLight measurement technique by measuring the Kerr effect in a silica slide, as will be developed in chapter 8.

The probe goes through a polariser (Polar.), which selects the horizontally polarised (p-pol.) component of the electric field and a neutral density filter (ND), which sets the suitable intensity of the incident probe pulse in the interferometer. A delay stage (MDS-1) is used to temporally synchronise later on the probe and the pump in the interaction area in the interferometer. Finally, the probe enters the Sagnac interferometer via a beamsplitter (BS-2), which is a 50/50 commercial femtosecond p-pol. beamsplitter (Semrock FS01-BSTiS-5050P-25.5). Its coating is produced by ion beam sputtering, which delivers uniform atomic layers on the substrate's surface. The theoretical reflection and transmission coefficients r^2 and t^2 (defined in equation 2.11), specified by the manufacturer, are $r^2 = t^2 \simeq 50 \pm 3\%$, over a spectrum between 650 and 1100 nm. The phase factor $\delta\phi$ of the BS is not characterised by the producer. Its thickness is 3 mm and its group delay dispersion (GDD) is less than $30\,\text{fs}^2$ for both reflection and transmission. The reflection factor of the anti-reflective coating on the rear side specified by the manufacturer is $r^2_{AR} \simeq 0.1\%$ at 800 nm.

The mirrors inside the interferometer are standard femtosecond dielectric mirrors (Thorlabs UM10-45A) with a low GDD value (less than $30\,\text{fs}^2$) and standard laser grade surface qualities, such as a flatness peak-to-valley under $\lambda/6$ at 633 nm, a quality 15-5 Scratch-Dig, and a roughness with typical RMS < 5Å. The beamsplitter and one of the mirrors (M-3) are controlled by kinematic mirror mounts with static piezoelectric adjusters (Polaris K1S2P Thorlabs) for horizontal and vertical alignment with an angular resolution of $0.5\,\mu$rad for a 0.1 V step. The lateral position of one mirror is controlled by a micrometric translation stage. A silica plate (5 mm thickness), which corresponds to the interaction area where the pump will be focused on the unfocused probe, is placed between M-1 and M-2 at roughly the same distance from BS-2. The probe pulse corresponds to the reflected pulse. The reference pulse corresponds to the transmitted pulse.

The dark output of the interferometer is read by a CCD camera (Basler acA1300-60gm) containing 1024×1280 pixels, and externally triggered at 10 Hz (as will be the case for every CCD cameras presented in this manuscript). The pixel dimension is $5.3 \times 5.3\ \mu m^2$ and the maximum charge storage capacity before saturation (full well capacity) is about 10^4 electrons per pixel. Additionally, an interferential multi-layer dielectric filter of spectral width $\Delta\lambda = 3$ nm, centred at 808 nm (Semrock), is placed in front of the CCD camera. Rotation of the incident angle of the spectral filter allows us to select a wavelength from 808 to 800 nm and thereby optimise the extinction factor in the dark output by minimising the r/t asymmetry coefficient δa of the BS (defined in section 2.5). Since r^2 and t^2 also depend on the polarisation of the incident beam, the deviation coefficient δa is also minimised by rotating the incident polarisation with a half-wave plate (WP) installed just after the polariser before the Sagnac interferometer.

Meanwhile, the pump first goes through a variable neutral density (V-ND), which will

be used to control the pump energy sent in the interaction area. Then, a shutter allows for the successive interaction and non interaction of the probe with the pump ("ON-OFF" measurements) at 5 Hz. Finally, a lens (L-1) of focal length $f = 500\,\text{mm}$ (Thorlabs LA1908-B), placed at a distance $f/2$ from the interaction area, is used to reduce the waist of the pump in the silica plate Si (3 mm thick NBK-7 window, Thorlabs WG10530-B) to reach half the waist at focus of the probe.

4.1.2 Alignment and synchronisation of the probe and pump pulses

The alignments required before doing data collection are as follows. Let us note that all throughout the setup, the beam is always aligned in the horizontal plane, at an incident angle on each mirror of 45°. First, we adjust the polariser (Polar.) on the probe to only let the p-polarisation component through. Same goes for the half-wave plate (WP). Moreover, the BS-2 is properly aligned at an incident angle of 45° using the optical mount placed on a rotation stage, thus allowing to switch the mirror angle from 0° to 45° to perform an auto-collimation alignment. Finally, the extinction in the dark output is optimised on the CCD camera (without the neutral density ND if necessary), using one of the Sagnac mirrors mounted on piezoelectric motors first and the half-wave plate (WP) second. Additionally, we add neutral densities before the Sagnac interferometer to adjust the intensity of the back-reflections in order to stay below the saturation threshold of the pixels on the CCD camera (usually with an intensity of $\approx 3000\,\text{ADU}$, the saturation being at 4096 ADU). Finally, we rotate the spectral filter if necessary to optimise the extinction.

After aligning the probe, we proceed with the pump by first aligning the beam on the lens (L-1), using the CCD camera placed far enough from it to reach a better pointing precision. To perform the spatial synchronisation between the probe and the pump at focus, we place the CCD camera as to have its sensor plane in place of the silica plane. Thus, we can control the position of the pump using the mirror (M-4) and adjust the impact parameter b between probe and pump at focus as desired. Moreover, we can adjust the temporal synchronisation by using the delay stage (MDS-1) until interference fringes appear on the CCD camera, with the best contrast possible which implies an optimal temporal synchronisation.

The last part of the alignment process consists of preparing the "ON/OFF" measurements by first turning the half-wave plate (WP) to see the interference signal and collect enough light on the CCD camera in the dark output (same intensity as the back-reflections), even if the extinction is degraded by doing so. This aspect will be detailed in chapter 5. Finally, we can turn on the ON/OFF shutter and collect measurements.

4.2 Prototype 2: triangular configuration of the Sagnac interferometer with focalisation

4.2.1 Experimental setup

The second prototype is a triangular Sagnac configuration composed of two mirrors, with focalisation of the probe beam in the interaction area using two optical lenses. The goal of

this setup, considered as the DeLLight pilot experiment, is to measure in a gas (here in air) the DeLLight deflection signal induced by the optical Kerr effect. This setup was developed in the main room of the LASERIX facility, in the final DeLLight vacuum chamber, and under a laminar flow.

The experimental setup is very similar to the final DeLLight setup, which will be used with intense pump pulses in the DeLLight vacuum chamber. However, for the measurements in air, the energy of the pump pulse is small (less than 15 μJ) and the probe and pump are co-propagating in order to integrate the Kerr deflection along the longitudinal overlap of the two pulses.

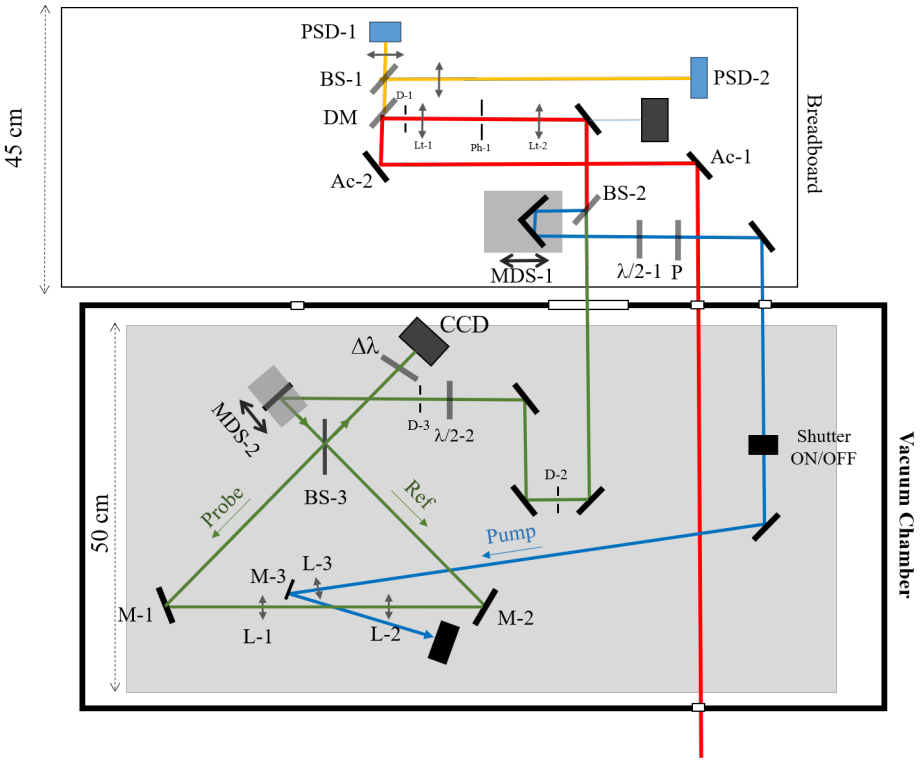

Figure 4.3: Schematic of the DeLLight Prototype 2: triangular Sagnac interferometer configuration with focalisation of the pump (blue) and the probe (green), in the DeLLight vacuum chamber. The red beam is the incident beam before pump/probe division.

The setup, displayed on figure 4.3, is installed on a devoted optical table composed of a breadboard and the DeLLight vacuum chamber. The p-polarised input beam (pulse duration $\tau_0 = 70\,\text{fs}$; energy $\mathcal{E} \approx 50\mu\text{J}$) is first sent on the optical breadboard to a beam pointing stabilisation system (produced by MRC company) composed of two actuators mirrors (Ac-1 and Ac-2) and two position sensitive detectors (PSD-1 and PSD-2) used to stabilise the incident beam both in the far field (angular stabilisation) and the near field (transverse position). However, this stabilisation system is still in development and is not yet used for the deflection measurements in air. For now, this system is only used to pre-align the beam by reading the signals of both PSDs on an oscilloscope on which the "zero position" corresponds to the chosen

position of reference on the actuators.

The transverse waist of the incident beam is then reduced to 1 mm (FWHM) by an confocal telescope composed of two lenses (Lt-1 and Lt-2) and a 150 μm diameter pinhole Ph-1 (spatial filter) at focus to obtain an almost Gaussian transverse intensity profile. Additionally, we use an iris (D-1) placed just before the telescope to better control the transverse beam size.

The next step consists of splitting the beam in half to obtain two distinct beams of equal energy, the pump beam (in blue on figure 4.3) and the probe beam (in green), using a 50/50 beamsplitter (BS-2).

Before entering the vacuum chamber, the pump pulse first reflect on a cubic mirror mounted on a delay motorised stage (MDS-1), which will be used to ensure the time coincidence of the pump and probe in the interaction area in the Sagnac interferometer. The energy of the pump can be chosen by the combination of a rotating half wave plate and a femtosecond polariser set to p-polarisation, or by using a variable neutral density with constant optical path length. Then, the pump goes into the vacuum chamber and is focused in the interaction area, using a best form spherical lens (L-3) of focal length 100 mm (Thorlabs LBF254-100-B) and a D-shape mirror (M-3) to adjust the spatial overlapping with the probe at focus. Additionally, the pump after interaction is focalised on the CCD camera in the dark output in order to monitor the presence of the pump on the CCD images (not shown on fig. 4.3 not to overcrowd the schematic). It is called the "optical counter".

On the other hand, the probe beam is sent directly in the vacuum chamber after passing through BS-2. The polarisation of the probe is precisely adjusted using a piezo motorised half-wave plate rotation ($\lambda/2 - 2$) to select the desired extinction in the dark output of the interferometer. The last mirror before the Sagnac interferometer is mounted on a piezo motorised linear stage (MDS-2) and is used to translate horizontally the incident beam as required in order to select the area on the optics of the interferometer which gives the minimum phase noise. Then, the beam is splitted in half by a 50/50 femtosecond p-pol. beamsplitter BS-3 (Semrock FS01-BSTiS-5050P-25.5, same as the one used in the first prototype): the transmitted pulse corresponds to the reference (Ref) and the reflected pulse corresponds to the probe (Probe). The interferometer has a right-angled isosceles triangle configuration, formed by BS-3, two dielectric mirrors positioned at a 22.5° incident angle (M-1 and M-2), and two best form spherical lenses (L-1 and L-2) of focal length 100 mm (Thorlabs LBF254-100-B), which focalise both Probe and Ref in the interaction area so that the probe is co-propagating with respect to the pump and is in time coincidence with it. The beamsplitter BS-3, the mirror M-2 and the lens L-2 of the interferometer are controlled by static piezoelectric adjusters with nanometric accuracy. The high reflective coating (R = 99.99 %) of M-1 and M-2 was produced by the Laboratoire des Matériaux Avancés (LMA, IP2I-Lyon). Additionally, the Ref is not in time coincidence with the pump and is therefore unaffected by it.

Finally, the DeLLight interference signal of the Probe and Ref is read in the dark output of the interferometer by a CCD camera (Basler acA3088-16gm, pixel size 5.84 × 5.84 μm). The spatial shot noise resolution of this CCD camera is studied and measured in chapter 6. An interferential multi-layer dielectric filter (Semrock) of spectral width $\Delta\lambda$ = 3 nm, centred at 808 nm, is placed in front of the CCD camera. By rotating the incident angle of the filter, we can select the wavelength from 808 to 800 nm to optimise the extinction factor in the dark output.

The energy of both Probe and Ref in the Sagnac interferometer is of a few μJ per pulse and the transverse beam size before focalisation is about 1 mm (FWHM). The energy of the pump can vary from 0.4 to 15 μJ. The duration of the pump and probe pulse is about $\tau \approx 70$ fs in the interaction area. It gets higher than that of the initial beam delivered by LASERIX because of dispersion phenomena in all the optics it encounters before reaching the Sagnac interferometer. The minimum waist at focus of the probe and the pulse beams in the interaction area varies from 25 to 40 μm depending on the data campaigns.

4.2.2 Alignment and synchronisation of the probe and pump pulses

The alignment steps of this experimental setup are as follows:

- Pre-alignment of the incident beam, using the MRC stabilisation system, by reading the signals of both PSDs (PSD-1 and PSD-2) on an oscilloscope on which the "zero position" corresponds to the chosen position of reference on the actuators (Ac-1 and Ac-2);
- Alignment of the confocal telescope (Lt-1, Lt-2) placed before BS-2, by adjusting the pinhole (Ph-1) and the iris (D-1) as needed to obtain a Gaussian transverse intensity profile (around 1 mm at FWHM);
- Alignment of the incident beam in the Sagnac interferometer, using iris D-2 and D-3;
- Alignment of the interferometer, using the half-wave plate $\lambda/2 - 2$ and the lens L-2 (piezoelectric motor) to adjust the extinction. Thus, the spatial overlap of the pump and probe pulses will remain unchanged when adjusting the alignment of the interferometer;
- Alignment of the rotation of the spectral filter $\Delta\lambda$ to maximise the extinction;
- Adjustment of the spatial overlap between the pump and the probe at focus in the interaction area, by placing a mirror before focus and a CCD camera of pixel size 1.85 x 1.85 μm^2 at focus;
- Adjustment of the time coincidence between the pump and the probe at focus in the interaction area, using the same CCD camera at focus and the delay translation (MDS-1). Both beams are synchronised when an interference fringe pattern appears, with the highest contrast possible;
- Alignment of the optical counter on the corner of the CCD camera.

4.2.3 Advanced prototype 2 with spatial filter in the dark output and CCD readout outside the vacuum chamber

An advanced version of the DeLLight Prototype 2 was developed. It consists of deporting the CCD camera in the dark output of the interferometer outside of the vacuum chamber. A spatial filtering stage is also placed in the dark output in front of the CCD in order to suppress the interference phase noise induced by the diffusion on the surface defects of the optics inside

the interferometer. The spatial filtering stage consists of a focusing best form optical lens (L-4) of focal length $f = 200$ mm and a pinhole (Ph-2) of diameter 200 μm at focus. The CCD camera is placed at exactly $2f$ so as to have a magnification of 1.

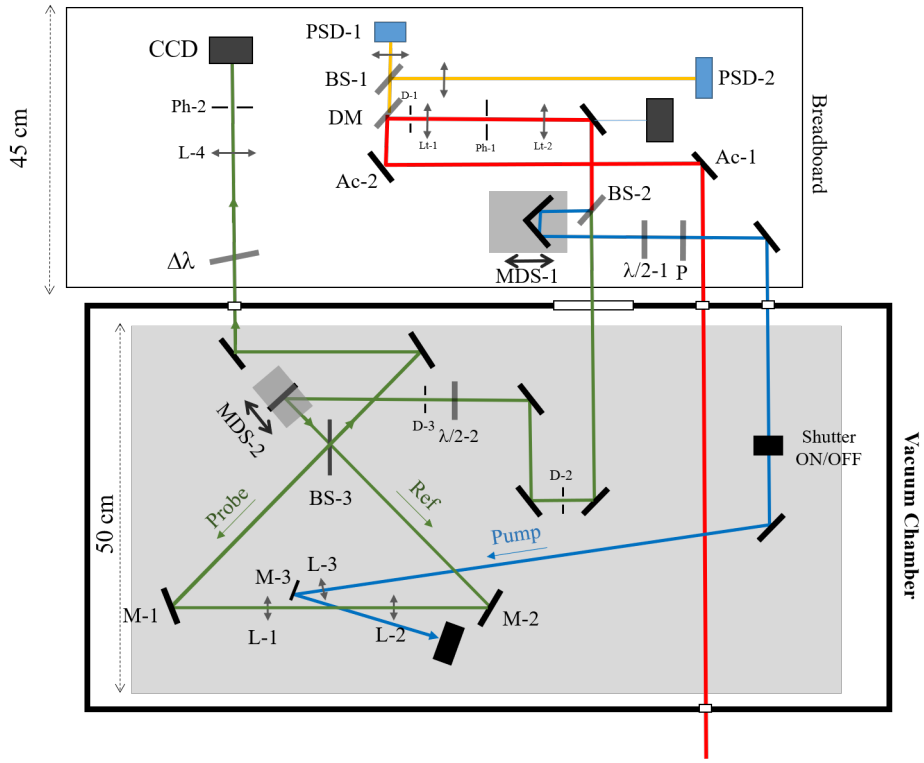

Figure 4.4: Schematic of the DeLLight advanced Prototype 2: triangular Sagnac configuration with pump (blue) and probe (green) focalisation, in the DeLLight vacuum chamber and with the CCD readout and spatial filter in the dark output deported outside the DeLLight vacuum chamber.

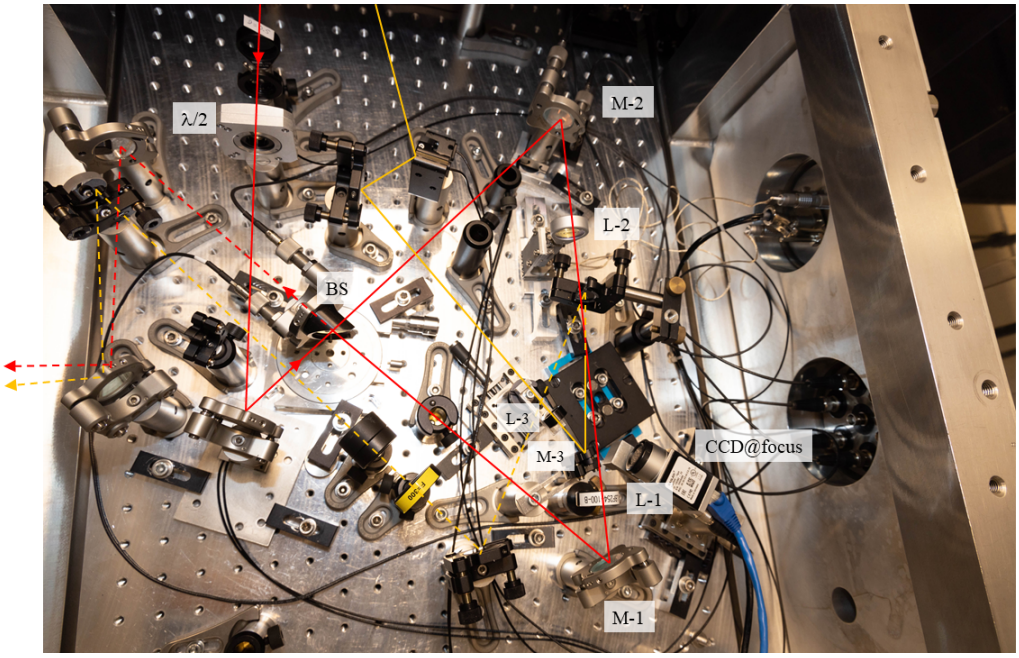

Figure 4.5: Photograph of the DeLLight advanced prototype inside the vacuum chamber. The spatial filter and the CCD readout in the dark output of the interferometer are outside the vacuum chamber and therefore not shown in this photo. The probe path is in red and the pump path is in yellow.

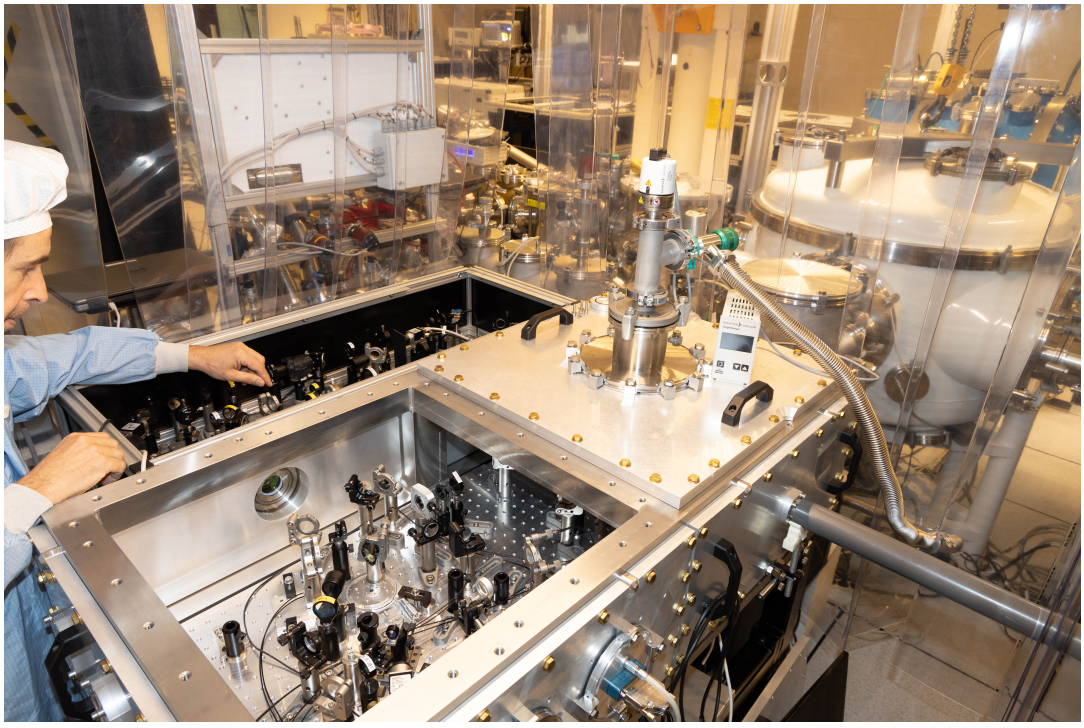

Figure 4.6: Photograph of the DeLLight vacuum chamber in the LASERIX laser clean room, under laminar flux.

Chapter 5

Measurement of the extinction in the dark output of the Sagnac interferometer

The extinction in the dark output of the Sagnac interferometer is one of the critical parameters to take into account in the DeLLight experiment, the other being the spatial and intensity resolution, as will be developed in chapters 6 and 7. In this chapter will be thoroughly developed the measurement of the extinction factor of the interferometer in the different stages of the DeLLight experiment. As seen in chapter 4, the first prototype is a rectangular configuration composed of three mirrors, without focalisation of the probe and pump beams. The second one is a triangular configuration composed of two mirrors, with focalisation in the interaction area using two optical lenses.

5.1 Measurement method of the extinction factor

The extinction factor $\mathcal{F}$ is defined as $\mathcal{F} = I_{\text{sig}}/I_0$, where I_{sig} is the intensity of the interference signal in the dark output of the interferometer and I_0 is the intensity of the incident beam entering the interferometer. The DeLLight interferometer enables a very strong extinction, corresponding to a very low extinction factor of the order of 10^{-5} to 10^{-6}. Therefore, a direct measurement cannot be carried out since it would require a very high dynamic range of the detector.

To solve this issue, the extinction factor is calculated by measuring the intensity of the interference signal in the dark output of the interferometer, relatively to the intensity $I_{AR,1}$ of the direct back-reflection on the rear side of the beamsplitter, which can be written (see section 2.7, equation 2.58):

$$I_{AR,1} = \frac{R_{AR}}{2} \times I_0 \tag{5.1}$$

where R_{AR} is the reflection factor of the anti-reflective coating of the beamsplitter.

The extinction factor of the interferometer then becomes:

$$\mathcal{F} = \frac{I_{\text{sig}}}{I_0} = \frac{I_{\text{sig}}}{I_{AR,1}} \times \frac{R_{AR}}{2} \tag{5.2}$$

Therefore, we first need to measure precisely the coefficient R_{AR} in order to measure the extinction factor. Then, by recording a CCD image in the dark output of the interferometer at maximal extinction (best alignment), we can estimate the extinction factor by calculating the ratio "$\frac{I_{\text{sig}}}{I_{AR,1}}$" given in equation (5.2).

The measurement of the rear-side reflection factor R_{AR} is detailed in appendix B. We have measured:

$$R_{AR} = (1.1 \pm 0.1) \times 10^{-3} \tag{5.3}$$

which corresponds to the manufacturer's approximate value. In the next section, we present the measurement of the extinction factor for the two successive interferometer prototypes.

5.2 Measurement of the extinction factor

The extinction factor $\mathcal{F}$ is measured by recording a CCD image in the dark output of the interferometer, at maximum extinction (best alignment). Using equations 5.2 and B.11, the extinction factor $\mathcal{F}(i, j)$ for the pixel (i, j) contained in the selected Region of Interest (RoI), is equal to:

$$\mathcal{F}(i, j) = \frac{I_{\text{sig}}(i, j)}{I_{\text{AR},1}(i, j)} \times 5 \times 10^{-4} \tag{5.4}$$

where $\frac{R_{AR}}{2} = 5 \times 10^{-4}$, and $I_{\text{sig}}(i, j)$ and $I_{\text{AR},1}(i, j)$ are the intensity profiles (in ADU unit) of the interference signal and the direct back-reflection respectively, in the dark output of the interferometer.

5.2.1 Extinction factor without spatial filter

First, we present the extinction for the two successive DeLLight prototypes, without spatial filter in the dark output of the interferometer. In both prototypes, the beamsplitter of the Sagnac interferometer is aligned at an incident angle of 45° to maximise the extinction. In both cases, a pass-band spectral filter $\Delta\lambda$, centred on $\lambda_0 = 808\ nm$ with a bandwidth of 3 nm (FWHM) is placed in the dark output in front of the CCD camera (see figures 4.1 and 4.3). The filter is slightly rotated, which allows to reduce the central wavelength λ_0 to the preferred value in order to minimise the asymmetric (R/T) coefficient δa of the beamsplitter, and therefore maximise the extinction factor.

An example of CCD images collected in the dark output of the interferometer at maximal extinction is shown figure 5.1 for the first prototype (rectangle interferometer without focusing), using the setup presented on figure 4.1. On the left panel, the upper image corresponds to the raw CCD image (colour scale in ADU content) where the interference signal I_{sig} is in the centre in the white dotted area corresponding to a RoI approximately equal to the width w (FWHM) of the intensity profile ($w_{RoI} \approx w$). The edge spots correspond to the back-reflections $I_{AR,1}$ and $I_{AR,2}$. The lower image is the same image, although with saturated back-reflections in order to better visualise the residual intensity pattern.

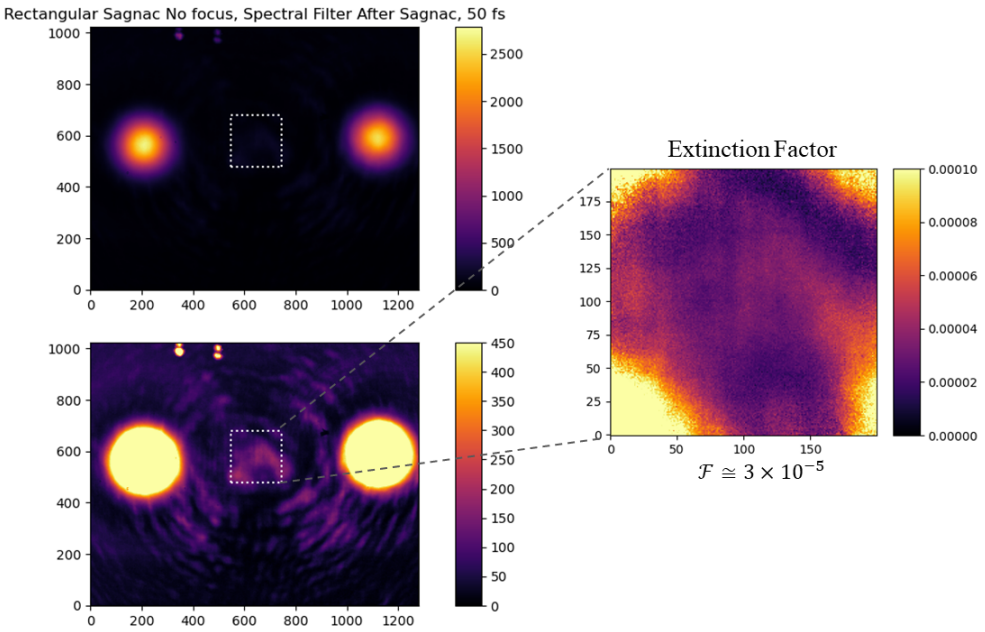

Figure 5.1: CCD images collected in the dark output of the interferometer at maximal extinction of the interferometer for the Prototype-1 (rectangular interferometer without focusing), with a colour scale in ADU content. (Left panel) Top image: raw image where the intensity profile of the interference signal I_{sig} is in the centre in the white dotted area corresponding to a RoI w_{RoI} equal to the beam width w (FWHM). Both spots on the edges correspond to the intensity profiles of the back-reflections $I_{AR,1}$ and $I_{AR,2}$; Bottom image: same raw image but with saturated back-reflections with respect to the colour scale in order to better visualise the residual intensity pattern of the interference signal in the middle. (Right panel) Distribution of the extinction factor in the same selected RoI as in the left panel. The maximal extinction factor achieved is $\mathcal{F} \approx 3 \times 10^{-5}$ in the centre.

Two types of phase noise pattern can be distinguished: hot spots in the central area of the expected intensity signal and interference rings with large transverse size (low spatial frequency). The diffraction rings correspond to a surface defect (flatness) on the mirrors at large scale (low spatial frequency), compatible with $\lambda/10$. The hot spots in the central area correspond to small sized surface defects due to roughness defect (high spatial frequency). Additionally, if we look at the distribution of the extinction factor $F(i, j)$ in centre area (right panel on figure 5.1), calculated using equation (5.4), we can see the influence of the phase noise pattern on the extinction. The maximal extinction factor achieved for the rectangular configuration of the Sagnac interferometer is:

$$\mathcal{F}_{max}(\text{Prototype 1}) = 3 \times 10^{-5} \tag{5.5}$$

NB: the gain of the CCD camera is uniform on the sensor, as will be thoroughly explained in chapter 6, section 6.2. Thus, there is no additional factor on the extinction results described in this chapter.

An example of CCD images collected in the dark output of the interferometer at maximal extinction is shown on figure 5.2 for the second prototype (triangle interferometer with focusing). We use the experimental setup presented on figure 4.3. For this measurement, the incident energy entering the Sagnac interferometer is $\mathcal{E}_{in} = 24\,\mu$J, the beam width (FWHM) is $w = 1$ mm and the pulse duration (FWHM) is about 70 fs, corresponding to a peak intensity of 4×10^{10} W/cm^2.

A similar extinction is observed, with a similar noise pattern. We measure the maximal extinction:

$$\mathcal{F}_{max}(\text{Prototype 2}) = 3 \times 10^{-5} \tag{5.6}$$

Therefore, the optical lenses introduced in this prototype did not introduce much more additional noise.

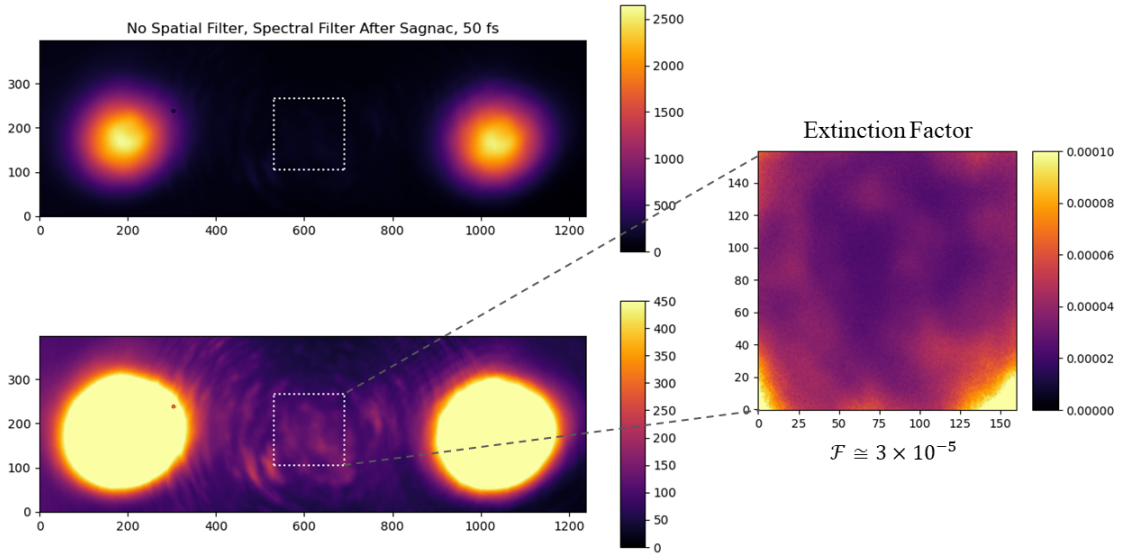

Figure 5.2: Same as figure 5.1, for the triangular Sagnac interferometer without spatial filter. The maximal extinction factor achieved is $\mathcal{F} \approx 3 \times 10^{-5}$ in the centre.

5.2.2 Extinction factor with a spatial filter in the dark output

In this section, we use the second prototype (triangle interferometer with focusing), as displayed on figure 4.4. The beamsplitter of the Sagnac interferometer is aligned at an incident angle of 45° to maximise the extinction in the dark output.

The residual phase noise of the interference signal observed in the previous extinction images seems to be induced by diffusion on surface defects on the optics in the interferometer (mirrors, lenses and/or beamsplitter). In order to suppress that noise, we added a spatial filter in the dark output of the interferometer, after the spectral filter and before the CCD readout camera,

as shown on figure 4.4 for Prototype 2 (triangle Sagnac with focusing, with the interferometer beamsplitter aligned at an incident angle of 45° to maximise the extinction.). The spatial filtering stage consists of a focusing best form optical lens (L-4) of focal length $f = 200$ mm and a pinhole of diameter 200 μm at focus. The CCD camera is placed at exactly $2f$ in order to have a magnification of 1.

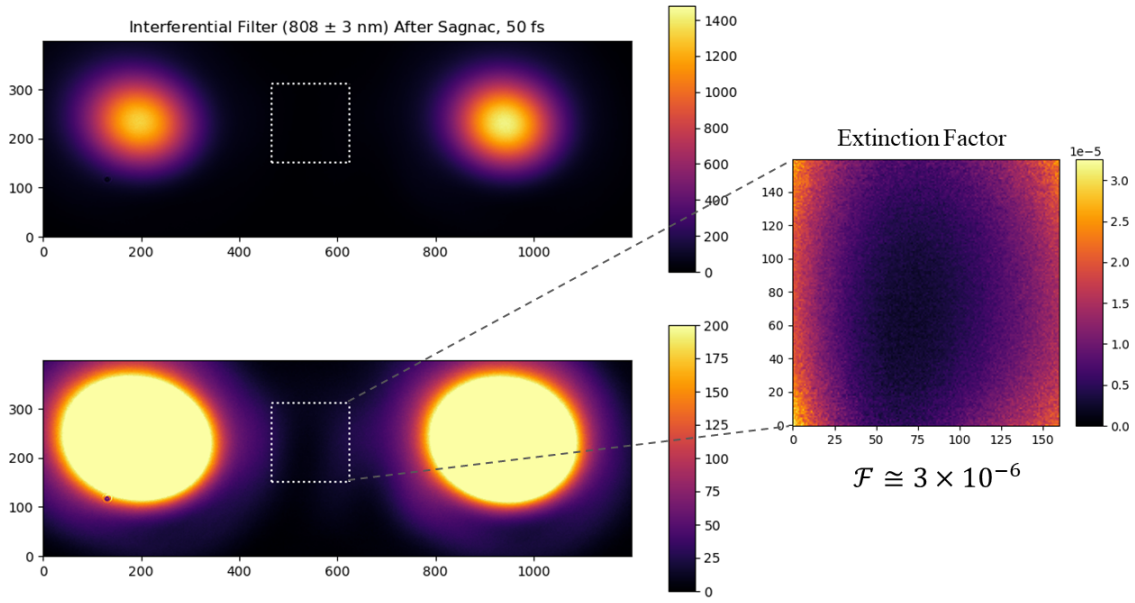

Figure 5.3: Same as figure 5.2, but with the spatial and spectral filters placed after the triangular Sagnac interferometer. The maximal extinction factor achieved is $\mathcal{F} \approx 3 \times 10^{-6}$ in the centre.

Figure 5.3 shows a typical CCD images recorded in the dark output of the interferometer, at maximum extinction, with the spectral filter ($\lambda_0 = 808$ nm, $\Delta\lambda = 3$ nm) placed after the interferometer. The spectral filter is also slightly rotated in order to maximise the extinction. For this measurement, the incident energy entering the Sagnac interferometer is $\mathcal{E}_{in} = 24\,\mu$J, the beam width (FWHM) is $w = 1$ mm and the pulse duration (FWHM) is about 70 fs, corresponding to a peak intensity of 4×10^{10} W/cm^2.

We can see that the diffraction rings and the residual noise pattern of the interference signal has been strongly suppressed by at least a factor 10. We now have a uniform residual signal with a very low intensity compared to the Sagnac configuration without spatial filter in the dark output. Thus, the spatial filter is able to get rid of all phase noise diffraction which were present on figure 5.2. The extinction factor in the centre area is then equal to:

$$\mathcal{F}_{max}(\text{Prototype 2 with spectral and spatial filter}) = 3 \times 10^{-6} \tag{5.7}$$

However, we still observe a deterioration of the phase noise on the x-axis (horizontal plan). We think that it is due to residual contribution of the intensity tails of the back-reflections.

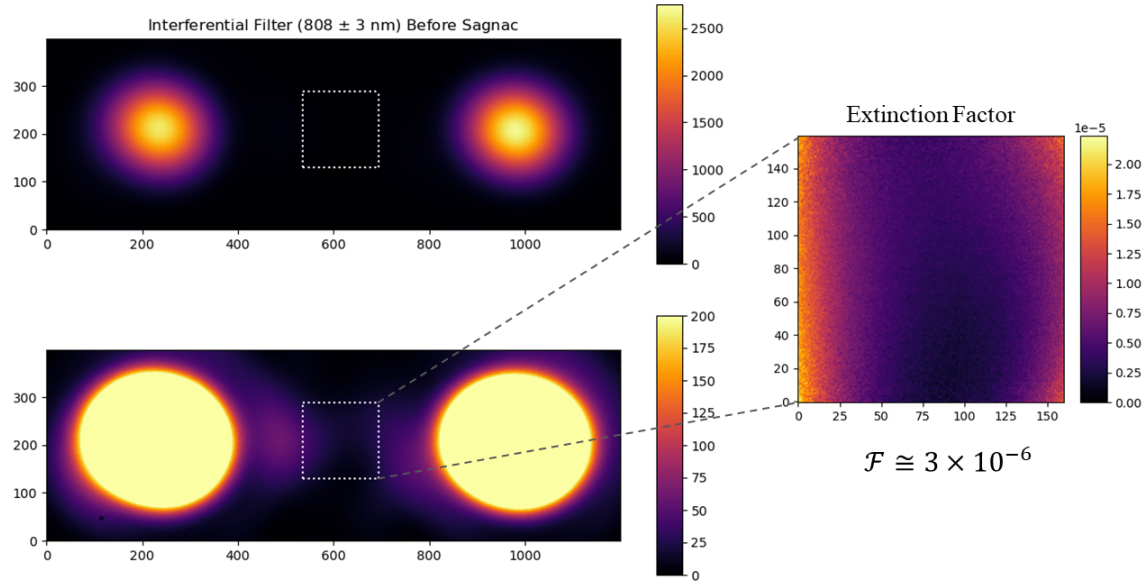

Figure 5.4: Same as figure 5.3, but with the spectral filter placed before the triangular Sagnac interferometer. The maximal extinction factor achieved is $\mathcal{F} \approx 3 \times 10^{-6}$ in the centre.

If we now place the spectral filter before the Sagnac interferometer, we observe the same quality of extinction, as shown on figure 5.4. In that case, the intensity of the incident pulse is reduced by a factor around 100 (a factor 10 due to the transmission of the filter, and another factor 10 due to the extension of the pulse duration), and is about 4×10^8 W/cm^2. Therefore, the extinction factor is unmodified whether the spectral filter is placed before or after the interferometer, although it is slightly less symmetrical and homogeneous when the spectral filter is placed after (figure 5.4). Thus, there is no non-linear effects caused by the energy of the probe at focus in the Sagnac interferometer, which could have significantly degraded the extinction in the centre.

5.2.3 Deterioration of the extinction with the full spectrum

In this section, we do the same measurements as the previous subsection with the exact same conditions, except that the spectral filter ($\Delta\lambda$) is replaced by a set of three neutral densities (ND) for which the attenuation is about 12 in order to match the attenuation provided by $\Delta\lambda$.

Figure 5.5 and 5.6 are the same as figures 5.3 and 5.4, but with the neutral densities instead of the spectral filter. The maximal extinction factor reached for this configuration is $\mathcal{F} \approx 6 \times 10^{-5}$ when ND is placed after the interferometer and is slightly better at $\mathcal{F} \approx 4 \times 10^{-5}$ when ND is placed before. The residual pattern of the interference signal stays homogeneous but the extinction is degraded by an order of magnitude compared to when we use the spectral filter, which is expected since all the spectrum of the laser is used without it. Thus, the refraction r^2 and transmission t^2 factors of the interferometer beamsplitter fluctuate depending on the wavelength, which degrades the asymmetry coefficient δa, according to equation 2.11

(section 2.5).

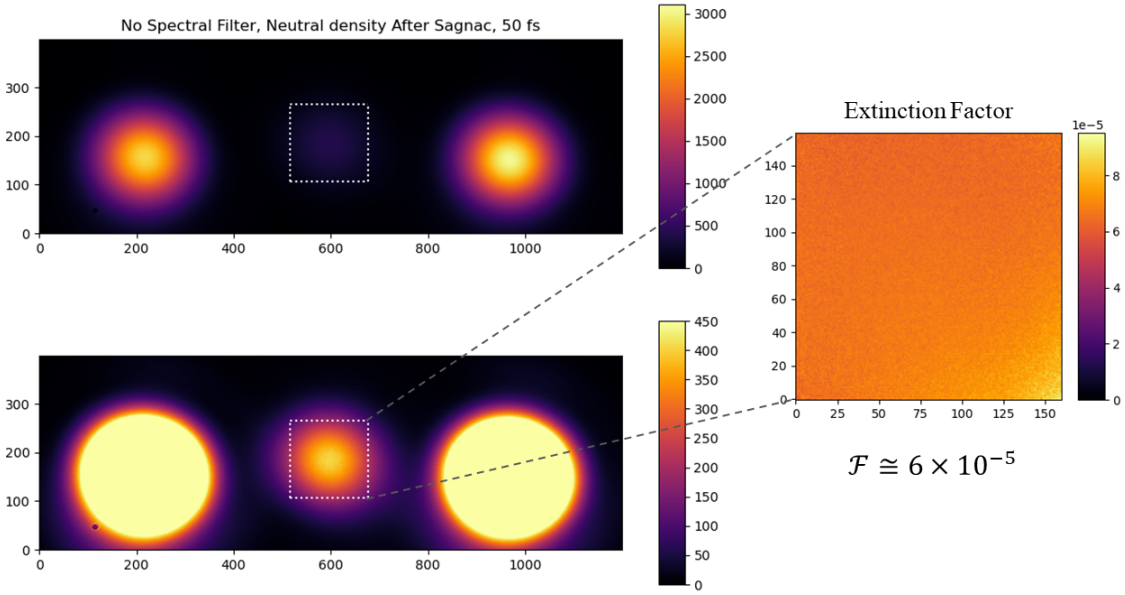

Figure 5.5: Same as figure 5.3, but with the neutral densities placed after the Sagnac interferometer instead of the spectral filter. The maximal extinction factor achieved is $\mathcal{F} \approx 6 \times 10^{-5}$ in the centre.

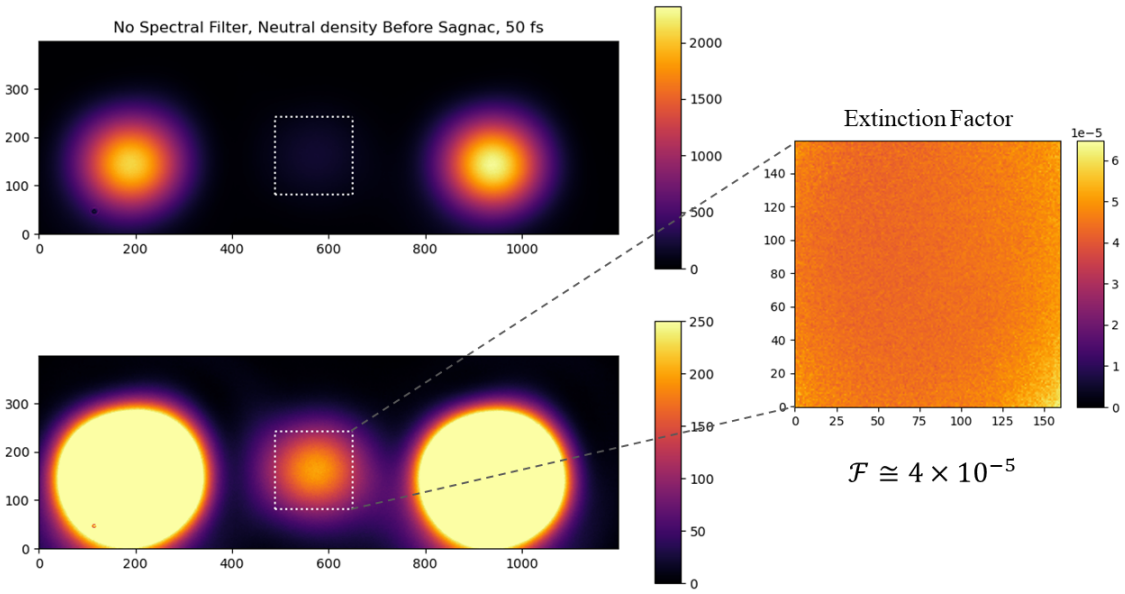

Figure 5.6: Same as figure 5.5, but with the neutral densities placed before the Sagnac interferometer. The maximal extinction factor achieved is $\mathcal{F} \approx 4 \times 10^{-5}$ in the centre.

5.3 Summary

The best extinction is achieved with a combination of a spectral filter and a spatial filter in the dark output of the interferometer, which allows to reach the goal value of the extinction factor $\mathcal{F} = 4 \times 10^{-6}$, with an incident peak intensity of 4×10^{10} W/cm^2 (incident energy $\mathcal{E}_{in} = 24\,\mu$J, waist $w = 1$ mm and duration $\tau = 70$ fs). Moreover, there are no non-linearity effects in the beamsplitter at this intensity.

Additionally, since the intensity tails of the back-reflections induce phase noise in the horizontal x-direction, it could be attractive to used a thicker beamsplitter in order to better separate the interference signal from the back-reflections.

Chapter 6

Spatial resolution of the CCD camera: the shot noise

The spatial resolution for the measurement of the barycenter of the intensity profile is one of the critical parameter of the DeLLight experiment. A spatial resolution of the order of 10 nm is requested to reach the requested sensitivity.

The spatial resolution is inherently limited by the intrinsic shot noise (or quantum noise) related to the statistical fluctuations of the average number of photo-electrons $N_{\text{p.e.}}$ detected by the CCD camera. Therefore the spatial resolution scales as $w/\sqrt{N_{\text{p.e.}}}$ where w is the beam width (FWHM) on the CCD camera. In addition, if the beam width is increased, then the energy of the incident pulse entering the Sagnac interferometer is adjusted to have the same number of detected photon per pixel. It means that the number of detected photons $N_{\text{p.e.}}$ is proportional to the square of the width. Therefore, when the spatial resolution is only limited by the shot noise, it becomes independent of the beam width, which is an important feature of the DeLLight experiment.

Moreover, if $n_{\text{p.e.}}$ is the average number of photo-electrons per pixel, and d_{pix} is the side length of each square pixel, then the spatial resolution scales as:

$$\sigma_y \propto \frac{d_{\text{pix}}}{\sqrt{n_{\text{p.e.}}}} \tag{6.1}$$

Therefore, in order to achieve the best spatial resolution, we need the highest charge storage capacity before saturation per unit surface of the optical readout. For a CCD camera, this is referred to as the *full well capacity* N_c, which corresponds to the maximum number of stored electrons per pixel before saturation.

The goal of this chapter is to measure the spatial and the intensity resolutions of the CCD cameras used on the DeLLight experiment. We will thoroughly present the experimental setup used to measure these resolutions. A spatial resolution of 13 nm is obtained with the most suitable commercial CCD camera, in agreement with the expected shot noise resolution calculated by Monte-Carlo simulations. We will show that the resolution is proportional to the square root of the number of photo-electrons, as expected for the quantum noise.

6.1 Experimental setup

In order to study the spatial resolution of each CCD camera used on the DeLLight experiment, we assembled a small test bench (shown on figures 6.1 and 6.2) using a standard quality laser diode of wavelength $\lambda = 850\,\text{nm}$ as the main light source. The transverse profile of the laser diode however is non Gaussian and cannot be used in its initial state. Therefore, we use the combination of an iris, a telescope with two focalising lenses of focal length $f_1 = 150\,\text{mm}$ and $f_2 = 100\,\text{mm}$, and a pinhole (PH) of diameter $75\,\mu\text{m}$ in order to properly filter the transverse intensity profile of the beam. Thus, we obtain a collimated Gaussian beam of width $w \approx 1.2\,\text{mm}$ (FWHM).

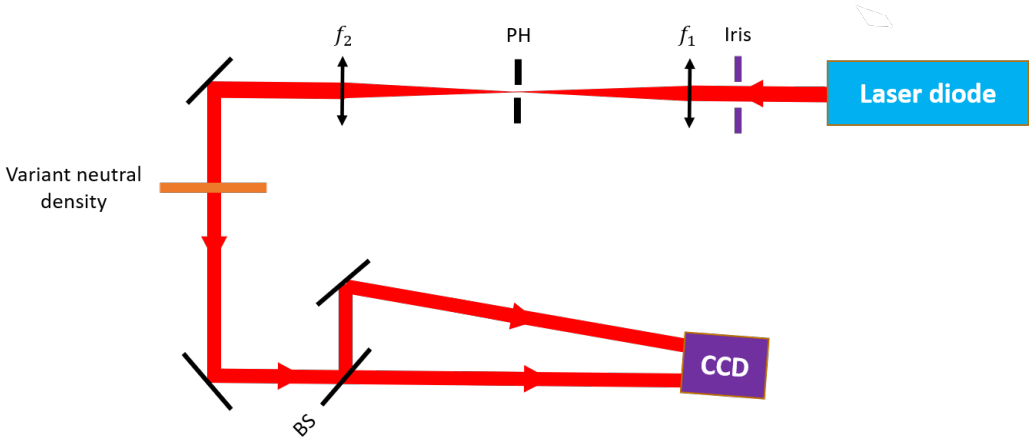

Figure 6.1: Schematic of the experimental setup to measure the spatial resolution. A telescope composed of two lenses (focal length $f_1 = 150\,\text{mm}$ and $f_2 = 100\,\text{mm}$) and a pinhole (PH) of diameter $75\,\mu\text{m}$ shape the incident beam profile coming from the laser diode.

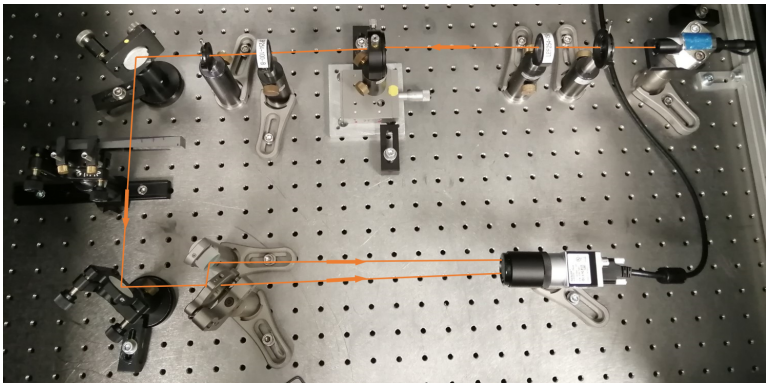

Figure 6.2: Photograph of the experimental setup to measure the spatial resolution (from figure 6.1).

Then, using a 50/50 beam splitter (BS), we split the collimated beam into two identical secondary beams, which will act as a reference and a signal beam on the CCD cameras in order

to monitor and subtract the beam pointing and intensity fluctuations, as explained in chapter 3. Moreover, a variable neutral density with constant optical path length is placed before the beamsplitter to vary the intensity of the signal and the reference beams on the CCD camera in order to measure its spatial and intensity resolutions, depending on the number of detected photons.

6.1.1 Choice of the CCD cameras

As mentioned before, we need a CCD camera with the highest charge storage capacity before saturation per unit surface ($n_{\text{p.e.}}$) in order to achieve the smallest spatial resolution possible. From the commercial Basler catalogue, we have selected two different CCD cameras:

- the CCD Basler acA1920-40gm is used in the current DeLLight pilot experiment in the dark output of the Sagnac interferometer. It has a pixel side size of 5.86 μm.
- the CCD Basler acA4024-29um has a smaller pixel size (1.85 μm) and higher performances. It will be used in the next stage of the DeLLight experiment.

The manufacturer specifications of these cameras are given in table 6.1.

	CCD 1.85 (acA4024-29um)	CCD 5.86 (acA1920-40gm)
Pixel size (μm)	1.85	5.86
Dark noise / pixel	3.3 e^-	6.7 e^-
Saturation / pixel	11000 e^-	31900 e^-
Theoretical gain	2.7	7.8
Pixel Bit Depth (Resolution ADU) (bits)	12	12

Table 6.1: Chart of the manufacturer specifications of the CCD cameras

6.1.2 Laser beam characterisation

Before studying the spatial resolution of each CCD camera, we need to characterise the reference and signal beams. We first studied the transverse intensity profile of each beam which is defined as a Gaussian intensity profile, such as:

$$I(x_i, y_i) = I(x_0, y_0) \times \exp\left(-\frac{2(x_i - x_0)^2}{w_x^2}\right) \times \exp\left(-\frac{2(y_i - y_0)^2}{w_y^2}\right) \tag{6.2}$$

where $I(x_i, y_i)$ and $I(x_0, y_0)$ are the intensity profiles of the laser beam in (x_i, y_i) and (x_0, y_0) position ; (x_0, y_0) are the centred coordinates on the RoI ; w_x and w_x are the minimal waists of the laser beam in x and y-direction.

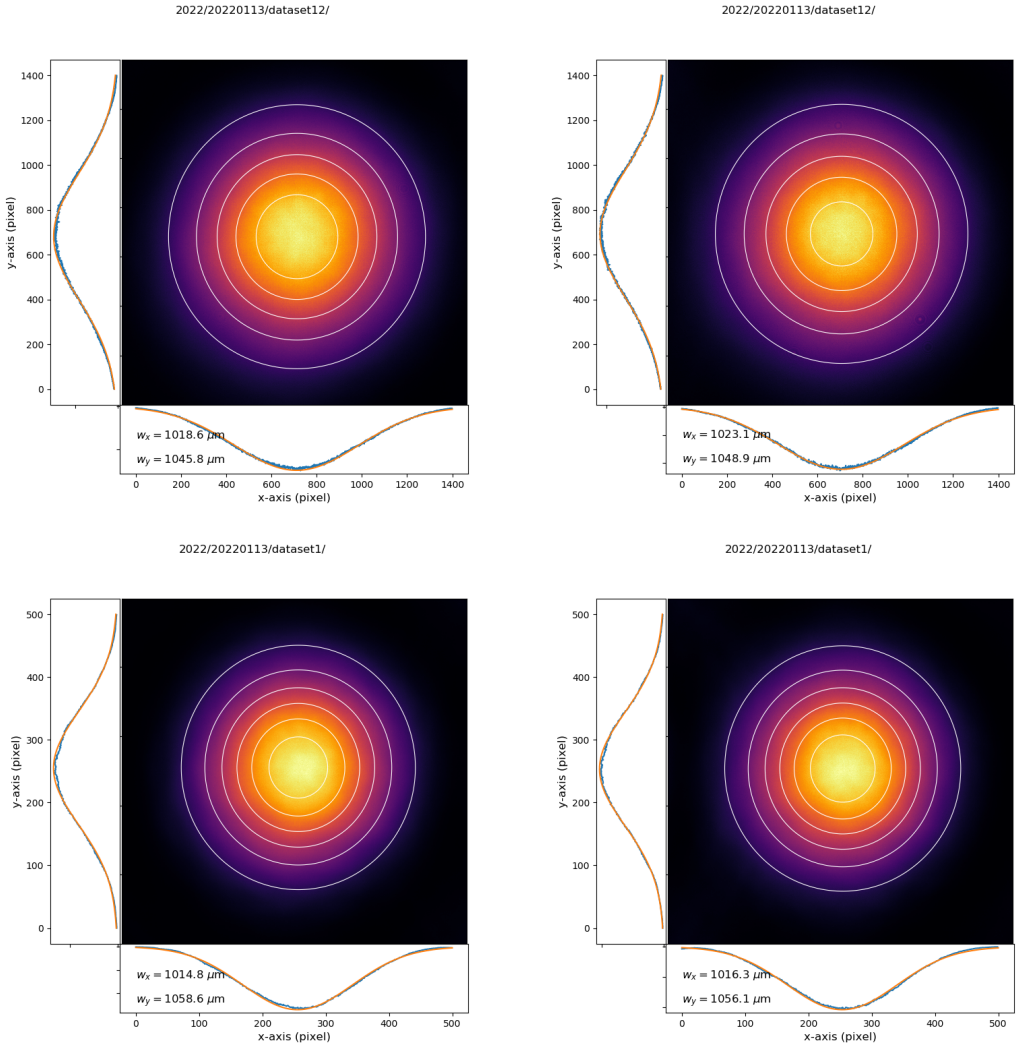

Figure 6.3: CCD images of the beam profiles (dataset at highest intensity $I^{1.85}_{ref,max} \approx 3040$ ADU) : (top left) reference beam on the CCD 1.85 ; (top right) signal beam on the CCD 1.85 ; (bottom left) reference beam on the CCD 5.86 ; (bottom right) signal beam on the CCD 5.86. The waist of the probe and pump beam is $w_x \approx w_y \approx 1.0$ mm, which corresponds to $FWHM \approx 1.2$ mm.

Figure 6.3 shows the intensity profiles of the probe and the pump for a CCD image collected on the CCD 1.85. We used a 2-dimensional Gaussian fit to deliver the waist of the laser pointer beam: $w_x \approx w_y \approx 1.0$ mm, which corresponds to $FWHM \approx 1.2$ mm.

Secondly, we need to estimate the raw beam pointing fluctuations of the laser pointer, which will be used later on in Monte-Carlo simulations to compare data and simulated resolutions (as will be explained in section 6.3). To this end, we look at the evolution of the raw barycenters in x and y-directions for the reference and signal beams on the CCD camera 1.85, as shown on figure 6.4 (for an intensity in ADU: $I^{1.85}_{ref,max} \approx 3040$ ADU). Let us note that we used a RoI-size equal to double the beam size ($w_{RoI} = 2 \times FWHM$), not to be biased by the efficiency due to

w_{RoI}. The raw beam pointing fluctuations (r.m.s.) of the laser pointer correspond to the standard deviation of the raw barycenter distribution, such as:

$$\begin{cases} \sigma_{BP,x} \approx 0.03\,\mu\text{m} \\ \sigma_{BP,y} \approx 0.07\,\mu\text{m} \end{cases} \tag{6.3}$$

Moreover, we can see on figure 6.4 that the evolution of the raw barycenter in y-direction includes beam pointing fluctuations and a systematic low drift of around $0.2\,\mu$m.

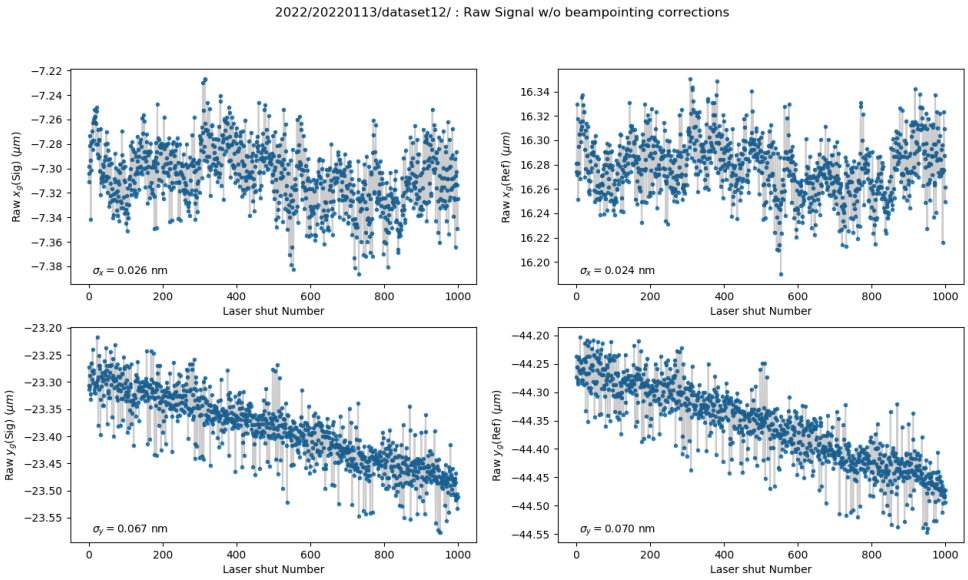

Figure 6.4: Evolution of the raw barycenter (without beam pointing corrections) of the reference (right) and signal (left) beams for the CCD 1.85 (for 1000 events, $w_{RoI} = 2 \times FWHM = 1400$ pix). The standard deviations of these barycenter distributions correspond to the beam pointing fluctuations of the laser pointer in x and y-directions: $\sigma_{BP,x} \approx 0.03\,\mu$m and $\sigma_{BP,y} \approx 0.07\,\mu$m (dataset 12, collected on January, the 13th, 2022).

NB: in this chapter, we use the data analysis method described in chapter 3, expect that the linear fit used for the correlation between the reference and signal raw barycenters is as $\tilde{f} = x + b$ instead of $f = ax + b$.

6.2 Gain measurement

The gain G of a CCD pixel i is defined as:

$$N_{\gamma.e}(i) = G_i \times N_{ADU}(i) \tag{6.4}$$

where $N_{\gamma.e}$ is the number of photo-electrons recorded in a pixel and N_{ADU} is the equivalent Analogic Digital Unit (ADU) content.

The uniformity of the gain per pixel of the CCD sensors is essential to ensure a good spatial resolution. The value of the gain is also an important input required for Monte-Carlo simulations to calculate the shot noise (as described in appendix D), since it defines the number of detected photo electrons per pixel. It is therefore important to measure precisely the gain of the CCD pixels of the two studied camera.

The gain of a pixel is obtained by measuring the statistical fluctuations of flat images. Let us explain the method.

The standard deviations (r.m.s.) $\sigma_{\gamma.e}$ and σ_{ADU} of the number of photo-electrons per pixel and the corresponding ADU content, respectively, are defined by:

$$\begin{cases} \sigma_{\gamma.e} = \sqrt{N_{\gamma.e}} \\ \sigma_{ADU} = \frac{\sigma_{\gamma.e}}{G} \end{cases} \tag{6.5}$$

Thus, we have:

$$\sigma_{\gamma.e} = G \times \sigma_{ADU} = \sqrt{N_{\gamma.e}} \tag{6.6}$$

$$\sigma_{ADU} = \frac{\sqrt{N_{\gamma.e}}}{G} = \sqrt{\frac{N_{ADU}}{G}} \tag{6.7}$$

By compiling the ADU content of each pixel in a histogram, we obtain the average ADU content value $\langle N_{ADU} \rangle$ and the r.m.s. value σ_{ADU} for a given CCD camera. Their gain G is finally written as:

$$G = \frac{\langle N_{ADU} \rangle}{\sigma^2_{ADU}} \tag{6.8}$$

In order to experimentally measure the gain of the CCD cameras, we collect a set of what we call "flat images" which corresponds to CCD images where the sensor is completely and uniformly lit by an uniform intensity profile. This way, each pixel of the sensor receives the same amount of photo-electrons in average which enables to check whether the gain per pixel is uniform or not. Then, the measurement of the standard deviation σ^2_{ADU} for each pixel gives the value of the gain of that pixel, using equation 6.8.

Details of the gain measurements are given in appendix C. We have verified that the gain is very uniform for the two studied cameras. The average values are:

$$\langle G_{5.86} \rangle = 7.72 \pm 0.02 \quad \text{for the CCD acA1920 – 40gm} \tag{6.9}$$

$$\langle G_{1.85} \rangle = 2.79 \pm 0.03 \quad \text{for the CCD acA4024 – 29um} \tag{6.10}$$

NB: Considering the manufacturer specifications given in table 6.1, we can estimate the gain of the CCD cameras such as the ratio of the number of electrons at saturation divided by the maximal ADU content. The maximal ADU content is $N^{max}_{ADU} = 4096$ ADU, which is an overestimation considering that we never work with ADU content so close to saturation: we usually never work over $0.75 \times N^{max}_{ADU} \approx 3000$ ADU. Therefore, the gains are expected to be of the order of $G^{5.86} = 7.8$ and $G^{1.85} = 2.7$, in agreement with our measurement.

6.3 Numerical simulations of the expected shot noise of the CCD camera

The expected spatial resolution, inherently limited by the intrinsic shot noise of the CCD camera, is calculated by Monte-Carlo simulations. The later are described in appendix D and include the shot noise, the beam pointing fluctuations and their corrections, and the ON-OFF subtraction in order to calculate the spatial resolution σ_y of the DeLLight experiment. Additionally, we can also extract the intensity resolution $\sigma_{\Delta I/I}$ (defined in section 2.6.2).

Simulations have been performed for the two selected CCD camera with the following inputs:

- CCD 1.85 : gain $G = 2.8$ and pixel size $d_x \times d_y = 1.8 \times 1.8\,\mu$m
- CCD 5.86 : gain $G = 7.7$ and pixel size $d_x \times d_y = 5.86 \times 5.86\,\mu$m

The beam size at full width at half maximum is set to $FWHM = 1200\,\mu m$. The analysis window or "Region of Interest" (RoI) is set to : $w_{RoI} = 650$ pixels for the CCD 1.85, and $w_{RoI} = 200$ pixel for the CCD 5.86, which correspond to the the FWHM of the beam. The intensity fluctuations are approximately 2%. The simulated beam pointing fluctuations (r.m.s.) in both directions are: $\sigma_{BP,x} = 0.03\,\mu$m and $\sigma_{BP,y} = 0.07\,\mu$m (from equation 6.3.

6.4 Measurement of the shot noise spatial resolution

We present in this section the experimental results of the spatial resolution measurements, which are in good agreement with the expected shot noise of the CCD camera calculated by Monte-Carlo simulations.

We first measure the spatial resolution of the two CCD cameras as a function of the intensity of the pulses, i.e. as a function of the number of detected photo-electrons (in ADU content). We use the variable neutral optical density (see section 6.1) to vary the intensity of the signal and the reference beams on the CCD cameras.

Several data sets of $N = 1000$ events (i.e. CCD images) each are taken for different intensity values and each are analysed following the method described in chapter 3, in order to extract the spatial resolution. An example of analysed data for a RoI-size $w_{RoI} = FWHM$ and for the highest intensity is shown on figure 6.5 for the CCD 5.86 ($I^{5.86}_{ref,max} \approx 2690$ ADU) and figure 6.6 for the CCD 1.85 ($I^{1.85}_{ref,max} \approx 3040$ ADU) with the measured values of the spatial resolution.

The results of the measured values of the spatial resolutions σ_x and σ_y are presented on figure 6.7 as a function of the intensity of the pulse, for the two CCD cameras 5.86 and 1.85. The intensity is given by the parameter $I_{ref,max}$, the ADU content of the pixel at the maximum of the intensity profile of the reference pulse. In the same figure, the measured values are compared to the expected shot noise spatial resolution calculated by Monte-Carlo simulations (see section 6.3). Data and Monte-Carlo simulations are in good agreement, especially for relatively high intensity.

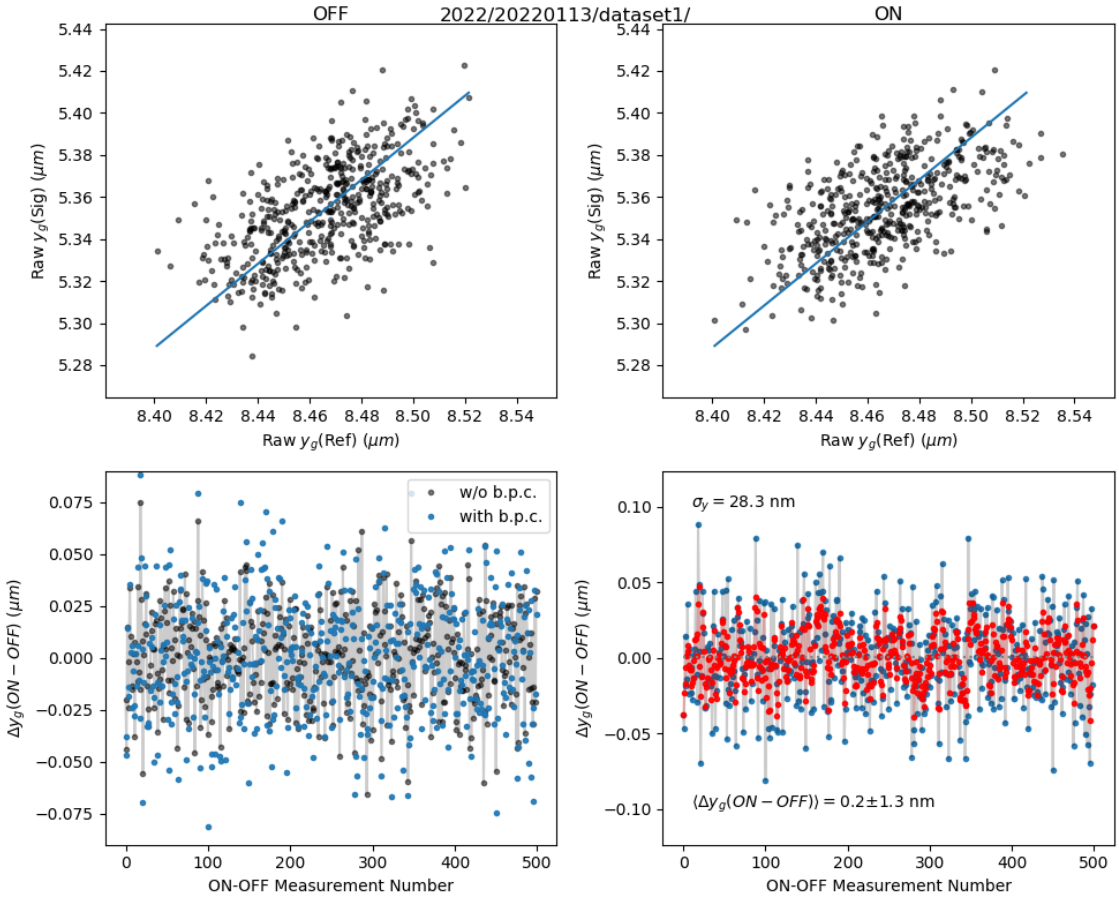

Figure 6.5: Results of the data analysis (method in chapter 3) for the camera CCD 5.86: (Upper plots) Linear correlation of the barycenters of the intensity profile of the signal $\bar{y}_{sig}(i)$ versus the reference $\bar{y}_{ref}(i)$, calculated along the vertical y axis. The data are shown as black points, for both even ("OFF", left panel) and odd ("ON", right panel) measurements. The result of the linear fit obtained using the OFF data only is shown in both panels as a blue line. (Lower plots) black points: ON-OFF raw signal $\bar{y}^{ON}_{sig}(i) - \bar{y}^{OFF}_{sig}(i)$ without beam pointing correction; blue points: ON-OFF reconstructed signal $\Delta y(i) = \bar{y}^{ON}_{corr}(i) - \bar{y}^{OFF}_{corr}(i)$ after beam pointing correction. We verify that the signal is null as expected: $\Delta y(ON - OFF) = 0.2 \pm 1.3$ nm. The spatial resolution is $\sigma_y = 28.3$ nm (dataset 1, collected on January, the 13th, 2022).

For a spatial resolution limited only by the shot noise of the CCD camera, we expect that the spatial resolution must vary as the square root of the number of detected photo-electrons, such as:

$$\sigma_y = \frac{a}{\sqrt{I_{ref,max}}} \tag{6.11}$$

with a a constant value. To test this, we fit this function with a as a free parameter, for the data (purple line) and for the Monte-Carlo simulations (orange line). The later are in good agreement with the fit result, as expected. However, an additional noise is clearly observed at

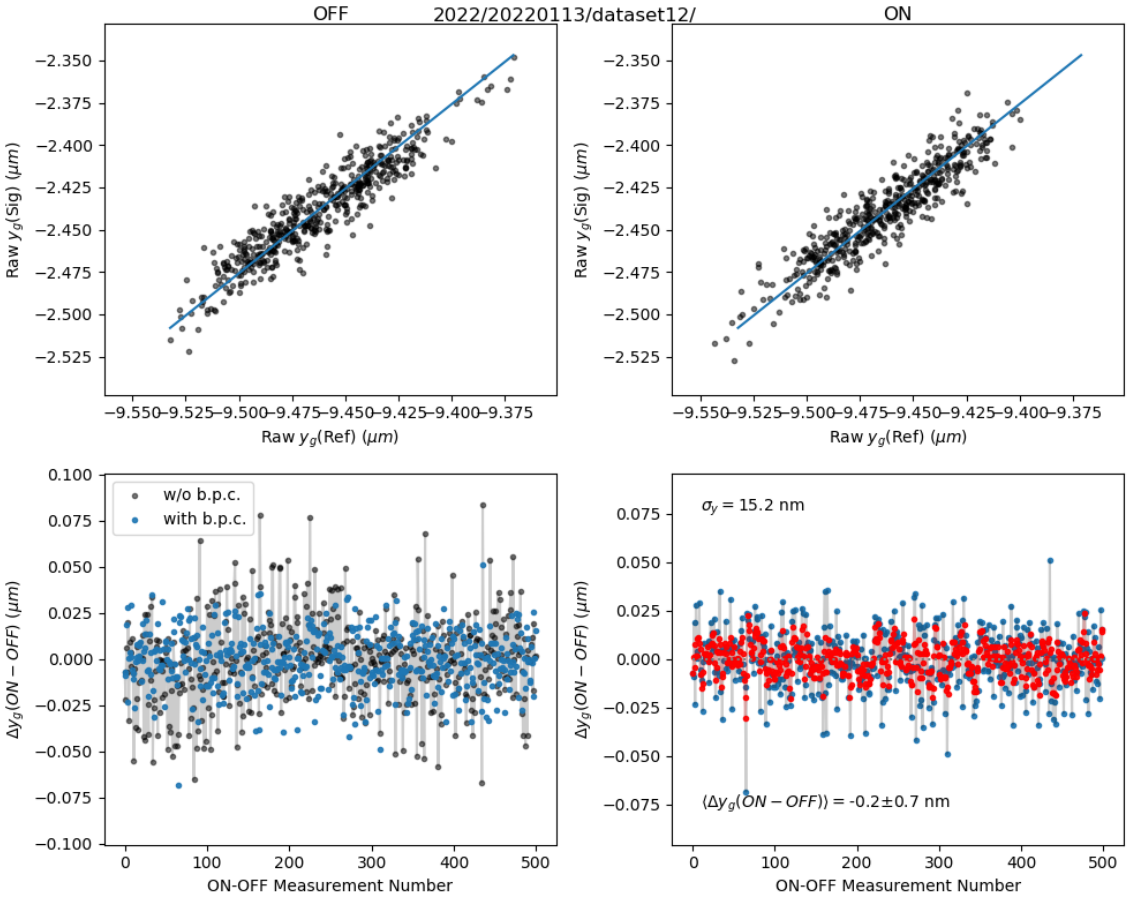

Figure 6.6: Same as Figure 6.5 but for the CCD camera 1.85. The signal is null as expected: $\Delta y(ON - OFF) = -0.2 \pm 0.7$ nm. The spatial resolution is $\sigma_y = 15.2$ nm (dataset 12, collected on January, the 13th, 2022).

low energy for data. Adding a constant dark current b, and fitting the following function:

$$\sigma_y = \sqrt{\frac{a^2}{I_{ref,max}} + b} \tag{6.12}$$

showed that the preferred value is $b = 0$, meaning that the dark current is negligible.

However, it is found that a noise inversely proportional to the intensity ($c/I_{ref,max}$ where c is a constant) is preferred as shown on figure 6.7, where we plot in a dashed purple line the result of the following fit:

$$\sigma_y = \sqrt{\frac{a^2}{I_{ref,max}} + \frac{c^2}{I_{ref,max}^2}} \tag{6.13}$$

Therefore, the measured spatial resolution in the data corresponds to the shot noise of the CCD camera when the ADU content of the pixel at maximal intensity profile ($I_{ref,max}$) is approximately above 1000 ADU.

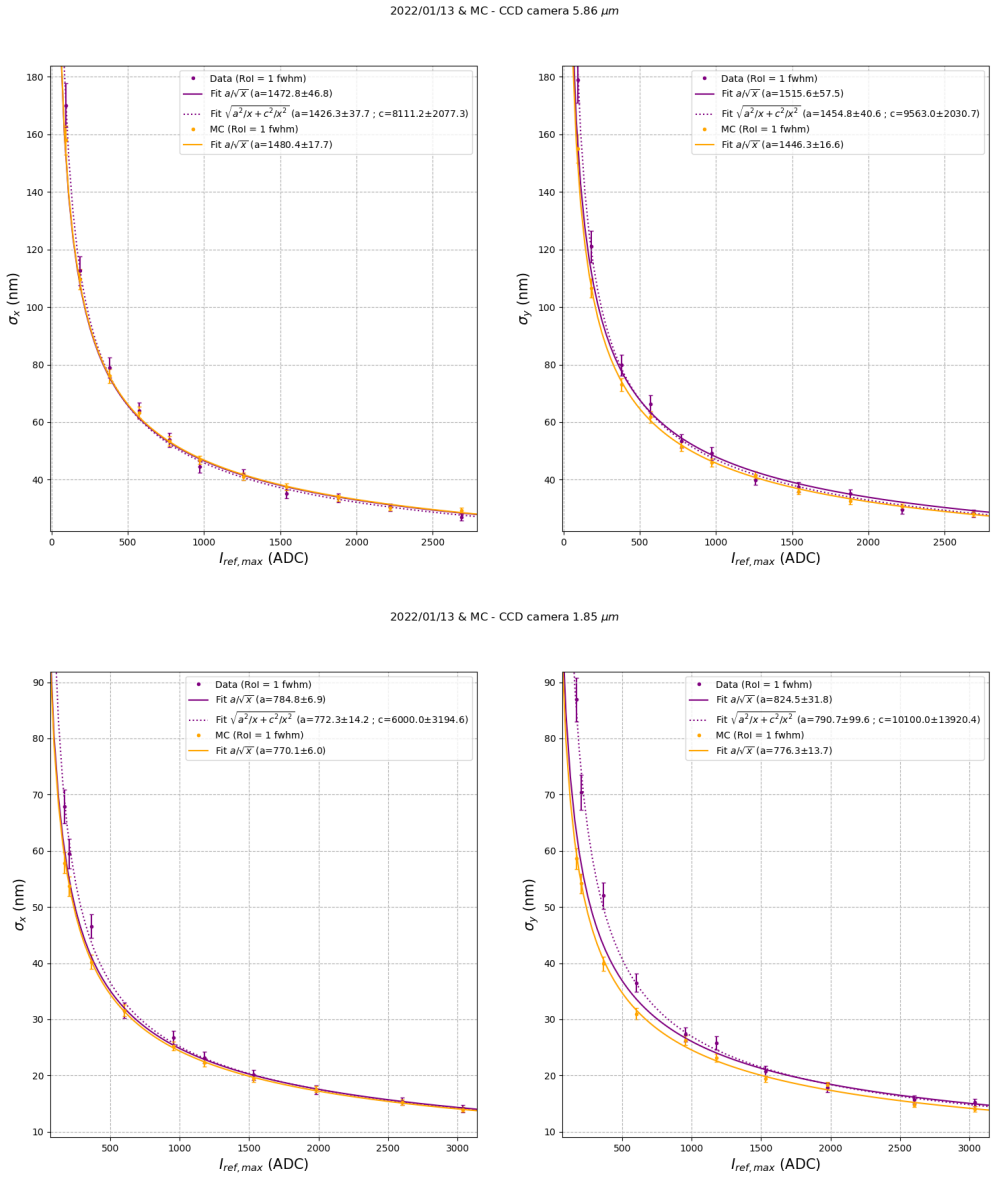

Figure 6.7: Spatial resolution σ_x (left panels) and σ_y (right panels), as a function of the intensity of the pulses, given by the parameter $I_{ref,max}$, the ADU content of the pixel at the maximum of the intensity profile of the reference pulse. The results are given for the camera CCD 5.86 (upper panels) and CCD 1.85 (lower panels). The purples points correspond to the measured values from data. The orange points correspond to the expected shot noise values calculated by Monte-Carlo. The fitted orange line corresponds to the expected variation of the shot noise as a function of the square root of the number of detected photo-electrons.

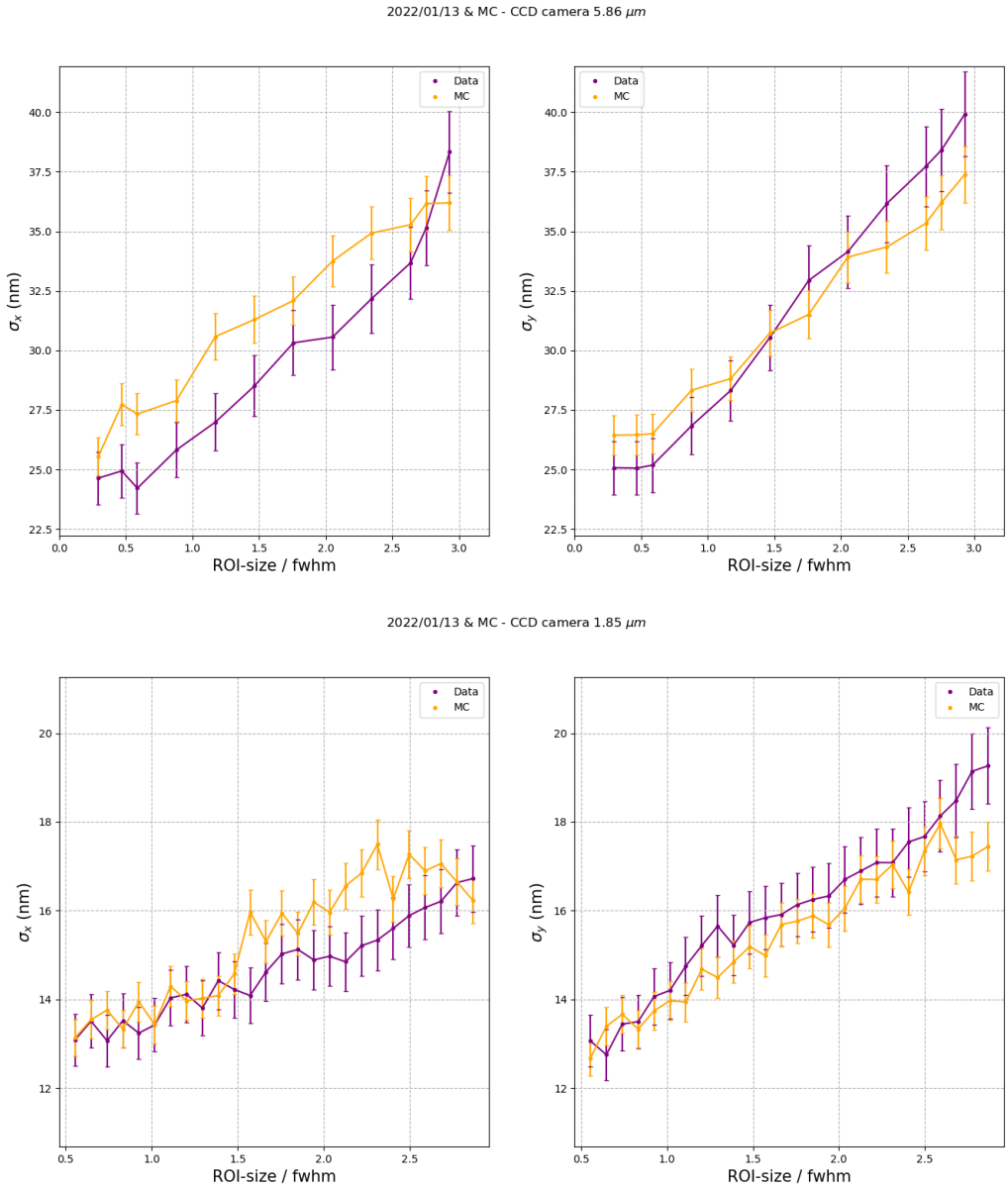

Figure 6.8: Evolution the spatial resolution in both direction σ_x (left panels) and σ_y (right panels), as a function of the RoI size over the spot size (FWHM) for both CCD cameras at the highest intensity $I_{ref,max}$ (in ADU content) of the reference pulse. The results are given for the CCD camera 5.86 with $I^{5.86}_{ref,max} \approx 2690$ ADU (upper panels) and CCD 1.85 with $I^{1.85}_{ref,max} \approx 3040$ ADU (lower panels).

For an intensity $I_{ref,max} \approx 3000$ ADU (75% of the full capacity of charge), which corresponds to the intensities used for DeLLight measurements to avoid saturation on the CCD camera in the dark output of the Sagnac interferometer, the measured spatial resolutions (shot

noise) are:

$$\sigma_{5.86}^{data} = 28 \text{ nm for the CCD camera 5.86} \tag{6.14}$$
$$\sigma_{1.85}^{data} = 14 \text{ nm for the CCD camera 1.85} \tag{6.15}$$

which correspond well to the simulated shot noise of the CCD cameras.

Additionally, we also study the influence of the RoI size on the spatial resolution σ_x and σ_y of both CCD cameras. To this end, the data are analysed following the method described in section 3.3 for different values of the RoI size. We analyse the datasets recorded at the highest intensities: $I_{ref,max}^{1.85} \approx 3040$ ADU for the CCD camera 1.85 (2022/01/13-dataset12, $N = 1000$ events) and $I_{ref,max}^{5.86} \approx 2690$ ADU for the CCD camera 5.86 (2022/01/13-dataset1, $N = 1000$ events). The data are then compared to Monte-Carlo simulations. The results are shown on figure 6.8 for each CCD camera. The measured spatial resolutions σ_x and σ_y (purple plots on fig. 6.8) are compatible with Monte-Carlo simulations (orange plots) and are evolving as expected, i.e. they are slightly degraded when the RoI-size becomes too large. This comes from the fact that, for higher RoI-size, the spatial resolutions become too sensitive to the residual phase noise integrated in the RoI.

6.5 Measurement of the intensity resolution

In this section, we do a similar analysis as for the spatial resolution in order to measure the intensity resolution $\sigma_{\Delta I/I}$ (described in section 3.4) of the same data. We then compare it to the intensity resolution calculated by Monte-Carlo simulations (see section 6.3). The results are shown on figure 6.9.

Similarly as for the spatial resolution, data and Monte-Carlo intensity resolution results are in good agreement, especially at high pulse intensity, given by the parameter $I_{ref,max}$, the ADU content of the pixel at the maximum of the intensity profile of the reference pulse ($I_{ref,max} \geq 1000$ ADU). This is promising for the DeLLight measurements since we usually work with intensities $I_{ref,max} \simeq 3000$ ADU in the dark output of the interferometer.

As for the spatial resolution, the intensity resolution must vary as the square root of the number of detected photo-electrons (see equation 6.11). We see on figure 6.9 that Monte-Carlo simulations are in agreement with the fit result. However, we need to introduce a noise inversely proportional to the intensity (see equation 6.13) to properly fit the data.

For an intensity $I_{ref,max} \approx 3000$ ADU (75% of the full capacity of charge), chosen to avoid saturation on the CCD camera in the dark output of the interferometer, the measured intensity resolutions for both CCD cameras are:

$$\sigma_{\Delta I/I}^{5.86} = 10^{-4} \text{ for the CCD camera 5.86} \tag{6.16}$$
$$\sigma_{\Delta I/I}^{1.85} = 5 \times 10^{-5} \text{ for the CCD camera 1.85} \tag{6.17}$$

which correspond well to the simulated shot noise of the CCD cameras.

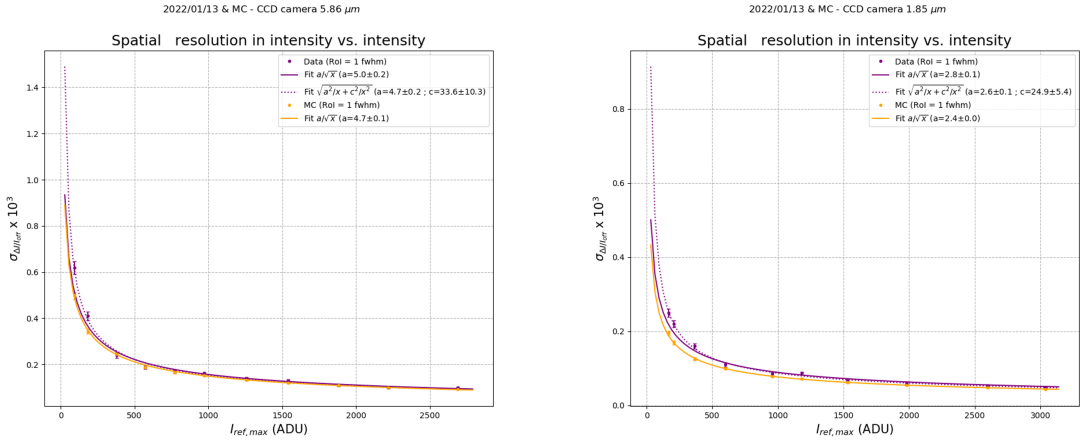

Figure 6.9: Same as figure 6.7, but for the intensity resolution $\sigma_{\Delta I/I}$ for the CCD camera 5.86 (left) and CCD 1.85 (right).

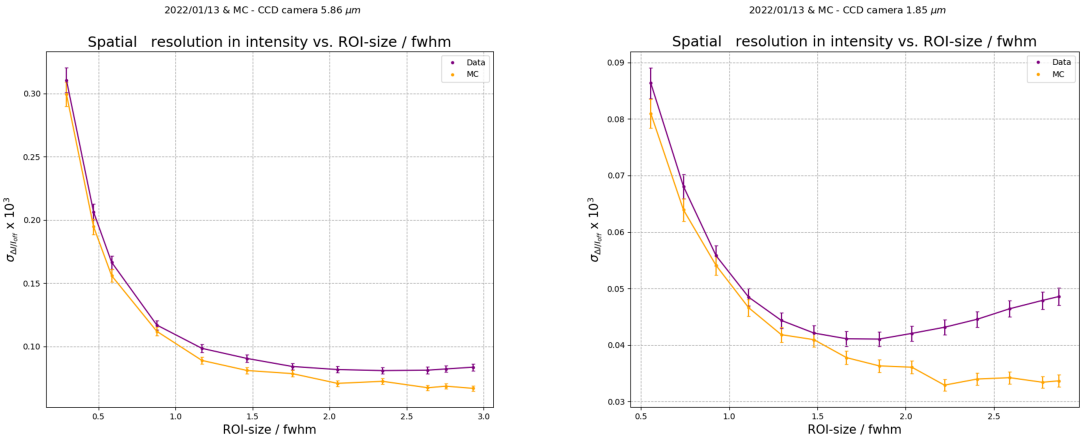

Figure 6.10: Same as figure 6.8, but for the intensity resolution $\sigma_{\Delta I/I}$ for the CCD camera 5.86 (left) and CCD 1.85 (right).

However, as explained in section 2.6.2, the request intensity resolution to reach a sensitivity (number of sigma) of $N_{\text{std}} = \sqrt{T_{\text{obs}}(\text{days})}$, is $\sigma_{\Delta I/I} = 2 \times 10^{-6}$. Since the intensity resolution is inversely proportional to the square root of the number of detected photons in the dark output, and for the goal extinction factor ($\mathcal{F} = 4 \times 10^{-6}$), it requires an incident energy entering the interferometer of about 100 mJ per pulse, As discussed in section 2.9, this energy is two orders of magnitude above the accepted incident intensity to avoid nonlinear phase noise in the beamsplitter.

Additionally, we also studied the influence of the RoI-size on the intensity resolution $\sigma_{\Delta I/I}$ for both CCD cameras, in the same way as previously described in section 6.4. The results are shown on figure 6.10. As expected, the measured intensity resolutions are inversely proportional to the RoI-size as previously explained. They are in good agreement with Monte-Carlo simulations, expect at larger RoI-size ($w_{RoI} \geq 1.5 \times FWHM$). This comes from the fact

that the reference and signal beams are very close to each other on the CCD camera, so the intensity distribution tails of the nearby spot are also integrated for larger RoI-sizes. Thus, the resolution gets degraded for data but not Monte-Carlo simulations. However, since we usually work with RoI-sizes close to the FWHM of the beam, this issue is not a concern at all.

6.6 Summary

For the CCD camera that will be used on the DeLLight experiment in vacuum (Basler acA4024-29um, with a charge capacity of 10^4 electrons per pixel of size $1.8 \times 1.8 \mu m^2$), we have successfully measured the spatial resolution σ_y and the intensity resolution $\sigma_{\Delta I/I}$:

$$\sigma_y = 13\,\text{nm} \tag{6.18}$$

$$\sigma_{\Delta I/I} = 5 \times 10^{-5} \tag{6.19}$$

It corresponds to the inherent limit due to the shot noise of the CCD camera, calculated by Monte-Carlo simulations.

We underline that these spatial and intensity resolution values take into account the corrections of the beam pointing and intensity fluctuations respectively, as well as the zero subtraction "ON-OFF" applied to the DeLLight measurements. Therefore, the intrinsic spatial σ_y^{CCD} and intensity σ_I^{CCD} resolutions of the CCD camera for a single spot measurement are $\sigma_y^{\text{CCD}} = \sigma_y/2 = 6.5\,\text{nm}$ and $\sigma_I^{\text{CCD}} = \sigma_{\Delta I/I}/2 = 2.5 \times 10^{-5}$

The intensity resolution measured here must be improved by a factor 25 in order to reach the requested intensity resolution $\sigma_{\Delta I/I} = 2 \times 10^{-6}$ of the DeLLight project. This is done by increasing the number of detected photons in the interference signal by a factor 625. As discussed in sections 2.6.2 and 2.9.1, this implies that the incident energy entering the Sagnac interferometer must be of 100 mJ, which is not acceptable (2 orders of magnitude too large) because it would generate a phase noise and would degrade the extinction.

The achieved spatial resolution is almost equal to the requested spatial resolution of the DeLLight project (10 nm). This is an important achievement. However, the spatial resolution depends on the number of detected photo-electrons per pixel, and thus depends on the number of ADU recorded per pixel, $N_{\text{adu/pix}}$, which scales as:

$$N_{\text{adu/pix}} \propto \frac{\mathcal{E}_{in} \times \mathcal{F} \times d_{pix}^2 \times QE}{w^2 \times G} \tag{6.20}$$

where $\mathcal{E}_{in}$ is the incident pulse energy entering the interferometer, w is the width of the probe beam, and QE is the quantum efficiency. The spatial resolution achieved in this measurement has been obtained with an ADU content about 3/4 of the maximum charge saturation, corresponding to the optimum running condition. In the current pilot experiment, with the BASLER camera acA1920-40gm ($d_{pix} = 5.86\ \mu$m, $G = 7.7$ and $QE \simeq 20\%$), with a waist $w = 1$ mm and with a degraded extinction factor $\mathcal{F} = 4 \times 10^{-4}$, this condition is verified when $\mathcal{E}_{in} \simeq 2\ \mu$J, as summarised in table 6.2. We can then calculate the required incident energy for the final DeLLight project goal in order to have the same number of ADU per pixel, taking into account the goal parameters summarised in 6.2 and assuming a quantum efficiency $QE = 80\%$. We

obtain a requested incident energy $\mathcal{E}_{in} \approx 8$ mJ. As calculated in section 2.9.1, this is a factor 8 above the maximal incident energy requested to avoid a phase noise induced by non linearity in the beamsplitter. A dedicated study of parameter optimisation will have to be carried out in order to maximise the signal while keeping a negligible non linearity phase noise.

	Goal experiment	Pilot experiment
CCD camera	acA4024-29um	acA1920-40gm
Pixel size d_{pix} (μm^2)	1.85	5.86
CCD gain G	2.8	7.7
Collimated beam waist w (mm)	7	1
Extinction factor $\mathcal{F}$	4×10^{-6}	4×10^{-4}
CCD quantum efficiency QE (%)	80	20
Incident energy $\mathcal{E}_{in}$	1 mJ	2 μJ

Table 6.2: Chart of the parameters of the goal and pilot experiments

Chapter 7

Spatial resolution in the dark output of the interferometer

In the previous chapter, we have verified experimentally that a spatial resolution of the order of 10 nm is achieved with the most suitable commercial CCD camera, and that it corresponds to the inherent quantum noise of the detected photo-electrons. This result has been obtained by measuring a direct intensity profile of femtosecond laser pulses.

In this chapter, we will measure the spatial resolution of the interference signal in the dark output of the Sagnac interferometer, which is now sensitive to the beam pointing fluctuations of the incident laser beam, and is also limited by the mechanical noise of the interferometer. We will show that the beam pointing fluctuations are well suppressed at the level of the requested shot noise. However, we will see that the mechanical noise is the main limitation and must be reduced by one to two orders of magnitude. A method to measure this noise online in order to subtract it will finally be proposed.

7.1 Deterioration of the extinction in the dark output of the interferometer

In order to measure and reach a good spatial resolution, high photons statistics in the interference signal intensity is required. Thus, to maintain a high extinction factor, as measured in our prototypes, we need to increase the intensity of the incident pulses entering the Sagnac interferometer. However, the intensity of the back-reflections would then saturate the CCD camera, as described in chapter 5. Additionally, the tail of the back-reflection intensity distributions would pollute the interference signal. The development of new beamsplitters including dedicated anti-reflective coating with lower back reflectivity coefficient, and with a larger thickness is programmed in the near future to counteract this issue.

Therefore, the measurements presented in this chapter with the available beamsplitter were achieved by degrading the extinction of the interferometer in order to obtain an interference signal intensity equal to the back-reflection intensities, corresponding to an extinction factor $\mathcal{F} = 5 \times 10^{-4}$. We remind that the extinction factor is $\mathcal{F} = (\delta a)^2$ (neglecting the phase noise),

where δa is the R/T asymmetry coefficient of the beamsplitter. So, to degrade the extinction, we need to increase δa. We take advantage of the fact that δa depends on two parameters: the polarisation and the incident angle of the incident beam. Thus, two configurations have been proposed to degrade the extinction:

- Configuration 1: The polarisation of the incident laser pulse is slightly rotated (few tens of mrad) with a half-wave plate placed on the probe path, just before the interferometer.
- Configuration 2: The beamsplitter of the interferometer is rotated (by about 1 degree) in the horizontal plan, changing the incident angle of the laser pulse.

The first configuration has been applied for the measurements carried out with the first prototype (rectangular interferometer without focus), described in section 4.1. However, it has come to light later on that this method poses the disadvantage of reducing the amplification factor $\mathcal{A}$ of the barycenter displacement in the dark output of the interferometer, as will be explained in the next section. Therefore, the two configurations have been applied consecutively for the second prototype (triangle interferometer with focalisation), described in section 4.2.

7.2 Low or high amplification, depending on the configuration of the degraded extinction

In this section, we will see why the amplification of the interference signal is strongly reduced for the first configuration, described in the previous section, for which the polarisation of the incident beam is rotated before entering the interferometer.

7.2.1 Definition of the interference intensity profile in the dark output, containing the noise

Before looking more closely into the effect of the polarisation of the beam, we first need to define the intensity profile in the dark output of the Sagnac interferometer. We assume that the residual noise is induced either by angular fluctuations of the mirrors and the beamsplitter, or by lateral shift of the optical lenses inside the Sagnac interferometer. These fluctuations generate, in the dark output of the interferometer, a relative lateral displacement δy_{noise} and a relative phase noise $\delta\Phi_{\text{noise}}$ between the two counter-propagating probe and reference pulses, without interaction with the pump.

Thus, using equation 2.32 in the y-axis, the intensity profile in the dark output for an OFF measurements i ($\delta\psi = 0$) can be written:

$$\begin{aligned} I_{\text{OFF},i}(y) &= (\delta a)^2 \times I_{in}(y + \mathcal{A} \times \delta y_{\text{noise},i}) \\ &\quad + \left(\delta\Phi_{\text{noise},i}(y)\right)^2 \, (1 - \delta a^2) \times I_{in}(y - \frac{\delta y_{\text{noise},i}}{2}) \end{aligned} \tag{7.1}$$

where $\mathcal{A}$ is the amplification factor of the interferometer, such as:

$$\mathcal{A} = \frac{1 - \delta a}{2\delta a} \tag{7.2}$$

7.2.2 Low amplification with rotated polarisation (Configuration 1)

Now, we look into the effect of the polarisation of the incident beam. When the extinction is maximal in the dark output, there is no R/T asymmetry yet, and the incident pulse entering the interferometer is only p polarised. The extinction factor is then: $\mathcal{F}_{max} \simeq 3 \times 10^{-6}$, as measured in section 5.2.2 for the triangular configuration of the interferometer with spatial filter.

Then, when the extinction is degraded by slightly rotating the polarisation of the incident probe beam by an angle β, a very small component of s polarisation appears. The degraded extinction becomes $\mathcal{F}_{rot} \simeq 5 \times 10^{-4}$ (same as for the back-reflections). Thus, the electric field $\vec{E}_{in}$ of the incident pulse can be split into two orthogonal p and s polarisation components:

$$\begin{aligned} \vec{E}_{in} &= \vec{E}_{in,p} + \vec{E}_{in,s} \\ |\vec{E}_{in,p}| &= |\vec{E}_{in}| \times \cos(\beta) \\ |\vec{E}_{in,s}| &= |\vec{E}_{in}| \times \sin(\beta) \end{aligned} \tag{7.3}$$

The corresponding incident intensities of the two polarisation component are thus:

$$\begin{aligned} I_{in} = |\vec{E}_{in}|^2 = I_{in,p} + I_{in,s} \\ I_{in,p} = I_{in} \times \cos^2(\beta) \\ I_{in,s} = I_{in} \times \sin^2(\beta) \end{aligned} \tag{7.4}$$

For each polarisation components p and s, we associate a phase noise $\delta\Phi_p(y)$ et $\delta\Phi_s(y)$ and an asymmetry coefficient δa_p and δa_s. On one hand, since the incident beam is p polarised at maximal extinction, the maximal extinction factor is (from equation 2.31):

$$\mathcal{F}_{max} = \frac{I_{out}}{I_{in}} = \frac{I_{out,p}}{I_{in,p}} = (\delta\Phi_p(y))^2 + (\delta a_p)^2 \simeq 3 \times 10^{-6} \tag{7.5}$$

On the other hand, when the polarisation of the incident beam is rotated, the degraded extinction becomes dominated by the s component of the beam, due to a large value of the asymmetry coefficient δa_s (although the probe beam is mostly p polarised). Indeed, this coefficient has been calculated by measuring the transmission and the reflection coefficients in intensity T and R of the beamsplitter with a pure s polarised incident beam: $T = 77.5\%$ and $R = 22.5\%$. Using equation 2.11, the asymmetry coefficient in s polarisation is thus $\delta a_s = 0.55$ and the degraded extinction in the dark output is:

$$\mathcal{F}_{rot} = \frac{I_{out}}{I_{in}} = \frac{I_{out,s}}{I_{in}} = \frac{((\delta\Phi_s(y))^2 + (\delta a_s)^2) \times I_{in,s}}{I_{in}} \simeq (\delta a_s)^2 \times \sin^2(\beta) \simeq 5 \times 10^{-4} \tag{7.6}$$

The degraded extinction $\mathcal{F}_{rot}$ is adjusted in order to be equal to the corresponding extinction of the back reflections $\mathcal{F}_{rot} = R_{AR}/2 = 5 \times 10^{-4}$ (from equation 5.4) when the rotation angle of the polarisation planes of the incident beam is $\beta \simeq 40$ mrad, as illustrated on figure 7.1.

In summary, in the first configuration where the polarisation of the incident beam is rotated by an angle β, the extinction in the dark output is strongly degraded, going from $\mathcal{F}_{max} \simeq 3 \times 10^{-6}$

(Prototype 2) to $\mathcal{F}_{rot} \simeq 5 \times 10^{-4}$. In this degraded state, the interference intensity in the dark output (equation 7.1) is dominated by the s component of the incident beam ($\delta a = \delta a_s = 0.55$), and the amplification factor of the interferometer (equation 7.2) is strongly reduced, such as: $\mathcal{A} = (1 - \delta a_s)/(2\delta a_s) \simeq 1/2$. Therefore, the relative displacement δy_{noise} induced by the noise is not amplified in the dark output, and the spatial resolution is only degraded by the phase noise $\delta\Phi_{\text{noise}}$ (equation 7.1).

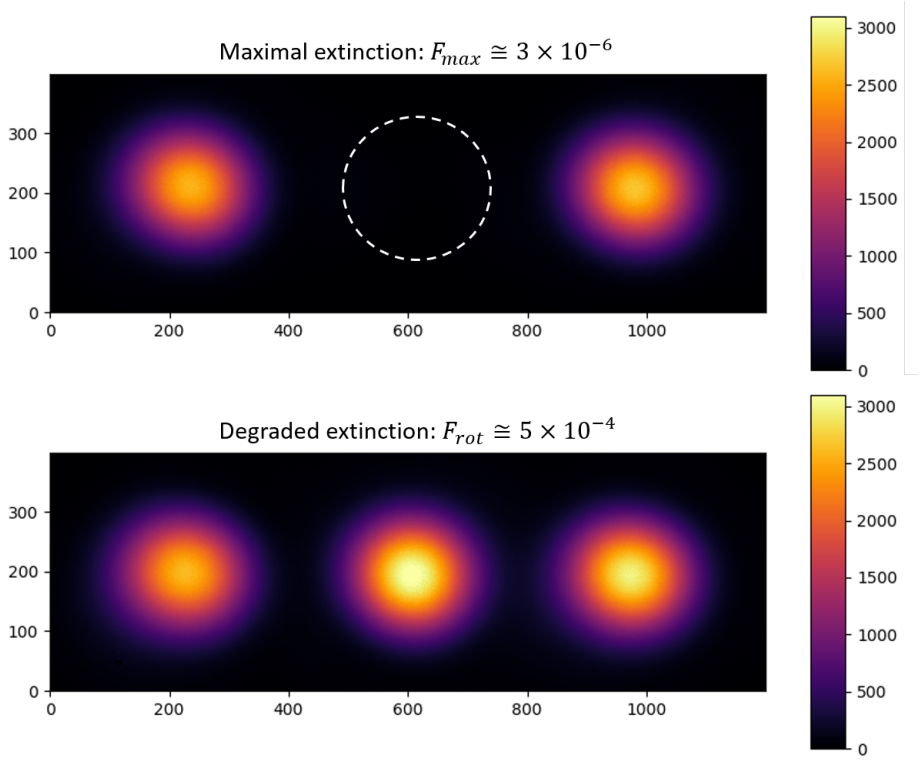

Figure 7.1: CCD images of the intensity profiles of the interference and the reference (back-reflection) in the dark output of the interferometer (Prototype 2 with spatial filter in the dark output). (Top) Intensity profiles at maximal extinction of the interference signal in the white dotted area, with $\mathcal{F}_{max} \simeq 3 \times 10^{-6}$. (Bottom) Intensity profiles for the first configuration where the polarisation of the incident beam is rotated by an angle $\beta \simeq 40$ mrad, and the extinction of the interference signal is degraded from $\mathcal{F}_{max} \simeq 3 \times 10^{-6}$ to $\mathcal{F}_{rot} \simeq 5 \times 10^{-4}$.

7.2.3 High Amplification with rotated beamsplitter (Configuration 2)

In this section, we will see how the DeLLight signal is amplified in the Sagnac interferometer for the second configuration where the beamsplitter is slightly rotated. This configuration was only used for the triangular interferometer with focusing (Prototype 2). In the resolution measurements presented in section 7.4.2, the BS was rotated to an incident angle of 46°.

In this configuration, the polarisation of the beam is purely p, which leads to an extinction

factor of:

$$\tilde{\mathcal{F}}_{max} = \frac{I_{out,p}}{I_{in,p}} = (\delta\tilde{\Phi}_p(y))^2 + (\tilde{\delta a}_p)^2 \tag{7.7}$$

However, since the BS is slightly rotated this time, there is a significant R/T asymmetry and the corresponding asymmetry coefficient $\tilde{\delta a}_p$ increases compared to the first configuration at maximal extinction. For the BS rotated at 46°, the R and T coefficients in intensity were measured in a similar way as in the previous section but with a pure p polarised incident beam: $R = 51\%$ and $T = 49\%$. Thus, the asymmetry coefficient is $\tilde{\delta a}_p = 0.02$, corresponding to an extinction of $\tilde{\mathcal{F}}_{max} \simeq (\tilde{\delta a}_p)^2 \simeq 4 \times 10^{-4}$. This result is compatible with the measured extinction in this configuration where the interference signal has an intensity similar to the back-reflections without rotating the polarisation planes of the incident beam ($\mathcal{F}_{rot} = R_{AR}/2 = 5 \times 10^{-4}$), as will be seen in section 7.4.2.

In summary, in the second configuration where the BS is rotated at 46°, the maximal extinction reachable in the dark output is $\tilde{\mathcal{F}}_{max} \simeq 4 \times 10^{-4}$. The interference intensity in the dark output (equation 7.1) is dominated by the p component of the incident beam ($\delta a = \tilde{\delta a}_p = 0.02$), and the amplification factor of the interferometer (equation 7.2) is $\mathcal{A} = (1 - \tilde{\delta a}_p)/(2\tilde{\delta a}_p) \simeq 24$. However, since the BS is slightly rotated this time, there is a significant R/T asymmetry and the corresponding asymmetry coefficient $\tilde{\delta a}_p$ increases compared to the first configuration at maximal extinction. Therefore, the relative displacement δy_{noise} induced by the noise is amplified in the dark output, and the spatial resolution is dominated by the asymmetry $\tilde{\delta a}_p$.

7.3 Numerical simulation of the spatial resolution

In this section, we describe the method to simulate the spatial resolution in the dark output of the Sagnac interferometer in both low and high amplification configurations.

The principle is first to generate a given number of laser shots with similar properties to the beam used on the DeLLight experiment (in term of intensity profile and size), using the Monte-Carlo simulation as described in appendix D. It includes the shot noise and the beam pointing fluctuations. Then, the same analysis method as for DeLLight data is used to calculate the probe and reference barycenters of the simulated pulses and the "ON-OFF" final measurement Δy with the associated resolution σ_y which corresponds to the standard deviation (r.m.s.) of the barycenter distribution over time, as described in chapter 3. More specifically, since the pump is shut off for resolution measurement, "ON-OFF measurements" are in fact "fake ON-OFF measurements" and actually correspond to "OFF-OFF measurements" of consecutive laser shots.

7.3.1 Modelling of the residual phase noise $\delta\Phi_{\text{noise}}$

In order to simulate the spatial resolution in low and high amplification configurations, we need to model a key parameter of a given OFF intensity profile in the dark output as seen in equation 7.1: the phase noise $\delta\Phi_{\text{noise}}$. It is induced by angular fluctuations of the mirrors and

beamsplitter or by lateral shift of the optical lenses inside the Sagnac interferometer. Thus, a rotation of an angle $\delta\theta_{\text{noise}}$ (of a mirror for instance), along the y-axis, generates a relative lateral displacement δy_{noise} in the dark output of the interferometer of either the probe or the reference, and by geometric considerations, we have:

$$\delta y_{\text{noise}} = 2 \times L_{opt} \times \delta\theta_{\text{noise}} \tag{7.8}$$

where L_{opt} is the average optical path length between the beamsplitter and the closest optical lens. We have $L_{opt} \approx 35$ cm in the experimental setup. Similarly, a translation of one of the lens of focal length f in the interferometer also generates a lateral displacement δy_{noise} in the dark output, but since $2f$ is of the same order as L_{opt}, we can assimilate a lateral displacement of the lens to a rotation of a mirror.

Moreover, the rotation of a mirror of an angle $\delta\theta_{\text{noise}}$ also produces a rotation of the wave plans of the two counter-propagating pulses in the dark output. Thus, the relative angle of the wave plans of the probe and the reference is then equal to $2 \times \delta\theta_{\text{noise}}$, and the phase between both pulses is a function of the vertical coordinate y, equal to:

$$\delta\Phi_{\text{noise}}(y) = \frac{2\pi}{\lambda_0} \times 2\delta\theta_{\text{noise}} \times y + \delta\Phi_0 = \frac{4\pi}{\lambda_0} \times \delta\theta_{\text{noise}} \times y + \delta\Phi_0 \tag{7.9}$$

where λ_0 is the wavelength of the laser, and $\delta\Phi_0$ is the intrinsic phase generated by the beamsplitter itself. It is constant and corresponds to a uniform phase in the ideal case of a perfectly aligned Sagnac interferometer.

Finally, using equations 7.1, 7.8 and 7.9, the simulated intensity profile in the dark output for an OFF measurement i is given by:

$$\begin{aligned} I_{\text{OFF},i}(y) &= (\delta a)^2 \times I_{in}\left(y + \frac{1-\delta a}{\delta a} \times L_{opt} \times \delta\theta_{\text{noise,i}}\right) \\ &\quad + \left(\frac{4\pi\,\delta\theta_{\text{noise,i}}}{\lambda_0} \times y + \delta\Phi_0\right)^2 (1 - \delta a^2) \times I_{in}(y - L_{opt}\,\delta\theta_{\text{noise,i}}) \end{aligned} \tag{7.10}$$

where the asymmetry coefficient is $\delta a = \delta a_s$ for the low amplification configuration (noise dominated by $\delta\Phi_{\text{noise}}$) and $\delta a = \delta a_p$ for the high amplification configuration (noise dominated by δy_{noise}).

7.3.2 Simulation parameters

For each laser shot k, we generate an angular noise $\delta\theta_{\text{noise,k}}$, which induces a lateral displacement $\delta y_{\text{noise,k}}$ in the dark output and a phase noise $\delta\Phi_{\text{noise,k}}$. The angular noise $\delta\theta_{\text{noise,k}}$ is generated as a Gaussian distribution of standard deviation σ_θ by Monte-Carlo simulations (it is added to the Monte-Carlo intensity profile generation described in appendix D).

In summary, the input parameters of the spatial resolution simulations are:

- σ_θ depicts the angular fluctuations of the optical mounts in the interferometer ;
- $\delta\Phi_0$ is the intrinsic phase of the beamsplitter ;

- L_{opt} is the optical path length between the beamsplitter and the closest optical lens, such as: $L_{opt} = 35\,\text{cm}$;
- δa is the asymmetry coefficient of the beamsplitter in intensity.

The results of these simulations for Prototype 2 at low and high amplification will be compared to the data resolution measurements.

7.4 Measurement of the spatial resolution at low amplification

7.4.1 Square interferometer without focusing (Prototype 1)

The spatial resolution measurements for the rectangular Sagnac interferometer (no focusing) (Prototype 1 presented in section 4.1) were only carried out with the first configuration where the polarisation of the incident beam is slightly rotated using a half-wave plate before the interferometer.

The spatial resolution has been measured by recording 8000 successive laser shots (at a 10 Hz repetition rate, corresponding to approximately 13 minutes), with no interaction between pump and probe pulses (the pump beam was shut off). Measurements have been performed on January, the 16th, 2020, dataset 7, using the CCD camera Basler acA1300-60gm (pixel size of 5.3 μm and saturation charge of 10^4 electrons per pixel). The expected shot noise, calculated by Monte-Carlo simulation (see appendix D), is $\sigma_y = 40$ nm.

Data of successive odd $(2i-1)$ and even $(2i)$ laser shots are arbitrarily separated into "OFF" and "ON" data in order to define a fake "ON-OFF" measurement i using two successive laser shots (at a 5 Hz repetition rate). As explained in chapter 3, section 3.3, the beam pointing fluctuations are suppressed for each ON and OFF measurement using the correlation of the barycenters of the signal $\bar{y}_{\text{sig}}(i)$ and the back-reflection $\bar{y}_{\text{ref}}(i)$. The corrected positions are then:

$$\begin{aligned} \bar{y}^{\text{OFF}}_{\text{corr}}(i) &= \bar{y}^{\text{OFF}}_{\text{sig}}(i) - \left(a_{\text{OFF}} \times \bar{y}^{\text{OFF}}_{\text{ref}}(i) + b_{\text{OFF}}\right) \\ \bar{y}^{\text{ON}}_{\text{corr}}(i) &= \bar{y}^{\text{ON}}_{\text{sig}}(i) - \left(a_{\text{OFF}} \times \bar{y}^{\text{ON}}_{\text{ref}}(i) + b_{\text{OFF}}\right) \end{aligned} \tag{7.11}$$

where a_{OFF} and b_{OFF} are constants, obtained by fitting the linear correlation between the signal and reference barycenters, using only the OFF measurements. The signal $\Delta y(i)$ of the fake "ON-OFF" measurement i is then:

$$\Delta y(i) = \bar{y}^{\text{ON}}_{\text{corr}}(i) - \bar{y}^{\text{OFF}}_{\text{corr}}(i) \tag{7.12}$$

Its average value $\Delta y = \langle \Delta y(i) \rangle$ is expected to be zero since there is no interaction between pump and probe pulses.

Figure 7.2 displays the result of such analysis, performed with a RoI-size w_{RoI} equal to half the FWHM of the intensity profile of the beam. Correlations of the barycenters of the signal and the back-reflections are shown in the upper plots, for both OFF and ON data, with the

result of the linear fit superposed (see legend of the figure for more details).

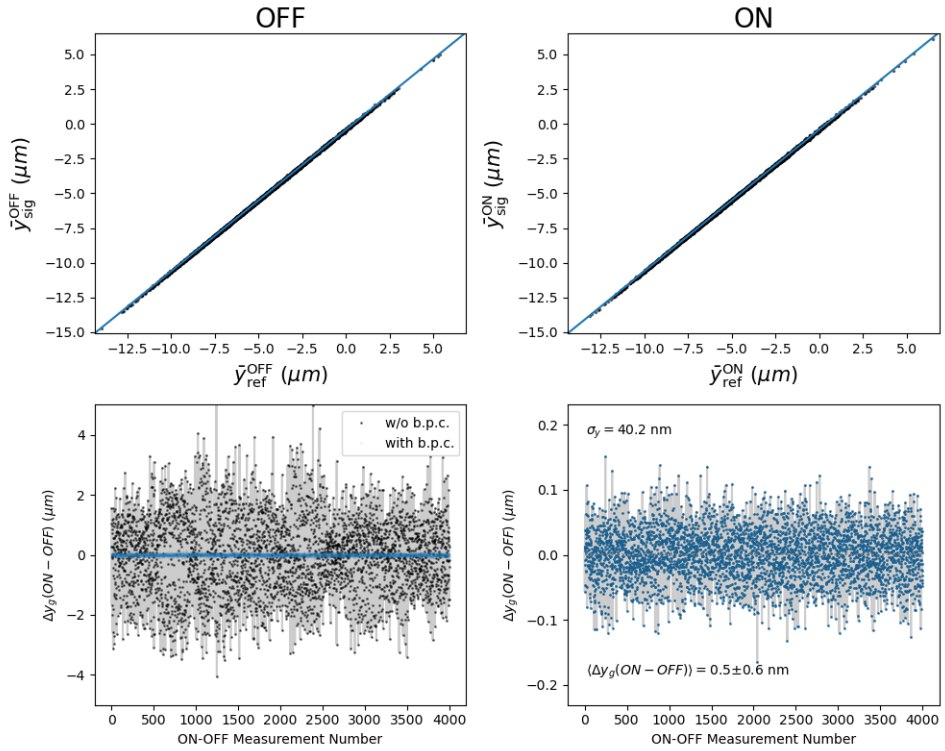

Figure 7.2: (Upper plots) Linear correlation of the barycenters in intensity of the interference signal $\bar{y}_{sig}(i)$ and the back-reflection $\bar{y}_{ref}(i)$, calculated along the vertical axis y, in a given RoI-size $w_{RoI} = w/2$, with w the FWHM of the intensity profile of the beam. The data are shown as black dots, for both OFF (left panel) and ON (right panel) measurements, while the result of the linear fit obtained using the OFF data only is shown in both panels as a blue line. (Lower plots) black dots: ON-OFF raw signal $\bar{y}^{ON}_{sig}(i) - \bar{y}^{OFF}_{sig}(i)$ without beam pointing correction ; blue dots: ON-OFF reconstructed signal $\Delta y(i) = \bar{y}^{ON}_{corr}(i) - \bar{y}^{OFF}_{corr}(i)$ after beam pointing correction. The average signal is $\Delta y = \langle \Delta y(i) \rangle = 0.5 \pm 0.6$ nm compatible with zero (no pump). The spatial resolution $\sigma_y = 40.2 \pm 0.6$ nm is equal to the shot noise of the CCD camera 5.3 (Basler acA1300-60gm). These data have been collected on January, the 16th, 2020, dataset 7.

The distribution of the raw barycenter position of the interference signal for the OFF data, $\bar{y}^{\mathrm{OFF}}_{\mathrm{sig}}(i)$, is presented on figure 7.3 (top left plot) as a function of the "ON-OFF" measurement number i (effectively, as a function of time). Strong beam pointing fluctuations are clearly observed and the spatial resolution is extremely large at about 2.9 μm. The frequency spectrum of this distribution is also presented (top right plot). We can observe a typical $1/\nu$ drift noise at low frequency and three harmonic peaks at 1 Hz, 2 Hz and 2.4 Hz.

The middle plots display the "ON-OFF" subtraction of the raw barycenter positions $\bar{y}^{\mathrm{ON}}_{\mathrm{sig}}(i) - \bar{y}^{\mathrm{OFF}}_{\mathrm{sig}}(i)$, and its corresponding frequency spectrum. We can see this subtraction acts as a "lock-

in" measurement, thus suppressing the low-frequency noise. However, the harmonic peaks are still present and the beam pointing fluctuations are still large with a poor spatial resolution of about 1.3 μm.

Finally, the bottom plot shows the distribution of the signal $\Delta y(i)$, after correction of the beam pointing fluctuations. We can see that the latter are indeed well suppressed for each ON-OFF measurements, leading to an excellent spatial resolution of $\sigma_y(w_{RoI} = w/2) = 40.2 \pm 0.6$ nm, which is in agreement with the expected shot noise limit of 40 nm for the CCD 5.3 (Basler acA1300-60gm). The average value of the transverse shift in the dark output over 4000 measurements is then $\Delta y = \langle \Delta y(i) \rangle = 540 \pm 640$ pm, which is compatible with the expected zero value (no pump/probe interaction), with sub-nanometer accuracy. Moreover, the frequency spectrum is completely flat, indicating that the residual noise is purely stochastic as expected for the quantum shot noise of the CCD camera.

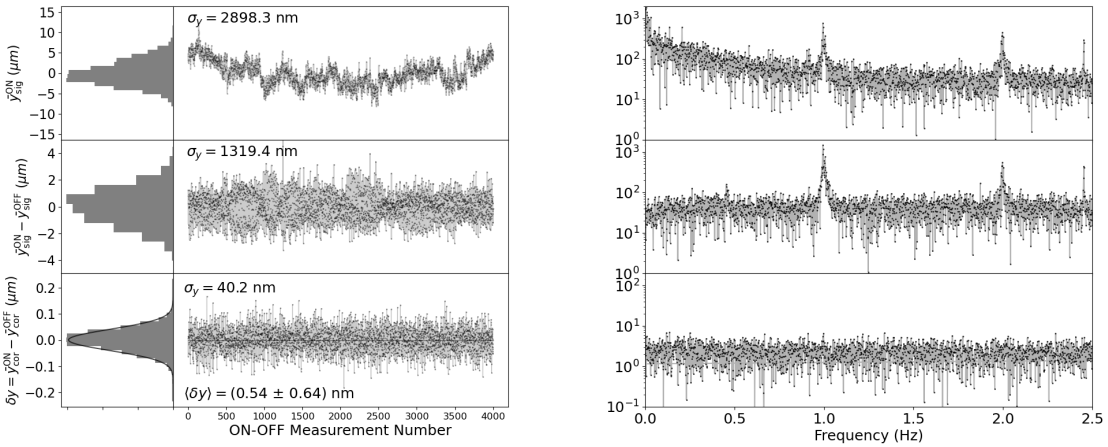

Figure 7.3: Measurement of the spatial resolution obtained with 8000 successive laser shots at 10 Hz (dataset 7, collected on January, the 16th, 2020). (Left) Distribution of the barycenters in intensity of the interference signal as a function of the ON-OFF measurement i (with $w_{RoI} = w/2$). Upper plot: Raw barycenter position for the OFF data $\bar{y}^{\mathrm{OFF}}_{\mathrm{sig}}(i)$ without any pointing correction. Middle plot: ON-OFF subtraction of the raw barycenter positions $\bar{y}^{\mathrm{ON}}_{\mathrm{sig}}(i) - \bar{y}^{\mathrm{OFF}}_{\mathrm{sig}}(i)$. Lower plot: corrected signal $\delta y(i)$, after beam pointing correction. The achieved spatial resolution is $\sigma_y(w_{RoI} = w/2) = 40.2 \pm 0.6$ nm and the average signal is $\Delta y = \langle \Delta y(i) \rangle = 540 \pm 640$ pm, which is compatible with the expected zero value. (Right) Corresponding frequency spectra.

In summary, we manage to reach the ultimate spatial resolution for the rectangular Sagnac interferometer (no focusing), at low amplification, which corresponds to the shot noise of the CCD camera. Moreover, the "ON-OFF" measurement method is very efficient at suppressing beam pointing fluctuations. However, we note that the ultimate shot noise resolution is achieved for a relatively small RoI ($w_{RoI} = w/2$) where the phase noise $\delta\phi_{noise}(y)$ is negligible. The

dependence of the spatial resolution as a function of the phase noise, and thus as a function of the RoI-size, is studied for the triangle interferometer with beam focus in the next sections.

7.4.2 Triangle interferometer with focusing and spatial filter (Prototype 2)

The spatial resolution measurements for the triangular Sagnac interferometer, namely with focusing and the spatial filter in the dark output (Prototype 2 presented in section 4.2) were carried out in the low and high amplification configuration. In this section is only presented the spatial results with the first configuration where the polarisation of the incident beam is slightly rotated using a half-wave plate before the interferometer. The second prototype configuration is much more sensitive to mechanical noise, and therefore more sensitive to air turbulence inside the laser clean room. It generates instabilities of the extinction pattern and thus disrupt the spatial resolution. This induces fluctuations of the phase noise pattern which deteriorates the spatial resolution (as previously discussed). That is why the resolution measurement presented here were carried out while the air conditioning in the laser clean room was shut off to reduce air turbulence, and also while the vacuum pumps close to the DeLLight vacuum chamber were shut off to reduce vibrations of the optical table.

The spatial resolution has been measured by recording 4000 successive laser shots (at a 10 Hz repetition rate, corresponding to approximately 7 minutes), corresponding to 2000 "fake ON-OFF measurements" with no interaction between pump and probe pulses. Measurements has been performed on September, the 23rd, 2022, dataset 6, using the CCD camera Basler acA1920-40gm (pixel size of 5.86 μm and saturation charge of 3×10^4 electrons per pixel). The expected shot noise, calculated by Monte-Carlo simulation (see chapter 6), is $\sigma_y \simeq 30$ nm.

Results are presented on figures 7.4 and 7.5. Similarly to the previous results for the first prototype, we can observe a typical $1/\nu$ drift noise at low frequency for the raw barycenters distribution $\bar{y}_{\mathrm{sig}}^{\mathrm{ON}}(i)$ (top plots on figure 7.5), but only one harmonic peak is visible at 2.4 Hz. The peaks at 1 and 2 Hz were suppressed thanks to the vacuum pumps that were shut off, as mentioned before. Moreover, the spatial resolution is rather large, at about 1.6 μm.

Then, just like in the previous section, the "ON-OFF" subtraction of the raw barycenter positions $\bar{y}_{\mathrm{sig}}^{\mathrm{ON}}(i) - \bar{y}_{\mathrm{sig}}^{\mathrm{OFF}}(i)$ nicely suppresses the low-frequency noise (middle plots). However, the harmonic peak at 2.4 Hz is still present and the beam pointing fluctuations are significantly reduced by a factor 10 compared to the raw signal, although with a spatial resolution equal to 1.4 μm, which is still more than an order of magnitude above the shot noise of the CCD camera.

Finally, the bottom plots show that the beam pointing fluctuations are well suppressed for "ON-OFF" measurements, with an excellent spatial resolution of $\sigma_y(w_{RoI} = w/2) = 32.5 \pm 0.7$ nm, which is very close to the expected CCD shot noise limit of 28 nm measured in section 6.4 for the CCD 5.86 (Basler acA1920-40gm). The average value of the transverse shift in the dark output over 2000 measurements is then $\Delta y = \langle \Delta y(i) \rangle = 0.89 \pm 64$ nm, which is compatible with the expected zero value (no pump/probe interaction), with sub-nanometer accuracy. Moreover, the flattened frequency spectrum indicates that the residual noise is purely stochastic as expected for the quantum shot noise of the CCD camera. Similarly as before, the

ultimate shot noise resolution is achieved for a relatively small region of interest ($w_{RoI} = w/2$) where the phase noise $\delta\phi_{noise}(y)$ is negligible.

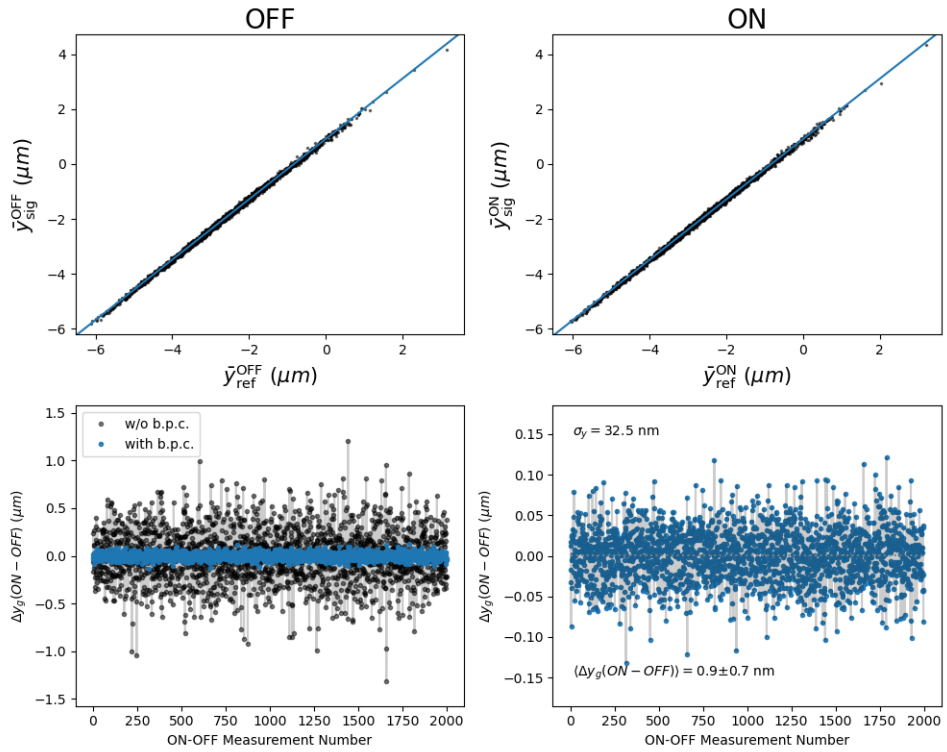

Figure 7.4: Same as figure 7.2 for data collected on September, the 23rd, 2022, dataset 6 (4000 successive laser shots at 10 Hz). The average signal is $\Delta y = \langle \Delta y(i) \rangle = 0.9 \pm 0.7$ nm compatible with zero when the pump is switched OFF, and a spatial resolution $\sigma_y = 32.5 \pm 0.7$ nm close to the shot noise of the CCD camera 5.86 (acA1920-40gm).

On the other hand, we emphasise that the spatial resolution highly depends on the RoI-size w_{RoI} chosen for the analysis, as explained in section 2.8. Indeed, the bigger the RoI-size is, the more noise is integrated, which then degrades the spatial resolution. If the RoI is too big, we also start to integrate the distribution tails of the back-reflections, thus skewing the interference signal barycenter measurements even further.

On figure 7.6, we present the spatial resolution σ_y as a function of the RoI-size w_{RoI}. The measured resolution is constant for a RoI-size $w_{RoI} < fwhm/2$ and equal to the expected shot noise resolution calculated by Monte-Carlo simulation, assuming only the shot noise of the CCD camera. For larger RoI-sizes, we observe a degradation of the spatial resolution. This degradation is in good agreement with the expected spatial resolution calculated by Monte-Carlo, where the mechanical noise has been added with the simulation parameters: $\sigma_\theta = 53$ nrad, $\delta\phi_0 = 200$ mrad, $L_{opt} = 35$ cm and $\delta a = \delta a_s = 0.55$. The mechanical noise parameter $\sigma_\theta = 53$ nrad is here correlated with the intrinsic phase noise $\delta\Phi_0$. However, the latter is constrained by its experimental estimation, using the fit of the Kerr measurements in

air depending on the relative polarisation between the probe and the pump, as will be explained in section 9.3.

The measurements presented here have been carried out with the closed vacuum chamber but with air still inside at atmospheric pressure. Same results have been obtained for dedicated measurements performed in vacuum, which confirms that the noise degrading the spatial resolution is not induced by the presence of air in the interferometer, but by its mechanical noise.

In summary, the ultimate spatial resolution limited by the shot noise of the CCD camera has been achieved for the triangular Sagnac interferometer with focalisation, at low amplification, for relatively small RoI-size $w_{RoI} < FWHM/2$. We observe a degradation of the spatial resolution for larger RoI-size, due to mechanical fluctuations of the optical mounts of the interferometer, for which the angular amplitude is about 50 nrad (r.m.s.).

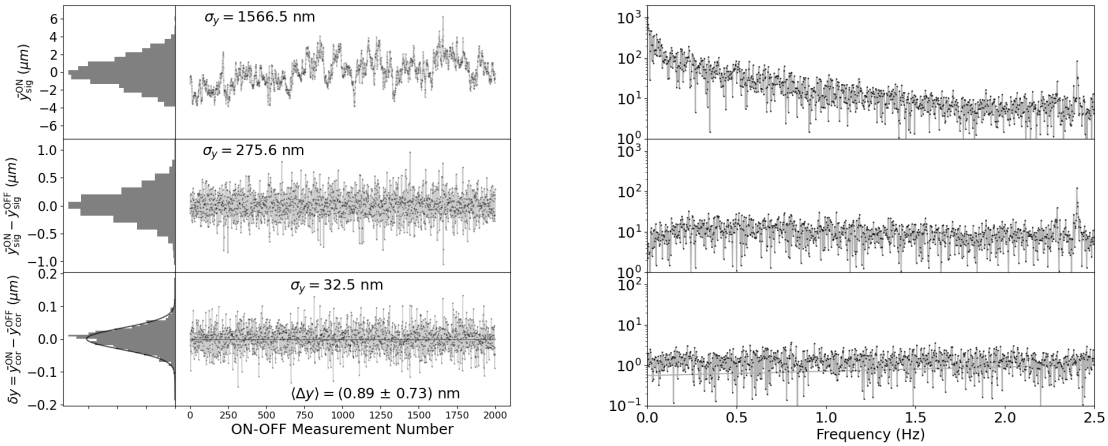

Figure 7.5: Same as figure 7.3 for data collected on September, the 23rd, 2022, dataset 6 (4000 successive laser shots at 10 Hz). The achieved spatial resolution is $\sigma_y(w_{RoI} = w/2) = 32.5 \pm 0.7$ nm and the average signal is $\Delta y = \langle \Delta y(i) \rangle = 890 \pm 730$ pm, which is compatible with the expected zero value. (Right) Corresponding frequency spectra.

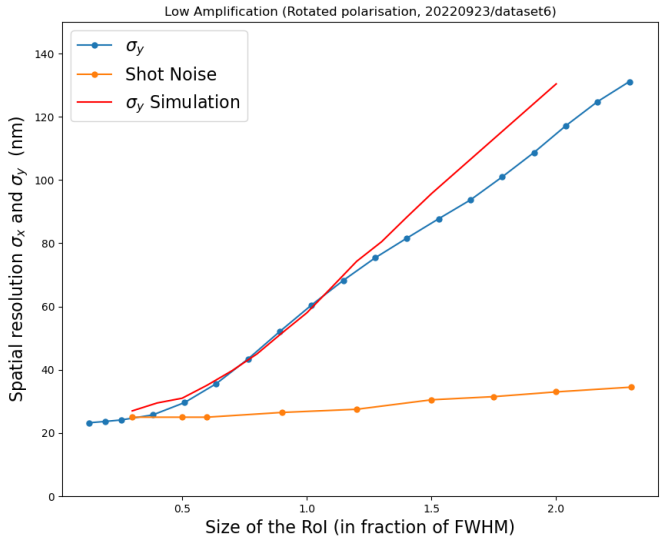

Figure 7.6: Spatial resolution depending on the RoI-size w_{RoI} (in FWHM w unit) for the triangular Sagnac interferometer with a spatial filter in the dark output in Configuration 1 (low amplification). (Blue plot) Spatial resolution in y-axis for data collected on September, the 23rd, 2022, dataset 6. (Red plot) Simulated spatial resolution with the following simulation parameters: $\delta\phi_0 = 200\,\text{mrad}$, $\sigma_\theta = 53\,\text{nrad}$, $L_{opt} = 35\,\text{cm}$ and $\delta a = 0.55$. (Orange plot) Shot noise of the CCD camera 5.86 (acA1920-40gm).

7.5 Measurement of the spatial resolution at high amplification

In this section, we present the spatial resolution measurements in the same experimental conditions as in the previous section, but with the second configuration at high amplification (amplification factor $\mathcal{A} = 25$) where the beamsplitter of the interferometer is rotated by about 1 degree in the horizontal plan, changing the incident angle of the laser pulse in the interferometer to 46°.

The spatial resolution has been measured by only recording 400 successive laser shots corresponding to 200 "fake ON-OFF measurements" with no interaction between pump and probe pulses. Measurements have been performed on September, the 26th, 2022, dataset 46, using the CCD camera Basler acA1920-40gm. The analysis results, performed with a RoI-size $w_{RoI} = fwhm/2$, are presented on figure 7.7. The average ON-OFF signal is $\Delta y = \langle \Delta y(i) \rangle = 19.9 \pm 13.1$ nm , which is compatible with zero. However, the spatial resolution is $\sigma_y = 185 \pm 13.1$ nm, which is more than an order of magnitude above the shot noise of the CCD camera (acA1920-40gm).

On figure 7.8, we present the spatial resolution σ_y as a function of the RoI-size w_{RoI} for data, and for Monte-Carlo simulations with the following parameters: $\sigma_\theta = 75\,\text{nrad}$, $\delta\phi_{noise} = 2\,\text{mrad}$,

$L_{opt} = 35\,\text{cm}$, $\delta a = \tilde{\delta a}_p = 0.02$. The value for $\delta\phi_{noise}$ has been chosen arbitrarily to a small value (10^{-2}) since its contribution is negligible at high amplification. Data and simulations are in good agreement up to $w_{RoI} \approx 1.25 \times w$ (for a larger RoI, there is a saturation effect of the spatial resolution of the data). We note that the noise is as expected amplified by a factor of the order of 10 in this high amplification configuration, as compared to the previous low amplification configuration.

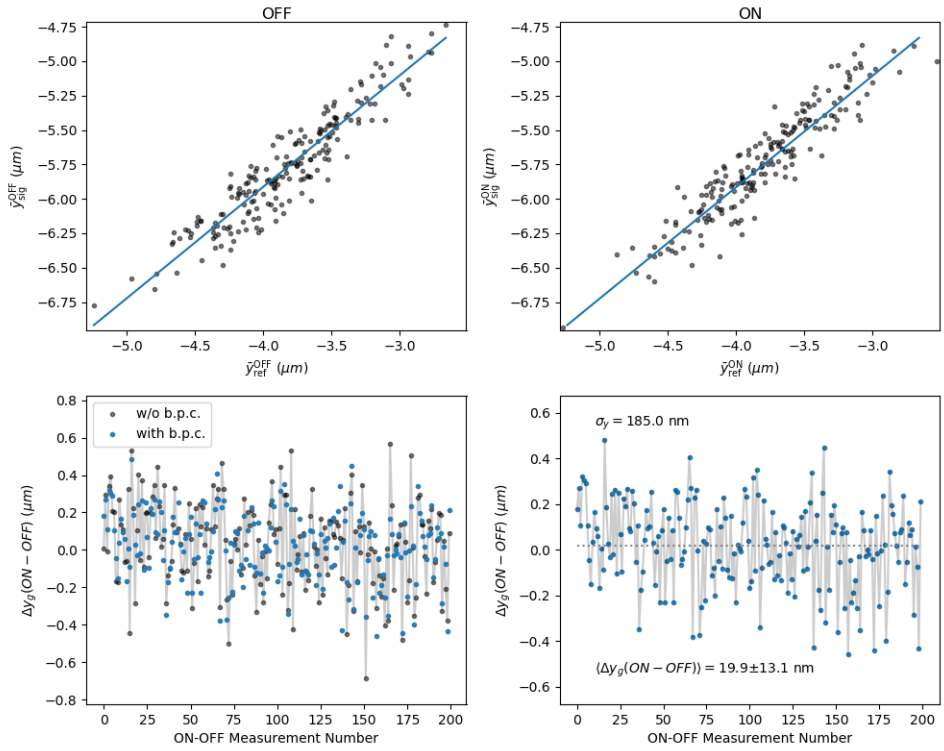

Figure 7.7: Same as figure 7.4 for data collected on October, the 26th, 2022, dataset 46 (400 successive laser shots at 10 Hz). The average signal $\Delta y = \langle \Delta y(i) \rangle = 19.9 \pm 13.1$ nm is compatible with zero (no pump), and the spatial resolution $\sigma_y = 185 \pm 13.1$ nm is more than an order of magnitude above the shot noise of the CCD camera 5.86 (acA1920-40gm).

In order to reach the shot noise resolution, while using a large RoI-size ($w_{RoI} = 1.5 \times w$, corresponding to an efficiency $\epsilon_s = 70\%$), the requested angular fluctuations must be of the order of $\sigma_\theta \approx 1$ nrad, i.e. a reduction of the mechanical noise by a factor of approximately 100. However, the current setup was not optimised to ensure low mechanical noise. We propose here some improvements to be implemented on the experimental setup during the next months to reduce the noise:

- To reduce vibrations on the Sagnac interferometer by isolating it from the optical table (currently very noisy) by placing it on a better isolated marble table, decoupled from the neighbouring devices around the DeLLight experimental setup in the LASERIX laser room.

- To reduce vibrations of the optical mounts of the beamsplitter and one of the interferometer mirrors. Indeed, they are currently mounted on Polaris piezo mounts (Thorlabs POLARIS-K1S2P), which are very stable, but are powered using rigid cables which vibrate and generate noise, thus would need to be mechanically isolated.
- To suppress electronic noise coming from the power supplies of these same Polaris piezo, by using batteries instead which do not generate any electronic noise.
- To reduce mechanical noise caused by the lens in the interferometer by using a fixed mount instead of a 2D piezo translation as is currently used for alignment purposes.

In summary, unlike the low amplification configuration, we cannot reach the shot noise of the CCD camera yet at high amplification for the triangular Sagnac interferometer (with focusing). Indeed, any mechanical noise is also amplified and is no longer negligible, thus degrading the spatial resolution. We present in the next section a method to suppress this noise.

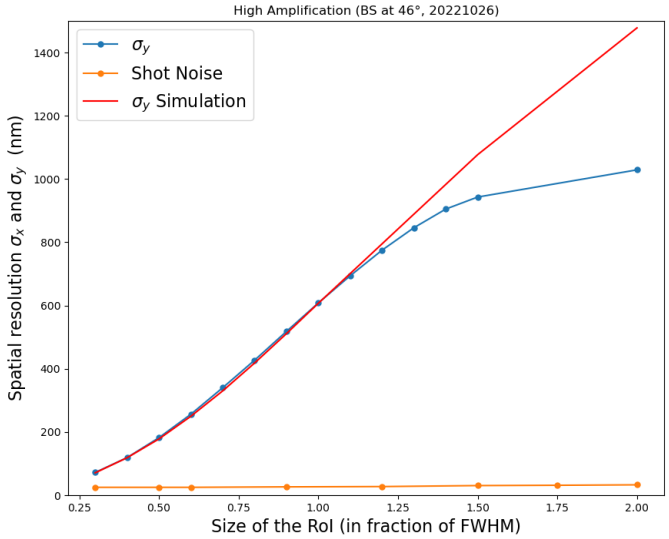

Figure 7.8: Same as figure 7.6 in Configuration 2 (high amplification), for data collected on October, the 26th, 2022, dataset 46. The simulation parameters are: $\delta\phi_0 = 2$ mrad, $\sigma_\theta = 75$ nrad, $L_{opt} = 35$ cm and $\delta\tilde{a}_p = 0.02$.

7.6 High frequency phase noise suppression

Inspired by the method of monitoring and suppression of the beam pointing fluctuations, we propose here a similar way to monitor and suppress the phase noise which currently limits the spatial resolution.

The principle, illustrated by the scheme on figure 7.9, is first to split the incident pulse before entering the Sagnac interferometer into two identical daughter pulses. By injecting the

second pulse in the interferometer with a delay of a few nanosecond, it will not be deflected by the pump in the interaction area but will travel through the same optical path as the probe and thus undergo the same phase noise. Indeed, a 10 ns delay corresponds to a noise frequency of 100 MHz. However, this second delayed pulse must be readout separately, on a second CCD camera. To this end, we propose to use a Pockels cell and a polarised mirror to distinguish the first interference signal (including the interaction with the pump) from the second interference signal (without pump interaction, used only to monitor the interferometer phase noise).

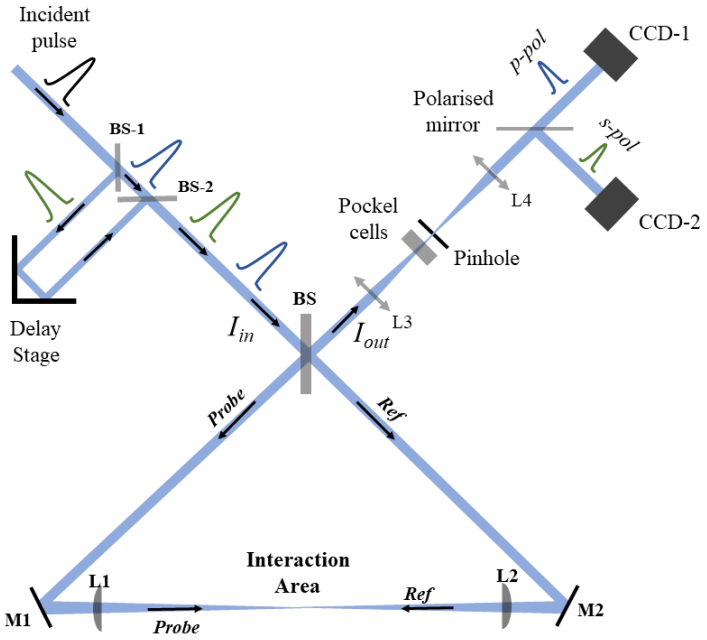

Figure 7.9: Schematic of the experimental setup for phase noise monitoring, for an off-line suppression. The incident pulse (black) is splitted by the beamsplitter (BS-1) into a first unmodified pulse (blue) and a delayed one (green) by 10 ns. Both interference signals in the dark output pass through a telescope (composed of lenses L3 and L4) with a spatial filter (Pinhole) and a Pockels cell at focus. Each signal then pass through a polarised mirror to then be collected by two CCD cameras: the first interference signal (interaction with the pump) is collected on CCD-1 and the second delayed one is collected on CCD-2.

As illustrated on figure 7.9, the incident pulse is first splitted by a beamsplitter (BS-1) into two secondary pulses (green and blue pulses in the figure). Both pulses are thus *p*-polarised. The secondary pulse (green) is delayed by approximately 10 ns. Then, both pulses enter the Sagnac interferometer but since the delayed pulse does not interact with the pump pulse, it is therefore not refracted. We use a Pockels cell in the dark output in order to change the polarisation of the delayed interference signal only. It is placed close to the pinhole of the spatial filter in the Rayleigh range of the focalisation of the afocal telescope (composed of lenses L3 and L4). Finally, a polarised mirror is placed after the lens L4, with total transmission for *p*-polarised beam and total reflection for *s*-polarisation (a polarimeter can be added in order to increase the efficiency). The Pockels cell is first adjusted for a *p*-polarisation output and the

first interference signal (blue) is recorded by the camera CCD-1. Then, a high voltage is applied to the Pockels cell for a half-wave rotation. Thus, the delayed interference signal (green), unmodified by the pump, is rotated to *s*-polarisation and recorded by the camera CCD-2.

This on-line monitoring method of the phase noise is currently being developed on the DeLLight experimental setup.

7.7 Summary

In summary, the ultimate spatial resolution limited by the shot noise of the CCD camera has been achieved for the triangular Sagnac interferometer with focalisation but with the low amplification configuration when a small *s*-polarisation is added in the probe pulse. However, in the high amplification configuration (with pure *p*-polarisation), the spatial resolution is degraded, due to the amplification of a phase noise induced by mechanical noise of the optical mounts inside the interferometer. Monte-Carlo simulations show that this noise corresponds to an angular fluctuation of the optical mounts of the order of $\sigma_\theta \simeq 50$ nrad (r.m.s.). The vibration isolation of the interferometer is currently of poor quality and can be improved in the future. We also propose a high frequency phase noise monitoring method in order to suppress that noise and to reach the ultimate shot noise spatial resolution.

Chapter 8

Measurement of the optical Kerr signal in silica with low energy pump pulses (prototype 1)

The first DeLLight prototype, a rectangular interferometer without focalisation of the beam (described in section 4.1), has been used to verify that we could detect a deflection signal due to a change of index in a silica plate, induced by a low pump energy by optical Kerr effect. We also wanted to verify that the measured signal is proportional to the pump energy.

The Kerr measurements in silica were fulfilled from April to December in 2019 in the first stages of the experimental work, and were more difficult to achieve and less efficient in terms of data collection, hence why so few statistics were collected. Moreover, the beam-pointing fluctuations were rather high because of the experimental conditions (interferometer far from the laser source and unstable optical table), thus exacerbating the alignment drifts and un-reproductibility of the measurements.

In this chapter, we present the results of the Kerr measurements in a NBK-7 silica plate (Thorlabs WG10530-B).

8.1 Probe and pump intensity profiles in the interaction area

Before performing Kerr measurements in silica, we first characterise the probe and pump profiles in the interaction area in order to optimise their spatial and temporal overlap, and to measure their transverse intensity profiles. In order to do that, the intensity of the incident beam is strongly reduced using neutral densities, placed before the pump/probe splitting (BS-1 on figure 4.1). Then, the intensity profiles are collected on a CCD camera (Basler acA1300-60gm, pixel size: $5.3 \times 5.3\,\mu m^2$), placed instead of the silica slide (Si) in the interaction area. The longitudinal position of the lens (L-1) used to focalise the pump beam is then adjusted to minimise the transverse size of the intensity profile of the pump, using the mirror M-4.

On figure 8.1 are shown the intensity profiles of the probe and pump pulses in the interaction area. Their profiles are fitted to Gaussian profiles (see equation 6.2), in a similar fashion as

done in section 6.1.2. Their respective transverse vertical w_y and horizontal w_x waists are:

$$\begin{aligned} w_x(\text{pump}) &= 564.8\ \mu\text{m} \\ w_y(\text{pump}) &= 509.3\ \mu\text{m} \\ w_x(\text{probe}) &= 797.6\ \mu\text{m} \\ w_y(\text{probe}) &= 751.2\ \mu\text{m} \end{aligned} \tag{8.1}$$

which correspond to beam sizes at FWHM:

$$\begin{aligned} FWHM_x(\text{pump}) &= 663.6\ \mu\text{m} \\ FWHM_y(\text{pump}) &= 598.4\ \mu\text{m} \\ FWHM_x(\text{probe}) &= 937.2\ \mu\text{m} \\ FWHM_y(\text{probe}) &= 882.7\ \mu\text{m} \end{aligned} \tag{8.2}$$

As we can see, the probe size (FWHM) was chosen at approximately $w_{probe} \approx 1.5 \times w_{pump}$.

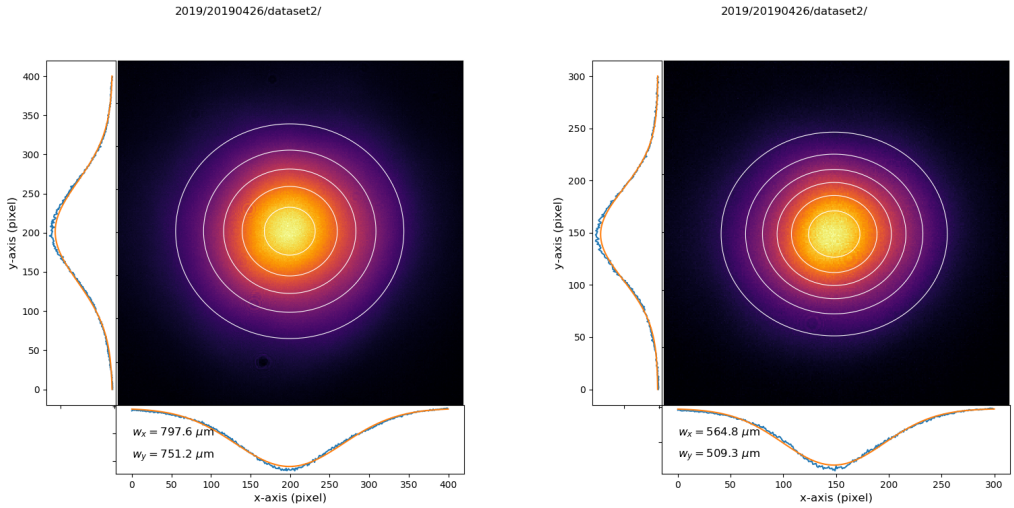

Figure 8.1: CCD images of the intensity profiles of the probe (left) and the pump (right) in the interaction area in the Sagnac interferometer. A 2-dimensional Gaussian fit delivers the beam waists in x and y-direction (dataset 2, collected on April, the 26th, 2019).

8.2 Probe/pump synchronisation and alignment of the Sagnac interferometer

The temporal synchronisation of the pump and probe is adjusted by using a delay line on the probe (MDS-1 on figure 4.1) until apparition of interference fringes in the interaction area, as described in more details in section 4.1.2.

The spatial overlap of the pump and probe is adjusted by using the mirror M-4, in order to have an optimal impact parameter between the two as close to its optimal value b_{opt} as

possible, at which the Kerr signal is maximal. This optimal impact parameter is defined by (see equation 2.5):

$$b_{opt} = \frac{\sqrt{w_y^2(\text{probe}) + w_y^2(\text{pump})}}{2} \tag{8.3}$$

Considering the transverse pump and probe sizes measured in the previous section, the optimal impact parameter is $b_{opt} \approx 454\,\mu$m, which is a little below the pump waist at focus.

Moreover, the alignment of the Sagnac interferometer in the rectangular configuration is described in section 4.1.2, and the extinction is adjusted to its optimum (measurements described in section 5.2). Then, before carrying out Kerr measurements, we turn the half-wave plate (WP on figure 4.3) located on the probe path in order to reveal the interference signal in the dark output, with approximately the same intensity as for the back-reflections (as described in section 7.2.2).

8.3 Kerr measurements in silica

The data collection process consists of taking multiple datasets of CCD images (200 images per dataset, i.e. 20 seconds of data collection) at different pump energy, using a variable neutral density (V-ND on figure 4.1), to see the evolution of the Kerr signal Δy in the vertical y-axis as a function of the pump energy $\mathcal{E}_{pump}$. On the data presented in this section, the duration of the pump and probe pulses is about 100 fs and the pump energy varies from $\mathcal{E}_{pump} \approx 0.1$ to $2.2\,\mu$J, which corresponds to peak intensities around $I_{pump} \approx 5 \times 10^8$ to 10^{10} W/cm^2 in the interaction area, for a pulse duration of $\tau = 100$ fs.

On figure 8.2 is shown a summary of a Kerr measurement in silica obtained for a pump energy of $\mathcal{E}_{pump} \approx 2.2\,\mu$J and a RoI equal to approximately $w_{RoI} \approx w_{pump}$, using the analysis method described in section 3.3.3. More specifically, the lower plot on the right shows the distribution of the ON-OFF measurements, corresponding to a vertical shift in the dark output due to the Kerr effect of $\Delta y = \langle \Delta y(i) \rangle = 1471.8 \pm 13.4$ nm, with a statistical error of $\sigma_y = 133.9$ nm (r.m.s.).

On figure 8.3 is displayed the evolution of the Kerr signal Δy, as a function of the pump energy in the interaction area. The linear correlation is as expected since the change of index induced by the pump by optical Kerr effect is proportional to the intensity of the pump ($\Delta n_K = n_{2,\text{Si}} \times I_{pump}$), as seen in section 2.1. It is worth noting that a positive signal has been successfully measured at very low energy ($\mathcal{E}_{pump} = 100$ nJ, $I_{pump} \approx 5 \times 10^8$ W/cm^2). The corresponding optical index change caused by the Kerr effect at this intensity is $\Delta n_K = n_{2,\text{Si}} \times I_{pump} \approx 10^{-7}$, showing that our instrument is very sensitive. Moreover, we verify the absence of off-set or artefact (caused by the diffusion of the pump light for instance) by measuring the deflection signal with the pump pulse very delayed in time compared to the probe pulse. It was done by inserting a silica plate in the pump beam before sending the pump pulse to the interaction area. For this dedicated run, we measured $\Delta y \approx -2.6 \pm 11$ nm, in agreement with a null signal as expected.

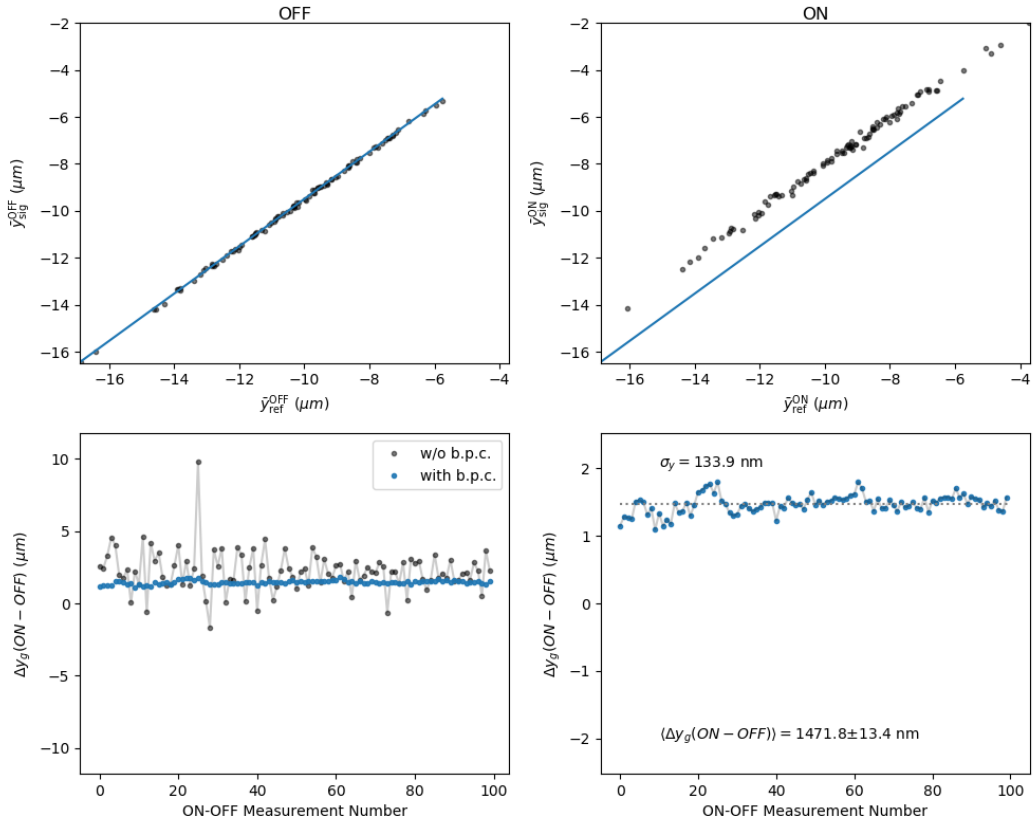

Figure 8.2: Summary of the data analysis, calculated along the vertical y-axis, for a Kerr measurement with a pump energy of $\mathcal{E}_{pump} \approx 2.2\,\mu$J. (Upper plots) Correlation of the barycenters in intensity of the interference signal $\bar{y}_{\mathrm{sig}}(i)$ and the back-reflection $\bar{y}_{\mathrm{ref}}(i)$. The data is shown as black points, for both OFF (left panel) and ON (right panel) measurements, while the result of the linear fit obtained using the OFF data only is shown in both panels as a blue line. (Lower plot, Left) Distribution of the ON-OFF subtraction, in grey of the raw barycenter positions $\bar{y}^{\mathrm{ON}}_{\mathrm{sig}}(i) - \bar{y}^{\mathrm{OFF}}_{\mathrm{sig}}(i)$, and in blue after beam pointing correction $\Delta y(i) = \bar{y}^{\mathrm{ON}}_{\mathrm{corr}}(i) - \bar{y}^{\mathrm{OFF}}_{\mathrm{corr}}(i)$. (Lower plot, Right) Distribution of the ON-OFF subtraction after beam pointing correction $\Delta y(i)$, for which the mean value $\Delta y = \langle \Delta y(i) \rangle = 1471.8 \pm 13.4$ nm corresponds to the DeLLight signal and the standard deviation $\sigma_y = 133.9$ nm corresponds to the spatial resolution (dataset 14, collected on May, the 15th, 2019).

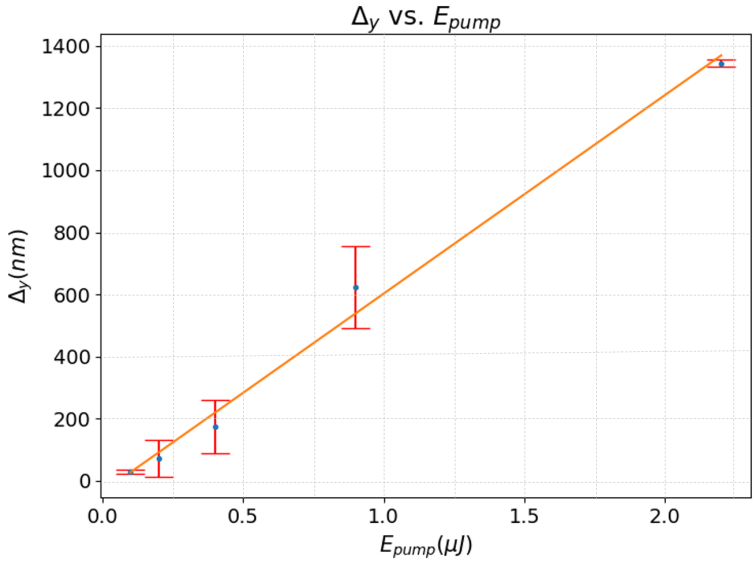

Figure 8.3: Evolution of the vertical displacement Δy (nm) of the intensity profile of the interference signal in the dark output of the Sagnac interferometer, for different pump energies $\mathcal{E}_{pump}$ (μJ). Data are in red and the linear fit is in orange.

8.4 Summary

In summary, we showed that, through interferometric measurements, we managed to significantly detect the change of index induced by the pump by optical Kerr effect in silica ($\Delta n_K \approx 10^{-7}$ in 20 seconds of data collection for $I_{pump} \approx 5 \times 10^8$) at low and moderately high pump intensities (pulse duration of 70 fs):

$$\begin{aligned} \Delta y &= 1471.8 \pm 13.4 \text{ nm} \quad \text{for } I_{pump} \approx 10^{10} \text{ W/cm}^2 \\ \Delta y &= 100 \pm 6 \text{ nm} \quad \text{for } I_{pump} \approx 5 \times 10^8 \text{ W/cm}^2 \end{aligned} \tag{8.4}$$

Thus, we managed to measure a significant transversal shift Δy, even at low intensities, which shows the good sensitivity of our instrument.

Chapter 9

Measurement of the optical Kerr signal in air with low energy pump pulses

The Kerr measurements in air, obtained with the triangular configuration of the Sagnac interferometer with focalisation (Prototype 2), are essential to validate the experimental setup of the DeLLight experiment, the measurement protocols and the "ON-OFF" subtraction technique used to obtain the DeLLight deflection signal.

In this chapter, we first present the measurement of the pump and probe intensity profiles at focus in the interaction area. Secondly, we present the 3D numerical simulations used to compute the expected DeLLight deflection signal. Then, we show the Kerr measurement results obtained in the low amplification configuration of the interferometer (rotated polarisation of the probe). Finally, we present the Kerr measurement results obtained in the high amplification configuration (rotated interferometer beamsplitter), which constitutes a proof of concept of the DeLLight experiment.

9.1 Probe and pump transverse intensity profiles at focus in the interaction area

In this section, we characterise the probe and pump intensity profiles in the interaction area. The goal is first to measure the transverse intensity profiles of both pulses at focus, then to optimise their spatial and temporal overlap and measure the tilt angle θ_{tilt} between the propagation axis of the pump and that of the probe (see figure 2.2). The relative position fluctuations between the beams at focus and their longitudinal waist variations are also studied.

9.1.1 Measurement of the probe and pump transverse intensity profiles at focus in the interaction area

In order to measure the probe and pump transverse intensity profiles at focus, the intensity of the incident beam is first strongly reduced by neutral densities, before being splitted into the pump and probe beams by the beamsplitter BS-2. A mirror, inserted between the focusing

lens of the probe (L-1) and the interaction area at focus, reflects the probe and pump beams before focalisation, which are then collected on an off-axis high resolution CCD camera with a small pixel size (Basler acA3088-16gm, pixel dimension: $1.86 \times 1.86\ \mu m^2$). The CCD camera is first placed at the focus point of the probe beam where the width of its transverse intensity profile is minimum. The longitudinal position of the CCD camera is then referred to as the position $z = 0$. The longitudinal position of the lens used to focalise the pump beam (L-3) is then adjusted in order to minimise the width of the transverse intensity profile of the pump. Finally, the intensity profiles of the probe and pump pulses are superposed.

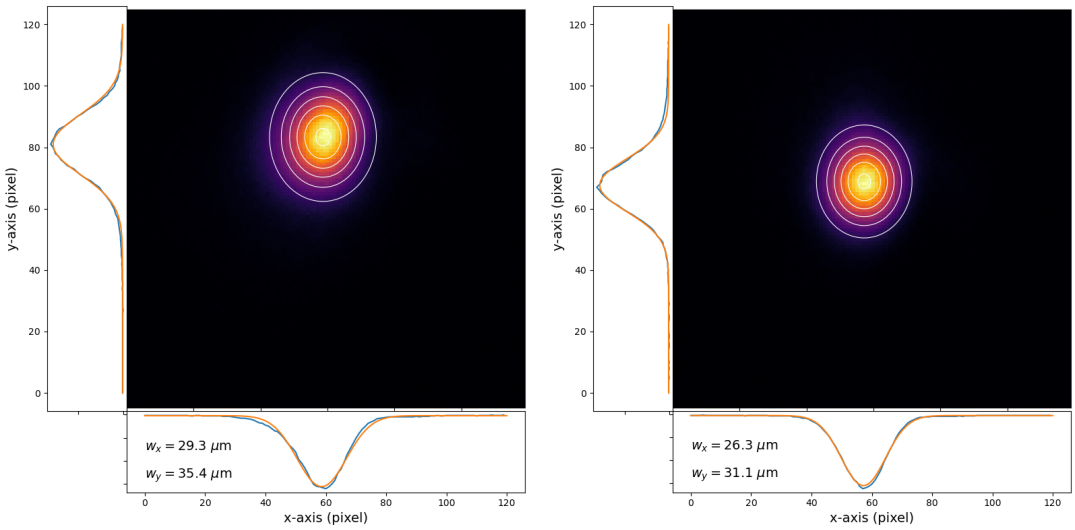

Figure 9.1: CCD images of the intensity profiles in the interaction area of the probe (left) and the pump (right) in the Sagnac interferometer. A 2-dimensional Gaussian fit delivers the beam waists in x and y-direction (collected on December, the 22th, 2021).

Figure 9.1 shows an example of the pump and probe intensity profiles recorded at focus at $z = 0$. For each pulse, a two-dimensional Gaussian profile (from equation 6.2) is fitted to the data in order to measure the transverse horizontal w_x and vertical w_y waists at focus of both pump and probe. The profiles at focus are well fitted by these Gaussian profiles and the minimum waists at focus are:

$$\begin{aligned} w_x(\text{pump}) &= 26.3\ \mu m \\ w_y(\text{pump}) &= 31.1\ \mu m \\ w_x(\text{probe}) &= 29.3\ \mu m \\ w_y(\text{probe}) &= 35.4\ \mu m \end{aligned} \tag{9.1}$$

The width (FWHM) of each beam is then proportional to their waist w, such as: $FWHM = 1.18 \times w$. In practice, for all measurements fulfilled with Prototype 2, the probe and pump sizes range from approximately 25 to 36 μm at focus in the interaction area.

9.1.2 Spatial overlap and time coincidence of the pump and probe pulses and measurement of the tilt angle

Now that both pump and probe pulses are longitudinally positioned at focus ($z = 0$), we can adjust their spatial overlap. The pump pulse is first vertically shifted with respect to the probe pulse in order to adjust the impact parameter b as close to its optimal value b_{opt}, at which the DeLLight deflection signal is maximal. From equations 8.3 and 9.1, we have an optimal value at $b_{opt} = 23.6\ \mu$m, where the experimental value is $b = 23.9\ \mu$m. Thus, the data are collected with the optimal impact parameter and the expected signal will be maximal.

Then, using the D-shaped mirror (M-3) placed on the pump path, we tilt the pump pulse in the horizontal direction until reaching its spatial overlap with the probe pulse in the interaction area (horizontal position difference null). Finally, the delay stage of the pump pulse (MDS-1) is adjusted until measuring interference fringes with maximal contrast on the CCD camera, which corresponds to the time coincidence between the probe and pump pulses. Figure 9.2 shows the spatial overlap of both pulses in time coincidence, which is portrayed by the interference fringes.

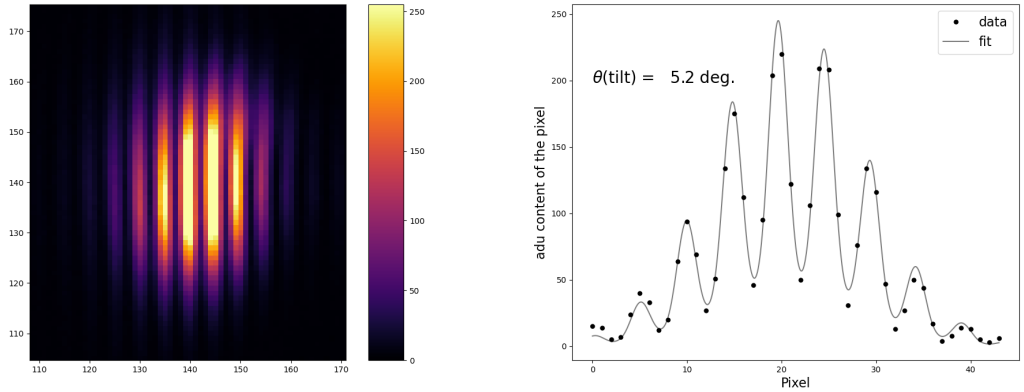

Figure 9.2: (Left) CCD image of the resulting intensity profile of the pump and probe at focus ($z = 0$) showing their space-time overlap, with the interference fringes. (Right) Corresponding intensity profile in ADU content, as a function of the pixel number. Data are showed in black dots and the result of the fit of the fringes is showed in grey line (collected on December, the 22th, 2021).

In order to calculate the tilt angle θ_{tilt} between the pump and probe pulses, the horizontal intensity profile $I(x, y = 0)$ of the interference fringes, shown on figure 9.2, is fitted by the following function:

$$I(x, y = 0) = a \times \left(b + \sin\left(\frac{2\pi x}{i} + \phi \right) \right)^2 \times \exp\left(-\frac{2(x - x_0)^2}{w_x^2} \right) \tag{9.2}$$

The fitted value for the interfringe distance is $i = 8.9 \pm 0.5\ \mu$m. It corresponds to a tilt angle

between the pump and probe beams of $\theta_{\text{tilt}} = \lambda/i = 5.2 \pm 0.9$ degrees. We also crosschecked this value with a simple pointing measurement.

9.1.3 Fluctuations of the probe and pump positions at focus

The pump and probe pulses are delivered (via the beamsplitter BS-2) from the same incident beam. Their beam pointing fluctuations are therefore correlated. As a consequence, the relative position fluctuations of the pump and probe intensity profiles at focus must be negligible. In order to test that out, we record a dedicated set of measurements of the pump and probe intensity profiles at focus during 50 minutes (3000 events with an acquisition rate of 1 Hz).

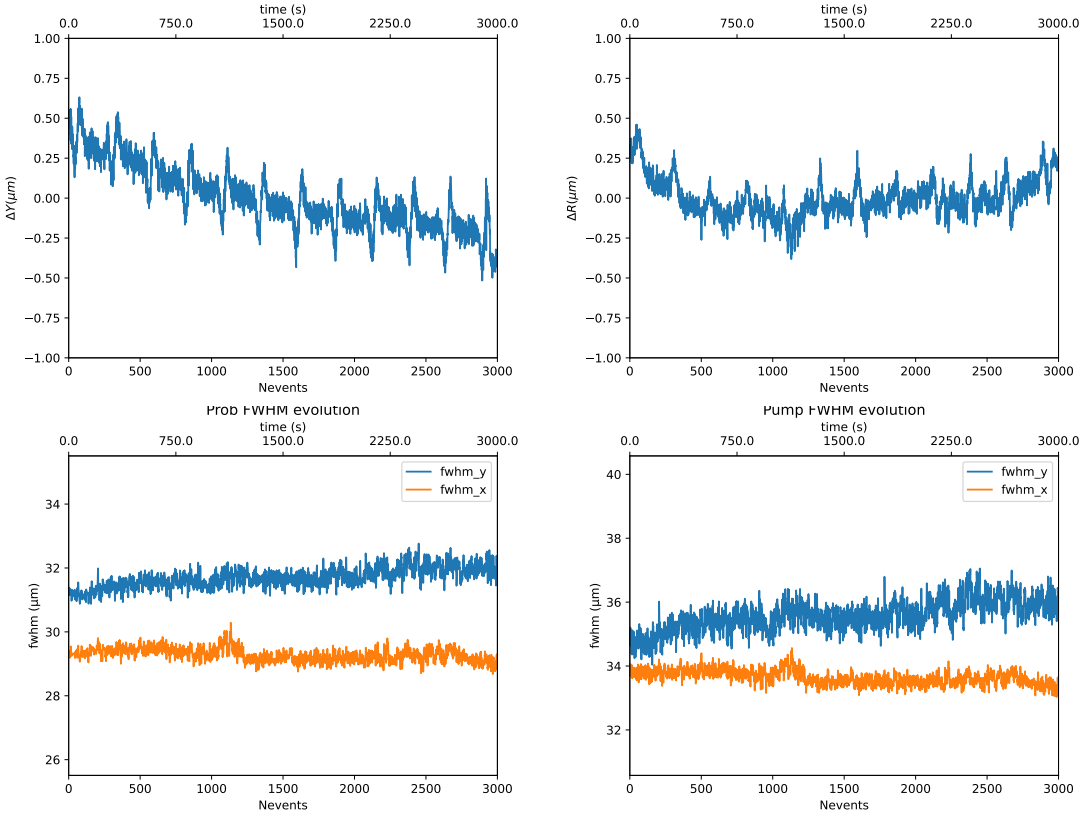

Figure 9.3: (Top left) Variation of the impact parameter b_{mes} which corresponds to the relative vertical positions of the probe (Y_g^{Probe}) and pump (Y_g^{pump}) pulses at focus in the interaction area, as a function of time: $b_{mes} = Y_g^{pump} - Y_g^{Probe}$; (Top right) Variation of the relative radial distance $\Delta R = \sqrt{(X_g^{pump} - X_g^{Probe})^2 + (Y_g^{pump} - Y_g^{Probe})^2}$ between pump and probe at focus, as a function of time; (Bottom) Evolution of the FWHM of the probe (left) and pump (right) pulses at focus over time, in the x (orange) and y-directions (blue), as a function of time.

Figure 9.3 shows the variation of the relative vertical positions of the two beams at focus (i.e. the impact parameter), $b_{mes} = Y_g^{pump} - Y_g^{Probe}$, and the corresponding relative radial

distance $\Delta R = \sqrt{(X_g^{pump} - X_g^{Probe})^2 + (Y_g^{pump} - Y_g^{Probe})^2}$, as a function of time. A vertical drift of the relative vertical position between pump and probe of about 750 nm is measured after 50 minutes of data collection, corresponding to approximately 3 μm after about 3 hours, which is typically the duration of a measurement campaign for DeLLight measurements in air. It is one order of magnitude smaller than the waist of the pulses at focus, which are $w_0(\text{pump}) \approx w_0(\text{probe}) \approx 25 - 36\,\mu\text{m}$ (see section 9.1.1). This drift is therefore negligible. The same goes for the 500 nm amplitude picks at 4 mHz that we can see on the first plot: they are also completely negligible compared to the waists at focus. Moreover, the relative radial distance ΔR between the pump and the probe is relatively stable with fluctuations of the order of 500 nm (r.m.s.), which is also negligible. Finally, we verify on figure 9.3 (lower plots) that the widths (FWHM) of the beams at focus are stable over time with fluctuations lower than 1 μm (r.m.s.).

In conclusion, we can consider that the spatial overlap of the pump and probe pulses at focus is stable and cannot introduce any variation of the induced deflection signal in the interferometer.

9.1.4 Longitudinal variation of the pump and probe waists around the interaction area

In order to study the longitudinal variation of the pump and probe waists during their interaction, the CCD camera is longitudinally translated (via a manual micrometric translation stage) along the bisector of the two beams, forward and backward.

We note z the longitudinal position of the CCD camera, with $z = 0$ the position at focus. For a waist at focus $w_0 \approx w_0(\text{probe}) \approx w_0(\text{pump})$, the longitudinal distance z_{max} up to which the pump and the probe pulses overlap transversely (at half of the waist) is of the order of $z_{max} \simeq w_0/\theta_{\text{tilt}} \simeq 330\,\mu\text{m}$, where the tilt angle θ_{tilt} has been calculated in section 9.1.2. Therefore, we study the longitudinal variation of the pump and probe waists by moving the CCD camera by steps of $\Delta z = 100$ μm from -500 μm to $+500$ μm. For each z longitudinal position, two independent two-dimensional Gaussian profiles (defined in equation 6.2) are fitted to the data in order to measure the transverse horizontal w_x and vertical w_y waists of the pump and probe pulses. Results of the measured waists as a function of the longitudinal position z are displayed on figure 9.4. Their longitudinal variation is in relatively good agreement with the expected longitudinal variation of the minimum waist for a Gaussian beam given by the relation $w(z) = w_0\sqrt{1 + (z/z_0)^2}$, where w_0 is the minimum waist at focus and $z_0 = \pi w_0^2/\lambda \simeq 3.5$ mm is the Rayleigh length. The difference between the measured and expected waist at focus is about 5% at most, which corresponds to a difference for the DeLLight signal of 15% since the latter is inversely proportional to the waist cube (see equation 2.48). This 15% systematic error is negligible as compared to the systematic error introduced by the phase noise uncertainty, as discussed afterwards.

Moreover, we verify that the measured impact parameter b_{mes} between the pump and probe (defined in the previous section) is relatively constant along the longitudinal interaction area (from $z = -500$ μm to $z = +500$ μm) and varies by less than ± 2 μm, corresponding to a variation of the deflection signal $\langle \delta\theta_y \rangle$ lower than 10% which is negligible (see figure 4 in [31],

showing $\langle \delta\theta_y \rangle$ as a function of the impact parameter).

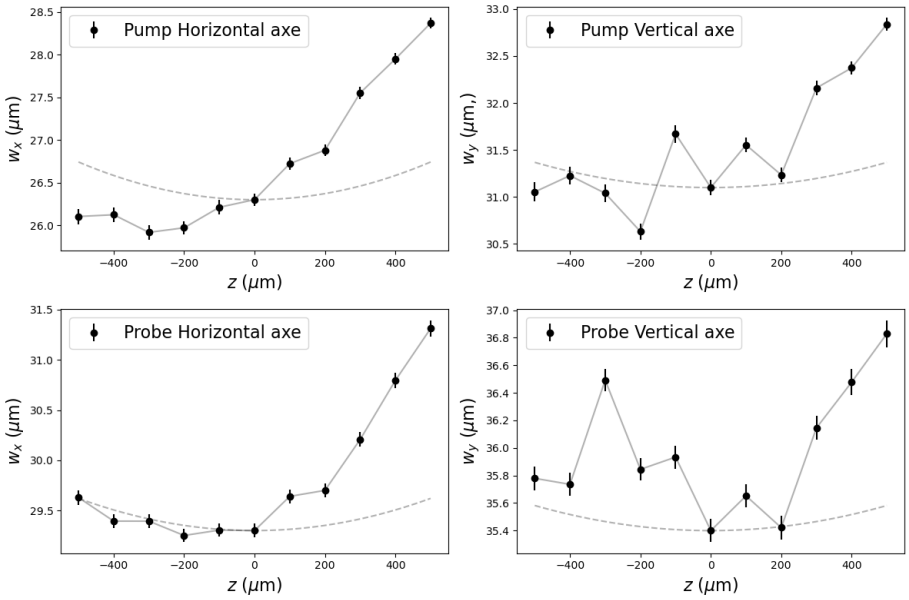

Figure 9.4: Evolution of the pump (top) and probe (bottom) waists at focus in x (left) and y-directions (right), as a function of the longitudinal z position of the CCD camera used for spatio-temporal synchronisation in the interaction area (with $z = 0$, the position at focus). The dashed lines correspond to the expected waist at focus for an ideal Gaussian beam (data collected on January, the 24th, 2022).

9.2 Numerical simulation of the expected signal in the dark output of the interferometer

In this section, we calculate the expected DeLLight deflection signal in a gas with co-propagating pump and probe pulses, using 3D numerical simulation developed by Scott Robertson [34]. The simulation takes into account both the Kerr effect induced by the pump in the interferometer and the contribution of the induced plasma index in the interaction area (see section 2.10.1).

9.2.1 Maximal intensity of the pump pulse in the interaction area

The intensity profiles of the pump and probe pulses are described by a Gaussian profile, given by:

$$I(x,y,t) = I_0 \exp\left(-\frac{2x^2}{w_x^2}\right) \exp\left(-\frac{2y^2}{w_y^2}\right) \cos^2(\omega t) \exp\left(-\frac{4\ \ln(2)\ t^2}{\tau^2}\right) \tag{9.3}$$

where w_x and w_y are the transverse horizontal and vertical waists, and τ is the duration (FWHM) of the pulse. Experimentally, we measure the total energy $\mathcal{E}$ of the pulse, defined by:

$$\mathcal{E} = \int\int\int_{-\infty}^{+\infty} I(x,y,z)\, dxdydz = \frac{\pi\sqrt{\pi}}{8\sqrt{\ln 2}} w_x w_y \tau \times I_0 \tag{9.4}$$

Thus, the maximal peak intensity for a Gaussian pulse is:

$$I_0 = \frac{8\sqrt{\ln 2}}{\pi\sqrt{\pi}} \frac{\mathcal{E}}{w_x w_y \tau} = 1.2 \times \frac{\mathcal{E}}{w_x w_y \tau} \tag{9.5}$$

For a pulse duration $\tau \simeq 100$ fs, and a waist of the pump at focus in the interaction area $w_0(\text{pump}) = 31.1\ \mu$m (see equation 9.1), the maximal pump peak intensity at focus is: $I_0 = 1.2\ (\text{TW/cm}^2) \times \mathcal{E}(\mu\text{J})$ (as we will see in section 9.3).

9.2.2 Contribution of the nonlinear Kerr index in air at higher orders

Up until now, we only treated the optical Kerr index Δn_K at first order, i.e. with Δn_K directly proportional to the laser pulse intensity I (in W/cm^2), such as: $\Delta n_K = n_2 \times I$, with the Kerr index n_2 in cm^2/W. However, it has been measured in various gas that, at higher intensities, a strong negative contribution with a higher non linearity appears, which leads to an overall negative nonlinear Kerr refractive index [30]. For instance in air, the Kerr index becomes negative for intensities above 34 TW/cm^2. Although not yet understood, this change of behaviour could be recognised as a saturation effect at high intensity. To take into account this possible non linear behaviour, the Kerr index is developed at higher order, such as:

$$\Delta n_K = n_2 I + n_4 I^2 + n_6 I^3 + n_8 I^4 + ... \tag{9.6}$$

Therefore, in the numerical simulations of the expected signal, we use values of the higher order indices up to n_8, given in [30], where the first order Kerr index in air is $n_2 = (1.2 \pm 0.3) \times 10^{-19}$ cm^2/W.

9.2.3 Contribution of the plasma induced by the pump in the interaction area

For the contribution of the plasma index, we consider the ionisation rate of oxygen and nitrogen calculated by Couairon and Mysyrowicz [35], and computed from the full Keldysh-PPT formulation with a determined pre-factor for diatomic molecules developed by Mishima et al. [36]. The generalised Keldysh–PPT formula describes the ionisation rate of a gas in the multi-photon regime (below $\simeq 10^{13}$ W/cm^2), and the tunnel regime (above $\simeq 10^{14}$ W/cm^2).

Figure 9.5 shows the ionisation rate of oxygen and nitrogen as a function of the pulse intensity (from [35]). We can clearly see that the ionisation in gas is a highly non linear process. Indeed, an increase of the laser pulse intensity by a factor 2 corresponds to an increase of the ionisation rate, and equivalently to an increase of the plasma index, by approximately a factor 10^2. This ionisation rate is introduced in the simulation. The electron density n_e is

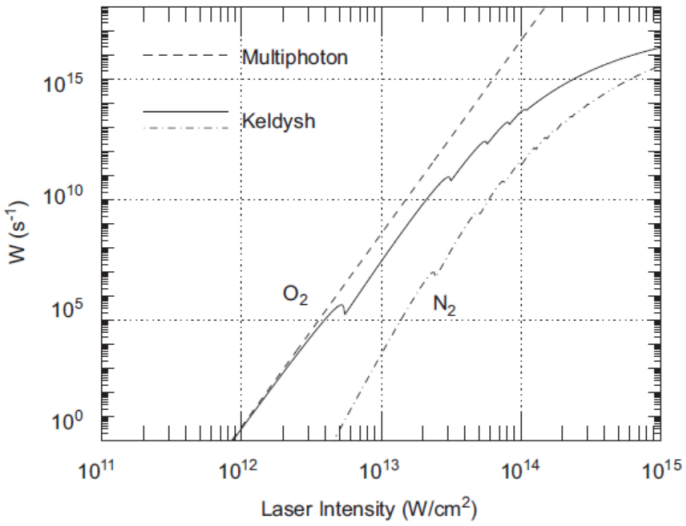

Figure 9.5: Evolution of the ionisation rate W of oxygen and nitrogen, as a function of the laser pulse intensity [35].

then calculated in the 3D simulation, during the propagation and interaction of the pump. At each step of the propagation, it gives the plasma index n_p defined in section 2.10.1, such as: $n_p = \sqrt{1 - n_e/n_c}$, where n_c is the critical density given in equation 2.75.

9.2.4 Expected deflection signal induced by the pump in the interaction area

The deflection angle $\langle \delta\theta_y \rangle$ of the probe pulse in the interferometer, induced by its interaction with the co-propagating pump pulse, is calculated via 3D numerical simulations [34], for various energy of the pump pulse.

Considering Gaussian profiles for the pump and probe pulses, the input parameters of the simulations are:

- a duration of the pump and probe pulses of 55 fs (FWHM);
- a minimum waist at focus equal to the measured values: w_0(pump) = 31.1 μm and w_0(probe) = 35.4 μm (from equation 9.1);
- an energy of 5 μJ for the probe pulse, corresponding to a peak intensity at focus of 6 TW/cm^2 (from equation 9.5);
- a pump energy $\mathcal{E}$, corresponding to a peak intensity at focus of $I_0 = 1.2$ (TW/cm^2)$\times\mathcal{E}(\mu$J) (from equation 9.5);
- a tilt angle θ_{tilt} between the pump and probe beam of 7 degrees.

NB: for the Kerr measurements in air studied in this chapter, the contribution of the probe pulse is not negligible when the pump intensity is relatively low (of the same order or below

the probe intensity), as we will see in sections 9.3 and 9.4. In the simulations, the 3D electric field at focus thus includes the sum (i.e. the interference) of the pump and probe fields, which requires a long calculation time. This is also why there are so few statistics on the simulation results.

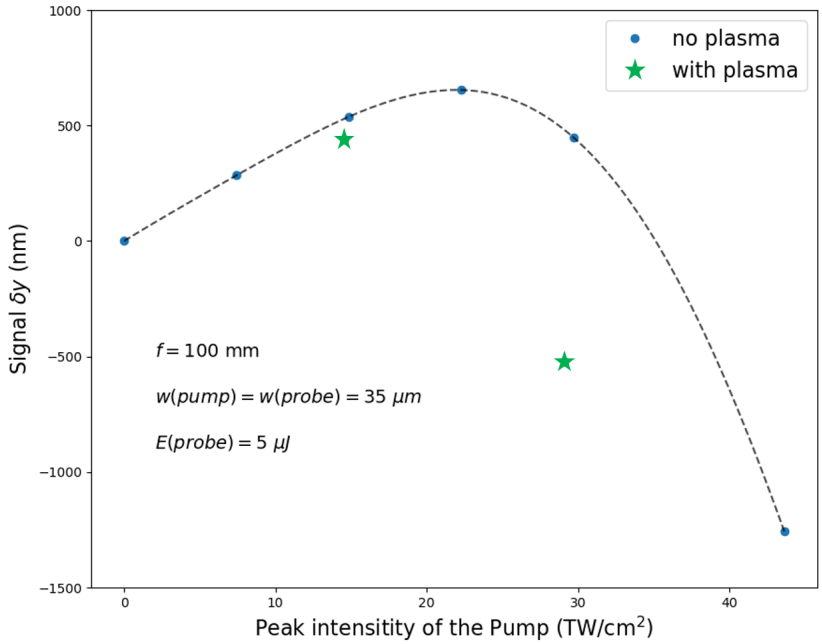

Figure 9.6: Expected un-amplified vertical shift $\delta y = f \times \langle \delta\theta_y \rangle$ (in nm) of the barycenter of the probe intensity profile after deflection by the pump pulse in the interferometer, as a function of the pump peak intensity at focus (in TW/cm^2), for a focal length in the interferometer $f = 100$ mm and an efficiency $\epsilon_s = 1$. The blue dots (with polynomial fit in dashed line) correspond to the expected values for the optical Kerr effect with higher order indexes (from equation 9.6). The green dots correspond to the expected values when the contribution of the plasma index is added. This simulation takes into account the contribution of the probe peak intensity at focus. The input parameters for Gaussian pulses are: minimum waists at focus w_0(pump) = 31.1 μm and w_0(probe) = 35.4 μm; pulse duration 55 fs; probe energy 5 μJ.

The simulations first compute the deflection $\langle \delta\theta_y \rangle^{simu}$ as a function of the pump peak intensity at focus (in TW/cm^2). Then, we plot on figure 9.6 the expected direct deflection signal $\delta y = f \times \langle \delta\theta_y \rangle^{simu}$, corresponding to the un-amplified vertical shift of the collimated probe intensity profile, as a function of the pump peak intensity, while only assuming the optical Kerr effect with high order indexes first (blue dots). For a pump peak intensity below 20 TW/cm^2 approximately, the signal δy is proportional to the pump intensity. However, above this intensity value, the signal decreases and even becomes negative, due to higher order negative indexes of the optical Kerr effect.

Now, by adding the contribution of the plasma index (green dots), we can also see a decrease of the expected signal for a pump peak intensity approximately above 20 TW/cm^2 as well, with a relatively large systematic uncertainty for this plasma threshold because of the highly non linear behaviour of the plasma ionisation rate.

In the next section, we will present the Kerr measurement results in air for pump energies below 15 μJ (corresponding to approximately 18 TW/cm^2 at focus), which is just around the threshold where the contributions of the high order Kerr indexes and the plasma index become non-negligible for the deflection signal δy. For measurements at energies lower than 15 μJ, these contributions will not be an issue but the measurements at 15 μJ should be taken with a grain of salt.

9.3 Kerr measurements in air with low amplification (rotated polarisation)

In this section, we present the Kerr measurements in air with the low amplification configuration, which corresponds to the Sagnac interferometer configuration where the polarisation of the incident laser pulse is slightly rotated by a few tens of mrad before entering the interferometer (as described in section 7.2.2).

Several run of measurements were done using Prototype 2 (see section 4.2) without spatial filter in the dark output. The measured signal was then very sensitive to the phase noise pattern containing hot spots. The data presented in this section have been collected on the 22nd of December, 2021, which provided the most stable and less dispersed results. The experimental parameters were the same as the simulation parameters described in section 9.2.4, and with a probe energy inside the interferometer of about 5 μJ per pulse, which corresponds to a maximum peak intensity at focus of $I_{\text{probe}} \simeq 6$ TW/cm^2.

The DeLLight signal Δy was first measured as a function of the pump intensity. To this end, several sets of Kerr measurements have been carried out at various energies of the pump pulses, from 2 μJ to 15 μJ, corresponding to peak intensities at focus from $I_{\text{pump}} \simeq 2$ TW/cm^2 up to $I_{\text{pump}} \simeq 18$ TW/cm^2. As discussed in section 9.2.4, the Kerr signal is expected to be proportional to the pump intensity below 20 TW/cm^2, although we may expect a negative contribution from the high order Kerr indexes and plasma index above this intensity value.

9.3.1 Control of the absence of signal when the pump pulse is ahead or delayed in time

First of all, we crosschecked that the DeLLight signal is null when the pump is delayed or in advance with respect to the probe at focus in the interferometer. To this end, the pump pulse crosses the interaction area with a 300 fs delay, and thus the probe pulse is not deflected by Kerr effect. This allows to effectively cancel the probe/pump interaction while also keeping the same possible systematic induced by the pump pulse as would be the case in regular measurements, such as possible light diffusion inside the vacuum chamber coming from the

pump beam, mechanical noise induced by the ON/OFF pump shutter, or even other unknown possible systematic.

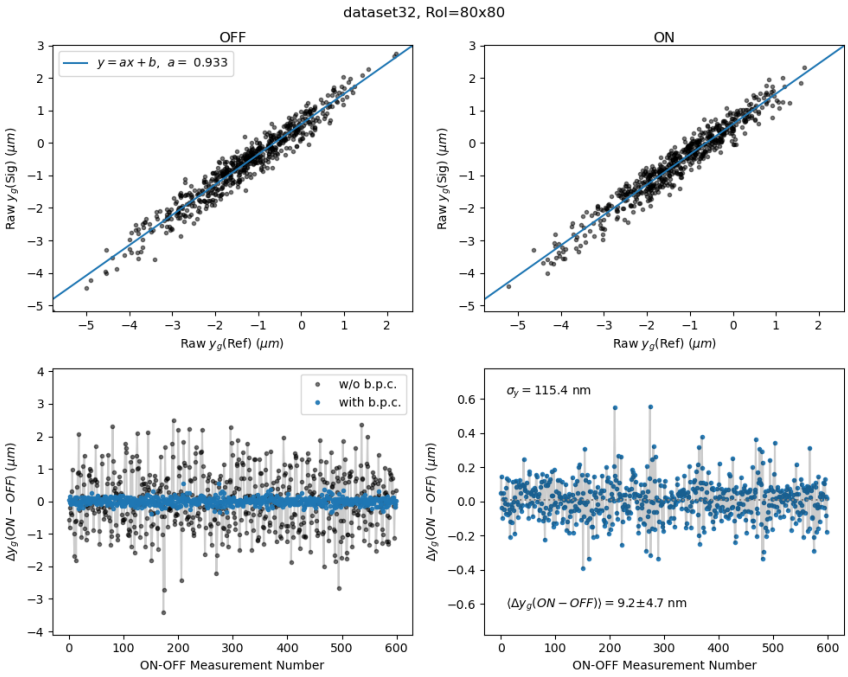

Figure 9.7: Summary of the data analysis, calculated along the vertical axis y, for a measurement with the pump delayed by -300 fs with respect to the probe in the interaction area. The pump energy is the same as the probe: $\mathcal{E}_{pump} = \mathcal{E}_{probe} \simeq 6\ \mu$J. (Top) Correlation of the barycenters in intensity of the interference signal $\bar{y}_{\mathrm{sig}}(i)$ and the back-reflection $\bar{y}_{\mathrm{ref}}(i)$. The data is shown as black points, for OFF (left) and ON (right) measurements, while the result of the linear fit obtained using the OFF data only is shown in both panels as a blue line. (Lower left) Distribution of the ON-OFF subtraction of the raw barycenter positions $\bar{y}^{\mathrm{ON}}_{\mathrm{sig}}(i) - \bar{y}^{\mathrm{OFF}}_{\mathrm{sig}}(i)$ in grey, and in blue after beam pointing correction $\Delta y(i) = \bar{y}^{\mathrm{ON}}_{\mathrm{corr}}(i) - \bar{y}^{\mathrm{OFF}}_{\mathrm{corr}}(i)$. (Lower right) Distribution of the ON-OFF subtraction after beam pointing corrections, where the mean value corresponds to the DeLLight signal $\Delta y = \langle \Delta y(i) \rangle = 9.2 \pm 4.7$ nm, compatible with zero as expected (dataset32, collected on the 22nd of December, 2021).

Figure 9.7 shows the result of the "ON-OFF" analysis for such data (with $\mathcal{E}_{pump} \simeq \mathcal{E}_{probe} \simeq 6\ \mu$J) when the pump pulse is delayed by -300 fs with respect to the probe pulse in the interaction area. The analysis is achieved using the method described in chapter 3. The vertical signal measured in the dark output is then: $\Delta y = 9.2 \pm 4.7$ nm (with a dispersion $\sigma_y = 115.4$ nm), which is compatible with zero as expected. Therefore, we have defined the "zero position" and we are certain that the measured signal in the dark output of the interferometer is really due to the Kerr effect and does not come from possible artefacts coming from the pump.

9.3.2 Deflection signal as a function of the pump peak intensity

After measuring the "zero signal", we measure the Kerr signal Δy in air at different pump intensities, in order to verify the expected linear relationship between the two. To this end, several sets of measurements have been carried out at various pump energies, from 2 to 15 μJ per pulse (corresponding to peak intensities from 2 to 18 TW/cm^2). The energy of the pump pulse is modified by the combination of a rotating half wave plate ($\lambda/2 - 1$ on figure 4.3) followed by a femto-polariser (P) set to $p-$polarisation. This way, the pump energy is maximal when the half wave plate is aligned with the polariser set in $p-$polarisation, and it decreases when the half wave plate is rotated while still keeping a $p-$polarisation pump pulse in the interaction area. Thus, the pump energy is minimal when the pump polarisation is completely rotated to $s-$polarisation after the half wave plate. The advantage of this method is that it maintains the time coincidence of the pump and probe pulses in the interaction area (i.e. there is no stretching of the pump pulse duration since the pulse passes through the same optics).

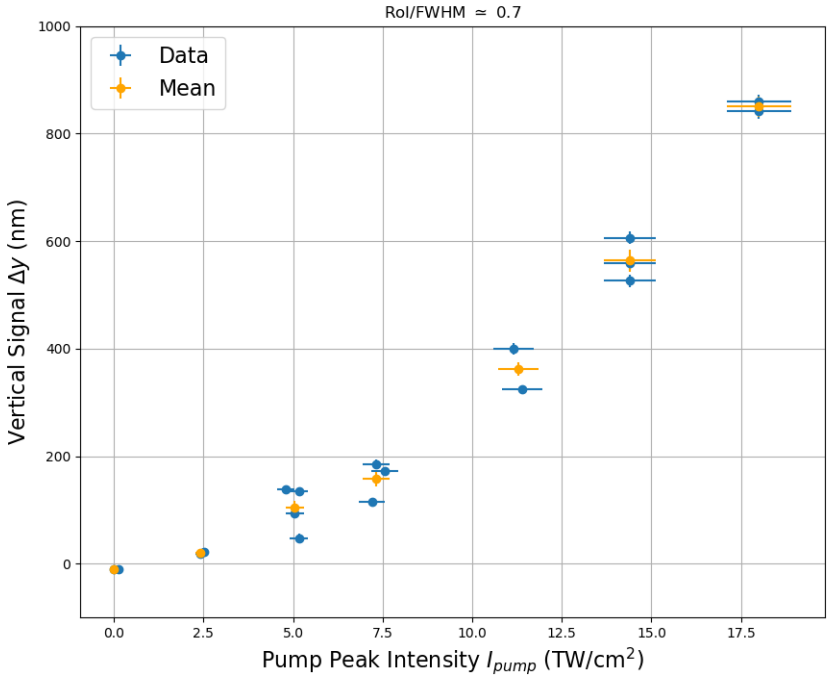

Figure 9.8: Kerr measurement results in air, translated by the vertical shift Δy (in nm) of the barycenter of the interference intensity profile measured in the dark output of the interferometer, as a function of the peak intensity of the pump pulse. This vertical shift corresponds to an "ON-OFF" measurement, such as $\Delta y = \bar{y}^{\mathrm{ON}}_{\mathrm{corr}} - \bar{y}^{\mathrm{OFF}}_{\mathrm{corr}}$, where $\bar{y}^{\mathrm{ON}}_{\mathrm{corr}}$ and $\bar{y}^{\mathrm{OFF}}_{\mathrm{corr}}$ are the corrected barycenters of the ON (pump/probe interaction) and OFF (no interaction) intensity profiles in the dark output. Theses signals were calculated with a RoI-size $w_{RoI} = 0.7 \times FWHM$. (Blue) All Kerr signal values Δy measured during the run presented here. (Orange) Averaged vertical shift Δy over several sets of measurements at the same pump peak intensities.

The duration of each measurements depends on the pump energy and therefore on the expected signal amplitude. It varies from 40 seconds at maximal pump energy (15 μJ), up to 2 minutes at minimum pump energy (2 μJ), which will naturally influence the error on the signal Δy accordingly. Moreover, between each set of measurements, the extinction of the Sagnac interferometer is adjusted if necessary, as well as the position of the lens L-2 (focusing the reference pulse). In order to check the repeatability of the results, we repeat the measurements as a function of the pump energy up to three times.

The results of the Kerr measurements in air are presented on figure 9.8, where the vertical shift Δy measured in the dark output is plotted as a function of the pump peak intensity. A clear correlation is observed: the signal increases with the pump intensity, as expected for the Kerr effect with pump intensities below 20 TW/cm^2, as explained in section 9.2.4. Moreover, the dispersion of the results illustrates the repeatability of the measurement. However, we can see a slight non linearity for pump intensities below 7 TW/cm^2. In the next section, we will see that this comes from the polarisation of the pump, which is not perfectly p-polarised but has a small fraction of s-polarisation, thus degrading the signal in the dark output.

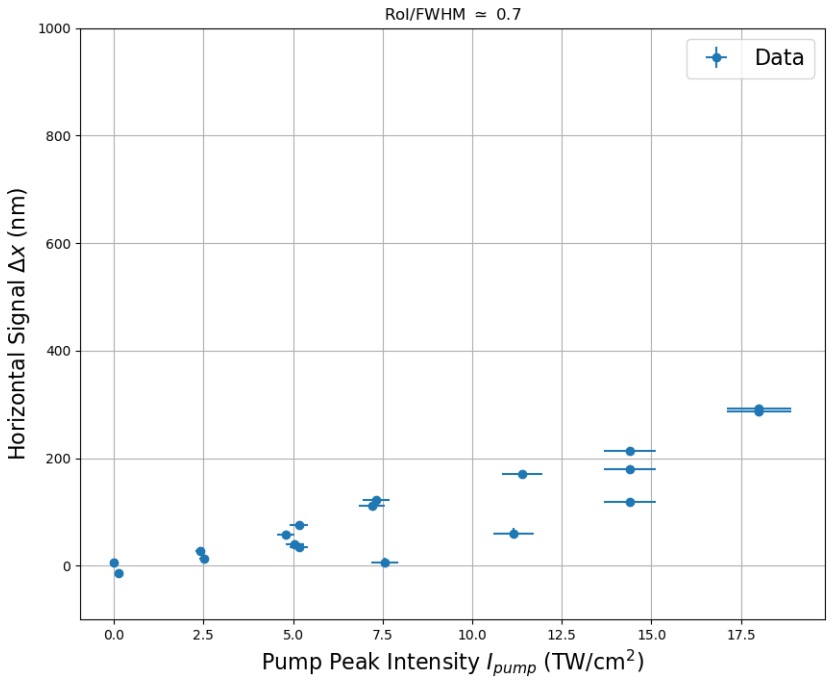

Figure 9.9: Same as figure 9.8, but for the deflection signal Δx along the x-direction.

We also plotted the signal Δx in the x-direction on figure 9.9. Since the pump pulse is only vertically shifted with respect to the probe pulse at focus in the interaction area, there should not be any horizontal deflection of the intensity profile in the dark output of the Sagnac interferometer. However, we can clearly see a signal (though weak compared to Δy) of about

Δx = 300 nm for an intensity equal to 18 TW/cm^2 (corresponding to a pump energy of 15 μJ). This effect is possibly due to an asymmetry of the horizontal x-component of the phase noise $\delta\phi(x, y)$, which dominates at low amplification as seen in section 7.2.2. Further investigations are still required to better understand this phenomenon.

9.3.3 Polarisation-dependent Kerr index

The Kerr index $n_{2,air}$ in the interaction area depends on the relative polarisation between the pump and probe pulses. Indeed, it is maximal when both polarisations are parallel and is theoretically divided by a factor 3 when the polarisations are perpendicular (we will see in section 9.4.5 that the deflection signal might even be null when the polarisations of the pump and the probe are perpendicular). However, we saw in the previous section that the polarisation of the pump pulse is rotated from p to s when the pump energy is decreased from its maximal to minimal value, using the half wave plate ($\lambda/2 - 1$). Then, the inefficiency of the femto-polariser (P) set in p-polarisation and placed right after allows the pump pulse to keep a s-polarisation component as well as a p-component. Therefore, the polarisation of the pump is p when its energy is maximal. However, when the pump energy decreases, the fraction of the s-component increases. Finally, when the pump energy is minimal, its polarisation is only s.

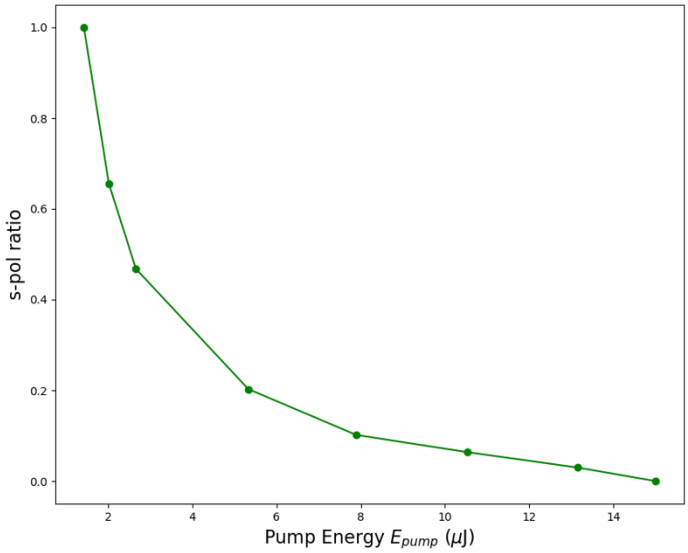

Figure 9.10: Fraction of the s-polarisation of the pump pulse, as a function of its energy, after crossing the combination of the half wave plate rotation followed by the femto-polariser set to p-polarisation (method used to reduce the energy of the pump pulse without changing the pump/probe time coincidence in the interaction area). The probe pulse is only p-polarised.

Figure 9.10 shows the fraction of the s-polarisation component of the pump as a function of its energy, which evolves as expected. Therefore, the DeLLight signal Δy, measured in the

previous section, can be corrected by taking into account the variation of the polarisation of the pump pulse. The corrected value Δy_{corr} is then given by:

$$\Delta y_{\text{corr}} = \frac{\Delta y}{\frac{s}{3} + p} = \frac{\Delta y}{1 - \frac{2s}{3}} \tag{9.7}$$

where the s-component comes from figure 9.10.

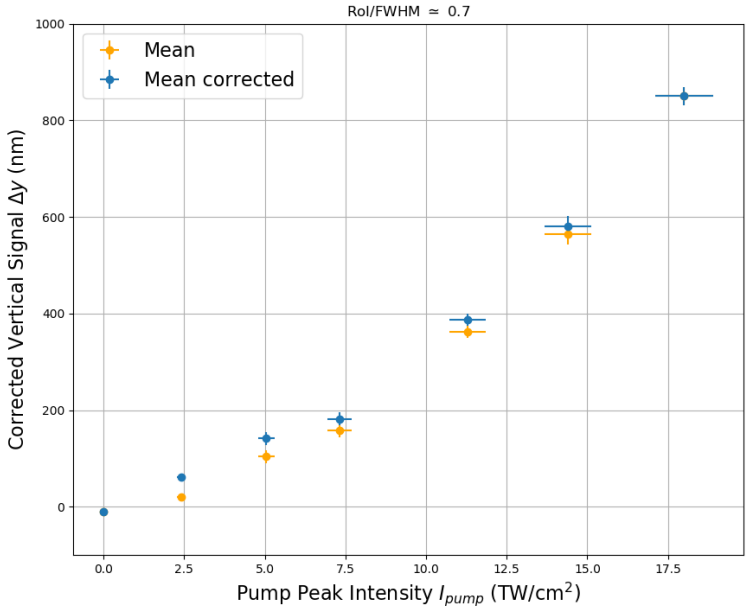

Figure 9.11: Same as figure 9.8, but after correction of the pump polarisation in the interaction area. The corrected signal (blue) is then $\Delta y_{\text{corr}} = \Delta y/(1 - \frac{2s}{3})$. The orange dots are the mean signal values from figure 9.8.

The corrected value of the signal Δy_{corr}, as a function of the peak intensity of the pump in the interaction area, is shown on figure 9.11. The corrected signal is now almost proportional to the peak intensity of the pump as expected, even at intensities below 7 TW/cm^2.

In order to avoid the effect of the polarisation of the pump pulse in future measurements, we will see in section 9.4 that another method to decrease the pump energy was used for Kerr measurements in the high amplification configuration of the Sagnac interferometer.

9.3.4 Deflection signal as a function of the RoI-size

As explained in section 3.2.2, the amplitude of the measured signal Δy depends on the RoI-size w_{RoI} chosen for the data analysis. Reducing the size of the RoI too much would truncate the intensity profile in the dark output of the interferometer, thus skewing the measured shift Δy caused by the Kerr effect. However, as seen on figure 6.8 in section 6.4, the spatial resolution σ_y is degraded for larger RoI-sizes because the signal to noise ratio then decreases

and the phase noise dominates in the dark output.

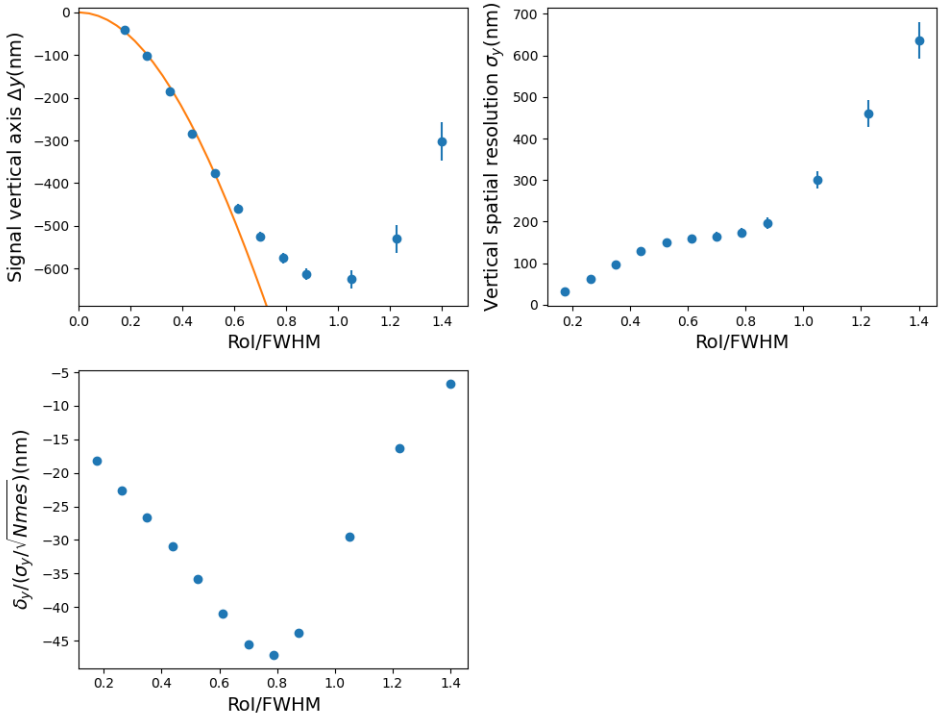

Figure 9.12: Effect of the size of the region of interest (RoI) on the Kerr signal Δy measured in the dark output, for a set of measurements with a pump energy of 12 μJ (i.e. a peak intensity of 14 TW/cm^2). (Upper left plot) Amplitude of the measured signal Δy as a function of the RoI-size over the width (FWHM) of the transverse intensity profile. The orange curve is the expected signal efficiency (defined in equation 3.11). (Upper right plot) Spatial resolution σ_y as a function of the RoI-size over FWHM. (Lower Plot) Statistical confidence level (in number of sigma) of the measured signal: $C = \Delta y/(\sigma_y/\sqrt{N_{mes}})$, N_{mes} being the number of "ON-OFF" measurements, as a function of the RoI-size over FWHM.

Figure 9.12 first shows the signal Δy measured in the dark output, as a function of w_{RoI}/w, where w is the width (FWHM) of the transverse intensity profile in the dark output. These data correspond to a pump energy of 15 μJ, equivalent to a peak intensity of 18 TW/cm^2. For $w_{RoI}/w \leq 0.6$, the signal increases with the size of the RoI, according to the expected signal efficiency defined in equation 3.11 (orange line on figure 9.12). However, for larger RoI-sizes, the amplitude of the measured signal saturates around $w_{RoI} = w$ and then decreases over that value. This is due to the contribution of the phase noise in the dark output which becomes dominant and thus deteriorates the "ON-OFF" signal reconstruction.

Secondly, the same figure also shows the spatial resolution σ_y as a function of w_{RoI}/w. We can see that, for $w_{RoI}/w \leq 0.8$, the spatial resolution is relatively stable. However, for $w_{RoI}/w \geq 0.8$, it is rapidly degrading due to a decrease of the signal-to-noise ratio. As already mentioned, the phase noise dominates for large RoI-sizes.

Finally, we define the statistical confidence level C of the measured signal (in number of sigma) by:

$$C = \frac{\Delta y}{\sigma_y / \sqrt{N_{mes}}} \tag{9.8}$$

where N_{mes} is the number of "ON-OFF" measurements. On figure 9.12, we plot this parameter as a function of w_{RoI}/w. It is maximal for $w_{RoI}/w \simeq 0.8$, as expected from the other two plots presented.

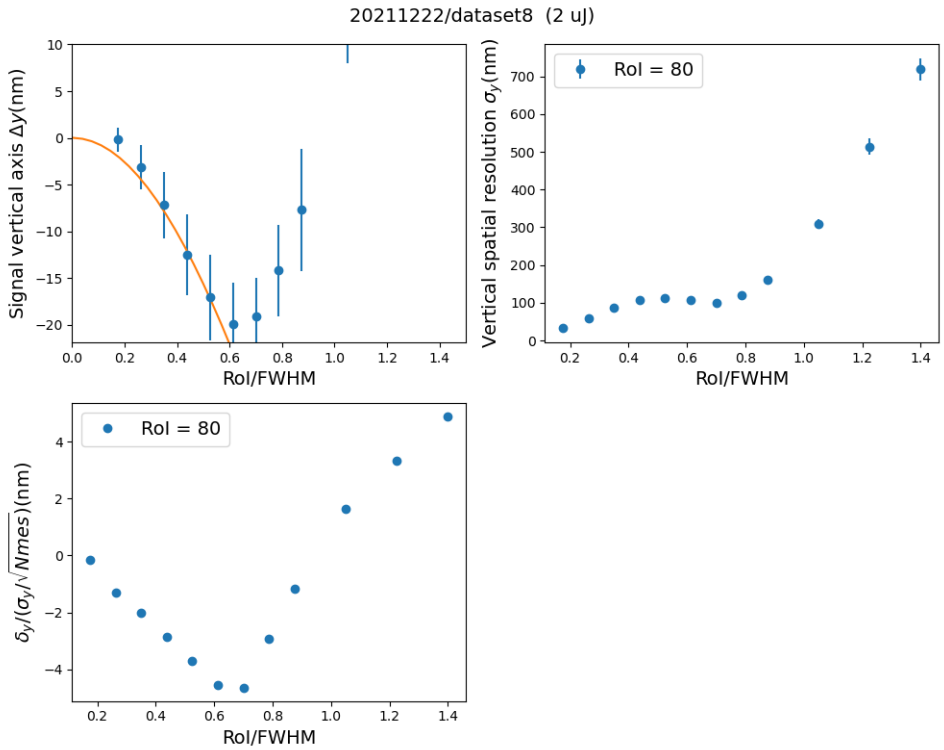

Figure 9.13: Same as figure 9.12, but for a pump energy of 2 μJ (i.e. an intensity of 2 TW/cm^2).

Additionally, the same kind of study was performed for other sets of measurements with different pump energy. Figure 9.13 shows the results for a pump energy of 2 μJ (corresponding to a peak intensity of 2 TW/cm^2.). Similar conclusions can be drawn. Thus, we remark that, for very low pump energies, and therefore for very low signals, the noise contribution also becomes important for large RoI-sizes and saturates sooner (at $w_{RoI}/w \simeq 0.6$). The measured signal can even change sign.

From this study, we conclude that the optimal RoI-size to maintain a stable and good spatial resolution and to optimise the signal-to-noise ratio is $w_{RoI}/w = 0.7$. That is why we have used such value for the analysis presented in the previous sections.

9.3.5 Contribution of the phases $\delta\phi(y)$ and $\delta\psi$ to the measured deflection signal

A major drawback of this low amplification configuration concerns the mix of p and s polarisation component of the probe beam. This mixture renders the understanding of the results presented here very complex and difficult to calculate. We explain here the reasons.

Let us consider the p and s-component of the interference intensity profile I_{ON} for an "ON" measurement (with interaction with the pump) in the dark output of the interferometer. From equations 2.29 and 7.5, we can write the intensity profile for an ON measurement as:

$$I_{ON}(y) = \cos^2(\beta) \times I_{ON,p}(y) + \sin^2(\beta) \times I_{ON,s}(y) \tag{9.9}$$

where the p and s-components are:

$$\begin{aligned} I_{ON,p}(y) = (\delta a_p)^2 \times I_{in}\Big(y + \frac{1-\delta a_p}{2\delta a_p} \times \delta y_p\Big) \\ + \Big(\delta\phi_p(y) + \frac{\delta\psi_p}{2}\Big)^2 \times (1-(\delta a_p)^2) \times I_{in}\Big(y - \frac{\delta y_p}{2}\Big) \end{aligned} \tag{9.10}$$

$$\begin{aligned} I_{ON,s}(y) = (\delta a_s)^2 \times I_{in}\Big(y + \frac{1-\delta a_s}{2\delta a_s} \times \delta y_s\Big) \\ + \Big(\delta\phi_s(y) + \frac{\delta\psi_s}{2}\Big)^2 \times (1-(\delta a_s)^2) \times I_{in}\Big(y - \frac{\delta y_s}{2}\Big) \end{aligned} \tag{9.11}$$

and where the parameters involved have already been discussed. We remind that:

- the angle between the p and s-polarisation planes is very small: $\beta \ll 1$ (from section 7.2.2: $\beta \simeq 4$ mrad);
- the p-component of the asymmetry coefficient is: $(\delta a_p)^2 \simeq 3 \times 10^{-6}$ (corresponding to the maximal measured extinction from figure 5.3);
- the phase noise pattern (containing hot spots) is: $(\delta\phi_p(y))^2 \simeq 3 \times 10^{-5}$ (measured in the dark output without spatial filter, as seen on figure 5.2);
- the s-component of the asymmetry coefficient is: $\delta a_s = 0.55$ (from section 7.2.2);

which lead to a s-component extinction factor of:

- $(\delta a_s)^2 \times \sin^2(\beta) = 5 \times 10^{-4} = R_{AR}/2$ (from equation 7.6);
- $\delta\phi_s \simeq 200$ mrad, i.e. $\delta\phi_s \simeq \delta a_s/3$ (estimated from a study of the intensity signal as a function of the polarisation, and not presented here);
- $\delta y_s, \delta\psi_s \ll \delta y_p, \delta\psi_p$ (coming from the measurement of the deflection signal when the relative polarisation between pump and probe is perpendicular, as will be seen in figure 9.18).

Finally, the intensity profile of the ON measurement can be simplified as:

$$\begin{aligned} I_{ON}(y) = \;& 3\times10^{-6}\times I_{in}\Big(y+290\times\delta y_p\Big) && \longrightarrow 3\times10^{-6} \\ +\;& \Big(\delta\phi_p(y)+\tfrac{\delta\psi_p}{2}\Big)^2\times I_{in}\Big(y-\tfrac{\delta y_p}{2}\Big) && \longrightarrow 3\times10^{-5} \\ +\;& 5\times10^{-4}\times I_{in}\Big(y+0.5\times\delta y_s\Big) && \longrightarrow 5\times10^{-4} \\ +\;& 0.7\times\Big(\delta\phi_s(y)+\tfrac{\delta\psi_s}{2}\Big)^2\sin^2(\beta)\times I_{in}\Big(y-\tfrac{\delta y_s}{2}\Big) && \longrightarrow 5\times10^{-4} \end{aligned} \tag{9.12}$$

where we have indicated by an arrow the orders of magnitude of each intensity term. The first term corresponds to a strongly amplified shift of the intensity profile, but with a relative intensity two orders of magnitude smaller. The second term corresponds to a shift induced by the coupling of the phase signal $\delta\psi_p$ with the phase noise $\delta\phi_p$ with a relative intensity an order of magnitude smaller. The two last terms are the dominant intensity terms with a shift relatively smaller and mainly induced by the coupling of the phases "$\delta\phi_s(y)\times\delta\psi_s$".

Therefore, for this configuration with rotated polarisation of the probe, the shift of the barycenter of the interference intensity profile measured in the dark output is actually a combination of all the different contribution depicted in equation 9.12, thus rendering the understanding of the results presented here very complex. Since the measured signal is dominated by the phase noise (which is not properly controlled), it is necessary to get rid of all *s*-components in order to properly amplify the direct deflection δy. This is done in the next section 9.4.

In summary, the DeLLight measurements presented here for the low amplification configuration of the Sagnac interferometer are not very satisfying, with room for improvement by using probe and pump pulses with parallel *p*-polarisations. However, these measurements were a huge step to highly enhance the experimental setup (in terms of efficiency, practicality and stability), as well as the measurement protocols and the "ON-OFF" signal extraction method. In the next section, we will discuss the Kerr measurements in air with high amplification by interferometry, i.e. without the introduction of *s*-polarisation between the pump and probe pulses.

9.4 Kerr measurements in air with high amplification (rotated beamsplitter)

In this section, we present the Kerr measurements in air with the high amplification configuration, which corresponds to the Sagnac configuration where the interferometer beamsplitter is slightly rotated by 1 degree on its horizontal plane in order to have an incident angle of 46° for the pulse entering the interferometer (as described in section 7.2.3). This means that now the probe beam is purely *p*-polarised in the interaction area.

The data presented in this section have been collected during Fall, 2022. These were fairly new at time of writing this manuscript, thus the results are preliminary.

The experimental setup is the same as the previous section (triangular interferometer with focusing), but with the spatial filter in the dark output and without the spectral filter. The experimental parameters are the following:

- The energy of the probe pulse inside the Sagnac interferometer is $\mathcal{E}_{probe} = 1\ \mu$J.
- The minimum waists at focus of the probe and pump are $w_0 \simeq 35\ \mu$m.
- The tilt angle between the pump and probe beams is $\theta_{tilt} \simeq 7°$.
- The T/R asymmetry parameter of the beamsplitter is $\delta a \simeq +2 \times 10^{-2}$, with an extinction factor of $\mathcal{F} = 4 \times 10^{-4}$, corresponding to a negative amplification factor of

$$\mathcal{A} = -\frac{1}{2\delta a} = -25 \tag{9.13}$$

  It means that the amplified interferometric deflection signal Δy and the direct deflection signal δy, related by $\Delta y = \mathcal{A} \times \delta y$, have opposite signs.

In this configuration, the polarisation of the probe beam is purely p with $\delta a = \delta a_p = 2\times10^{-2}$. Therefore, the interference intensity profile I_{ON} for the "ON" measurement (with interaction with the pump) in the dark output of the interferometer is simply:

$$\begin{aligned} I_{ON}(y) &= (\delta a)^2 \times I_{in}\Big(y + \frac{1}{2\,\delta a} \times \delta y\Big) + \Big(\delta\phi(y) + \frac{\delta\psi}{2}\Big)^2 \times I_{in}\Big(y - \frac{\delta y}{2}\Big) \\ &= (\delta a)^2 \times I_{in}\Big(y - \mathcal{A} \times \delta y\Big) + \Big(\delta\phi(y) + \frac{\delta\psi}{2}\Big)^2 \times I_{in}\Big(y - \frac{\delta y}{2}\Big) \end{aligned} \tag{9.14}$$

We have measured the DeLLight deflection signal Δy as a function of four experimental parameters:

- the time delay δt between the pump and the probe pulses at focus,
- the pump peak intensity,
- the impact parameter b,
- the polarisation of the pump, relative to the probe.

For the results presented below, the analysis have been done using a RoI-size of $w_{RoI} = w/2$ where w is the width (FWHM) of the intensity profile in the dark output. This corresponds to an efficiency to reconstruct the barycenter shift of $\epsilon_s = 0.12$ (see section 3.2.2).

9.4.1 Measurement of the direct deflection signal δy

For this new campaign of measurements, we used the direct back-reflection of the beamsplitter (defined in section 2.7) to measure simultaneously the direct deflection signal $\delta y = f \times \delta\theta$ of the probe, and this in addition to the amplified interferometric deflection signal Δy. We remind that both signals are related by $\Delta y = \mathcal{A} \times \delta y$, $\mathcal{A}$ being the amplification factor. Therefore, measuring simultaneously δy and Δy allows to quantify and to validate the effect of said amplification through the Sagnac interferometer.

The position of the direct back-reflection of intensity $I_{AR,1}$ (see figure 2.5) allows to measure the direct deflection of the probe. Indeed, this back-reflection corresponds to the direct image of the probe pulse after a single reflection on the backside of the beamsplitter. This pulse is therefore also deflected by the pump pulse in the interaction area, but without being amplified via interference with the probe pulse in the dark output. Moreover, the second back-reflection of intensity $I_{AR,2}$ (see figure 2.5) corresponds to the constructive interference of the two laterally offset beams which are not in coincidence with the pump (delayed). Therefore this second back-reflection is not affected by the pump and is used as a reference for beam-pointing correction, in a similar way as done for the amplified signal Δy (see chapter 3).

That way, we can simultaneously measure the direct deflection signal δy using the direct back-reflection $I_{AR,1}$ in reference to the second back reflection $I_{AR,2}$, and the amplified deflection signal Δy using the interferometric signal in the dark output in reference to the second back-reflection $I_{AR,2}$.

9.4.2 Deflection signal as a function of the time delay δt between the pump and probe pulses at focus

We first measured the deflection signal as a function of the time delay δt between the probe and the pump pulses. To scan different delay values, we use a motorised piezo translation stage (MDS-1), for which the steps are calibrated. However, the absolute position is unknown. In order to avoid hysteresis on the absolute position, the scan on the delay time has been performed starting with a pump in advance, relatively to the probe, then by delaying the pump progressively. The measurements of the delay time scan have been done with an energy of the pump pulse $\mathcal{E}_{pump} = 2\ \mu$J and a pulse duration of 70 fs (FWHM), corresponding to a peak intensity at focus of about 3 TW/cm^2.

The result of this time scan is shown on figure 9.14 (left panel). A positive time delay corresponds to a pump pulse in advance while a negative time delay correspond to a delayed pump. The measured profile of the amplified deflection signal Δy as a function of the time delay is in agreement with the expected longitudinal profile of the pump pulse, namely close to a Gaussian profile where its maximum corresponds to the optimal time synchronisation between the probe and pump pulses at focus. Moreover, when the delay between the probe and pump pulses is about $\delta t = -200\,fs$, the deflection signal is $\Delta y = 5.7 \pm 6.8$ nm, which is in agreement with a null signal, as expected. This constitutes the "zero signal".

We also detect a small but significantly non null direct deflection signal δy which is maximal at the time coincidence of the pump and probe pules. At $\delta t = 0$, we measure $\delta y \simeq -20$ nm and $\Delta y \simeq 220$ nm, which corresponds to an effective amplification factor $\mathcal{A} \simeq -11$. It is a

factor 2 smaller than the expected amplification factor. We will see in section 9.4.4 that the amplification is reduced by the presence of the phase. We also verify here that δy and Δy have opposite sign, as expected.

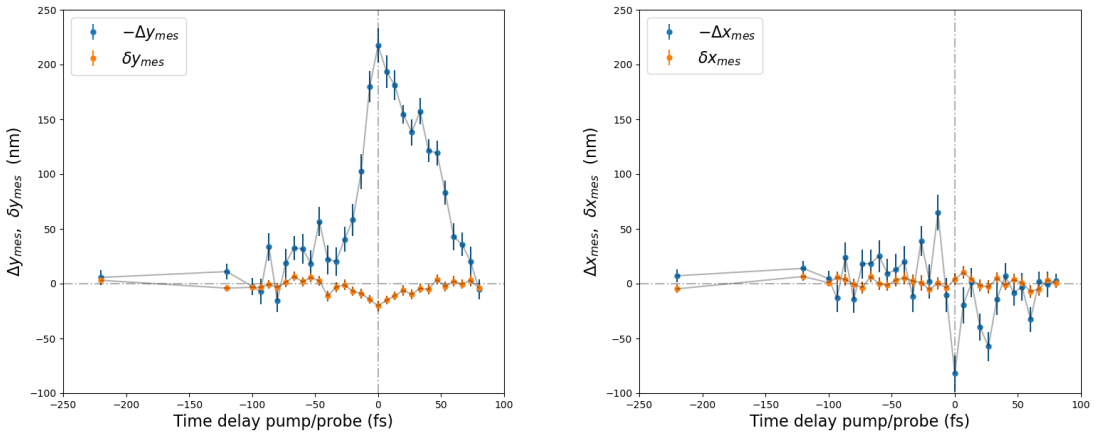

Figure 9.14: (Blue) Measured DeLLight deflection signals, Δy_{mes} in the y-direction (left) and Δx_{mes} in the x-direction (right), as a function of the time delay δt between the pump and probe pulses at focus. (Orange) Direct deflection signals, δy_{mes} (left) and δx_{mes} (right), as a function of the time delay δt. Measurements have been performed ob November, the 4th, 2022, with a pump energy of 2 μJ and a pulse duration of 70 fs (FWHM), corresponding to a peak intensity of the pump at focus of about 3 TW/cm^2.

Additionally, figure 9.14 also shows, on the right panel, the measured deflection signal Δx (along the horizontal x-axis) as a function of the time delay δt of the pump pulse. At first order, the expected deflection signal is null. However, we can see that a small signal could occur when delaying the pump pulse, possibly due to a horizontal shift of the interference fringes between the pump and the probe pulses. This effect is not well understood yet, so numerical simulations are required to study it.

9.4.3 Deflection signal as a function of the pump intensity

We have measured the deflection signal Δy as a function of the pump intensity at focus in the interaction area. Similarly to section 9.3.2, we collect several data sets, at different pump energies ranging from 1 to 13 μJ, with pulses duration of 70 fs (FWHM), which corresponds to peak intensities from 1 to 14 TW/cm^2. At such intensities, the Kerr signal is expected to be proportional to the pump intensity (as shown on figure 9.6). Let us note that the pump energy was decreased using a variable neutral density with constant optical path length in order to avoid any experimental bias due to a possible rotation of the pump polarisation, as was the case in section 9.3.3.

Figure 9.15 shows the result of the measurements of the direct deflection δy and amplified deflection Δy as a function of the pump peak intensity. A clear correlation is observed between

the deflection signal Δy and the pump intensity, as expected for the Kerr effect with pump peak intensities below 15 TW/cm^2. A small but significant direct deflection signal δy is also measured. The measured amplification factor is then $\mathcal{A} \simeq -23$, in agreement with the expected value of 25. We also verify that the amplification factor is negative as expected (δy and Δy have opposite signs).

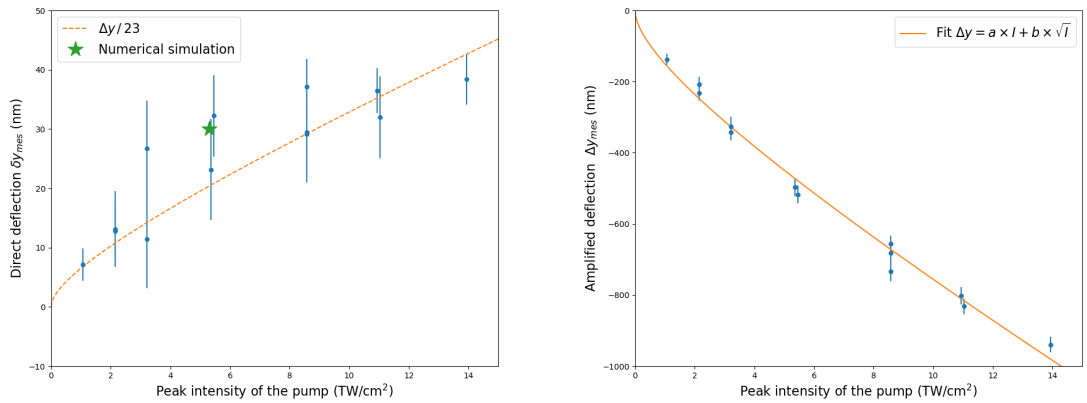

Figure 9.15: Deflection signal as a function of the pump peak intensity at focus in the interaction area. (Left) Direct deflection signal δy without amplification. The expected signal calculated by numerical simulations is shown by the green star. (Right) Amplified deflection signal $\Delta y = \mathcal{A} \times \delta y$ with the fitted function (orange line) given by equation 9.16. The amplification factor $\mathcal{A} \simeq -23$ is in agreement with the expected value and is negative as expected. The fitted function divided by the amplification factor has been superposed on the left figure (dashed orange line) to verify the good agreement with the direct deflection signal.

The expected direct deflection signal δy^{simul} has been calculated by numerical simulations (described in section 9.2). For an energy of the pump of 5 μJ, a pulse duration of 70 fs (FWHM), a minimum waist at focus of $w_0 = 40\,\mu$m (corresponding to a peak intensity of 5 TW/cm^2), a tilt angle of $\theta_{tilt} = 7°$ and an impact parameter of $b = b_{opt}$, the expected value is $\delta y^{simul} = 250$ nm. Taking into account the efficiency to measure the signal $\epsilon_s = 0.12$ (corresponding to a RoI-size $w_{RoI} = FWHM/2$), the expected measured value is $\delta y^{simul}_{mes} = 30$ nm. This value, reported on figure 9.15, is in good agreement with the measured direct deflection signal.

We note that the measured signal is not perfectly proportional to the peak intensity of the pump. It is due to the interference of the pump with the probe at low intensity. Indeed, at low energy, the pump energy is of the same order, or even smaller than the probe energy. Therefore, the interference at focus of the amplitude of the electric fields of the probe E_{probe} and the pump E_{pump} contribute to the resulting intensity at focus. The shift Δy then becomes:

$$\Delta y \propto (E_{\text{pump}} + E_{\text{probe}})^2 \propto I_{\text{pump}} + I_{\text{probe}} + 2|E_{\text{pump}} E_{\text{probe}}| \tag{9.15}$$

where I_{pump} and I_{probe} are the intensities of the pump and probe respectively. The term I_{probe} must be removed since the effect of the probe on itself is cancelled when applying the ON-OFF subtraction. The energy of the probe pulse being constant during the measurements, the

deflection signal becomes:

$$\Delta y = a \times I_{\text{pump}} + b \times \sqrt{I_{\text{pump}}} \tag{9.16}$$

where a and b are constants. This function has been fitted to the data of the amplified deflection signal Δy and a good agreement is obtained. The same function, divided by the measured amplification factor $\mathcal{A} = -23$, is superposed to the data of the measured direct deflection signal δy. There is a good agreement, despite the large statistical errors.

9.4.4 Deflection signal as a function of the impact parameter

In this section, we present the results of the measurements of the deflection signal as a function of the impact parameter b, for a pump energy of 6 μJ, a minimum waist at focus of $w_0 = 35\,\mu$m, and a pulse duration of about 200 fs (corresponding to a peak intensity of about 3 TW/cm^2). To this end, we first adjust the pump pulse position at focus to have the optimal impact parameter $b = b_{opt}$, using a dedicated CCD camera placed at focus (as explained in section 9.1.2). Then, we vary the impact parameter value by vertically translating the pump beam at focus, using a piezo-motorised mirror placed before the focusing lens (L-3) on the pump path. However, the piezo-motor steps only provide the relative position of the pump (i.e. the impact parameter) and the absolute position remains unknown. Therefore, we first shift the pump upward (with respect to the probe at focus) to a large impact parameter value, at about $b = 3 \times b_{opt}$ where the deflection signal is almost null. Then, we shift the pump downward step by step to the opposite impact parameter value.

The direct deflection signal δy varies as a function of the impact parameter b, such as (see equation 2.7):

$$\delta y(b) = \delta y_{max} \, \frac{b}{b_{\text{opt}}} \, e^{\frac{1}{2}\left(1-\left(\frac{b}{b_{\text{opt}}}\right)^2\right)} \tag{9.17}$$

The direct deflection is null when the pump and probe pulses are completely overlapped in the interaction area ($b = 0$), and is maximal and equal to δy_{max} when $b = \pm b_{opt}$. This dependence is used to calibrate the absolute value of b, namely its zero value $b = 0$ and its optimal value $b = b_{opt}$. Figure 9.16 (left panel) shows the measurements of the direct deflection signal measured as a function of the impact parameter and the result of the fit of the function given in equation 9.17.

On the other end, the amplified deflection signal Δy is given by the "ON-OFF" barycenter measurement in the dark output of the interferometer, for which the intensity profiles $I_{ON}(y)$ and $I_{OFF}(y)$ of the ON and OFF barycenters respectively are defined by (from equations 9.14 and 2.30, with $\delta a \ll 1$ for high amplification):

$$\begin{aligned} I_{ON}(y) &= (\delta a)^2 \times I_{in}\Big(y + \mathcal{A} \times \delta y(b)\Big) + \left(\delta\phi(y) + \frac{\delta\psi(b)}{2}\right)^2 \times I_{in}\left(y - \frac{\delta y(b)}{2}\right) \\ I_{OFF}(y) &= \Big((\delta a)^2 + (\delta\phi(y))^2\Big) \times I_{in}(y) \end{aligned} \tag{9.18}$$

where I_{in} is the input intensity entering the interferometer, $\delta\phi(y)$ is the phase noise of the interferometer which may vary along the vertical y coordinate, and $\delta\psi$ is the phase signal

which is uniform but also depends on the impact parameter b, such as (see also equations 2.9 and 2.10):

$$\delta\psi(b) = \delta\psi_0 \, e^{-\frac{1}{2}\left(\frac{b}{b_{\text{opt}}}\right)^2} \tag{9.19}$$

It means that the phase signal $\delta\psi$ is maximal when $b = 0$.

Therefore, the amplified deflection signal Δy is sensitive to both the direct deflection signal $\delta y(b)$ and the phase signal $\delta\psi(b)$, knowing that both vary differently as a function of the impact parameter.

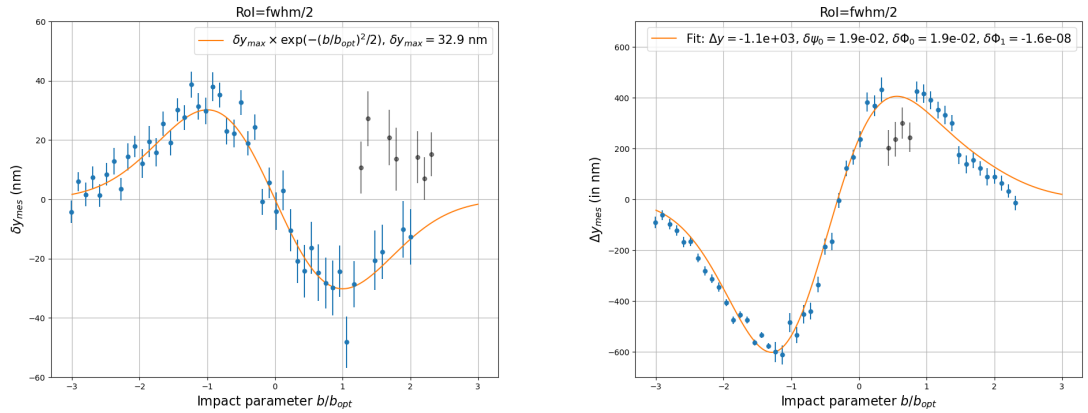

Figure 9.16: Measured deflection signal as a function of the impact parameter b of the pump pulse in the interaction area over its optimal value b_{opt}. (Left) Direct deflection signal δy_{mes} without amplification. We fit, in orange, that signal using the function: $\delta y(b) = \delta y_{max}\,(b/b_{\text{opt}})\,\exp((1-(b/b_{\text{opt}})^2)/2)$. (Right) Amplified deflection signal $\Delta y_{mes} = \mathcal{A} \times \delta y_{mes}$, where the amplification factor $\mathcal{A}$ is negative as expected. In orange line is the result of the fit taking into account the phase signal $\delta\psi(b)$ and the phase noise $\delta\phi(y) = \delta\phi_0 + \delta\phi_1 y$ (see text for details).

Figure 9.16 (right panel) shows the measurements of the amplified deflection signal Δy_{mes}, as a function of the impact parameter b of the pump pulse. Firstly, we verify that the amplification is negative as expected: a positive un-amplified signal δy_{mes} will lead to a negative amplified signal Δy_{mes}. Secondly, we can see that the amplified signal Δy_{mes} is not null at $b = 0$ and its two maxima are not equal (i.e. asymmetric in amplitude). This is precisely due to the influence of the phase noise $\delta\phi(y)$ through the coupling term $\delta\phi(y) \times \delta\psi(b)$, where $\delta\psi(b)$ varies differently as a function of the impact parameter b. A numerical fit has been applied to the data. It is based on equation 9.18 and takes into account the deflection signal $\delta y(b)$, the phase signal $\delta\psi(b)$ and the phase noise $\delta\phi(y)$ which is modelled at first order as a linear dependence on y, such as:

$$\delta\phi(y) = \delta\phi_0 + \delta\phi_1 \times y \tag{9.20}$$

The fit is calculated with four free parameters: δy_{max}, $\delta\psi_0$, $\delta\phi_0$ and $\delta\phi_1$. The result of the fit, plotted on figure 9.16, is in remarkably good agreement with the data. The amplification factor

is $\mathcal{A} \simeq -17$ at $b = -b_{opt}$, and $\mathcal{A} \simeq -11.5$ at $b = +b_{opt}$. This asymmetry is precisely due to the presence of the phase noise which also reduce the amplification factor. To illustrate this phenomenon, we plot on figure 9.17 the fitted function when the phase noise is null: $\delta\phi_0 = \delta\phi_1 = 0$ (green dashed line). The expected deflection signal Δy is now symmetrical in amplitude and null when $b = 0$. More importantly, we also note that the maximal expected deflection signal Δy_{max} (when $b = b_{opt}$) increases when the phase noise is null (the difference is marginal if we also assume a null phase signal $\delta\psi_0 = 0$ which is physically not realistic, as shown in purple dashed line). Thus, the phase noise reduces the amplitude of the amplified interferometric deflection signal Δy, which is a very important result. The value of the amplification factor is biased by the presence of the vertical gradient of the phase noise. As of yet, the exact value of the amplification factor is one of the main limitations, for which the measurement is not completely mastered with all systematic involved. Finally, we also plot the expected signal when the phase noise is uniform and independent of y ($\delta\phi = \delta\phi_0$ and $\delta\phi_1 = 0$). In that case, the expected signal is even slightly smaller than the measured signal, meaning that the vertical dependence of the phase noise ($\delta\phi_1 \times y$) tends to slightly increase the measured signal.

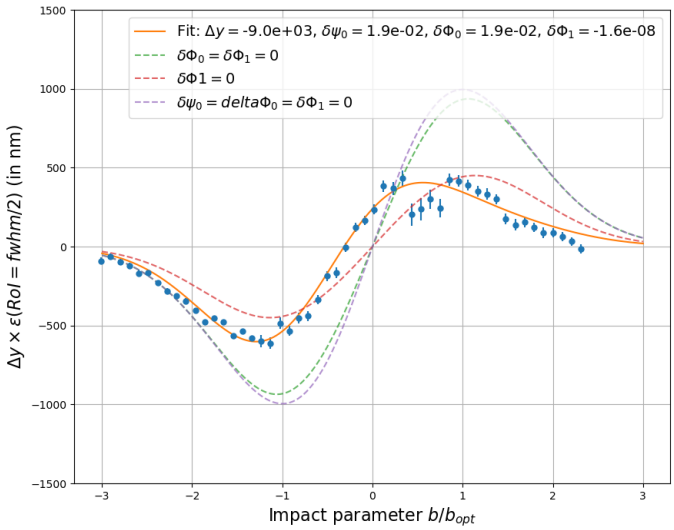

Figure 9.17: Measurement of the amplified interferometric deflection signal Δy as a function of the impact parameter b, normalised to b_{opt}. In orange line is the result of the fit, taking into account the phase signal $\delta\psi(b)$ and the phase noise $\delta\phi(y) = \delta\phi_0 + \delta\phi_1 y$. In dashed line, the same function is plotted but with different hypothesis for the phase noise and phase signal (see text for details).

9.4.5 Deflection signal as a function of the polarisation of the pump

In this section, we present the results of the measurements of the amplified interferometric deflection signal, as a function of the polarisation p of the pump in the interaction area, for a pump energy of 6 μJ, a minimum waist at focus of $w_0 = 35\,\mu$m and a pulse duration of about

200 fs (corresponding to a peak intensity of about 3 TW/cm^2).

To this end, we vary the polarisation orientation of the pump pulse from p to s-polarisation, by rotating the half wave plate ($\lambda/2 - 1$) placed on the pump optical path, mounted on a piezo-motorised rotation in the vertical plane. Meanwhile, the probe pulse remains p-polarised. Noting α the rotation angle of the half wave plate, the relative polarisation angle between the pump and the probe is then $\theta_{\text{pol}} = 2\alpha$. The intensity of the pump is decomposed along its two linear polarisations I_p^{pump} and I_s^{pump}, such as:

$$I^{\text{pump}} = I_p^{\text{pump}} \times \cos^2(\theta_{\text{pol}}) + I_s^{\text{pump}} \times \sin^2(\theta_{\text{pol}}) \tag{9.21}$$

Figure 9.18 shows the result of the measurements of the amplified deflection signal Δy as a function of the relative polarisation angle θ_{pol} between the pump and probe pulses. Data are in good agreement with the fitted function $\Delta y = \Delta y_{max} \times \cos^2(\theta_{\text{pol}})$ (in dashed line). The signal is maximal when the relative polarisation angle is null, i.e. when the probe and pump polarisations are parallel, and the signal is null when their polarisations are perpendicular. This is an important result, which needs to be confirmed with better accuracy. Indeed, we can see a slight asymmetry of the signal amplitude for relative polarisation angles of $\theta_{\text{pol}} = 0°$ and $\theta_{\text{pol}} = 180°$, which is probably due to the preferential polarisation axis of the half wave plate. We also observe a small horizontal shift Δx for $\theta_{\text{pol}} = 180°$, while this signal is absent for the symmetric angle $\theta_{\text{pol}} = 0°$. This might come from a variable phase noise $\delta\psi(x, y)$ during data collection. Indeed, this phase noise has a variable component in the horizontal x-direction, thus generating a small deflection signal at $\theta_{\text{pol}} = 180°$.

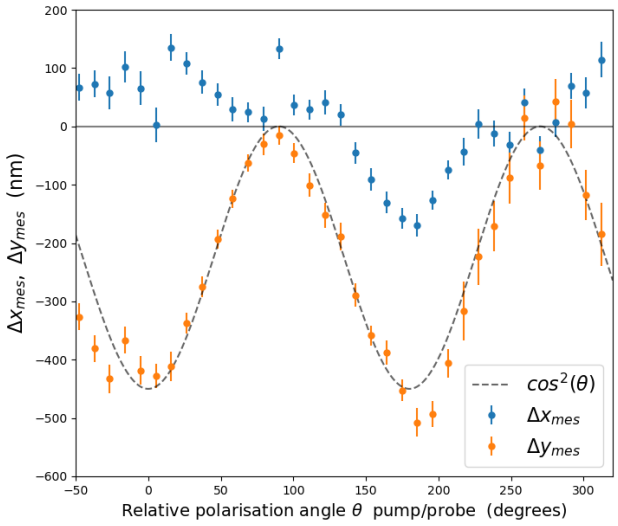

Figure 9.18: Amplified deflection signals Δy (orange) and Δx (blue), in y and x-directions, as a function of the relative polarisation angle θ_{pol} between the pump and probe pulses in the interaction area. The dotted curve corresponds to the expected signal $\Delta y \propto \cos^2(\theta_{\text{pol}})$.

9.4.6 Deflection signal as a function of the RoI-size

The variation of the deflection signal as a function of the RoI-size is an important test to verify that the residual phase noise does not introduce any bias, as already discussed in section 9.3.4. Figure 9.19 shows an example of the variation of the amplified interferometric deflection signal Δy, as a function of the RoI-size w_{RoI} (normalised to the width w FWHM of the transverse intensity profile), for a pump energy of 5 μJ, a minimum waist at focus of $w_0 = 35\,\mu$m and a pulse duration of about 70 fs (corresponding to a peak intensity of about 7 TW/cm^2). The variation of the signal amplitude is in remarkably good agreement with the fitted expected signal efficiency (defined in equation 3.11) for $w_{RoI}/w \leq 1.5$.

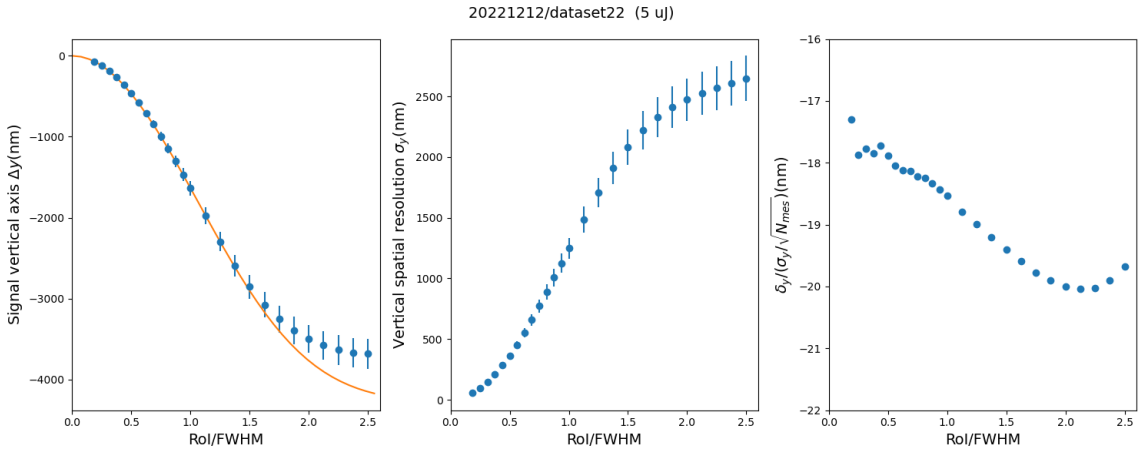

Figure 9.19: Effect of the RoI-size (normalized to the width FWHM of the transverse intensity profile) on the amplified deflection signal Δy, for a set of measurements with a pump energy of 5 μJ and a pulse duration of 70 fs (FWHM), corresponding to a peak intensity of 7 TW/cm^2. (Upper left plot) Amplitude of the measured signal Δy_{mes} as a function of the RoI-size. The orange curve is the expected signal efficiency (defined in equation 3.11). (Upper right plot) Spatial resolution σ_y as a function of the RoI-size. (Lower Plot) Statistical confidence level (in number of sigma) of the measured signal: $C = \Delta y/(\sigma_y/\sqrt{N_{mes}})$, N_{mes} being the number of "ON-OFF" measurements, as a function of the RoI-size.

In contrast to the result obtained in section 9.3.4, where the phase noise and its hot spots strongly affected the signal amplitude for $w_{RoI}/w \geq 0.5$, here the phase noise affect the signal only for a RoI-size $w_{RoI}/w \geq 2$ corresponding to an efficiency $\epsilon_s(w_{RoI}/w = 2) \simeq 0.9$.

Moreover, we also plot the spatial resolution σ_y as a function of w_{RoI}/w (top right panel on figure 9.19). As already studied and discussed in chapter 7, the spatial resolution is degraded when the RoI-size increases due to the mechanical vibrations of the interferometer. Finally, we plot the statistical confidence C (defined in equation 9.8), as a function of w_{RoI}/w (lower panel on figure 9.19). The statistical confidence is relatively constant, and is maximal for a RoI-size $w_{RoI}/w \approx 2$.

In conclusion, unlike the measurements at low amplification without spatial filter where the signal was biased by the phase noise, the amplified signal measured here with a pure

p-polarised probe and with a spatial filter in the dark output of the interferometer varies as the expected theoretical efficiency, showing that now the phase noise does not bias the signal anymore when the RoI-size is increased.

9.5 Summary

In conclusion, these measurements in air are an important achievement of the DeLLight project since they validate the DeLLight interferometric measurement of a deflection signal induced by an index gradient produced by a pump pulse. The amplitude of the signal varies as expected as a function of the experimental parameters, namely the intensity, the impact parameter, the time delay and the polarisation of the pump. Moreover, these measurements demonstrate the amplification of the deflection signal through the interferometric technique. It also shows the role of the phase signal and the phase noise as a possible systematic bias. Finally, we plan to measure in the next month the deflection signal as a function of the air pressure inside the vacuum chamber.

Conclusion and outlook

During this PhD thesis, we managed to prove the feasibility of the DeLLight project and the characterisation of critical parameters limiting the sensitivity of the experiment, namely the extinction factor $\mathcal{F}$, the spatial resolution σ_y and the focalisation quality of the probe and pump pulses at focus. To this end, we developped two interferometer prototypes in femtosecond regime (with and without focalisation in the interaction area).

The best extinction factor we managed to reach is $\mathcal{F} = 3 \times 10^{-6}$ using Prototype 2 (with focalisation), as was the goal.

Then, we measured the ultimate shot noise resolution of the CCD cameras, using a dedicated test bench, and we managed to reach $\sigma_y = 13$ nm.

Furthermore, the measurement of the spatial resolution in the dark output showed that beam pointing fluctuations are completely suppressed (using the "ON-OFF" subtraction method to extract the signal), which allowed to reach the shot noise for the low amplification configuration of the interferometer (rotated polarisation of the probe pulse). However, for the high amplification configuration (rotated interferometer beamsplitter), the resolution is still limited by the phase noise induced by mechanical noise coming from the optics of the interferometer.

At last, the interferometric measurement technique of the DeLLight experiment was validated by measuring the Kerr effect in a material medium using low energy (μJ) co-propagating probe and pump pulses. We first measured the Kerr effect in a silica slide, without focalisation of the probe and pump pulses in the interferometer (Prototype 1). We then measured the Kerr effect in air, with focalisation of the probe and pump pulses (Prototype 2), with an amplification of about 25 (obtained by comparing the amplified shift Δy with the direct deflection signal δy). Thus, we checked that the shift Δy of the intensity profile in the dark output fluctuated with four experimental parameters as expected, namely the pump energy, the impact parameter between the probe and the pump in the interaction area, the relative polarisation probe-pump, and the temporal synchronisation delay of the pump with the probe. Let us note that the measurements in air were conducted with the pilot interferometer that will be used for the first measurements in vacuum in the near future.

Several improvements and development prospects of the DeLLight project are planned. One of the important experimental limitations as of now is the phase noise in the dark output of the interferometer, induced by mechanical vibrations of the interferometer itself, which degrades the spatial resolution and prevents us to reach the shot noise resolution. Indeed, the current spatial resolution is an order of magnitude above the shot noise. An improvement of the mechanical isolation is needed. It is also needed to develop the high frequency phase noise

suppression technique which has been proposed in this dissertation, in order to measure and suppress the phase noise. First tests are planned for the next months.

Let us note that all the measurements presented in this manuscript were fulfilled with co-propagating pump and probe pulses in the interaction area. That is why, before moving on to Kerr measurements in vacuum where counter-propagating pulses are mandatory, the spatio-temporal synchronisation of counter-propagating pulses will have to be tested in air first. This will be one of the main focus of next year. Stability and overlapping control of the probe and pump pulses in the interaction area will need to be properly studied.

Finally, an important needed improvement is to reduce the minimum waist at focus of the probe and pump pulses in the interaction area. Indeed, the DeLLight signal is inversely proportional to the cube of the waists at focus, which are themselves inversely proportional to the size of the collimated pulses before focus. The current waists at focus are approximately 30 μm while the goal is 5 μm. Focusing the pump pulse to a minimum waist of 5 μm is realistic. It is however more difficult for the probe beam. Indeed, it requires larger beam sizes in the interferometer, which encounter two difficulties. First, the phase noise will be increased. Second, it will increase non linear effects in the interferometer beamsplitter because a larger probe beam entails a thicker beamsplitter to properly separate the back-reflections from the interference signal on the CCD camera. Another approach to reduce the waist at focus while keeping a relative small size of the collimated beam in the interferometer is to lower the probe wavelength from 800 nm to 400 nm. This also constitutes a planned upgrade in the DeLLight project.

The journey is only just beginning for the DeLLight project, and I for one can not wait to see what happens next ~

Appendix A

π-phase shift between the probe and the reference in the dark output of the Sagnac interferometer

In the output of the Sagnac interferometer, the probe and the reference interfere destructively, thanks to the π phase-shift between them. Hence, an extinction occurs in what we call the "dark output". As illustrated in figure A.1, this phase-shift comes from the fact that the electromagnetic field of a given pulse coming from a low index medium n_1 (air) and reflected on a higher index medium n_2 (beamsplitter of the interferometer here) is shifted by π. The contrary is not true, namely there is no phase-shift of the field for a pulse coming from a higher (n_2) to a lower (n_1) index medium. Indeed, the continuity principle can be written:

$$r = \frac{n_1 - n_2}{n_1 + n_2} \tag{A.1}$$

where r is the reflection coefficient of the beamsplitter in amplitude. Thus, the reflection coefficient is negative ($r < 0$) for $n_1 < n_2$ and there is a π phase-shift. Similarly, we have $r > 0$ when $n_1 > n_2$ and there is no phase-shift.

Finally, for the beamsplitter of the interferometer with a coating on the input side, there is a π phase-shift of the probe on the first reflexion and no phase-shift on the second reflexion. Moreover, there are no phase-shifts for the reference which is transmitted two times. Thus, the total phase-shift in the dark output is π.

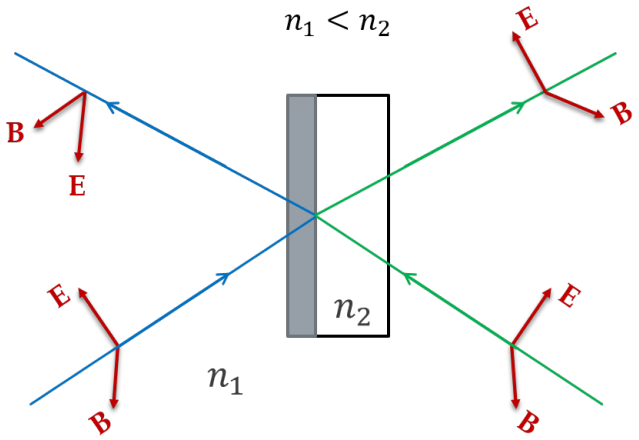

Figure A.1: Schematic showing: (Blue) the electromagnetic field of a beam coming from a low index medium n_1 (air) and reflected on a higher index medium n_2 (beamsplitter of the interferometer), which then induces a π phase-shift ; (Green) the electromagnetic field of a beam coming from a high index medium n_2 and reflected on a lower index medium n_1, which then induces a null phase-shift.

Appendix B

Measurement of the anti-reflective coating factor of the beamsplitter of the Sagnac interferometer

B.1 Measurement method

The method to measure the anti-reflective coating factor R_{AR} of the beamsplitter is schematised on figure B.1.

The photo-diode in position 1 (left schematic) measures the intensity I_1 of the reflected pulse inside the Sagnac interferometer, with the incident beam attenuated by a set of low neutral optical densities of total density $D2$, along with a stronger one of density $D1$. The detected intensity is then:

$$I_1 = \frac{I_0}{2} \times 10^{-D1-D2} \tag{B.1}$$

for which the equivalent amplitude of the electrical signal recorded on an oscilloscope connected to the photo-diode is V_1.

The photo-diode in position 2 (right schematic) measures the intensity I_2 of the back-reflection ($I_{AR,1}$) in the dark output of the interferometer, with the incident beam attenuated by only the same set of low neutral optical densities of total density $D2$. The detected intensity is then:

$$I_2 = \frac{I_0}{2} \times 10^{-D2} \times R_{AR} \tag{B.2}$$

for which the equivalent amplitude of the electrical signal is V_2.

Thus, the reflection factor R_{AR} of the anti-reflective coating of the beamsplitter is given by:

$$R_{AR} = \frac{V_2}{V_1} \times 10^{-D1} \tag{B.3}$$

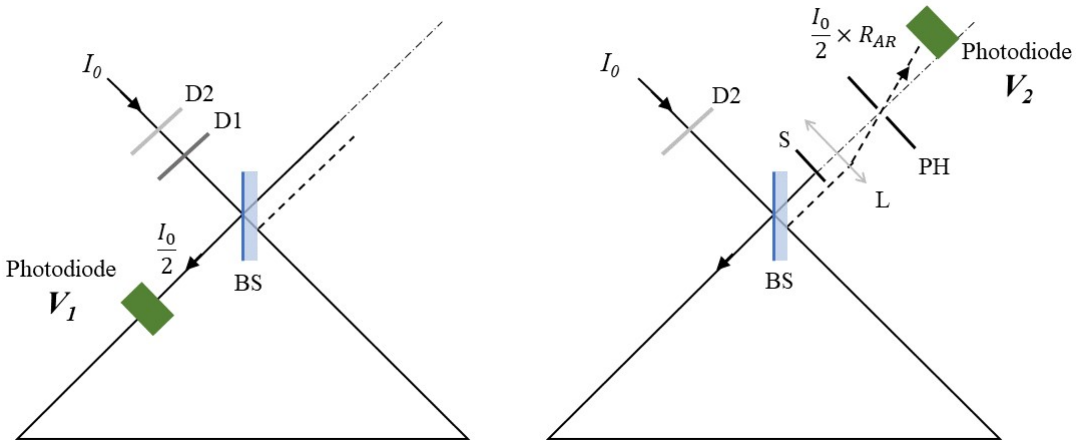

Figure B.1: Schematic of the measurement method of the anti-reflective coating factor R_{AR} of the beamsplitter. (Left) The photo-diode measures the intensity I_1 of the reflected pulse inside the Sagnac interferometer. $D2$ and $D1$ are neutral optical densities used to attenuate the incident beam of intensity I_0 ($D2 < D1$). The electrical current measured by the photo-diode is V_1. (Right) The photo-diode measures the intensity I_2 of the back-reflection in the dark output of the interferometer, after spectral filtering (with the spectral filter S) and spatial filtering (with the spatial filter PH positioned after the lens L). Only $D2$ attenuates the incident beam this time. The electrical current measured by the photo-diode is V_2.

B.2 Calibration of the neutral densities

First of all, we need to calibrate the neutral optical densities needed for the measurement, using a calorimeter in the micro-joule range and measuring the energy of the laser pulse before and after crossing each of the optical densities. To this end, we use the incident pulse before before it separates into the probe and pump beams (i.e. before beamsplitter BS-2 on figure 4.4). The incident energy per pulse is then $E_{0,1} = 57\,\mu$J. The duration of the pulse is about 70 fs and its diameter (FWHM) is about 1 mm.

We first measure two low neutral optical densities for which the nominal density values of the manufacturer are $d_1 = d_2 = 0.3$. The measured densities are then:

$$d_{1,mes} = d_{2,mes} = -log\left(\frac{28.5\,\mu J}{57\,\mu J}\right) = 0.3 \tag{B.4}$$

which is in agreement with the nominal value.

Secondly, two stronger densities with unknown nominal values d_3 and d_4 are measured using higher energy pulses at the output of the compressor (from figure 2.3), such as $E_{0,4} = 192\,\mu$J (same duration and diameter of the beam). The measured densities are then:

$$d_{3,mes} = -log\left(\frac{35.5\,\mu J}{192\,\mu J}\right) = 0.75 \tag{B.5}$$

$$d_{4,mes} = -log\left(\frac{0.59\,\mu J}{192\,\mu J}\right) = 2.5 \tag{B.6}$$

Moreover, we check that there is no saturation effect by measuring the four densities at an even higher energy (620 μJ): the same density values are obtained.

Finally, according to the measurement experimental setup shown on figure B.1, $D1$ corresponds to the high density d_4 and $D2$ corresponds to the set of the 3 low densities d_1, d_2 and d_3. Thus, the final neutral densities used for this measurement are:

$$D1 = d_4 = 2.5 \tag{B.7}$$

$$D2 = d_1 + d_2 + d_3 = 0.3 + 0.3 + 0.75 = 1.35 \tag{B.8}$$

B.3 Measurement of R_{AR}

Firstly, we measure the intensity of the beam inside the Sagnac interferometer by using the photo-diode (Thorlabs). The experimental setup of the interferometer used for this measurement is shown on figure 4.4. The interferometer is first adjusted at maximal extinction, with the incidence beam arriving at 45° on the Sagnac beamsplitter. Then, the neutral optical densities $D1 + D2$ measured before are added before the interferometer. To avoid background light from diffusing external light, a black tube (around 4 cm long) is placed in front of the photo-diode and the vacuum chamber is closed using a black cover. The photo-diode signal is readout by an oscilloscope, so that we measure its amplitude V_1. After checking that there is no signal offset when the beam is blocked just before the interferometer beamsplitter (signal amplitude below 3 mV), we measure (after neutral densities $D1 + D2$ before the beamsplitter) then amplitude:

$$V_1 = 3.6 \text{ Volts} \tag{B.9}$$

Secondly, we measure the intensity of the back-reflection by placing the photo-diode in the dark output of the interferometer (as seen on figure B.1). After removing the high optical density $D1$, we need to isolate the back-reflection spot in the dark output. To this end, we record intensity profile in the dark output with the CCD camera which is placed after the spatial filtering stage composed of the optical lens L and the pinhole PH at the focal point of the lens (see figure B.1 and section 4.2.3). We then use a razor blade to block off the second back-reflection and the interference signal. The latter has a very low intensity since we are at maximal extinction. The possible diffraction generated by the blade edge is suppressed by the spatial filter. Thus, we only record the direct back-reflection $I_{AR,1}$ on the CCD camera. Additionally, we place an iris (mounted on a black tube) in front of the CCD camera, centred around the back-reflection.

Finally, we can remove the CCD camera and place the photo-diode behind the iris and tube in order to measure the current amplitude V_2 which is proportional to the back-reflection intensity. We measure: $V_2 = 1.2$ Volts. The signal reach a maximal value of $V_2' \approx 1.5$ Volts when the iris in front of the photo-diode is further opened. It indicates the possible systematic error on the measurement, so wee take the average value:

$$V_2 = 1.35 \pm 0.15 \text{ Volts} \tag{B.10}$$

At last, using equation (B.3), we calculate the reflection factor of the anti-reflective coating of the beamsplitter:

$$R_{AR} = \frac{V_2}{V_1} \times 10^{-D1} = (1.1 \pm 0.1) \times 10^{-3} \tag{B.11}$$

which corresponds to the manufacturer's approximate value.

Appendix C

Measurement of the CCD gain

In order to experimentally measure the gain of the CCD cameras, we need to collect what we call "flat images" which corresponds to CCD images where the sensor is completely and uniformly lit by an uniform intensity profile. This way, each pixel of the sensor receives the same amount of photo-electrons in average which enables to check whether the gain per pixel is uniform or not.

Using the same test bench as described in section 6.1, we use a simple LED light and an optical diffuser to uniformly light up the CCD camera. It is important to illuminate the sensor as uniformly as possible, in order to avoid an intensity gradient that could skew the measurements. On figure C.1 are shown flat images of the CCD 1.85 (left) and 5.86 (right). As we can see, the flat image of the CCD 5.86 is even. However, the flat image of the CCD 1.85 seems to have an intensity gradient in the vertical direction but this doesn't come from the way the sensor was lit. The CCD camera was uniformly lit but, because of the very high number of pixels for this camera, its acquisition mode (called "Global Reset Release Shutter" which is a rolling shutter mode) integrates the intensity from top to bottom with a certain latency, hence the difference in intensity between the top and bottom of the sensor. We will verify in the next section that the distribution of the reconstructed gains of each pixel is well uniform.

C.1 Analysis and gain measurement results

C.1.1 CCD 5.86

In this section, we want to measure the gain per pixel of the CCD 5.86. The data presented here were collected on March, the 14th, 2022 (dataset 8 containing 600 flat images). A reminder that the size of the sensor is 1920 x 1200 pixels.

The analysis method first consists of collecting the ADU content $N_{ADU}^{i,j,k}$ of each pixel (i, j), for each image k of the dataset. Then, for each pixel (i, j), we calculate the mean ADU content $\langle N_{ADU}^{i,j} \rangle$ over all the events and the associated standard deviation $\sigma_{ADU}^{i,j}$. Finally, we obtain the gain per pixel: $G^{i,j} = \frac{\langle N_{ADU}^{i,j} \rangle}{)\sigma_{ADU}^{i,j})^2}$.

The distribution of the gain $G^{i,j}$ per pixel is shown on figure C.2 and the corresponding histogram on figure C.3. The mean value of the gains, averaged over all the pixels, is $\langle G \rangle^{5.86} =$

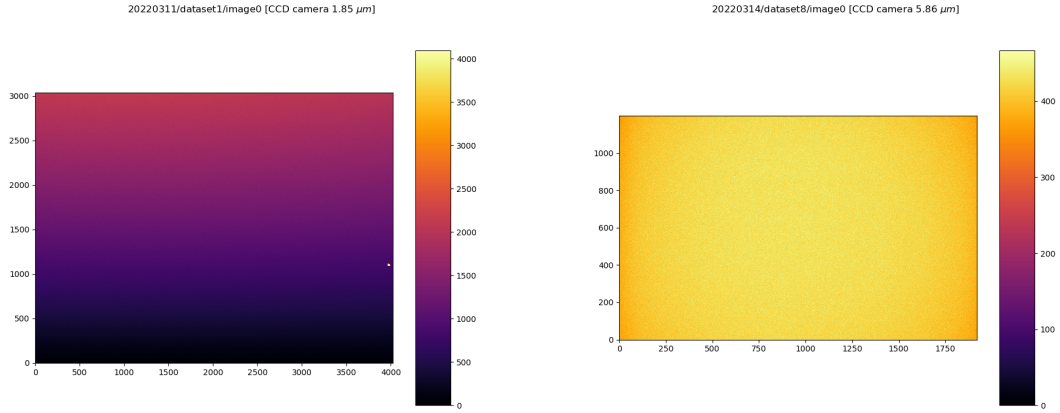

Figure C.1: Flat CCD images of the CCD 1.85 (left) and the CCD 5.86 (right), obtained by uniformly lighting up the CCD sensor using a LED light and an optical diffuser. The colour scales are in ADU content.

7.68 ± 0.02 (standard deviation of $\sigma^{5.86} = 0.45$). The histogram distribution of the gains is also in good agreement with the fitted Gaussian distribution of mean value of the fitted Gaussian distribution is $\langle G \rangle_{fit}^{5.86} = 7.66 \pm 0.02$ (standard deviation of $\sigma_{fit}^{5.86} = 0.45$).

Additionally, we show on figure C.4 the evolution of the intensity over all the events which correspond to the sum of the ADU content of all pixels for each flat image. We clearly notice two different pattern for the first 300 events and the last 300. Thus, we can make the analysis again and plot a histogram for each pattern which will give an estimation of a possible systematic error on the gain value per pixel. We obtain:

$$\begin{cases} \text{first 300 events: } \langle G \rangle^{5.86} = 7.72 \ (\sigma^{5.86} = 0.64) \ ; \ \langle G \rangle_{fit}^{5.86} = 7.66 \ (\sigma_{fit}^{5.86} = 0.63) \\ \text{last 300 events: } \langle G \rangle^{5.86} = 7.73 \ (\sigma^{5.86} = 0.64) \ ; \ \langle G \rangle_{fit}^{5.86} = 7.68 \ (\sigma_{fit}^{5.86} = 0.63) \end{cases} \tag{C.1}$$

C.1.2 CCD 1.85

Using the same kind of analysis, we measured the gain per pixel of the CCD 1.85. The data presented here were collected on March, the 11th, 2022 (dataset 1 containing 500 flat images). The size of the sensor is 3000 x 4000 pixels but only a window of 1000 x 2000 pixels was used for technical problems with Python's memory storage capacity.

The gain per pixel $G^{i,j}$ in colour scale is shown on figure C.5 and the histogram of the gain per pixel $G^{i,j}$ is shown on figure C.6, along with the Gaussian fit (purple). The gain of the CCD camera 1.85 and the corresponding standard deviation are: The results are:

$$\begin{cases} \langle G \rangle^{1.85} = \langle G \rangle_{fit}^{1.85} = 2.79 \pm 0.01 \\ \sigma^{1.85} = \sigma_{fit}^{1.85} = 0.19 \end{cases} \tag{C.2}$$

Finally, we plot the evolution of the intensity for the CCD 1.85 on figure C.7. We can distinguish two pattern (although less pronounced than for the CCD 5.86) for the first 340

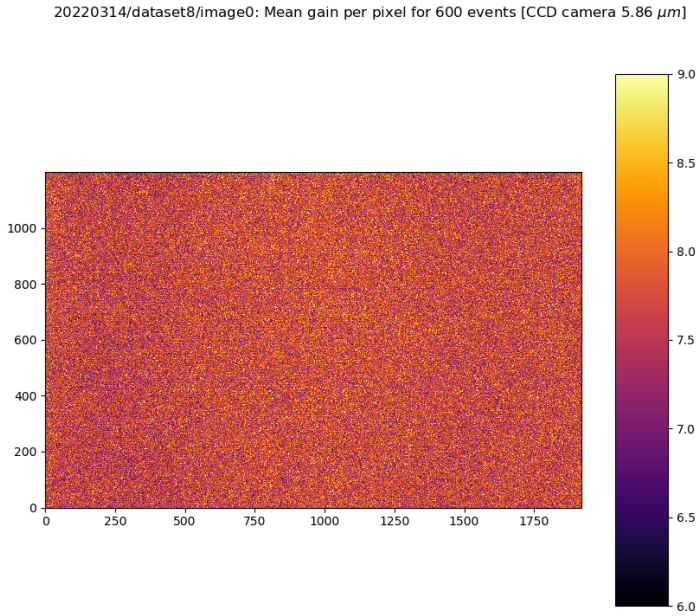

Figure C.2: Distribution of the calculated gain $G^{i,j}$ per pixel (i, j) for the CCD camera 5.86 (dataset 8, collected on March, the 14th, 2022).

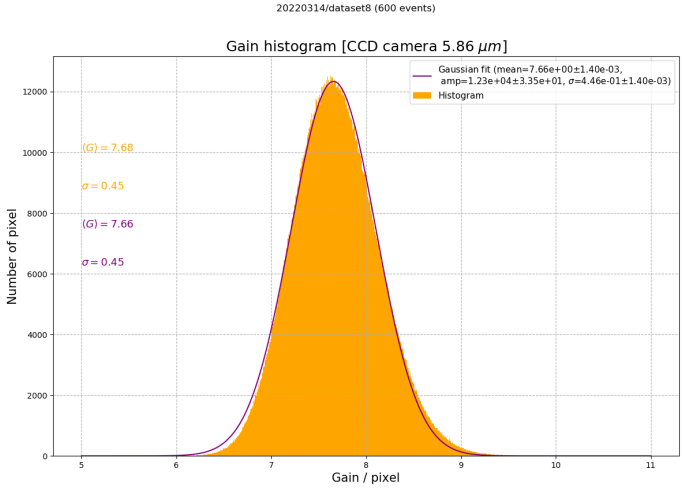

Figure C.3: (Orange) Histogram of the gain $G^{i,j}$ of each pixel (i, j) for the CCD camera 5.86, where the mean gain is $\langle G \rangle^{5.86} = 7.68 \pm 0.02$ (standard deviation $\sigma^{5.86} = 0.45$) ; (Purple) Gaussian fit of the histogram, where the mean gain is $\langle G \rangle^{5.86}_{fit} = 7.66 \pm 0.02$ (standard deviation $\sigma^{5.86}_{fit} = 0.45$) (dataset 8, collected on March, the 14th, 2022).

events and the last 160 events, which gives an idea of the errors on the gain values per pixel

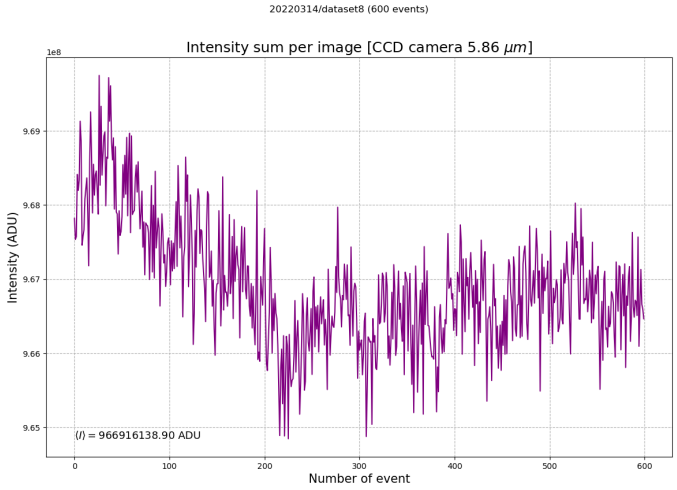

Figure C.4: Plot of the evolution of the integrated intensity per flat image (in ADU) over time for the CCD camera 5.86 (dataset 8, collected on March, the 14th, 2022).

(for 500 events):

$$\begin{cases} error(\langle G \rangle^{1.85}) = 0.03 \\ error(\langle G \rangle^{1.85}_{fit}) = 0.01 \end{cases} \tag{C.3}$$

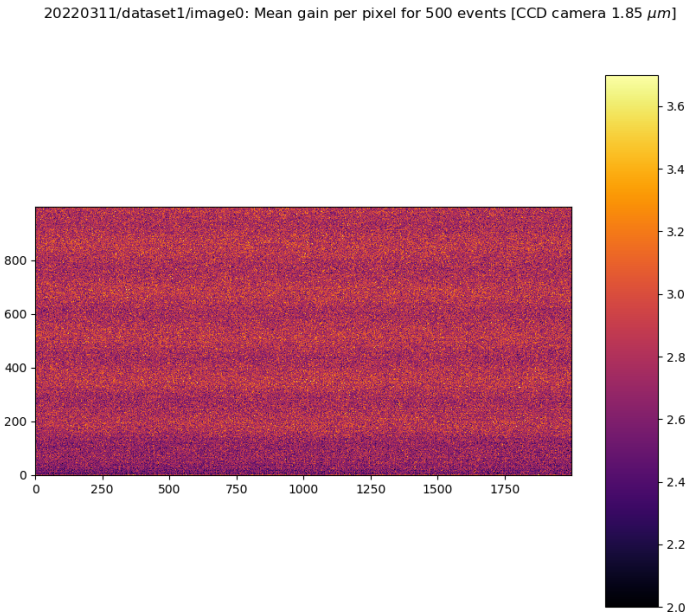

Figure C.5: Distribution of the calculated gain $G^{i,j}$ per pixel (i, j) for the CCD camera 1.85 (dataset 1, collected on March, the 11th, 2022).

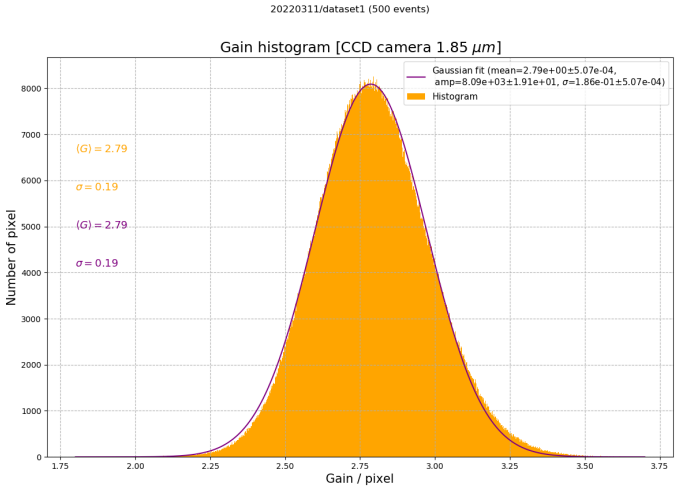

Figure C.6: (Orange) Histogram of the gain $G^{i,j}$ of each pixel (i, j) for the CCD camera 1.85 ; (Purple) Gaussian fit of the histogram. The mean gain is $\langle G \rangle^{1.85} = \langle G \rangle^{1.85}_{fit} = 2.79 \pm 0.01$, with standard deviation $\sigma^{1.85} = \sigma^{1.85}_{fit} = 0.19$ (dataset 1, collected on March, the 11th, 2022).

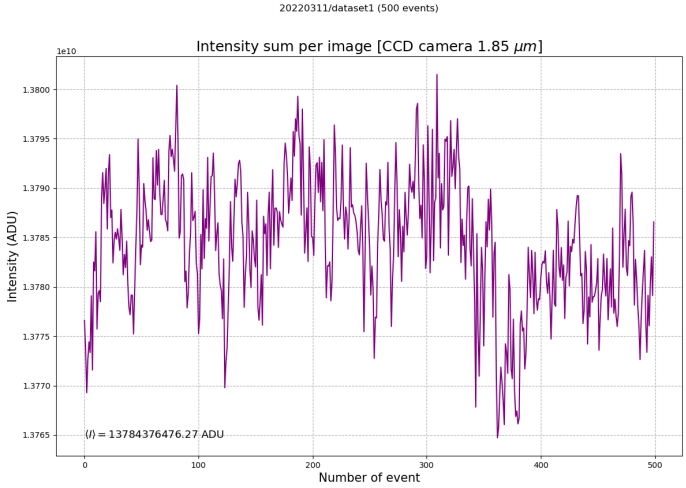

Figure C.7: Plot of the evolution of the integrated intensity per flat image (in ADU) over time for the CCD camera 1.85 (dataset 1, collected on March, the 11th, 2022).

Appendix D

Monte-Carlo Simulations of the shot noise and the beam pointing fluctuations

We generate N_{shot} laser pulses by Monte-Carlo. For each pulse k we calculate a transverse intensity profile for the signal $I_k^s(x,y)$ and the reference $I_k^r(x,y)$ with a gaussian distribution. For each pixel of size $d_x \times d_y$, we calculate the number of photo-electrons $N_k^{\gamma.e.}(x_i, y_j)$ given by:

$$N_k^{\gamma.e.}(x_i, y_j) = N_0^{adu} \times G_{ccd} \times \exp\left(-\frac{(x_i - x_{0,k})^2 + (y_j - y_{0,k})^2}{2\sigma_{xy}^2}\right) \tag{D.1}$$

where

- N_0^{adu} is the adu content of the pixel with maximal intensity,
- G_{ccd} is the gain of the CCD,
- The width (fwhm) of the transverse intensity profile is $\Delta_{xy} = 2\sqrt{2\ln 2} \times \sigma_{xy}$

For each laser pulse k, we have introduced a random beam pointing fluctuation $(x_{0,k}, y_{0,k})$ with a gaussian distribution of r.m.s. σ_{beam}. This fluctuation is the same for the signal and the reference profile since both beam are supposed to be correlated and altered by the same beam pointing fluctuations.

We define an analysis window equivalent to the Region of Interest *RoI* with dimensions $N_{pix} \times N_{pix}$. The positions (x_i, y_j) of the pixels are defined as:

$$x_i = (i - 1 - N_{pix}/2) \times d_x, \quad i = 1, N_{pix} + 1 \tag{D.2}$$

$$y_j = (j - 1 - N_{pix}/2) \times d_x, \quad j = 1, N_{pix} + 1 \tag{D.3}$$

$$\tag{D.4}$$

In order to simulate the statistical fluctuation of the number of photo-electrons per pixel $N_k^{\gamma.e.}(x_i, y_j)$ (shot noise), we add for each pixel a statistical gaussian fluctuation of the number of photo-electron of this pixel:

$$N_k^{\gamma.e.}(x_i, y_j) = N_k^{\gamma.e.}(x_i, y_j) + \delta N_k^{\gamma.e.}(x_i, y_j) \tag{D.5}$$

where $\delta N_k^{\gamma.e.}(x_i, y_j)$ is calculated using a random gaussian sampling centered at 0, and with sigma $\sigma = \sqrt{N_k^{\gamma.e.}(x_i, y_j)}$.

The intensity profile $I_k(x_i, y_j)$ (adu content per pixel) of the pulse k is obtained by dividing the number of phto-electrons by the gain of the camera:

$$I_k(x, y) = N_k(x_i, y_j)/G_{adc} \tag{D.6}$$

Finally, we analyse the simulated CCD image of the two pulses, the "signal" and the "reference", as standard data using the same analysis method and same python analysis program as the one used to analyse real data, and applying the analysis method to suppress the beam pointing fluctuations. We obtain the simulated spatial and intensity resolutions σ_x^{MC}, σ_y^{MC} and $\sigma_{\Delta I/I}^{MC}$.

Appendix E

Synthèse

En électrodynamique classique, les équations de Maxwell sont linéaires dans le vide. La vitesse de la lumière, la perméabilité et la permittivité du vide sont des constantes universelles. L'indice optique ne dépend pas des champs électromagnétiques externes et est constant ($n = 1$). En revanche, dans un milieu diélectrique, les équations de Maxwell ne sont plus linéaires : la vitesse de phase n'est alors plus constante et l'indice optique dépend cette fois-ci des champs externes appliqués sur ce milieu optique. Un effet non-linéaire bien connu et qui utilise des champs lasers en tant que champs externes s'appelle l'effet Kerr optique. L'indice optique vu par une impulsion laser dans le milieu considéré est modifié, ce qui induit une variation d'indice δn proportionnelle à l'intensité laser I_{laser} (W/cm^2) telle que : $\delta n = n_2 \times I_{laser}$, où n_2 est appelé l'indice Kerr (cm^2/W).

En 1936, Euler et Heisenberg montrent que le vide quantique devrait également être un milieu optique non linéaire, dû aux couplages des champs électromagnétiques avec les pairs électrons-positrons du vide. Leur description, purement ondulatoire, montre que l'indice optique du vide devrait être augmenté, c'est-à-dire que la vitesse de la lumière devrait diminuer lorsque le vide est soumis à des champs électromagnétiques externes intenses. Cette prédiction théorique a été reformulée plus tard dans le formalisme de l'électrodynamique quantique (QED) en tant que diffusion photon-photon. Cet effet optique non linéaire dans le vide, prédit par Euler et Heisenberg, n'a encore jamais été observé.

L'expérience DeLLight (Deflection of Light by Light) cherche à mesurer cet effet en utilisant des impulsions laser femtosecondes intenses délivrées par la plate-forme LASERIX ($\mathcal{E} = 2.5$ J, 30 fs, 10 Hz), situé au laboratoire IJCLab (Université Paris-Saclay). La méthode expérimentale DeLLight ainsi que les paramètres critiques de l'expérience sont décrits dans le chapitre 2. L'expérience DeLLight est de type pompe-sonde où une impulsion laser focalisée de basse intensité (sonde) interagit de façon contre-propageante avec une impulsion externe focalisée de haute intensité (pompe), décalée verticalement (selon l'axe y) par rapport à la sonde. Le couplage des champs de ces deux impulsions induit alors un gradient d'indice dans le vide, proportionnel au profil en intensité de la pompe, effet similaire à l'effet Kerr optique mais dans le vide. La sonde se réfracte alors sur ce gradient d'indice, avec une rotation de ses plans d'ondes produisant une deflection moyenne du faisceau sonde. En focalisant les impulsions pompe de 2.5 Joules délivrées par LASERIX sur une largeur transverse de 5 μm, équivalent à une intensité pic laser de $I_{laser} \approx 10^{20}$ W/cm^2 ($B \approx 10^5$ T et $E \approx 3 \times 10^{13}$ V/m), la variation

d'indice optique attendue dans le vide est $\delta n \approx 1.6 \times 10^{-13}$ et l'angle de déflection moyen du faisceau sonde est $\langle \delta\theta \rangle_y \approx 0.1$ prad.

Cette déflection étant trop faible pour être mesurée de façon directe, elle est amplifiée par méthode interférométrique. L'interféromètre utilisé est un interféromètre de Sagnac qui possède une configuration "fermée". Il est constitué d'une lame séparatrice 50/50, de deux miroirs et de deux lentilles. Les deux faisceaux contre-propagants dans le Sagnac constituent alors la sonde et la référence, tous deux focalisés par les lentilles. Ils sont déphasés de π en sortie sombre et interfèrent ensuite destructivement. Ce profil en intensité résiduel, appelé l'extinction, est mesuré en sortie par une caméra CCD. Le facteur d'extinction $\mathcal{F}$ est alors défini comme le rapport de l'intensité en sortie sombre par l'intensité du faisceau incident.

Lorsque la pompe focalisée est envoyée dans le Sagnac, elle perturbe uniquement la sonde puisque la référence n'est pas synchronisée temporellement avec la pompe. La déflection angulaire $\langle \delta\theta \rangle_y$ de la sonde se traduit par un déplacement spatial vertical δy direct après recollimation tel que $\delta y = f \times \langle \delta\theta \rangle_y$, où f est la longueur focale des lentilles. L'interférence destructive des impulsions de sonde et de référence à la sortie de l'interféromètre produit un déplacement vertical transversal Δy du barycentre du profil d'intensité résiduelle, mesuré par une caméra CCD. Ce déplacement Δy est amplifié par rapport au déplacement direct δy. Le facteur d'amplification $\mathcal{A}$, définit comme $\mathcal{A} = \Delta y / \delta y$, est inversement proportionnel à la racine carrée du facteur d'extinction de l'interféromètre : $\mathcal{A} \propto 1/\mathcal{F}$. Cette mesure est possible en réalisant des mesures successives avec (ON) et sans (OFF) interaction avec la pompe (mesure relative). On réalise ainsi une succession de mesures "ON-OFF" pour obtenir de la statistique et mesurer le signal moyen $\langle \Delta y \rangle$.

Le signal attendu Δy est inversement proportionnel à la racine du facteur d'extinction et inversement proportionnel au cube des largeurs de faisceaux au foyer, qui constituent donc les paramètres critiques de l'expérience. L'objectif est d'atteindre une extinction de $\mathcal{F} = 4 \times 10^{-6}$ (correspondant à une amplification $\mathcal{A} = 250$) et des largeurs de faisceaux focalisés au foyer dans la zone d'interaction de $w = 5$ μm. Le signal attendu est alors $\Delta y \approx 15$ pm. De plus, un autre paramètre à prendre en compte pour la sensibilité de l'expérience est la résolution spatiale, dont l'objectif est d'atteindre $\sigma_y = 10$ nm qui correspond au bruit quantique ultime de la meilleure caméra CCD à notre disposition. Avec le taux de répétition de 10 Hz du laser LASERIX, le signal attendu pourrait être observé à 5 sigma après 25 jours de données collectées.

Le principe des méthodes d'analyses de données CCD pour l'extraction du signal $\langle \Delta y \rangle$ recherché et la suppression des fluctuations de pointé du faisceau laser est décrite au chapitre 3 de cette thèse. On montre que les fluctuations de pointés sont corrigées grâce à la mesure simultanée de la position du faisceau donnée par la réflexion en face arrière. Tout d'abord, on définit une taille de fenêtre d'analyse, ou Region of Interest (RoI), pour le calcul des barycentres du profil en intensité du signal d'interférence d'une part, et de la réflexion en face arrière d'autre part. On définit également l'efficacité de mesure du signal de déplacement du barycentre comme le rapport entre le déplacement mesuré sur le déplacement réel. On calcule alors comment cette efficacité dépend de la taille de la RoI. Plus la RoI est grande et plus le déplacement mesuré est proche du déplacement réel.

Pour mesurer les paramètres critiques de l'expérience, deux prototypes successifs d'interféromètre de Sagnac en régime femtoseconde ont été développés (avec et sans focalisation dans l'air) au cours de cette thèse, pour lesquels les setup expérimentaux et les méthodes d'alignement sont présentés dans le chapitre 4. Ils ont permis de démontrer la faisabilité du projet et de caractériser les paramètres critiques limitant actuellement la sensibilité de l'expérience. Il est important de noter que ces prototypes utilisent des impulsions sonde et pompe co-propagantes dans l'air, et non pas contre-propagantes comme l'expérience DeLLight dans le vide.

Le premier paramètre étudié est l'extinction de l'interféromètre. Sa mesure est présentée dans le chapitre 5. On montre que le prototype avec focalisation a permis d'atteindre un facteur d'extinction de $\mathcal{F}_{max} = 3 \times 10^{-6}$, mesuré relativement par rapport aux réflections en face arrière sur la séparatrice (et collectées sur la caméra) pour lesquels l'extinction est de $\mathcal{F}_{AR} = 5 \times 10^{-4}$. L'objectif d'extinction maximal est finalement atteint. Cependant, pour réaliser des mesures DeLLight de déplacement de profil en sortie sombre, il faudra plus d'intensité sur la caméra CCD pour optimiser la résolution spatiale, ce qui n'est actuellement pas possible car les réflections en face arrières sont trop intenses et trop proche de la zone du signal d'interférence. Il faudra donc par la suite développer une nouvelle lame séparatrice ayant un coefficient de réflexion en face arrière plus faible, et une lame plus épaisse pour éloigner les réflexions en face arrière de la zone du signal d'interférence.

Le second paramètre étudié est la résolution spatiale de l'expérience, qui est limitée par le bruit quantique des caméras CCD, les fluctuations de pointés du faisceau laser, et le bruit de phase. Cette étude est présentée dans les chapitres 6 et 7.

Dans le chapitre 6, on présente les résultats de mesures du bruit quantique obtenus sur un banc de test dédié pour deux caméra CCD sélectionnées. La méthode d'extraction numérique du signal et de mesure de résolution spatiale est identique à celle utilisée pour l'expérience DeLLight et décrite dans le chapitre 3. La mesure de bruit quantique a montré qu'on pouvait atteindre une résolution spatiale de $\sigma_y = 13$ nm. Ainsi l'objectif initiale d'une résolution spatiale de l'ordre de 10 nm limitée par le bruit quantique est atteint.

Le chapitre 7 présente la mesure de la résolution spatiale du signal d'interférence en sortie sombre qui inclue cette fois-ci le bruit des fluctuations de pointé du faisceau et le bruit de phase de l'interféromètre. Pour mener à bien ces mesures, il a fallu tout d'abord dégrader l'extinction de l'interféromètre afin d'augmenter l'intensité en sortie sombre (on est en effet limité par les réflexions en face arrière). Il existe pour cela deux méthodes : la basse et haute amplification. Leur principe est comme suit :

- Basse amplification : on tourne légèrement la polarisation du faisceau incident dans l'interféromètre grâce à une lame demi-onde. L'impulsion incidente étant polarisée p, on introduit une petite composante s. De plus, la séparatrice étant optimisée en polarisation p, on introduit une asymétrie en intensité entre le faisceau réfléchi et le transmis, ce qui dégrade l'extinction en sortie sombre. Finalement, comme le facteur d'amplification dépend de cette asymétrie en intensité en polarisation s, le facteur d'amplification devient égale à 1, donc il n'y pas d'amplification par interférométrie.

- Haute amplification : cette fois-ci, on ne touche plus aux polarisations mais on tourne la séparatrice sur son axe d'un degré. L'impulsion incidente arrive donc à 46° au lieu de

45°, angle pour lequel la séparatrice est optimisée. Cela introduit donc à nouveau une asymétrie en intensité et le facteur d'amplification attendu est de 25.

En utilisant les méthodes d'analyses décrites au chapitre 3, on montre qu'on arrive à supprimer les fluctuations de pointés grâce à la mesure de la position de la réflexion en face arrière. On montre alors qu'on peut atteindre le bruit quantique de la caméra CCD lorsque l'interféromètre est réglé à faible amplification. En revanche à haute amplification, la résolution reste pour l'instant limitée par le bruit de phase. Ce dernier est induit par le bruit mécanique de l'interféromètre qui est actuellement mal isolé mécaniquement. On montre que la variation du bruit en fonction de la taille de la RoI est en accord avec une simulation Monte-Carlo d'un bruit mécanique correspondant à une rotation des optiques de l'interféromètre de l'ordre de 50 nrad (r.m.s.). Une méthode de mesure et de suppression du bruit de phase à haute fréquence est proposée dans ce manuscrit.

Finalement, on a pu valider la méthode de mesure interférométrique de l'expérience DeLLight en mesurant l'effet Kerr dans un milieu matériel en utilisant une impulsion pompe de faible énergie (μJ). Tout d'abord, comme développé dans le chapitre 8, on mesure l'effet Kerr dans une lame de silice, avec le premier prototype d'interféromètre composé de 3 miroirs et sans focalisation de l'impulsion sonde en zone d'interaction. L'objectif de ces mesures était de voir si la mesure d'un déplacement Δy du profil en intensité en sortie sombre était possible et le cas échéant, de voir si ce signal variait de façon croissante comme attendu avec l'intensité pic de la pompe. Ces mesures ont permis également d'identifier les sources de bruit pouvant perturber le signal, ou encore d'affiner les méthodes d'analyses et de protocoles expérimentaux.

Dans un second temps, des mesures d'effet Kerr dans l'air ont été réalisées avec un interféromètre focalisé à 2 miroirs, dans les deux configurations d'extinction dégradée, comme développé dans le chapitre 9. A basse amplification, ces mesures n'étaient pas concluantes, notamment à cause de biais de mesure non contrôlés. En effet, l'amplification du signal de déflection étant faible, on était alors très sensible au biais lié au bruit de phase. En revanche, ces mesures étaient primordiales à l'amélioration du setup expérimental : son optimisation, son efficacité et sa practicalité. Les protocoles d'alignements, de mesures et d'analyses ont également été fortement optimisés. Il est important de noter que l'obtention d'un signal robuste et reproductible à basse amplification a été très complexe et a donc nécessité beaucoup de temps.

Finalement, les mesures DeLLight dans l'air ont été réalisées à haute amplification. Le principal objectif était de valider l'amplification de la mesure interférométrique DeLLight (amplification attendue à $\mathcal{A} = 25$). Pour cela, il a été possible de mesurer simultanément le signal direct non amplifié δy et le signal amplifié Δy, et ce grâce à une des réflections en face arrière sur la séparatrice correspondant à la déflection directe δy. Le signal mesuré a été étudié en fonction de différents paramètres : l'intensité pic de la pompe, le délai temporel entre la pompe et la sonde, la polarisation relative entre la pompe et la sonde, et le paramètre d'impact (distance transverse entre la pompe et la sonde au foyer). Nous avons tout d'abord vérifié que le signal mesuré augmente comme attendu lorsque l'intensité de la pompe augmente. De plus, le facteur d'amplification a été mesuré à 25, comme attendu. Ensuite, l'optimisation

du délai pompe/sonde est très important pour obtenir le plus grand signal possible. Le signal mesuré évolue comme attendu avec le délai pompe/sonde, autrement dit le signal est maximal lorsque les deux impulsions sont parfaitement synchronisées et le signal est compatible avec zéro lorsque la pompe est en retard de 200 fs. Par ailleurs, comme mentionné précédemment, la polarisation relative pompe/sonde est essentielle pour optimiser le signal. La mesure a montré une évolution également comme attendue : le signal est maximal lorsque les polarisations pompe/sonde sont parallèles et minimal lorsqu'elles sont perpendiculaires. Finalement, un autre paramètre important pour optimiser le signal est le paramètre d'impact qui correspond au recouvrement spatial entre la pompe et la sonde au foyer. Le signal direct δy mesuré est alors nul lorsque les impulsions sont superposées, ce qui est attendu car la perturbation de la sonde par la pompe est symétrique et la déflection moyenne est nulle. Il y a ensuite deux optimums de valeur du paramètre d'impact optimal, ce dernier étant défini comme la largeur de faisceau au foyer divisé par la racine de 2. Cependant, la mesure du signal amplifié Δy met en évidence l'influence du bruit de phase généré par le désalignement résiduel de l'interféromètre. Ce bruit de phase introduit une asymétrie en amplification entre les deux optimums du paramètre d'impact, autrement dit les deux facteurs d'amplification sont $\mathcal{A} = 12$ et $\mathcal{A} = 17$. De plus, le signal ne s'annule pas comme attendu lorsque les deux impulsions sont superposées. Ce bruit de phase résiduel est actuellement le paramètre le plus limitant de l'expérience. Une méthode de suppression du bruit de phase à haute fréquence est actuellement en court de développement. De plus, le setup expérimental devra être mieux isolé mécaniquement pour réduire le bruit de phase.

Pour conclure, les deux principaux paramètres critiques limitant la sensibilité de l'expérience, l'extinction et la résolution spatiale ont été mesurés. L'objective d'extinction a été atteint à $\mathcal{F} = 3 \times 10^{-6}$ et la résolution spatiale ultime, correspondant au bruit quantique de la meilleure caméra CCD, a été atteint à $\sigma_y = 13$ nm. Cependant, la résolution spatiale mesurée en sortie sombre de l'interféromètre a uniquement été atteinte dans la configuration à basse amplification. En revanche, à haute amplification, le bruit de phase est actuellement trop important et dégrade considérablement la résolution. Une méthode de suppression du bruit de phase a été proposée.

Par ailleurs, les mesures DeLLight réalisées dans l'air ont été essentielles pour démontrer la faisabilité de l'expérience. Le signal DeLLight a été mesuré avec succès en fonction de différents paramètres comme l'intensité pic de la pompe, le délai entre la pompe et la sonde, la polarisation relative pompe/sonde au foyer, ainsi que le paramètre d'impact au foyer. Ces mesures ont également montré l'efficacité de l'amplification du signal de déflection par méthode interférométrique.

Bibliography

[1] M. Faraday, Philos. Mag. Vol. 28, No. 294 (1846)

[2] J. Kerr, Philos. Mag. 50, 332 (1875)

[3] N. Bloembergen, Nonlinear Optics, 4th ed. (World Scientific, Singapore, 1996)

[4] M. Born and L. Infeld, Proc. R. Soc. London, Ser. A 144, 425 (1934)

[5] H. Euler and B. Kockel, Naturwissenschaften 23, 246 (1935)
H. Euler, Ann. Phys. Leipzig 26, 398 (1936)
W. Heisenberg and H. Euler, Z. Phys. 98, 714 (1936)

[6] D. L. Burke *et al.*, Phys. Rev. Lett. 79, 1626 (1997)

[7] H. Abramowicz et al., 'Letter of Intent for the LUXE experiment', arXiv:1909.00860

[8] ATLAS Collaboration, Nature Phys. 13 (2017), pp. 852

[9] CMS Collaboration, Phys. Lett. B 797 (2019) 134826

[10] A. Ejlli et al., Physics Reports 871 (2020) 1–74

[11] A. Cadène et al., Eur. Phys. J. D 68 (2014) 16

[12] X. Fan et al., Eur. Phys. J. D 71 (2017) 308

[13] S.-J. Chen, H.-H. Mei and W.-T. Ni, Modern Phys. Lett. A 22 (2007) 2815

[14] G. Zavattini et al., "Intrinsic mirror noise in Fabry–Perot based polarimeters: the case for the measurement of vacuum magnetic birefringence", Eur. Phys. J. C 78, 585 (2018)

[15] R. Ballou et al., "Letter of Intent to measure Vacuum Magnetic Birefringence: the VMB@CERN experiment", CERN-SPSC-2018-036 / SPSC-I-249 (2018)

[16] G. Zavattini et al., "Polarimetry for measuring the vacuum magnetic birefringence with quasi-static fields: a systematics study for the VMB@CERN experiment", Eur. Phys. J. C 82, 159 (2022)

[17] E. B. Aleksandrov, A. A. Ansel'm, and A. N. Moskalev, "Vacuum birefringence in an intense laser radiation field", Sov. Phys. JETP 62, 680 (1985)

[18] T. Heinzl et al., "On the observation of vacuum birefringence", Opt. Commun. 267, 318 (2006)

[19] B. King and T. Heinzl, "Measuring vacuum polarization with high-power lasers", High Power Las. Sci. Eng. 4, 1 (2016)

[20] H.-P. Schlenvoigt et al., "Detecting vacuum birefringence with x-ray free electron lasers and high-power optical lasers: a feasibility study", Phys. Scr. 91, 023010 (2016)

[21] R.V. Jones, Nature 186, 706 (1960)

[22] R.V. Jones, Proc. Roy. Soc. London Ser. A 260, 47 (1961)

[23] D. Tommasini and H. Michinel, Phys. Rev. A 82, 011803 (2010)

[24] B. King and C. H. Keitel, New J. Phys. 14, 103002 (2012)

[25] A. Di Piazza et al., Phys. Rev. Lett. 97, 083603 (2006)

[26] H. Gies et al., New J. Phys. 15, 083002 (2013)
H. Gies et al., New J. Phys. 17, 043060 (2015)

[27] X. Sarazin et al., ”Refraction of light by light in vacuum”, Eur. Phys. J. D 70, 13 (2016)

[28] S. Robertson, "Optical Kerr effect in vacuum", Phys. Rev. A 100, 063831 (2019)

[29] S.R. Flom et al., "Ultrafast Z-scan measurements of nonlinear optical constants of window materials at 772, 1030, and 1550 nm", Applied Optics F123, 242086 (2015)

[30] V. Loriot et al., ”Measurement of high order Kerr refractive index of major air components: erratum”, Opt. Express, OSA, Vol. 18 No. 3, pp.3011 (2010)

[31] S. Robertson, A. Mailliet, X. Sarazin et al., ”Experiment to observe an optically induced change of the vacuum index”, Phys. Rev. A 103, 023524 (2021)

[32] P. B. Dixon, D. J. Starling, A. N. Jordan, and J. C. Howell, "Ultrasensitive Beam Deflection Measurement via Interferometric Weak Value Amplification", Phys. Rev. Lett. 102, 173601 (2009)

[33] M. D. Turner et al., "Picoradian deflection measurement with an interferometric quasi-autocollimator using weak value amplification", Opt. Lett. 36, 1479 (2011)

[34] S. Robertson, ”Numerical simulation of the DeLLight setup: calculation of the expected signal”, DeLLight Internal Note available at: https://groups.ijclab.in2p3.fr/projetdellight/publications/ (2020)

[35] A. Couairon, A. Mysyrowicz, ”Femtosecond filamentation in transparent media”, Physics Reports 441, 47-189 (2007)

[36] K. Mishima et al., ”Generalization of Keldysh’s theory”, Phys. Rev. A 66 (3) 033401 (2002)

[37] S. Robertson, A. Mailliet, X. Sarazin et al., ”Study of the plasma index generated by the low energy pump pulses used in the DeLLight measurements in air”, DeLLight Internal Note available at: https://groups.ijclab.in2p3.fr/projetdellight/publications/